SISSA
Scuola
Internazionale
Superiore di
Studi Avanzati

International School for Advanced Studies
(SISSA)

PHD Thesis:

Beyond simple variational approaches to strongly correlated electron systems

Candidate: **Daniele Guerci**

Supervisor: Michele Fabrizio
Massimo Capone

Trieste
October, 2019

Via Bonomea, 265
34136 Trieste – Italy
T +39 0403787111
E info@sissa.it
sissa.it

Abstract

For weakly interacting many-body quantum systems one can apply the extensive framework of perturbative quantum field theory. On the other hand, strong interactions can not be treated practically in perturbation theory because of the absence of a small control parameter. In this context variational methods are a powerful tool to obtain reliable informations regarding the properties of the ground state of the strongly correlated electron system. In this thesis we present novel formulations of two widely used methods: the Gutzwiller wave function and the slave-spin theory. These techniques share a similar philosophy and the extensions are based on the common attitude towards a more detailed description of the high-energy incoherent excitations characterizing interacting electron systems together with low-energy quasiparticles excitations, captured by standard approaches. Our task is not only crucial for a faithful description of the insulating phase but also improves the variational characterization of the low-energy quasiparticle excitations.

We apply the novel *ghost*-Gutzwiller wave function technique to tackle an intriguing phenomenon, namely the exciton Mott transition in photoexcited semiconductors. Despite being a quite old topic that goes back to the 1970's, the nature of the exciton Mott transition still defies a complete understanding. By considering an idealised model of photoexcited semiconductors we unveil the important role of the exciton binding energy in determining the nature of the transition. Moreover, our results uncover rather anomalous electron-hole liquid phase next to the transition, which still sustains excitonic excitations although being a degenerate Fermi liquid of heavy mass quasiparticles.

By means of the Dirac-Frenkel variational principle, we generalize the ghost-Gutzwiller wave function to study the out of equilibrium dynamics of strongly correlated electron systems. Numerical results on the single-band Hubbard model show a remarkable agreement with those obtained with time-dependent dynamical mean field theory. We believe that the method opens the way to several promising developments and future applications.

Concerning the slave-particle approach, we consider Anderson impurity models and we show that, within our formulation, the constraint on the slave-spin variable can be removed, leaving thermal average free by any projection on the "physical" subspace of the enlarged Hilbert space. To the best of our knowledge, this represents an exception and shows that our formulation is more convenient than other slave-particle approaches, where the constraint have to be implemented explicitly. The method, suited to deal with impurity models, finds direct application in studying time-dependent transport across an interacting quantum dot. To this aim we formulate, by means of the Keldysh Green's function, the slave-spin mean-field theory in the out of equilibrium framework and we apply the method to the dynamics of a driven quantum dot.

Finally we study the current-voltage characteristic of an interacting quantum dot tunnel-coupled to the edge of a superconductive nanowire. The appearance of the topological Majorana edge mode is signalled by distinctive features in the charge transport properties of the junction. Apart from the well known half-integer zero bias conductance we find that the topological region is characterized by a vanishing Fano factor, that can be measured in experiments to detect the presence of a Majorana zero mode hybridized with the quantum dot.

Contents

1 Introduction

In this Section we briefly introduce the main ideas and results of this thesis, ranging from the main methodological advances to the physical results obtained with these new techniques.

1.1 Methodological advances

Strong correlations in condensed matter physics are at the origin of a plethora of intriguing collective phenomena, high-T_c superconductivity, and a variety of other conventional and unconventional phase transitions. The understanding of the microscopic mechanisms underlying these phenomena has a central importance not only reflected in the theoretical advances but also in potential technological applications. The typical number of interacting constituents in solids, $\sim 10^{23}$, makes their experimental and theoretical study extremely challenging. To clarify this aspect let us consider the simple example of a system composed of N lattice site each occupied by a single spin that can point either $\uparrow$ or $\downarrow$. It is not hard to realize that the number of configurations contained in the many-body wave function grows exponentially with the system size $\sim 2^N$. Even for writing the informations contained in the ground state the computational time and memory required is prohibitive large already for small lattice size. Therefore, it is crucial to develop techniques that are tractable and yet remain flexible enough to allow theorists to incorporate material-specific details into the calculations. There has been a great theoretical effort in developing reliable and efficient schemes to treat strongly correlated electron systems that allow to provide a consistent and robust description of emergent collective phenomena in Condensed Matter Physics, like for instance dynamical mean field theory (DMFT), quantum Monte Carlo, improved density functional theory in the local density approximation LDA+DMFT, matrix-product states and tensor networks.

A class of particularly physically transparent and flexible approximations are based on variational wave functions that often capture the main aspects of the ground-state properties. This thesis finds its place in this framework, and it is motivated by the need of simple and semi-analytical variational methods for strongly correlated electron systems. Our main contribution from a methodological point of view are two remarkable extensions of the standard approaches of this kind, namely a constraint-free slave-spin method and a generalization of the Gutzwiller wave function. Despite the existence of more precise many body techniques, these methods

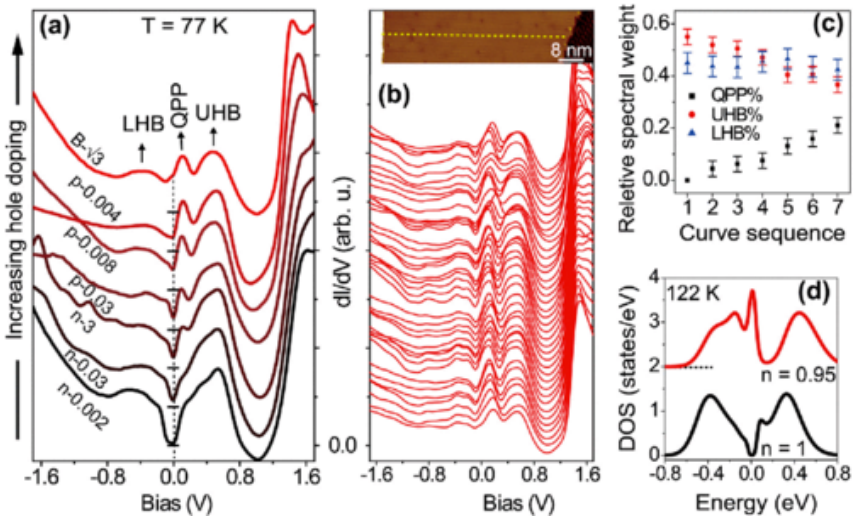

Figure 1.1: Scanning tunnel microscopy measurements of the local density of states of a monolayer Sn on the Si(111) surface with various bulk doping levels. As the density of hole increases, we observe the growth of the low-energy quasiparticle peak (QPP) that is accompanied by the reduction of the spectral weight of the lower (LHB) and upper (UHB) Hubbard bands. Adapted from [190].

are still largely used and often allow to interpret the results of more accurate calculations. For instance, we mention the Brinkman-Rice scenario for the metal-to-insulator Mott transition [38], built with the Gutzwiller approximation, or early theories for high-T_c superconductors based on analytical calculations performed with slave-boson mean-field theory [155, 168]. Moreover, given the complexity of the electronic structure of real materials it would be desirable to have at disposal approximate techniques enough simple and flexible to deal with realistic situations otherwise prohibitive with more accurate numerical approaches, as those previously mentioned.

The conventional Gutzwiller wave function [81] and the slave-particle mean-field theory [156] generally capture only the low-energy coherent quasiparticles, but cannot describe incoherent charge excitations located at energies of the order of the Coulomb repulsion $\sim U$, that form the higher and lower Hubbard bands, see Fig. 1.1. Therefore, these variational approaches describe properly the low-energy properties of the correlated metal (Fermi liquid) but are not able to provide a faithful description of the Mott insulating regime, where low-energy fermionic quasiparticles are absent. A major breakthrough in this direction is represented by the development of the dynamical mean field theory (DMFT) [95], which provides a tool for treating the different energy scales that competes in a strongly correlated electron system. The approach, which neglects spatial dependence of the correlations among the electrons, becomes exact in the limit of infinite lattice coordination [187]. DMFT is nowadays one of the few approaches able to give a detailed description of both low- and high-energy excitations and of the first-order metal-to-insulator Mott transitions. In this thesis we present a novel variational wave function that successfully overcomes the aforementioned problem characterizing the conventional Gutzwiller wave function and slave-particle mean-field theories. The method, named ghost-Gutzwiller wave function variational technique, is characterized by the introduction of N subsidiary fermionic degrees of freedom, it provides a more accurate description of the Mott insulator and captures the coexistence region between the correlated metal and the insulator in the Mott transition. Numerical results in the single-band Hubbard model show noteworthy agreement between the ghost-Gutzwiller wave function and the dynamical mean field theory (DMFT). We will see that the number of auxiliary fermionic levels N represents a crucial parameter and, by increasing N,

we will observe an improvement in the variational energy and in the physical properties of the ground state. This perspective introduces similarities between our variational wave function and matrix-product states or neural network states where the number of "hidden" degrees of freedom is directly connected with the amount of entanglement in the variational wave function. Remarkably, our variational method can be directly extended to the out of equilibrium evolution of strongly correlated electron systems. In this thesis we will present in details the time-dependent ghost-Gutzwiller technique [106] and we will benchmark the method with DMFT and conventional Gutzwiller results on the single-band Hubbard model [72, 73, 247, 248] demonstrating a substantial improvement over the basic Gutzwiller.

In the framework of the slave-particle approach, we will focus on Anderson impurity models and we will introduce a new slave-spin formulation free from any constraint on the slave-spin variables, eliminating the need of any projection on the "physical" subspace of the enlarged Hilbert space. This clearly shows that the new formulation is more convenient than other slave-particle approaches, where the constraints have to be implemented explicitly. Our mapping applies straightforwardly to multi-orbital Anderson impurity models in the absence of local exchange terms on the impurity. Notably, we will also show that single-particle Green's functions of the physical electron can be calculated without any constraints. The latter result enables to perform perturbative calculations that, within a Random Phase Approximation, reproduces not only the low-energy Kondo resonance but also incoherent valence fluctuation peaks. A possible application of the method as DMFT impurity solver for particle-hole nonsymmetric multi-band Hubbard models is foreseen. This slave-spin mapping can be more convenient than working in the original representation. Indeed, as already shown in Ref. [121], the slave-spin mapping endows the Mott transition of a genuine order parameter associated with the local Z_2 gauge symmetry. Thus, it allows to develop an equivalent of the Landau-Ginzburg energy functional for the Mott transition [152]. We conclude by observing that the slave-spin mapping finds direct application to transport in quantum dots. To this aim we will further extend the method to study the out of equilibrium evolution of Anderson impurity models by employing the Keldysh Green's function approach [105]. In order to highlight the improvement achieved with respect to more conventional techniques, we benchmark the results of our novel approaches with numerical renormalization group (NRG) [157, 158] and DMFT ones, by studying well-known model Hamiltonian, such as the Anderson impurity model and the lattice single-band Hubbard model.

In the following we briefly list the four problems that we studied with the above methods as well as our main results.

1.2 Mott transition in photoexcited semiconductors

Photoexcited electron-hole systems in semiconductors offer a unique arena to study novel collective ground states emerging from the electron-electron interaction. One of the intriguing aspects of these systems is that the strength of the Coulomb interaction can be effectively controlled by changing the density of photoexcited electron-hole pairs through the screening effect, by simply changing the excitation light intensity. Above the exciton condensation temperature, the change of the photoexcited carriers causes a metal-to-insulator Mott transition (exciton Mott transition), or crossover, from the insulating exciton gas phase in the low density regime to the metallic electron-hole plasma in the high density regime, see fig. 1.2.

In order to clarify the mechanism that drives the exciton Mott transition we recall the argument originally presented by Sir Neville Mott [197] to explain the insulating phase observed in transition-metal oxides with partially filled bands [63]. Let us consider an ideal system of

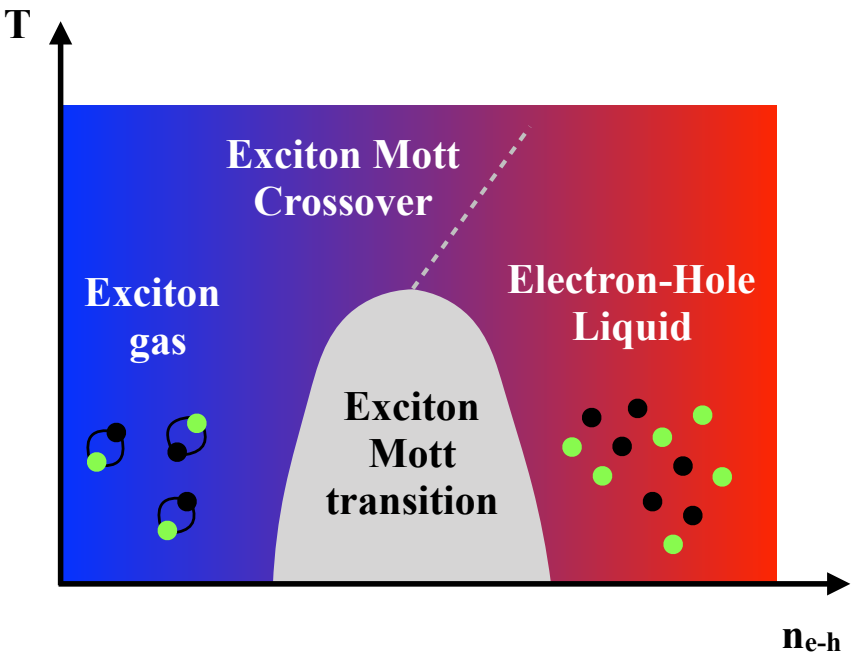

Figure 1.2: Sketch of the typical phase diagram of a photoexcited semiconductor above the exciton condensation temperature.

Hydrogen atoms arranged in a d-dimensional cubic lattice of lattice constant a, that can be varied by an external pressure. Each Hydrogen provides one electron, that can move on the lattice formed by positively charged protons and is subjected to the Coulomb repulsion of the other electrons. The electron hopping amplitude depends on the overlap between the s-atomic orbitals, which, ultimately, is determined by the intersite lattice spacing a. In the atomic regime, when the lattice constant is so large that the hopping amplitude is vanishing, the Coulomb repulsion drives the system towards localization and each site is occupied by a single electron. As soon as the lattice constant becomes finite, it is clear, even in the Mott insulating phase, that the system must allow for charge fluctuations around the mean value, implying some doublon and holon, or it would lose all the hopping energy-gain. In order to describe an insulator, doublons and holons have to be confined in a bound state; otherwise a small electric field could induce an electric current. If we further reduce the lattice constant the density of charge excitations grows and, eventually, due to the screening of the Coulomb excitations, the doublon-holon bound states dissociate into a plasma of free carriers, see Fig. 1.3. Thus, the metal-to-insulator Mott transition can be understood as the transition from an unbound to a bound state of doubly occupied sites (doublons) and empty sites (holons) induced by the screening of the Coulomb interaction.

The most natural realizations of the Mott-Hubbard physics are strongly correlated oxides. Yet, an even more idealized experimental setup for a Mott transition is realized in photoexcided semiconductors above the exciton condensation temperature. In particular, these systems are characterized by a pure Mott transition which is not accompanied by spatial symmetry breaking, in contrast with transition-metal oxides where antiferromagnetic order is usually realized. In this regard, electrons in conduction band and holes in valence one play the role of doublons and holons excitations, the Mott insulator corresponds to the exciton gas and the correlated metal to the electron-hole liquid.

In this thesis we tackle this problem using a powerful extension of the Gutzwiller wave function, named ghost-Gutzwiller wave function, which appears well suited to address some

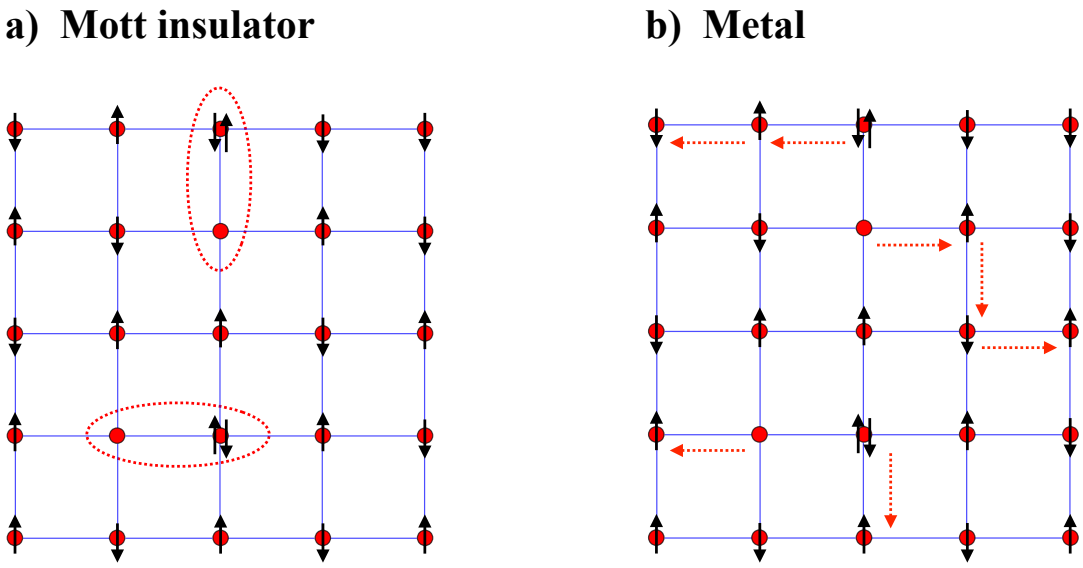

Figure 1.3: Left panel shows schematically the Mott insulating phase, where doublons and holons bind to form "chargeless" states. Right panel, instead, represents the metal, where doublons and holons are free excitations that hop around the lattice. The transition is driven by the density of charge excitations.

important questions raised by the controversial experimental observations and in general by the intriguing physics of photoexcited semiconductors. In this perspective we consider a minimal model that, since the seminal work by Nozières and Schmitt-Rink [213], is believed to capture the essential physics of the exciton Mott transition, i.e., the half-filled single-band Hubbard model at fixed, and large, spin-polarization. Quite surprisingly, despite the half-filled single-band Hubbard model has been scrutinized in depth by an incredible number of different state-of-the-art techniques, including dynamical mean field theory and Quantum Monte Carlo variational approach, yet the nature of the Mott transition at fixed spin-polarization remains controversial. We will show that this upgraded variational approach substantially improves over the standard Gutzwiller approximation in the description of magnetized Mott insulator in lattices with large coordination number, that, in our model, maps into the exciton gas. Our results on the Mott transition in photoexcited semiconductors, that we present in this thesis, agree with experiments and allow identifying the key parameter that controls the nature of the transition: the magnitude of the exciton binding energy. Specifically, we find that for large exciton binding energies (small dielectric constant), the exciton Mott transition occurs as a gradual transition, where in the coexistence region, as the density of electron-hole pairs increases, the fraction of electron-hole droplets grows continuously till the formation of a finite spectral width at the Fermi level. Instead, in the regime of small exciton binding energies (large dielectric constant), the intermediate region is characterized by bistability with a sharp transition from the exciton gas to the electron-hole liquid.

1.3 Nonequilibrium Dynamics

Photoexcited semiconductors can be also seen as a paradigmatic and pioneering example of a novel metastable state, induced by a laser pulse, that provides new informations, complementary to those attainable by studying the matter at equilibrium [28, 51]. Recent years have seen enormous experimental progress in preparing, controlling and probing strongly interacting

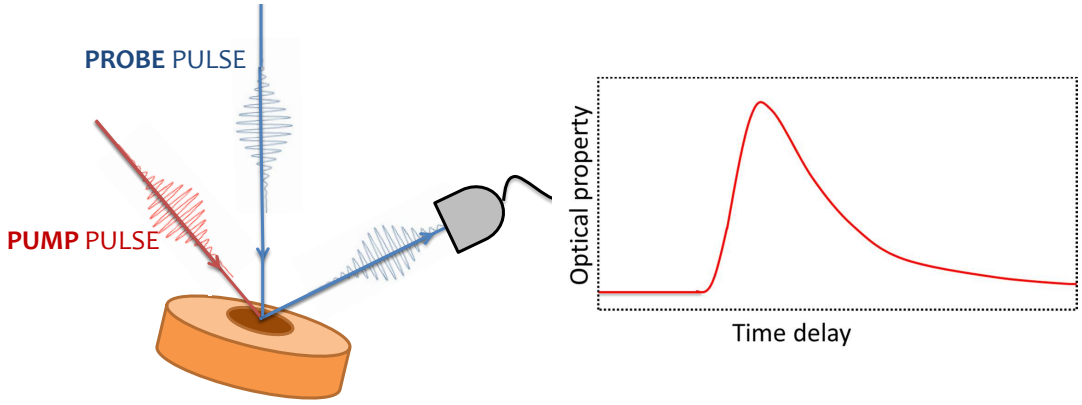

Figure 1.4: Schematic set-up of a time resolved pump probe experiment. The pump excite the sample in an out of equilibrium state. After a delay time Δt the probe pulse measure the pump-induced changes in the optical properties of the system.

quantum systems in different nonequilibrium regimes which led to the development of an entire new field of nonequilibrium quantum physics which aims at the control and manipulation of nonequilibrium matter. Pump-probe experiments, for instance, allow to selectively excite specific degrees of freedom in correlated materials and to disentangle high and low-energy scales otherwise entangled in single-particle excitations and open the way to create novel metastable phase, that cannot be reached via thermodynamic transformations. In this experiments, an ultrafast laser pulse (10-100 fs) is split in two portions; a stronger beam (pump) is used to excite the sample generating an out of equilibrium state, and a weaker beam (probe) is used to measure the transient state, see Fig. 1.4. Monitoring the changes in the optical constants as a function of the delay time yields informations about the relaxation of the system towards the steady-state. Theoretically, a popular protocol to study the nonequilibrium evolution of closed quantum systems consists of the so-called quantum quench [45]. Here the system is initially, at time $t = 0$, prepared in the many-body ground state $|\Psi_i\rangle$ of some Hamiltonian H_i. For times $t > 0$ the system evolves unitarily according to the dynamics given by a different Hamiltonian H_f, which may be related to H_i by varying a parameter such as an external field.

From a theoretical perspective the amount of information, needed to describe the evolution of the ground state of a strongly correlated system, grows exponentially [8] with time and makes the description of the out of equilibrium evolution an extremely challenging problem. Thus, state of the art numerical methods, such as the time-dependent density matrix renormalization group (tDMRG) and time-dependent DMFT, can only access the short-time dynamics and their predictions are limitated to the transient dynamic regime at least in their current implementations.

Motivated by the remarkable improvement observed by introducing subsidiary degrees of freedom in the Gutzwiller wave function at equilibrium, in this thesis we extend the ghost-Gutzwiller method to study the out of equilibrium evolution of strongly correlated systems [106]. Differently from the equilibrium case, where the saddle-point is determined by optimizing the variational energy, the variational principle for the nonequilibrium evolution, also known as the Dirac-Frenkel principle, is obtained by requiring the stationarity of the time-dependent action. This will allow us to cast the time-dependent many-body Schrödinger equation into a simpler, yet non trivial, one. We formulate the method for a generic multi-band Hubbard model. In the out of equilibrium dynamics the subsidiary degrees of freedom induces dephasing mechanism that reduces substantially the coherent oscillations observed in the conventional

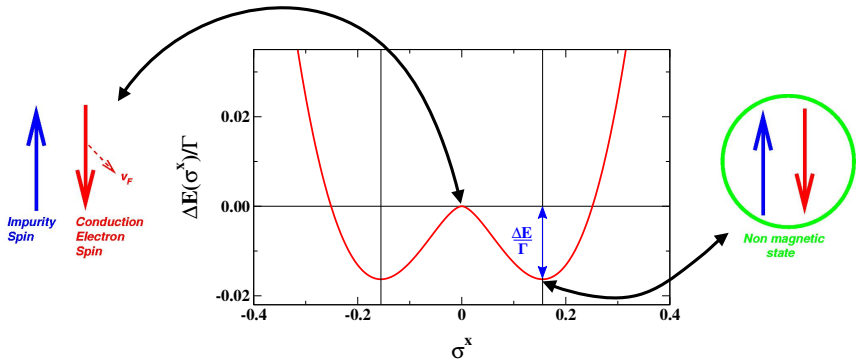

Figure 1.5: Red line shows the ground state energy of a magnetic impurity embedded in a metallic host, measured respect atomic configuration where the magnetic moment on the impurity site is free. The system gain energy in forming a singlet bound state between the spin density of the contacts and the magnetic moment on the quantum dot.

Gutzwiller technique. In particular we will show that the addition of just 2 subsidiary fermions in the Gutzwiller wave function ($N = 3$) provides a more realistic description of the evolution of the charge and quasiparticles degrees of freedom, that much resembles the more accurate results obtained by DMFT [72, 73]. Despite being closer to DMFT results, the method still lacks convergence toward a stationary state in the limit of large time. In this respect, the number of subsidiary degrees of freedom N appears to have a crucial role and we believe that only in the limit of $N \gg 1$ relaxation towards a steady-state can be observed. Our approach is richer than the conventional time-dependent Gutzwiller dynamics, it can be easily applied to realistic materials and shows noteworthy agreement with nonequilibrium DMFT results. Thus, the ghost-Gutzwiller represents a computationally cheap alternative to DMFT, which, in the time-dependent case, becomes an extremely demanding method.

1.4 Transport in quantum dots

While in bulk materials the electron-electron interaction can be screened by the large concentration of carriers, the behavior of quantum dots is greatly affected by the large Coulomb repulsion experienced by localized electrons. In these interesting systems the effect of interaction gives rise to the Kondo effect, that can be considered the simplest collective phenomenon due to strong correlations. Originally observed in magnetic alloys [17, 153], this effect arises in quantum dots with an odd number of electrons, where the ground state of the isolated dot is typically a spin doublet[1]. Connecting the dot to external leads induces a novel state. In particular, the tunnel-coupling amplitude between the contacts and the quantum dot lifts the spin-doublet degeneracy and creates a collective state where, as displayed in Fig. 1.5, the electronic spin density of the contacts screens the localized magnetic moment[2]. In quantum dots the Kondo effect is manifested by the unitary conductance observed by measuring the charge-current characteristic of the junction, that is composed by two metallic contacts coupled to a quantum dot (N-QD-N), see Fig. 1.6. The state of art technique to actually see the screening of the impurity magnetic moment below the Kondo temperature T_K is the Numerical Renormalization

[1] A minimal model that allows to describe the physics of quantum dot is the Anderson impurity model.

[2] The energy splitting of the spin-doublet is controlled by the Kondo temperature T_K, a collective energy scale that measures the energy gain in forming the singlet state between the localized magnetic moment and the spin density of the leads.

Group method (NRG). The method developed by K.G. Wilson in the early 1970's [287] allows to understand the Kondo and related effects at equilibrium.

Differently from metallic alloys, nanoscale quantum dots can be driven out of equilibrium by applying, for instance, a time-dependent gate voltage to the quantum dot or a charge bias to source and drain contacts. From a theoretical perspective, the interplay between the time dynamics and strong correlation effects makes the description the nonequilibrium dynamics of quantum dots extremely challenging. In order to address this problem many innovative approaches have been developed. However, these methods are often limited to study the short-time evolution minimal models, such as the Anderson impurity models or Kondo models, and hence they become intractable for more realistic situations. To fulfill the need of simple and flexible methods, in this thesis, we extend a recently developed slave-spin technique [107] to study the out of equilibrium dynamics of quantum dots [105]. Remarkably, we will show that the time-dependent evolution of these systems can be described in the slave-spin representation without any constraint. The advantages with respect to other slave-particles are twofold. On one side we reduce the number of dynamical equations. On the other side, we avoid the mean-field mixing of the physical and unphysical subspaces.

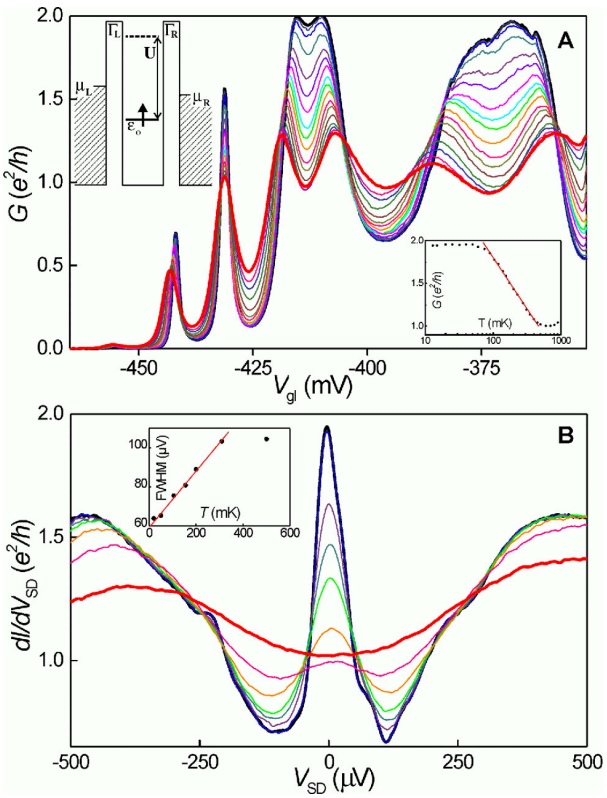

Figure 1.6: Top panel: charge conductance as a function of the barrier gate voltage. Different lines correspond to different values of the temperature, in particular the temperature increases from the blue to the red line. At low temperature the conductance approaches the unitary limit, $G = 2e^2/h$, in correspondence of an half-integer number of electrons in the quantum dot. Bottom panel: differential conductance by applying bias between source and drain contacts. As the temperature increases the zero-bias anomaly is suppressed and disappears for $T \gg T_K$. Adapted from [276].

To highlight the importance of our formulation we apply the method to study nonequilibrium transport properties of a single-level Anderson impurity model. In the steady-state regime a simple self-consistent Hartree-Fock calculation is able to show not only the zero-bias anomaly but also the expected peak at bias of the order of the on-site Coulomb repulsion $\sim U$. Furthermore, we study the time evolution induced by a time-dependent voltage applied to the metallic contacts. After a transient regime $\sim T_K$, the dynamic relaxes to a nonequilibrium steady-state characterized by a finite current through the quantum dot.

Finally, we consider the problem of two quantum dots coupled via a tunnel amplitude. We devise a slave-spin mapping to write the Hamiltonian of the system in the enlarged Hilbert space without any need of local constraint. Although the slave-spin representation allows us to evidence some distinctive features of the model, a simple mean-field calculation predicts a first order transition instead of the expected crossover from the Kondo screened phase to the singlet

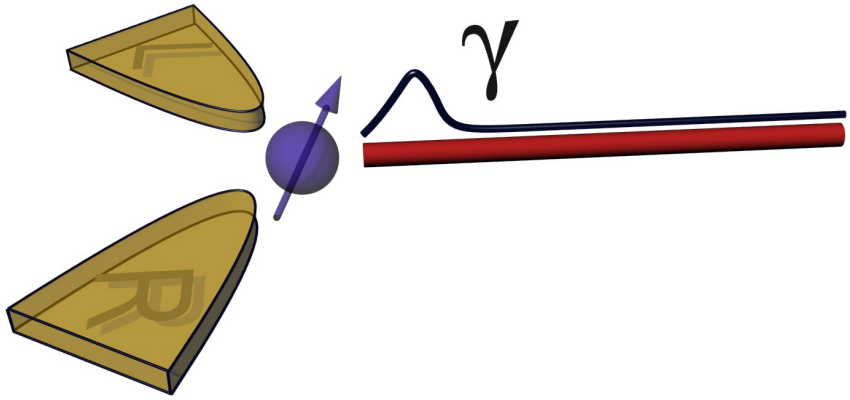

Figure 1.7: The edge of a semi-infinite superconductive nanowire is tunnel-coupled with an interacting dot. To measure influence on the current-voltage characteristic of the MZM, located at the edge of the nanowire, we couple the system to L and R metallic contacts.

one (localized magnetic moments bind to form a singlet state and decouple from the contacts).

1.5 Transport across a Majorana-Anderson junction

One of the most intriguing collective behavior that is realized in Condensed Matter Physics is the emergence of edge states at the boundary of topological materials. An example of these striking phenomena is the appearance of Majorana zero modes (MZM) at the edge of a 1D p-wave topological superconductor, that was originally predicted by Kitaev in Ref. [148]. Strong evidence suggests MZMs have been observed in experiments on proximitized semiconductor nanowires [199] and ferromagnetic chains [128]. Stimulated by the promising application of the MZMs as topologically protected qubits for quantum computations [10, 11, 204], the past few years have seen a large number of theoretical proposal exploiting their non-Abelian nature to produce intriguing phenomena, an outstanding example is the topological Kondo effect [31].

Recently, a new direction has emerged which explores the interplay between pure Majorana physics and electronic correlations. The characterization of phase of matter due to strong Majorana-Majorana interactions predicts novel phenomena that connects Condensed Matter systems to phenomena usually observed in High Energy Theory, i.e. Sachdev-Ye-Kitaev model can be used to describe black-holes. Motivated by theoretical studies [258] and recent experiments [66, 293], we consider electronic transport through a novel class of Hamiltonian models, named Majorana-Anderson impurity models, that consist of a semi-infinite topological superconductor tunnel-coupled with an interacting quantum dot that can be used as a spectrometer to detect the topological properties of the nanowire. By coupling the dot to two metallic contacts we compute the current and the shot noise across the junction which is displayed in Fig. 1.7. Our work shows that the presence of the MZM is manifested by an half-integer zero-bias conductance $G_0 = e^2/2h$. Differently from the in-gap Yu-Shiba-Rosinov-like bound states, the MZM signature in the conductance is robust and is not affected by the Coulomb interaction on the quantum dot. Moreover, we point out that the topological region is characterized by a Fano factor $F = 0$, induced by the tunnel-coupling with the MZM. Combined measurements of the conductance and the shot noise allow to detect the topological properties of the superconducting wire and to distinguish the low-energy contribution of a MZM from other possible sources of zero-bias anomaly. We argue that the predicted behavior of the Fano factor persist even for more realistic

models, that include a more detailed description of the quantum dot and the surrounding leads.

1.6 Plan of the thesis

After introductory Sections, where we will introduce the Gutzwiller wave function and slave-particle techniques with a particular emphasis on the relations between the approaches, we will present in Chapters 3 and 6 the original theoretical methods which have been developed in our work, the ghost-Gutzwiller variational wave function and the slave-spin technique. For details we refer to Appendixes A and C. Additional results of this thesis will be presented in Chapters 4, 5, 7 and 8.

In Chapter 4 we will study photoexcited semiconductors by drawing their phase diagram in the full $E_{\text{ex}} - n_{\text{e-h}}$ plane (Exciton binding energy vs. density of electron-hole pairs), with particular interest in the intermediate regime where the exciton Mott transition occurs. This way we will highlight the important role of exciton binding energy in determining the character of the Mott transition. The evaluation of the single-particle spectral function allows to show the presence of the characteristic excitonic peak, below the bottom of the conduction band, that persists even in the electron-hole liquid phase. Moreover, we find that the effective mass of the unbound electrons and holes is quite large, as is clear from the narrow width of the coherent peak at the chemical potential. Both of these features have been observed experimentally. Additional details on the physics of photoexcited can be found in Appendix B.

In Chapter 5 we present the time-dependent ghost-Gutzwiller variational approach. After a first technical Section, where we formulate the nonequilibrium variational approach for multi-band Hubbard models in the absence of superconductive correlations, we apply the method to the interaction quench dynamics of the single-band Hubbard model. Numerical calculations show a remarkable agreement with more accurate DMFT results.

In Chapter 7 we discuss the extension of the novel formulation of slave-spin technique to nonequilibrium dynamics, a method that allows to study the out of equilibrium dynamics of quantum dots. Notably, the out of equilibrium dynamics of the quantum dot can be obtained in the slave-spin representation without any constraint. Finally we extend the slave-spin mapping to the case of two impurities coupled via a tunnel-coupling amplitude. More details and explicit calculations are left to Appendix D.

In Chapter 8 we study charge transport in a new class of Hamiltonian, named Majorana-Anderson Hamiltonian. These models are not only interesting from an academic point of view but can be realized experimentally. Our aim is to present a complete characterization of the low-energy charge transport properties induced by the presence of a MZM at the edge of a superconductive nanowire. Transport measurements allow to detect the topological properties of the superconductive nanowire and, consequently, to reconstruct the topological phase diagram. The explicit expression of the scattering states, average current and shot noise can be found in Appendix E.

2

Overview on the Gutzwiller wave function and slave-particle theories

In this Chapter we provide an overview of approaches based on the Gutzwiller wave function and slave-particle theories with particular emphasis on the parallelism between these two different methods. Our aim is not only to give a basic introduction to these techniques but also to show their weaknesses and strengths that, in part, are going to be successfully overcome in this work. We provide some crucial considerations that are going to be develop in Chapter 3 and 6, where we report the novel formulation of the Gutzwiller wave function and the constraint-free slave-spin theory.

2.1 The Gutzwiller wave function

A simple wave function that allows to describe correlations effect beyond the independent particle methods (Hartree Fock, Density Functional Theory etc.) was conceived by M. Gutzwiller [111, 112] to describe the ferromagnetism in transition metals. The Gutzwiller wave function is constructed starting from the non-interacting ground state $|\Psi_*\rangle$ and then applying a local projector $\mathcal{P}$ that suppresses the weight of configurations with doubly occupied sites:

$$|\Psi_G\rangle = \prod_i \mathcal{P}(i)|\Psi_*\rangle. \tag{2.1}$$

This wave function can then be used within the variational principle, where both $|\Psi_*\rangle$ and $\mathcal{P}(i)$ are determined minimizing the expectation value of the Hamiltonian. Despite the simplicity of the wave function (2.1), the aforementioned average value on a finite dimensional lattice model cannot be computed exactly and one has to resort to a numerical evaluation or to further approximations. The latter direction has been taken by Gutzwiller, who gave a classical combinatorial estimation of the expectation value of the lattice kinetic energy and Coulomb correlation energy on the quantum wave function (2.1) (Gutzwiller approximation).

Remarkably, the simple Gutzwiller approximation, used to describe the metal-insulator transition in the half-filled single-band Hubbard model [111, 119, 140], predicts that the Mott-Hubbard transition is signalized by a diverging effective electron mass and a vanishing spectral weight at the Fermi level. This prediction, that is also known as *Brinkman-Rice scenario* [38], is

qualitatively confirmed by DMFT, the exact theory in infinite dimensions $d \to \infty$. On the other hand, the numerical optimization of the Gutzwiller wave function on a finite dimensional lattice never stabilizes a genuine Mott insulator, i.e. an insulator that does not break any symmetry. The explanation of these contrasting results relies on the following considerations, that are based on Mott original picture of a correlation-driven insulator [197]. At half-filling, there is, on average, one particle per site and density excitations are represented by doublons (doubly-occupied sites) and holons (empty sites). In the non-interacting state $|\Psi_*\rangle$, these excitations are free to move and then responsible for the conductivity (we are imagining the lattice as a positive background so that a doublon (holon) has charge -1 (+1)). The effect of the local projector is to penalize the formation of such excitations; however, once created, doublons and holons are no longer correlated, thus being free to move independently. Therefore, as long as the value of the electron-electron repulsion is finite, the system is characterized by a non vanishing the density of charge fluctuations and the ground state is metallic.

In order to observe the Mott insulator one has to introduce spatial correlations [47], neglected in the Gutzwiller wave function (2.1), among doublons and holons. This can be achieved by the following generalization:

$$\mathcal{P} = \exp\left[-g\sum_i (n_i - 1)^2\right] \to \mathcal{J} = \exp\left[-\sum_{i,j} \frac{v_{i,j}}{2}(n_i - 1)(n_j - 1)\right],$$

where $\mathcal{J}$ is the so-called Jastrow factor.

At this point one may think that the wave function (2.1) is not a good variational Ansatz to describe the Mott transition. However, we observe that in lattices with infinite coordination number the effect of the non-local Jastrow factor disappears. Indeed, the variational coefficients have to be rescaled for the lattice coordination number $\mathbf{Z}$, and

$$\lim_{\mathbf{Z}\to\infty} \frac{v_{i,j}}{\mathbf{Z}^{d_{ij}}} \to 0,$$

where d_{ij} is the Manhattan distance on the lattice. Thus, only in that limit wave function like (3.1) can faithfully describe a Mott insulator. Furthermore, Metzner and Vollhardt [187] showed that right in the limit $\mathbf{Z} \to +\infty$ the Gutzwiller approximation provides exact expressions of average values and becomes a variational wave function approach. However, the same expressions for expectation values are typically used also for finite-dimensional lattices, hence the name Gutzwiller approximation.

Moreover, the development of DMFT [94, 95] has brought novel insights in the physical meaning of the Gutzwiller approximation. The comparison with DMFT, which is exact in the limit of infinite coordination number, clarifies that the Gutzwiller wave function provides a variational prescription to determine an approximate low-frequency behavior of the [165] self-energy, that reads:

$$\Sigma(\omega) \simeq \Sigma(0) + \omega\left(1 - \frac{1}{Z}\right), \tag{2.2}$$

hence describing a Fermi liquid with quasiparticle residue Z. On the other hand, the Mott insulator is described with the conventional Gutzwiller wave function as a featureless collection of independent sites that corresponds to the limit of infinite Coulomb repulsion among the electrons. This is a major limitation of the method when compared with DMFT.

Notably, it is possible to go beyond the conventional Gutzwiller wave function by introducing auxiliary fermionic degree of freedom in the on-site projector $\mathcal{P}(i)$, and, correspondingly, in the Slater determinant $|\Psi_*\rangle$ [109, 163]. In brief, the novel wave function, named ghost-Gutzwiller

wave function, provides an accurate description of both the low-energy quasiparticles and the incoherent high-frequency Hubbard bands, and allows us to describe faithfully the Mott insulating phase. We will introduce the ghost-Gutzwiller wave function in Chapter 3, where we will present a detailed derivation of the method and then consider several interesting applications.

Motivated by experimental advances in driving and probing strongly correlated electron systems out of equilibrium, the standard Gutzwiller wave function has also been applied to study the real time dynamics of closed quantum systems in many circumstances, for a detailed review we refer to Ref. [81]. The method allows to approximate in a simple way the Schrödinger equation of the complicated many-body problem with a set of coupled equations, that describe the evolution of the on-site projector and the Slater determinant wave function. In particular, the time-dependent equations are obtained by requiring the stationarity of the action with respect to the time-dependent variational parameters. The method, originally applied to the single-band Hubbard model [247, 248], shows remarkable agreement with more accurate DMFT results [72, 73], which justifies the use of the Gutzwiller wave function as a valid alternative to more numerically expensive approaches like DMFT.

Within this approach it is possible to follow the evolution of both the low-energy quasiparticle, described by the non-interacting Slater determinant, and the charge degrees of freedom that are encoded in the parameters of the local projector. The coupling between these degrees of freedom is treated in a mean-field fashion and, therefore, the method lacks relaxation mechanisms that are responsible for driving the system toward a stationary regime. Encouraged by the remarkable improvement in the equilibrium calculations we present the generalization of the ghost-Gutzwiller variational wave function to the time-dependent evolution. A detailed discussion is left to Chapter 5.

2.2 Slave-particle approaches

Another class of widely employed methods to study strongly correlated electron systems are slave-particles techniques. Originally formulated as slave-bosons, they have been pionereed in the context of magnetic impurities in metals [25, 58, 206, 232], and applied to study the Mott transition at half-filling [156] and high-T_c superconductors in doped Mott insulators [125, 168]. More recently slave-particles have been extended to new implementations such as rotationally invariant slave-boson [126, 166], slave-spin [65, 107, 120, 240] and slave-rotor [87]. These approaches are based on the idea that, in a strongly correlated system, the electrons are "dressed" by a cloud of spin and density excitations of the medium. Formally, this qualitative idea is implemented by rewriting the original electron operators in terms of pseudofermion and bosonic operators that encode charge fluctuations. For instance, in the original slave-boson formulation by Barnes [25], the electrons $\uparrow$ and $\downarrow$ annihilation d_σ operators are replaced by:

$$\begin{aligned} d_\uparrow &\to f_\downarrow^\dagger b + e^\dagger f_\uparrow \,, \\ d_\downarrow &\to e^\dagger f_\downarrow - f_\uparrow^\dagger b \,, \end{aligned} \tag{2.3}$$

where b and e annihilate doublon and holon bosonic excitations, respectively, while f_σ are fermionic operators, that preserve the fermionic statistics of the original electrons. As consequence of the bosonic nature of b and e operator, by performing the mapping, we add an ∞ number of additional configurations. The physical subspace $\mathscr{H}$ of the enlarged Hilbert space $\mathscr{H}_*$ is defined by the operatorial condition:

$$Q = b^\dagger b \; + e^\dagger e \; + \sum_\sigma f_\sigma^\dagger f_\sigma = 1. \tag{2.4}$$

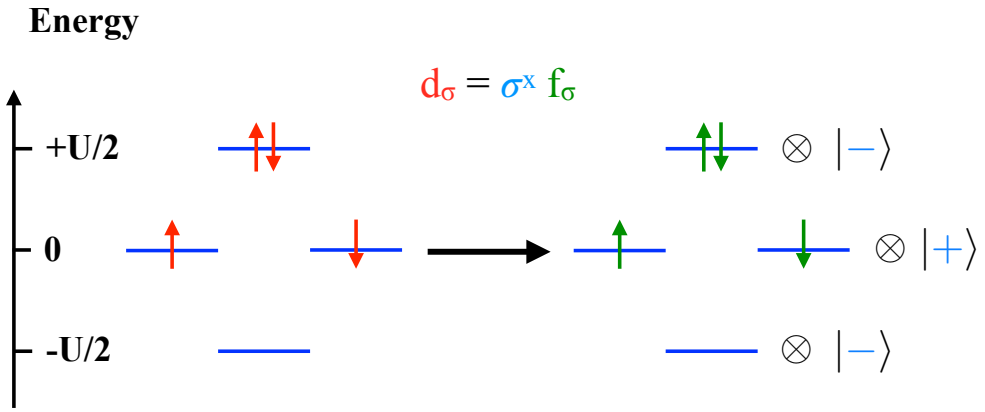

Figure 2.1: Schematic representation of the slave-spin mapping. Whilst the pseudofermion describes low-energy fermionic excitations, the Ising spin variable $\boldsymbol{\sigma}$ encodes the charge fluctuations with characteristic energy scale given by the on-site Coulomb repulsion $\sim U$. Notice that we consider only those configurations of $\mathscr{H}_*$ belonging to the physical subspace $\mathscr{H}$.

In the physical subspace, Eq. (2.3) becomes an identity and the model Hamiltonian H_* is equivalent to the original one, H. The previous representation Eq. (2.3), that looks at first sight more cumbersome, allows to encode valence fluctuations in terms of the number operator of bosonic degrees of freedom: $n_\uparrow n_\downarrow = b^\dagger b$ and $(n_\uparrow - 1)(n_\downarrow - 1) = e^\dagger e$. Within this convenient formulation the low-energy coherent excitations (f_σ pseudofermion) are disentangled from the incoherent background (e and b bosons), and a simple self-consistent mean-field calculation allows to describe non-perturbative effects, that are hard to obtain solving the original fermionic model with conventional approaches.

We observe that the slave-boson theory (2.3) is invariant under the $U(1)$ transformation:

$$\begin{aligned} f_\sigma &\to f_\sigma\, e^{i\varphi}, \\ e &\to e\, e^{i\varphi}, \\ b &\to b\, e^{i\varphi}. \end{aligned} \tag{2.5}$$

A crucial problem with the mean field in slave-particle theories is that the constraint (2.4) is only satisfied *on average*, which implies an unphysical gauge-symmetry breaking, i.e., mean-field solutions mixing the physical subspace with the nonphysical one. For instance, in the case of the slave-bosons, we observe that the mean-field solution is characterized by $\langle e\rangle, \langle d\rangle \neq 0$, that breaks the $U(1)$ gauge symmetry (2.5). This result is an artifact of the mean-field approximation. Gauge symmetry is restored beyond the saddle-point approximation as discussed in Ref. [232].

In this thesis, this problem is successfully overcome by introducing a novel constraint-free slave-spin mapping. In its simplest formulation the slave-spin theory is based on the correspondence:

$$d_\sigma \to \sigma^x f_\sigma$$

where σ^x is the x component of a spin 1/2 operator and f_σ is a fermionic operator, see Fig. 2.1 for a schematic representation. As we discuss in Section 6, within our slave-spin theory a generic single-level Anderson impurity model can be mapped, *without any constraint*, onto a resonant level model coupled to two Ising spins, or just one in the simpler case when the hybridization with the bath is particle-hole symmetric. The result extends straightforwardly to the multi-orbital Anderson impurity models, if the electron interaction does not include

Coulomb exchange terms. Thus, under this assumption, the multi-orbital Anderson impurity model can be written as N resonant level model coupled with $2N$ Ising spin, where N is the number of orbitals, without any need of local constraints. The slave-spin formulation posses a local $Z_2 \times \cdots \times Z_2 = (Z_2)^{2N}$ gauge symmetry, which, depending on the model at hand, can be spontaneously broken at zero temperature. It is important to remark that here the symmetry breaking is not an artifact of the mean-field approximation but a real feature of the model [26].

Furthermore, we will also show that single-particle Green's functions of the physical electron can be calculated without any constraints. Considering the single-Anderson impurity model, we find that the mean-field decoupling of the pseudofermion is able to reproduce quite accurately the magnetic properties of the model even deep inside the large-U Kondo regime and it improves considerably the results obtained by conventional slave-boson mean-field theory.

The slave-spin theory can be readily extended in the framework of the Keldysh Green's function to deal with transport properties in quantum dots. This application will be discussed in details in Chapter 7.

2.3 Connection between the approaches

In spite of their formal difference, the conventional Gutzwiller approximation and slave-particles theories are intimately related. Already in Ref. [156], Kotliar and Ruckenstein pointed out that the saddle-point of the slave-boson action coincide with the results obtained with the conventional Gutzwiller wave function. However, they observe that, as a consequence of the $U(1)$ gauge symmetry, within the slave-boson formulation there are many Hamiltonians that lead to the same spectrum as the original model when restricted to the physical subspace. This arbitrariness presents no difficulties as long as the constraints are handled exactly. However, the mean-field decoupling, that treats the constraint on average, is sensitive to the precise choice of the slave-boson Hamiltonian. In any practical calculation the ambiguity is removed by requiring that the saddle-point solution agrees with the expected results in the uncorrelated limit (vanishing on-site interaction $U = 0$) and in the atomic limit (vanishing hopping amplitude between different sites $t = 0$).

Differently from the slave-boson technique, slave-spin theory is not affected by the aforementioned ambiguity and the saddle-point of the slave-spin action coincides with the conventional Gutzwiller in the limit of lattices with infinite coordination. Considering the simple case of the single-band Hubbard model, it is interesting to observe that in this limit the hopping renormalization amplitude $\langle \sigma_i^x \sigma_j^x \rangle$ goes like:

$$\langle \sigma_i^x \sigma_j^x \rangle \to \langle \sigma^x \rangle^2 \neq 0$$

in the Z_2 symmetry broken phase, that corresponds to the metallic solution. On the contrary, when the symmetry is restored, then $\langle \sigma^x \rangle = 0$, that corresponds to the Mott insulating phase [121]. We notice that $\langle \sigma^x \rangle^2$ coincide with the quasiparticle residue Z[1], and at mean-field level the slave-spin theory gives the same result obtained with the Gutzwiller approximation. We conclude by observing that a finite value of $\langle \sigma^x \rangle$ is possible in spite of Elitzur's theorem because we are working in the limit of infinite lattice coordination [183]. The same consideration applies to the Anderson impurity model, where a finite $\langle \sigma^x \rangle$ signals the formation of the Kondo singlet between the localized magnetic moment and the metallic host.

[1]The quasiparticle residue Z quantifies the amount of coherent quasiparticle excitations in an interacting Fermi liquid. In metals Z can be computed experimentally from measurements of the specific heat. For more details we refer to the original work by Landau [165] and classic books on many-body theory [2, 211].

We observe that the novel Gutzwiller wave function, presented in Chapter 3, does not correspond to a saddle-point of any current formulation of the slave-particle theory. As we will see the method accounts for the charge fluctuations and, in order to do so, introduces more than one pseudofermion degree of freedom for each physical orbital. Differently from other slave-particle approaches, our slave-spin theory for the Anderson impurity models is free by any projection on the physical subspace of the enlarged Hilbert space. This feature avoids the mean-field mixing of the physical subspace and the unphysical one that affects other slave-particles theories, where the constraints have to be implemented explicitly. Consequently, our saddle-point is more accurate than conventional Gutzwiller wave function results [252] and provides a qualitatively good description of the magnetic properties of the impurity even deep inside the large-U Kondo regime. Moreover, the technique allows, by performing a simple self-consistent calculation, us to reproduce not only the low-energy spectral properties but also the high-energy charge-fluctuation peaks. We will discuss in detail these results in Chapter 6.

3

Beyond the Gutzwiller wave function: theory and relevant applications

In this chapter we present a very powerful variational technique that improves the Gutzwiller approximation by adding N auxiliary degrees of freedom. We formulate the method for a generic multi-band lattice model, neglecting superconducting correlations. The additional degrees of freedom allow describing not only the low-energy quasiparticles but also the high-energy charge fluctuations, which are neglected in the conventional Gutzwiller wave function. To highlight the new features of the method we apply the variational approach to the single-orbital Anderson impurity and to the single-band lattice Hubbard model.

3.1 Introduction

A simple approach that allows us to describe strong correlations in lattice models of interacting electrons is the Gutzwiller approximation. In this Chapter we go beyond the simple Gutzwiller wave function, presented in Section 2.1, introducing subsidiary fermionic degrees of freedom both in the local projector and in the Slater determinant. For the sake of clarity we remind that the Gutzwiller wave functions reads:

$$|\Psi_G\rangle = \prod_i \mathcal{P}(i)|\Psi_*\rangle \tag{3.1}$$

where $|\Psi_*\rangle$ is a variational Slater determinant, and $\mathcal{P}(i)$ a linear operator that acts on the local Hilbert space at site i and depends on a set of variational parameters. As already explained in Section 2.1, the wave function (3.1) is a good variational Ansatz in the limit of large coordination, that is the limit we consider hereafter.

The Gutzwiller approximation is generally able to describe only the low-lying quasiparticle excitations, and for this reason it becomes a very poor approximation in the Mott regime where the number of coherent quasiparticle excitation is vanishing and the quantum dynamics is determined by the spin degrees of freedom and incoherent charge fluctuations. A recent work [163] pointed out a novel class of variational Gutzwiller wave functions, named *ghost*-Gutzwiller wave functions (g-GWs), which is able to describe not only the low-frequency behavior but also

to give a faithful representation of the high-frequency Hubbard bands characteristic for the Mott insulator. The crucial ingredient that enriches the Gutzwiller description of strongly interacting models lyes in the decomposition of the physical electrons in terms of auxiliary fermionic degrees of freedom, which is performed by defining in Eq. (3.1) both the Slater determinant $|\Psi_*\rangle$ and the local projector $\mathcal{P}(i)$ in an enlarged Hilbert space. Hence, the optimization of the g-GW energy determines the redistribution, induced by the electron-electron interaction, of the spectral weight to different energy scales. The trick of adding subsidiary degrees of freedom to improve the accuracy of a variational wave function has a long history that goes back to the shadow wave functions for ^{4}He [278], and is still very alive, as testified by the great interest in matrix-product states and tensor networks [217, 236], or, more recently, in neural-network quantum states [50]. In this respect the parameter N, that defines the number of subsidiary fermionic degrees of freedom, can be considered as a counterpart of the the bond dimension in matrix product states and somehow is related to the amount of entanglement in the variational wave function (3.1). This point of view poses a question about the limit of large number of subsidiary degrees of freedom, $N \gg 1$, as to whether the variational g-GW solution approaches the exact DMFT result [95]. To clarify the connection between these two methods we believe that a detailed analysis of the g-GW solution as a function of N will be necessary.

In the next Section we introduce the g-GW for the ground state calculations in detail by considering the generic case of a multi-band Hubbard model, while neglecting superconductive correlations. After a brief introduction on the method we will focus on all the new features that we have developed and that considerably improve the Gutzwiller approximation. The extension of the method to the out of equilibrium dynamics of strongly correlated electron systems is left to Chapter 5.

3.2 The ghost-Gutzwiller wave function for a multi-orbital model

Let us consider the general tight-binding multi-orbital Hubbard model:

$$H = -\sum_{ij}\sum_{\alpha\beta=1}^{2M}\left(d^\dagger_{i\alpha}\frac{t^{\alpha\beta}_{ij}}{\sqrt{\mathbf{Z}}}d_{j\beta} + \text{H.c.}\right) + \sum_i H_i \tag{3.2}$$

where the operator $d^\dagger_{i\alpha}$ creates and $d_{j\beta}$ annihilates an electron at site i and j, respectively, and indices α and β denote single particle states and stand both for different orbital (assuming M orbitals) and spin ($\uparrow$ and $\downarrow$) degrees of freedom. The first term accounts for the kinetic energy where $t^{\alpha\beta}_{ij}$ represents the hopping amplitude between the two sites i and j, and $\mathbf{Z}$ the lattice coordination number. The second term is associated to a purely local two-body interaction H_i.

The g-GW differs from the standard Gutzwiller wave function by the addition of subsidiary degrees of freedom. In order to provide a variational description of both low- and high-energy features of strongly interacting electron systems the Slater determinant $|\Psi_*\rangle$ in Eq. (3.1) is taken as the ground state of a tight-binding Hamiltonian H_* defined in an enlarged Hilbert space with $2N \geq 2M$ spinful orbitals, while

$$\mathcal{P}_i = \sum_{\Gamma\gamma}\lambda_{\Gamma\gamma}(i)|\Gamma_i\rangle\langle\gamma_i| \tag{3.3}$$

is a linear map at site i, parametrized by the variational parameters $\lambda_{\Gamma\gamma}(i)$, from the local $2N$-orbital Hilbert space, spanned by the states $|\gamma_i\rangle$, to the physical orbital local space, spanned

instead by $|\Gamma_i\rangle$. In what follows, we shall denote as c_{ia}, $a = 1, \cdots, 2N$, the fermionic operators, respectively, of the N spinful orbitals per each site i in the enlarged Hilbert space, while $d_{i\alpha}$, $\alpha = 1, \cdots, 2M$, denote the operator of the physical spinful orbitals. We note that for $N = M$ the approach reduces to the conventional Gutzwiller wave function [111, 112]. Both $\mathcal{P}(i)$ and $|\Psi_*\rangle$ have to be determined variationally to minimize the total energy:

$$E\left[\Psi_G\right] = \frac{\langle\Psi_G|H|\Psi_G\rangle}{\langle\Psi_G|\Psi_G\rangle}, \tag{3.4}$$

where $E\left[\Psi_G\right] > E_{\rm gs}$ is an upper bound to the ground state energy $E_{\rm gs}$.

Analogously to the conventional Gutzwiller, expectation values of the local and nonlocal operators in the g-GW (3.1) can be computed analytically in lattices with infinite coordination provided the following constraints are satisfied:

$$\begin{aligned} &\langle\Psi_*|\mathcal{P}^\dagger(i)\mathcal{P}(i)|\Psi_*\rangle = 1, \\ &\langle\Psi_*|\mathcal{P}^\dagger(i)\mathcal{P}(i)\, c^\dagger_{ia}\, c_{ib}|\Psi_*\rangle = \langle\Psi_*|c^\dagger_{ia}c_{ib}|\Psi_*\rangle \equiv \Delta_{ab}(i), \end{aligned} \tag{3.5}$$

where $\Delta_{ab}(i)$ is the single-particle density matrix and the fermionic operators c_{ia} belong to the enlarged Hilbert space, $a = 1, \cdots, 2N$. Constraints in Eq. (3.5) simplify considerably all the calculations in infinite lattice-coordination limit, and allow to compute explicitly expectation values. Instead of proving this well-known result, that can be found in the review [81], in the following we focus on a key point that allows rewriting the variational parameters in terms of the amplitudes of an impurity wave function and clarifies the connection between g-GW and DMFT [162]. Before presenting the mapping, we briefly report the expressions of average quantities in terms of the variational parameters $|\Psi_*\rangle$ and $\lambda_{\Gamma\gamma}(i)$.

3.2.1 The expectation values in infinite lattice coordination

As already discussed in the previous Section 3.2, in the limit of infinite coordination the average values of the local and non-local operators can be computed exactly if the two constraints in Eq. (3.5) are satisfied.

Local operators; given a generic local many-body bosonic[1] operator O_i acting on site i, its expectation value on the Gutzwiller wave function reads:

$$\langle\Psi_G|O_i|\Psi_G\rangle = \langle\Psi_*|\mathcal{P}^\dagger(i)O_i\mathcal{P}(i)|\Psi_*\rangle. \tag{3.6}$$

Non-local operator; the average value of a non-local bosonic operator O_{ij} reads:

$$\langle\Psi_G|O_{ij}|\Psi_G\rangle = \langle\Psi_*|\mathcal{P}^\dagger(i)\mathcal{P}^\dagger(j)O_{ij}\mathcal{P}(j)\mathcal{P}(i)|\Psi_*\rangle. \tag{3.7}$$

Particularly interesting is the average value of the inter-site single-particle density operator $d^\dagger_{i\alpha}d_{j\beta}$ which appears in the hopping Hamiltonian:

$$\langle\Psi_*|\mathcal{P}^\dagger(i)d^\dagger_{i\alpha}\mathcal{P}(i)\mathcal{P}^\dagger(j)d_{j\beta}\mathcal{P}(j)|\Psi_*\rangle = \sum_{ab=1}^{2N} R^\dagger_{a\alpha}(i)R_{\beta b}(j)\langle\Psi_*|c^\dagger_{ia}c_{jb}|\Psi_*\rangle, \tag{3.8}$$

where the wave function renormalization $R(i)$, which describes the redistribution of the spectral weight induced by correlations, is a rectangular matrix $R_{\alpha a}(i)$ composed by $2N$ columns $a =$

[1] Many-body bosonic operators are composed by an even number of fermionic ones.

$1, \cdots, 2N$ and $2M$ rows $\alpha = 1, \cdots, 2M$. In other words, in infinite coordination lattices the action of the on-site projector is to renormalize the creation and annihilation operators:

$$\mathcal{P}^\dagger(i) d_{i\alpha} \mathcal{P}(i) \rightarrow \sum_{a=1}^{2N} R_{\alpha a}(i) c_{ia}, \tag{3.9}$$

where, if $N > M$, the annihilation of a physical fermion $d_{i\alpha}$ corresponds to destroy a cloud of auxiliary fermions c_{ia} in the extended Hilbert space. We conclude by noticing that the wave function renormalization matrix is obtained by solving the algebraic equation:

$$\langle \Psi_* | c_{ib}^\dagger \mathcal{P}^\dagger(i) d_{i\alpha} \mathcal{P}(i) | \Psi_* \rangle = \sum_{c=1}^{2N} R_{\alpha c}(i) \Delta_{bc}(i), \tag{3.10}$$

where the local single-particle density matrix $\Delta_{bc}(i)$ has been introduced in (3.5).

Following Ref. [80], we introduce the parametrization:

$$\phi(i)_{\Gamma\gamma} = \sum_{\eta} \lambda_{\Gamma\eta}(i) \left(\sqrt{\mathcal{P}_0(i)} \right)_{\eta\gamma}, \tag{3.11}$$

where $\mathcal{P}_0(i)$ is the uncorrelated local probability distribution, defined as:

$$\mathcal{P}_0(i)_{\gamma\eta} = \langle \Psi_* | \eta_i \rangle \langle \gamma_i | \Psi_* \rangle, \tag{3.12}$$

where γ and η are local configurations belonging to the enlarged Hilbert space. We notice that in the conventional Gutzwiller variational approach $\phi(i)_{\Gamma\gamma}$ is equivalent to the slave-boson saddle-point value within the rotationally invariant slave-bosons (RISB) [126, 166], which extends the original Kotliar-Ruckenstein scheme [156]. In the context of the g-GW the correspondence between $\phi(i)$ and the slave-bosons suggests a promising extension of the Kotliar-Ruckenstein approach that involves an enlarged number of bosonic degrees of freedom as well as additional fermionic ones. The parametrization in Eq. (3.11) allows writing expectation values in a convenient form. In terms of $\phi(i)_{\Gamma\gamma}$ the Gutzwiller constraints read:

$$\begin{aligned} &\mathrm{Tr}\left(\phi^\dagger(i) \cdot \phi(i) \right) = 1, \\ &\mathrm{Tr}\left(\phi^\dagger(i) \cdot \phi(i) \cdot C_{ia}^\dagger \cdot C_{ib} \right) = \Delta_{ab}(i), \end{aligned} \tag{3.13}$$

where $\cdot$ is the ordinary matrix product, C_{ia} is the matrix representation of the fermionic operator c_{ia} in the enlarged Fock space:

$$(C_{ia})_{\gamma\eta} \equiv \langle \gamma_i | c_{ia} | \eta_i \rangle. \tag{3.14}$$

The expectation value of a bosonic local operator O_i (3.6) is:

$$\langle \Psi_* | \mathcal{P}^\dagger(i) O_i \mathcal{P}(i) | \Psi_* \rangle = \mathrm{Tr}\left(\phi^\dagger(i) \cdot \mathcal{O}_i \cdot \phi(i) \right), \tag{3.15}$$

where the matrix $\mathcal{O}_i$ is defined as

$$(\mathcal{O}_i)_{\Gamma\Omega} = \langle \Gamma_i | O_i | \Omega_i \rangle, \tag{3.16}$$

with $|\Gamma_i\rangle$ and $|\Omega_i\rangle$ Fock states of the physical Hilbert space. Finally, Eq. (3.10) becomes:

$$\mathrm{Tr}\left(\sqrt{\mathcal{P}_0(i)} \cdot C_{ib}^\dagger \cdot \sqrt{\mathcal{P}_0(i)}^{-1} \cdot \phi^\dagger(i) \cdot D_{i\alpha} \cdot \phi(i) \right) = \sum_{c=1}^{2N} R_{\alpha c}(i) \, \Delta_{bc}(i) \tag{3.17}$$

whose solution is

$$R(i) = Q(i) \cdot S(i), \tag{3.18}$$

where $Q(i)$ is a $2M \times 2N$ matrix:

$$Q_{\alpha a}(i) = \mathrm{Tr}\left(C_{ia}^{\dagger} \cdot \phi^{\dagger}(i) \cdot D_{i\alpha} \cdot \phi(i)\right) \tag{3.19}$$

and $S(i)$ a $2N \times 2N$ one:

$$S^{T}(i) = \left[\sqrt{\Delta(i) \cdot (\mathbf{1} - \Delta(i))}\right]^{-1}. \tag{3.20}$$

Combining the results in Eqs. (3.6) and (3.8) with the parametrization in Eq. (3.11) of the Gutzwiller projector, we readily obtain the variational g-GW energy for the multi-orbital Hubbard model (3.2):

$$E\left[\phi(i), \Psi_*\right] = \sum_i \mathrm{Tr}\left(\phi^{\dagger}(i) \cdot \mathcal{H}_i \cdot \phi(i)\right) + \langle \Psi_* | H_* | \Psi_* \rangle, \tag{3.21}$$

where H_* is the quasiparticle Hamiltonian that reads:

$$H_* = -\sum_{ij} \sum_{ab=1}^{2N} \sum_{\alpha\beta=1}^{2M} \left(c_{ia}^{\dagger} R_{a\alpha}^{\dagger}(i) \frac{t_{ij}^{\alpha\beta}}{\sqrt{\mathbf{Z}}} R_{\beta b}(j)\, c_{jb} + \mathrm{H.c.} \right). \tag{3.22}$$

The g-GW ground state wave function is obtained by minimizing $E\left[\phi(i), \Psi_*\right]$ with respect to the variational parameters $\phi(i)$ and $|\Psi_*\rangle$ under the conditions in Eq. (3.13). To this aim we introduce a convenient mapping of the variational parameters $\phi(i)_{\Gamma\gamma}$ into the amplitudes of an embedded impurity model $\psi(i; \Gamma, \gamma)$.

3.2.2 Mapping to the embedded impurity model

The space of $2^{2M} \times 2^{2N}$ matrices $\phi(i)$ can be conveniently mapped into an embedded impurity model, where $d_{i\alpha}$ plays the role of the impurity while c_{ia} is one of the bath levels. To this aim we introduce the impurity wave function

$$\begin{aligned} |\psi(i)\rangle &= \sum_{\Gamma\gamma} e^{i\pi N_\gamma (N_\gamma - 1)/2} \phi(i)_{\Gamma\gamma} U_{\mathrm{PH}} |\Gamma_i\rangle \times |\gamma_i\rangle \\ &= \sum_{\Gamma\gamma} \psi(i; \Gamma, \gamma) |\Gamma_i\rangle \times |\gamma_i\rangle \end{aligned} \tag{3.23}$$

where the coefficients $\phi(i)_{\Gamma\gamma}$ are the Gutzwiller amplitudes in Eq. (3.5), the Fock state:

$$|\Gamma_i\rangle = \prod_{\alpha=1}^{2M} \left(d_{i\alpha}^{\dagger}\right)^{\nu_\alpha^\Gamma} |0\rangle, \tag{3.24}$$

describes the configuration on the impurity at site i with N_Γ electrons:

$$N_\Gamma = \sum_{a=1}^{2M} \nu_\alpha^\Gamma, \tag{3.25}$$

where $\nu_\alpha^\Gamma = 0, 1$. The ket $|\gamma_i\rangle$ describes the bath configuration

$$|\gamma_i\rangle = \prod_{a=1}^{2N} \left(c_{ia}^{\dagger}\right)^{\nu_a^\gamma} |0\rangle, \tag{3.26}$$

where the number of electrons in the bath levels is

$$N_\gamma = \sum_{a=1}^{2N} \nu_\alpha^\gamma, \tag{3.27}$$

with $\nu_\alpha^\gamma = 0, 1$. In Eq. (3.23) we have introduced the unitary particle-hole transformation $U_{\rm PH}$ that acts on the bath levels:

$$U_{\rm PH}^\dagger c_{ia} U_{\rm PH} = c_{ia}^\dagger, \tag{3.28}$$

and leaves the impurity invariant:

$$U_{\rm PH}^\dagger d_{i\alpha} U_{\rm PH} = d_{i\alpha}. \tag{3.29}$$

Remarkably, expectation values in Eqs. (3.13), (3.15) and (3.19) can be rewritten in terms of averages on the embedded wave function $|\psi(i)\rangle$ [162], which allows rephrasing the optimization of the Gutzwiller energy as a non-linear eigenvalue problem of a self-consistent impurity model. This important result, that is proved in the Appendix A.1, is summarized by the following identities

$$\begin{aligned} \langle\psi(i)|\psi(i)\rangle &= \mathrm{Tr}\left(\phi^\dagger(i)\cdot\phi(i)\right), \\ \langle\psi(i)|c_{ib}c_{ia}^\dagger|\psi(i)\rangle &= \mathrm{Tr}\left(\phi^\dagger(i)\cdot\phi(i)\cdot C_{ia}^\dagger\cdot C_{ib}\right). \end{aligned} \tag{3.30}$$

Furthermore, given a bosonic operator O_i acting on the physical Hilbert space $O_i[\{d_{i\alpha}^\dagger\},\{d_{i\alpha}\}]$ we have

$$\langle\psi(i)|O_i|\psi(i)\rangle = \mathrm{Tr}\left(\phi^\dagger(i)\cdot O_i\cdot\phi(i)\right). \tag{3.31}$$

Finally, the overlap between spinful orbital $d_{i\alpha}$ and the bath level c_{ia} reads:

$$\langle\psi(i)|c_{ia}^\dagger d_{i\alpha}|\psi(i)\rangle = \mathrm{Tr}\left(C_{ia}^\dagger\cdot\phi^\dagger(i)\cdot D_{i\alpha}\cdot\phi(i)\right) = Q_{\alpha a}(i). \tag{3.32}$$

Thanks to Eqs. (3.30), (3.31) and (3.32), the g-GW Lagrange function, which gives the g-GW energy when evaluated at the saddle-point, reads

$$\begin{aligned} \mathcal{L}\left[\psi(i),\Psi_*,\mu(i),\Lambda(i)\right] = &\sum_i \langle\psi(i)|H_i|\psi(i)\rangle + \langle\Psi_*|H_*|\Psi_*\rangle \\ &- \sum_i \Lambda(i)(\langle\psi(i)|\psi(i)\rangle - 1)) - \Lambda_*\left(\langle\Psi_*|\Psi_*\rangle - 1\right) \\ &- \sum_i \sum_{ab=1}^{2N} \left[\mu_{ab}(i)\left(\langle\psi(i)|c_{ib}c_{ia}^\dagger|\psi(i)\rangle - \langle\Psi_*|c_{ia}^\dagger c_{ib}|\Psi_*\rangle\right)\right] \end{aligned} \tag{3.33}$$

where $\mu_{ab}(i)$ and $\Lambda(i)$ are Lagrange multipliers that impose the constraints in Eq. (3.5).

In order to provide evidence of the quality of the g-GW wave function and, in turn, to validate the improvement obtained by introducing auxiliary fermionic degrees of freedom in the Gutzwiller projector, in Sections 3.3 and 3.4 we provide benchmark calculations of the single-band Anderson Impurity model (SIAM) and the Mott metal-to-insulator transition in the half-filled single-band Hubbard model. We will compare our numerical results with numerical renormalization group (NRG) and DMFT calculations. Before entering the discussion, we present in the next Section 3.2.3, two optimization schemes for the saddle-point solution of (3.33).

3.2.3 Numerical optimization of the g-GW Lagrangian

The optimization of the ghost-Gutzwiller wave function is reduced to the minimization of the g-GW Lagrange function in Eq. (3.33). Depending on the problem at hand, we can adopt different optimization strategies. In the following we illustrate two minimization schemes, that we are going to use for solving different problems presented in this work.

Wave function optimization

In this case we treat all the components $\psi(i;\Gamma,\gamma)$ of the wave function as free variational parameters, except for those determined by the normalization and the constraints imposed by the symmetries that we would like to preserve in the variational ground state (e.g. $SU(2)$ spin symmetry). As a consequence of the symmetries the coefficients $\psi(i;\Gamma,\gamma)$ of the embedded wave function are not all independent. Apart from these details that depend on the specific properties of the lattice model, the optimization of the g-GW Lagrangian reduces to the solution of the following equations:

$$\Delta_{ab}(i) = \langle\psi(i)|c_{ib}c_{ia}^{\dagger}|\psi(i)\rangle, \tag{3.34}$$

$$R(i) = Q(i)\cdot S(i), \tag{3.35}$$

$$\langle\Psi_*|c_{ia}^{\dagger}c_{ib}|\Psi_*\rangle = \Delta_{ab}(i), \tag{3.36}$$

$$\left(H_* - \sum_i \sum_{ab=1}^{2N} \mu_{ab}(i)c_{ia}^{\dagger}c_{ib}\right)|\Psi_*\rangle = \Lambda_*|\Psi_*\rangle, \tag{3.37}$$

$$\mathcal{F}[\psi(i),\Lambda(i)] = \left(H_i - \sum_{ab=1}^{2N}\mu_{ab}(i)c_{ib}c_{ia}^{\dagger}\right)|\psi(i)\rangle + \frac{\partial}{\partial\langle\psi(i)|}\langle\Psi_*|H_*|\Psi_*\rangle - \Lambda(i)|\psi(i)\rangle = 0. \tag{3.38}$$

Given $|\psi(i)\rangle$ and $\Lambda(i)$, we compute $\Delta_{ab}(i)$ and the wave function renormalization matrix $R(i)$ through Eqs. (3.34) and (3.35), respectively. By solving Eq. (3.36) we compute the matrix of Lagrange multipliers $\mu_{ab}(i)$ that allows us to determine the Slater determinant as the ground state of the Schrödinger Eq. (3.37). Then, we update the values of $|\psi(i)\rangle$ and $\Lambda(i)$ by looking for the solution of the eigenvalues problem in Eq. (3.38). The saddle-point wave function $|\psi(i)\rangle$ and $\Lambda(i)$ satisfy the vector equation

$$\mathcal{F}[\psi(i),\Lambda(i)] = 0, \tag{3.39}$$

i.e. $|\psi(i)\rangle$ and $\Lambda(i)$ are eigenstate and eigenvalue of the embedded impurity Hamiltonian. We conclude by noticing that this approach is convenient if one needs to introduce additional conditions on the ground state properties, i.e. fixed magnetization or number of particles. To be more specific, we will adopt this strategy to study the Mott transition in photoexcited semiconductors, Chapter 4, where we fix the number of holes and electrons in valence and conduction bands, respectively, on the variational wave function $|\psi(i)\rangle$.

Single-particle density matrix optimization

A different strategy, presented in Ref. [162], consists in introducing three additional set of Lagrange multipliers $V_{a\alpha}(i)$, $\lambda_{ab}(i)$ and $\lambda^{c}_{ab}(i)$ that enforce the identities (3.18) and (3.13):

$$\langle\psi(i)|c_{ia}^{\dagger}d_{i\alpha}|\psi(i)\rangle = \sum_{b=1}^{2N} R_{\alpha b}(i)\left[\left(\sqrt{\Delta(i)\cdot(\mathbf{1}-\Delta(i))}\right)^{T}\right]_{ba}, \tag{3.40}$$

$$\langle\psi(i)|c_{ib}c_{ia}^{\dagger}|\psi(i)\rangle = \Delta_{ab}(i), \tag{3.41}$$

$$\langle\Psi_*|c_{ia}^{\dagger}c_{ib}|\Psi_*\rangle = \Delta_{ab}(i), \tag{3.42}$$

where $\Delta_{ab}(i)$ and $R_{\alpha a}(i)$ are matrices of independent parameters that at the saddle-point correspond to the local single-particle density matrix and the wave function renormalization factors,

respectively. Thus, the g-GW Lagrangian becomes:

$$\begin{aligned}\tilde{\mathcal{L}}\left[\psi(i),\Psi_*,\mu(i),\Lambda(i),V(i),R(i),\lambda(i),\lambda^c(i),\Delta(i)\right] &= \sum_i \langle\psi(i)|H_i|\psi(i)\rangle + \langle\Psi_*|H_*|\Psi_*\rangle \\ &- \Lambda_*\left(\langle\Psi_*|\Psi_*\rangle - 1\right) - \sum_i \Lambda(i)(\langle\psi(i)|\psi(i)\rangle - 1)\rangle \\ &- \sum_i \sum_{ab=1}^{2N}\left[\lambda_{ab}(i)\left(\langle\Psi_*|c_{ia}^\dagger c_{ib}|\Psi_*\rangle - \Delta_{ab}(i)\right)\right] - \sum_i \sum_{ab=1}^{2N}\left[\lambda^c_{ab}(i)\left(\langle\psi(i)|c_{ib}c_{ia}^\dagger|\psi(i)\rangle - \Delta_{ab}(i)\right)\right] \\ &+ \sum_i \sum_{a=1}^{2N}\sum_{\alpha=1}^{2M} V_{a\alpha}(i)\left\{\langle\psi(i)|c_{ia}^\dagger d_{i\alpha}|\psi(i)\rangle - \sum_{b=1}^{2N} R_{\alpha b}(i)\left[\left(\sqrt{\Delta(i)\cdot(\mathbf{1}-\Delta(i))}\right)^T\right]_{ba}\right\} \\ &+ \sum_i \sum_{a=1}^{2N}\sum_{\alpha=1}^{2M} V_{\alpha a}^\dagger(i)\left\{\langle\psi(i)|d_{i\alpha}^\dagger c_{ia}|\psi(i)\rangle - \sum_{b=1}^{2N}\left[\left(\sqrt{\Delta(i)\cdot(\mathbf{1}-\Delta(i))}\right)^T\right]_{ab} R_{b\alpha}^\dagger(i)\right\}.\end{aligned} \tag{3.43}$$

Under the assumption of having the translational invariant ground state (i.e. variational parameters do not depend on the site index), the saddle-point condition for $\tilde{\mathcal{L}}$ provides the following equations:

$$\langle\Psi_*|c_{ia}^\dagger c_{ib}|\Psi_*\rangle = \Delta_{ab}, \tag{3.44}$$

$$\sum_{c=1}^{2N}\left[\left(\sqrt{\Delta\cdot(\mathbf{1}-\Delta)}\right)^T\right]_{ac} V_{c\alpha} = \frac{1}{V}\sum_{\mathbf{k}}\sum_{b=1}^{2N}\sum_{\beta=1}^{2M}\langle\Psi_*|c_{\mathbf{k}b}^\dagger R_{b\beta}^\dagger \epsilon_{\mathbf{k}}^{\beta\alpha} c_{\mathbf{k}a}|\Psi_*\rangle, \tag{3.45}$$

$$\begin{aligned}\lambda^c_{ab} &= -\lambda_{ab} + \frac{\partial}{\partial\Delta_{ab}}\sum_{cd\gamma} V_{c\gamma}R_{\gamma d}\left[\left(\sqrt{\Delta\cdot(\mathbf{1}-\Delta)}\right)^T\right]_{dc} \\ &+ \frac{\partial}{\partial\Delta_{ab}}\sum_{cd\gamma}\left[\left(\sqrt{\Delta\cdot(\mathbf{1}-\Delta)}\right)^T\right]_{cd} R_{d\gamma}^\dagger V_{\gamma c}^\dagger,\end{aligned} \tag{3.46}$$

$$\mathcal{H}_{\text{emb}}[V,V^\dagger,\lambda^c]|\psi\rangle = \Lambda|\psi\rangle, \tag{3.47}$$

$$\mathcal{F}_1[R,\lambda] = \langle\psi|c_{ib}c_{ia}^\dagger|\psi\rangle - \Delta_{ab}(i) = 0, \tag{3.48}$$

$$\mathcal{F}_2[R,\lambda] = \langle\psi(i)|c_{ia}^\dagger d_{i\alpha}|\psi(i)\rangle - \sum_{b=1}^{2N} R_{\alpha b}(i)\left[\left(\sqrt{\Delta(i)\cdot(\mathbf{1}-\Delta(i))}\right)^T\right]_{ba} = 0, \tag{3.49}$$

where $\mathbf{k}$ is the momentum, belonging to the Brillouin zone, and $\epsilon_{\mathbf{k}}^{\alpha\beta}$ from Eq. (3.45) is the dispersion relation of a generic multi-band model, which is defined in the Eq. (A.12) of Appendix A.3. Moreover, in Eq. (3.47) we have introduced the embedded impurity Hamiltonian that reads:

$$\mathcal{H}_{\text{emb}}[V,V^\dagger,\lambda^c] = H_i + \sum_{a=1}^{2N}\sum_{\alpha=1}^{2M}\left(c_{ia}^\dagger V_{a\alpha}d_{i\alpha} + d_{i\alpha}^\dagger V_{\alpha a}^\dagger c_{ia}\right) - \sum_{ab=1}^{2N}\lambda^c_{ab}c_{ib}c_{ia}^\dagger. \tag{3.50}$$

Given $R_{\alpha a}$ and Δ_{ab} we compute λ_{ab} through Eq. (3.44). In order to obtain the embedded impurity model $\mathcal{H}_{\text{emb}}[V,V^\dagger,\lambda^c]$, we invert Eq. (3.45) for the tunnel-coupling amplitudes $V_{a\alpha}$ and we compute the single-body potential λ^c_{ab} in Eq. (3.46). Then, the eigenvalue equation (3.47) is solved for the ground state eigenvector $|\psi\rangle$ with eigenvalue Λ. Finally, we compute the embedded single-particle density matrix and the overlap matrix elements in Eqs. (3.48) and (3.49), respectively. In conclusion, the saddle-point $R_{\alpha a}$ and Δ_{ab} solve the following equations:

$$\mathcal{F}_1[R,\lambda] = 0, \quad \mathcal{F}_2[R,\lambda] = 0. \tag{3.51}$$

This optimization scheme is more convenient when the number of bath levels becomes large and the size of the Hilbert space grows exponentially. Indeed, the number of Eqs. in (3.51) is considerably smaller than the number of independent amplitudes, that compose the embedded impurity wave function $|\psi(i)\rangle$, in the eigenvalue problem Eq. (3.38).

3.3 Magnetic Impurity embedded in a metallic host

Originally introduced by Anderson to describe localized magnetic moments dissolved in non-magnetic metals [17], the single-impurity Anderson model (SIAM) and its extension have had a tremendous impact in condensed matter theory [117]. Generalizations to higher spins and different kinds of conduction electrons media have been constructed and studied in Refs. [59, 124, 192]. Mesoscopic electronic devices such as quantum dots offer new physical realizations, where the parameters of the AIM can be controlled to unprecedented accuracy [60, 99, 101, 186, 207]. In a different context SIAM serves as the simplest reference system to describe lattice models via the dynamical mean field theory (DMFT) mapping [95]. Some of these topics will be covered in other Sections of this work.

The SIAM Hamiltonian reads:

$$\begin{aligned} H = &\sum_{\sigma}\sum_{\mathbf{k}} \epsilon_{\mathbf{k}} \psi^{\dagger}_{\mathbf{k}\sigma}\psi_{\mathbf{k}\sigma} + \frac{1}{\sqrt{V}}\sum_{\mathbf{k}\sigma}\left(d^{\dagger}_{\sigma} V^{*}_{\mathbf{k}}\psi_{\mathbf{k}\sigma} + \psi^{\dagger}_{\mathbf{k}\sigma} V_{\mathbf{k}}\, d_{\sigma}\right) + U\left(n_{\uparrow}-\frac{1}{2}\right)\left(n_{\downarrow}-\frac{1}{2}\right) \\ &- \frac{h}{2}\left(n_{\uparrow}-n_{\downarrow}\right) - \frac{\mu}{2}\left(n_{\uparrow}+n_{\downarrow}-1\right), \end{aligned} \tag{3.52}$$

where $n_{\sigma} = d^{\dagger}_{\sigma} d_{\sigma}$, U is the on-site Coulomb repulsion, μ the chemical potential and h the Zeeman field. The properties of the metallic host are encoded in the hybridization function:

$$\Delta^{R}(\omega) = \frac{1}{V}\sum_{\mathbf{k}} \frac{|V(\epsilon_{\mathbf{k}})|^2}{\omega - \epsilon_{\mathbf{k}} + i0^{+}} = \int \frac{d\epsilon}{\pi}\frac{\Gamma(\epsilon)}{\omega - \epsilon + i0^{+}} \tag{3.53}$$

where $\Gamma(\omega) = \pi\rho(\omega)|V(\omega)|^2$ and $\rho(\omega)$ is the density of state of the metal.

In the regime $U/\Gamma(0) \gg 1$, $\mu = h = 0$, the local atomic configurations $\{|\uparrow\rangle, |\downarrow\rangle\}$ are degenerate and well separated in energy $\sim U$ from $\{|\uparrow\downarrow\rangle, |0\rangle\}$ states. The tunnel-coupling amplitude induces an effective magnetic exchange between the magnetic moment of the impurity and the electron bath such that at low temperature the impurity spin is entangled in a singlet state with the metallic host. The energy gained by forming the singlet bound state is known as Kondo temperature [153] and can be computed exactly using the Bethe Ansatz [273]:

$$T_K = \frac{\sqrt{2U\Gamma(0)}}{\pi}\exp\left(\frac{-\pi U}{8\Gamma(0)}\right). \tag{3.54}$$

The conventional Gutzwiller wave function gives a quantitatively poor description of the strong coupling regime, also known as Kondo regime. In particular, it has been shown in Ref. [107] that the conventional Gutzwiller predicts an unphysical spontaneous magnetization of the impurity above some critical value of the interaction[2]. To improve the variational description we introduce auxiliary degrees of freedom in the Gutzwiller wave function, that reads:

$$|\Psi_G\rangle = \mathcal{P}\,|\Psi_*\rangle \tag{3.55}$$

[2]For detailed calculations we refer to Section C.4 in Appendix C.

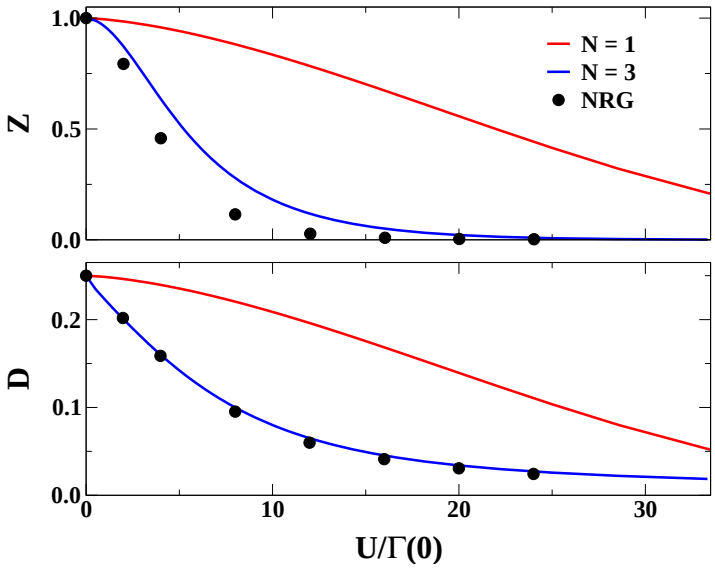

Figure 3.1: Comparison between the conventional Gutzwiller ($N = 1$), g-GW with $N = 3$ and NRG. Top panel: quasiparticle residue as a function of $U/\Gamma(0)$. Bottom panel: double occupancy as a function of $U/\Gamma(0)$. In both panels black dots represent NRG results obtained employing the open source code in Ref. [291]. Results are computed adopting a flat hybridization function (3.58), where W is the half-bandwidth of the metallic host that we use as the unit of energy, $U/W = 0.1$ and we consider different values of the hybridization $\Gamma(0)$.

where the projector $\mathcal{P}$ acts on the impurity site and the Slater determinant $|\Psi_*\rangle$ is the ground state of the effective resonant level model (RLM) characterized by $2N$ spinful orbitals at the impurity site, $N \geq 1$. Applying Eq. (3.10) we readily find the effective RLM

$$\begin{aligned}\mathcal{H}_*^{\mathrm{RLM}} = &\sum_{\sigma}\sum_{\mathbf{k}} \epsilon_{\mathbf{k}}\, \psi^{\dagger}_{\mathbf{k}\sigma}\psi_{\mathbf{k}\sigma} + \frac{1}{\sqrt{V}}\sum_{\mathbf{k}\sigma}\sum_{a=1}^{N}\left(c^{\dagger}_{a\sigma}\, R^{*}_{\sigma,a\sigma}\, V^{*}_{\mathbf{k}}\, \psi_{\mathbf{k}\sigma} + \psi^{\dagger}_{\mathbf{k}\sigma}\, V_{\mathbf{k}} R_{\sigma,a\sigma}\, c_{a\sigma}\right) \\ &- \sum_{\sigma}\sum_{ab=1}^{N} c^{\dagger}_{a\sigma}\lambda_{ab,\sigma} c_{b\sigma},\end{aligned} \tag{3.56}$$

where we separate the spin $\sigma = \uparrow, \downarrow$ and the orbital $a = 1, \cdots, N$ indices. In Hamiltonian (3.56) both the wave function renormalization $R_{\sigma,a\sigma}$, defined in Eqs. (3.18), and the matrix of Lagrange multipliers $\lambda_{ab,\sigma}$ have to be determined by the saddle-point condition (3.51). On the other hand, the embedded impurity model reads:

$$\begin{aligned}\mathcal{H}_{\mathrm{emb}}[V, V^{\dagger}, \lambda^{c}] = &U\left(n_{\uparrow} - \frac{1}{2}\right)\left(n_{\downarrow} - \frac{1}{2}\right) - \frac{h}{2}\left(n_{\uparrow} - n_{\downarrow}\right) - \frac{\mu}{2}\left(n_{\uparrow} + n_{\downarrow} - 1\right) \\ &+ \sum_{\sigma}\sum_{a=1}^{N}\left(c^{\dagger}_{a\sigma}\, V_{a\sigma,\sigma}\, d_{\sigma} + d^{\dagger}_{\sigma}\, V^{\dagger}_{\sigma,a\sigma}\, c_{a\sigma}\right) - \sum_{\sigma}\sum_{ab=1}^{N}\lambda^{c}_{ab,\sigma} c_{b\sigma} c^{\dagger}_{a\sigma},\end{aligned} \tag{3.57}$$

where the variational tunnel-coupling amplitudes $V_{a\sigma,\sigma}$ and the Lagrange multipliers $\lambda^{c}_{ab,\sigma}$ are given by Eqs. (3.45) and (3.46), respectively.

In the following we present the results obtained for an impurity embedded in a metallic host characterized by a flat hybridization function:

$$\Gamma(\omega) = \Gamma(0)\theta(W - |\omega|) \tag{3.58}$$

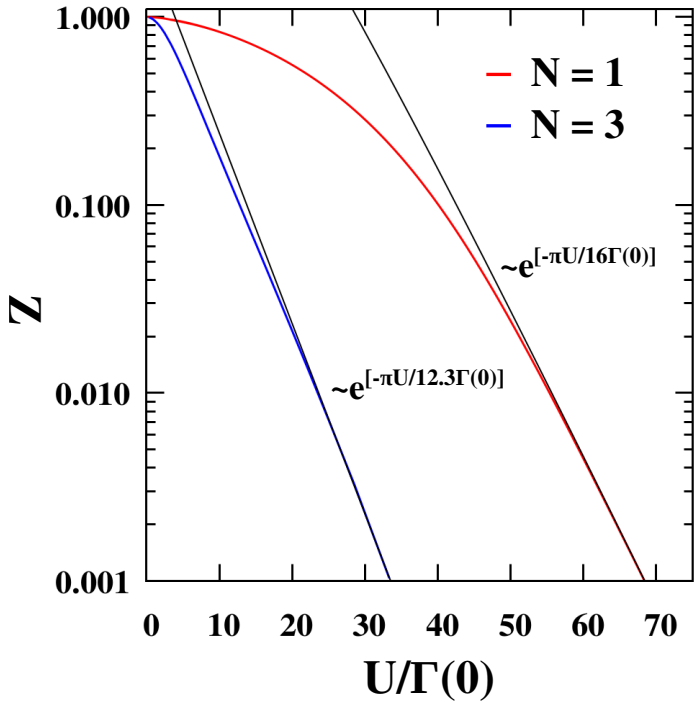

Figure 3.2: Comparison between quasiparticle residue for $N = 1$ and $N = 3$. Logarithmic scale reveals the different prefactor of $U/\Gamma(0)$ in the exponential behavior of Z. Data are obtained by fixing $U/W = 0.1$ and varying $\Gamma(0)$.

where $\theta(x)$ is the Heaviside step function and W is the half-bandwidth of the metallic host that is going to be used as the unit of energy. Our calculations of the SIAM are benchmarked against NRG [157, 158, 287, 291]. The results of the optimization for $h = \mu = 0$ are shown in Fig. 3.1 where we plot the quasiparticle residue Z, which is defined in the Appendix A.4, and the double occupancy on the impurity site, $D = \langle\psi|d_\uparrow^\dagger d_\uparrow d_\downarrow^\dagger d_\downarrow|\psi\rangle$, as a function of $U/\Gamma(0)$. In particular, in the top panel of Fig. 3.1 we compare the quasiparticle residue Z as a function of the on-site repulsion $U/\Gamma(0)$ obtained with g-GW with $N = 1$ (red line), $N = 3$ (blue line) and NRG (black dots). On another side, in the bottom panel of Fig. 3.1 we show the comparison between the double occupancy obtained with these methods. By adding two auxiliary degrees of freedom the results given by g-GW improve considerably compared to the conventional Gutzwiller wave function calculations. It is interesting to analyze more in detail the behavior of Z, which is proportional to the Kondo temperature, in the Kondo regime. For $U/\Gamma(0) \gg 1$ Fig. 3.2 shows the improvement on the evaluation of the quasiparticle residue Z while increasing the number of bath levels from $N = 1$ to $N = 3$. A numerical analysis of the results shows that the g-GW with $N = 3$ provides a more accurate estimate of the Kondo temperature $T_K \propto \exp[-\pi U/12.3\Gamma(0)]$, which is, however, still overestimated with respect to the exact universal prefactor $\pi/8$ of $U/\Gamma(0)$ Eq. (3.54) obtained with Bethe Ansatz [273].

The effect of a magnetic field h on the impurity site is shown in Fig. 3.3, where we plot the quasiparticle residue and the magnetization as a function of $U/\Gamma(0)$ at small magnetic field, $h/U = 0.001$. The top panel of Fig. 3.3 shows the quasiparticle residue as a function of $U/\Gamma(0)$. Initially, by increasing the value of the interaction, the quasiparticle residue Z decreases due to correlations. Then, when the magnetization on the impurity site increases (lower panel of Fig. 3.3), it changes its curvature and eventually $Z \to 1$ in the $U/\Gamma(0) \to +\infty$ limit, i.e. fully-polarized solution is not correlated. Indeed, in the limit of large magnetization the dominant effect of the

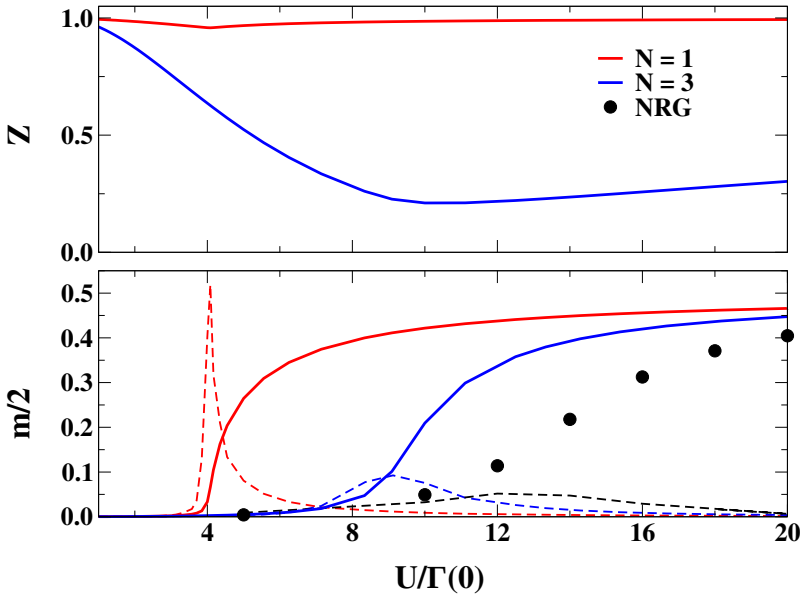

Figure 3.3: Top panel: quasiparticle residue as a function of $U/\Gamma(0)$ at fixed magnetic field. Bottom panel: magnetization as a function of $U/\Gamma(0)$ at fixed magnetic field. Dashed lines represent the variation of m by varying interaction strength U. The sharp peak denotes the instability of $N = 1$ toward spontaneous magnetization. This unphysical feature of the conventional Gutzwiller wave function is discussed in detail in Section C.4. Data are obtained using the half-bandwidth of the metallic host W as unit of energy, $U/W = 0.1$, $h/U = 0.001$ and varying the tunnel-coupling with the bath $\Gamma(0)$.

interaction is to introduce a spin-dependent Hartree shift that enhances the spin $\uparrow$ occupation while decreases the spin $\downarrow$ one. In the bottom panel we compare the magnetization obtained with g-GW and NRG. In comparison with the conventional Gutzwiller, the g-GW solution with $N = 3$ is less susceptible to the applied Zeeman field, and the magnetic susceptibility, which is diverging for $N = 1$ (for more details we refer to Appendix C.4), becomes a smooth function of $U/\Gamma(0)$.

Despite the remarkable improvement with respect to the conventional Gutzwiller, g-GW with $N = 3$ still overestimates the magnetization if compared with the more accurate NRG solution. Finally, in Fig. 3.4 we compare the spectral functions obtained with the two different techniques (details on the evaluation of spectral functions in the g-GW approach are given in Appendix A.3). As a consequence of the larger susceptibility the splitting induced on the low-energy resonance is overestimated with respect to the exact result obtained with NRG. In agreement with NRG results, we notice that the spin unbalance effect is stronger in the high-energy Coulomb peaks than in the low-energy Kondo resonance.

3.3.1 Pseudogap Anderson impurity model

In this Section we apply the g-GW variational approach to a magnetic impurity described by the Hamiltonian in (3.52) with $h = \mu = 0$ and coupled to a fermionic bath characterized by a pseudogap hybridization function, which we parametrize as

$$\Gamma(\omega) = (1 + r)\Gamma \left| \frac{\epsilon}{W} \right|^r \theta(W - |\epsilon|). \tag{3.59}$$

The chosen functional form interpolates between the metallic case $r = 0$ and the hard-gap case $r = +\infty$. These two limiting regimes are characterized by two completely different strong

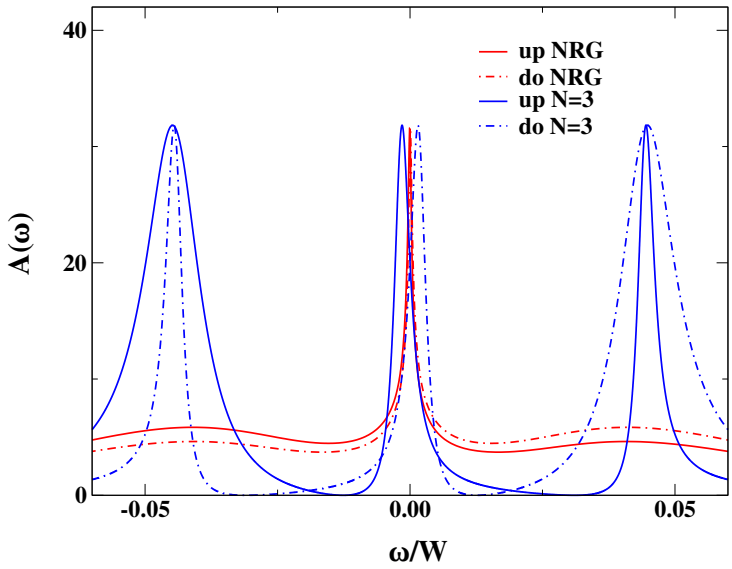

Figure 3.4: Spin resolved spectral functions, comparison between g-GW $N = 3$ (blue) and NRG (black). Solid and dashed lines represent the spin $\uparrow$ and $\downarrow$ impurity density of states, respectively. The effect of the Zeeman term on the low-energy Fermi liquid is less pronounced in NRG than in the g-GW, which, thus, overestimates the magnetic susceptibility of the SIAM. Numerical results are computed for $U/W = 0.1$, $\Gamma(0)/W = 0.01$ and $h/U = 0.001$.

coupling fixed points. As we have already seen in the previous Section 3.3, for $r = 0$ the impurity magnetic moment is screened by the metallic host, leading to the screened phase (SC). In the $r = +\infty$ regime, the absence of low-energy electrons suppresses the exchange coupling and the spin on the impurity site is a free magnetic moment. The latter behavior is known as the local moment (LM) regime. The pseudogap case, realized for the intermediate values of r, leads to a very rich behaviour, in particular to a continuous transition between a LM and a SC [89, 102, 288] which represents an ideal test for our approach.

We notice that for $r = 0$ (metallic bath), Z smoothly crosses over to an exponentially small value in the strong coupling Kondo regime and the system flows to the SC Kondo screened fixed point. However, we can see from the top panel of Fig. 3.5 that, as soon as $r \neq 0$, it is possible to have a vanishing quasiparticle residue at finite U/Γ. In Fig. 3.6 we show the line of the critical points $U_c(r)/\Gamma$ where the quantum phase transition between the SC and the LM regimes occurs. For $U < U_c(r)$ the variational ground state has a finite Z (see Fig. 3.5), meaning the system is a local Fermi liquid, as one expects at the Kondo strong-coupling fixed point. On the contrary, for $U > U_c(r)$, the low-energy Kondo resonance disappears due to the vanishing quasiparticle residue $Z = 0$ as shown in Fig. 3.5. It is important to notice that in this regime the impurity is still coupled to the high-energy bath levels that induce the broadening of the charge fluctuation peaks in the physical electron spectral function depicted in Fig. 3.7.

A more complete inclusion of quantum fluctuations would reveal an even richer phase diagram. Indeed, it has been shown by means of NRG [102] and field-theoretical analysis [89], that the QCP is present only for $r \in (0, 1/2)$, while for $r > 1/2$ the system always flows to the LM fixed point. This is not captured by the novel Gutzwiller variational wave function for $N = 3$ that, as displayed in Fig. 3.6, predicts a finite U_c for $r \geq 1/2$. We expect that by increasing the number N the phase diagram would improve and possibly approach the exact vanishing value of the critical interaction $U_c = 0$ in the regime $r \geq 1/2$. It is interesting to look at the different behavior of the impurity spectral function in the two different regimes. As shown in Fig. 3.7,

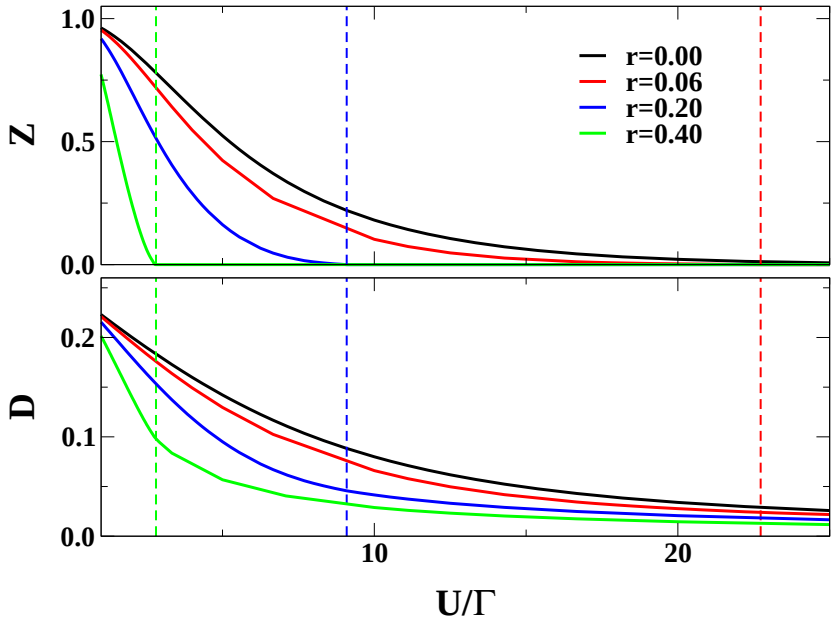

Figure 3.5: Top panel: quasiparticle residue as a function of U/Γ for different values of r. Bottom panel: double occupancy as a function of U/Γ for different values of r. Vertical dashed lines denote the critical value of the on-site interaction. We notice that the double occupancy is finite in the LM regime.

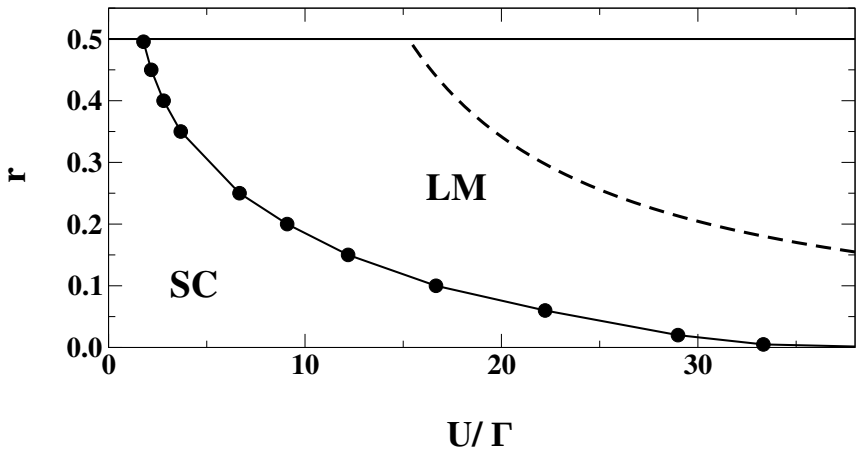

Figure 3.6: Phase diagram r versus U/Γ. Solid black points are computed with g-GW $N = 3$, while dashed black line is the critical line $U_c = 16\Gamma(1 + r)/\pi r$ obtained with conventional Gutzwiller [245]. By fixing the value of r the system undergoes a quantum phase transition at the critical value of the interaction U_c/Γ depicted by the black line. For $r > 1/2$ no Kondo effect occurs.

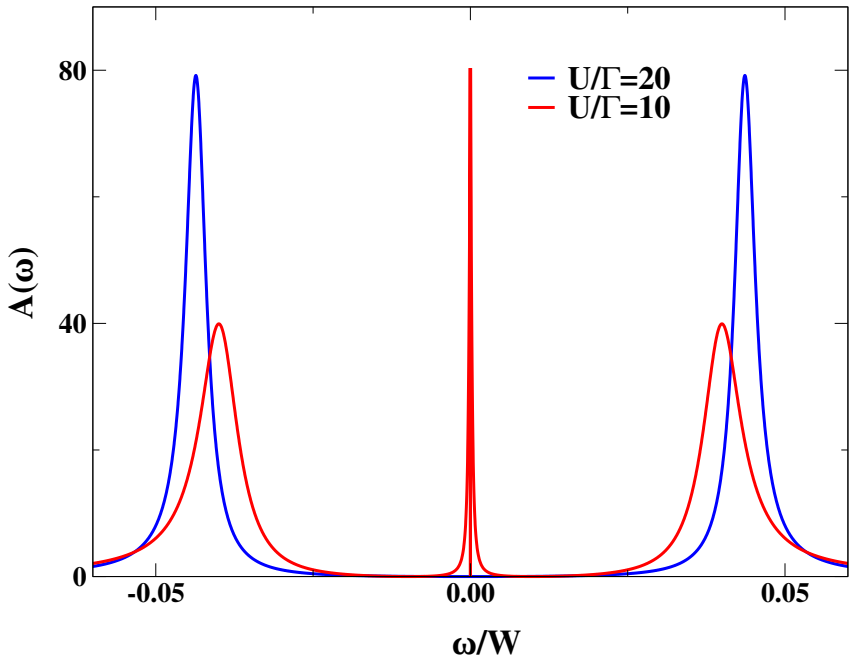

Figure 3.7: Spectral function computed for $r = 0.1$. Red and blue lines are computed at $U/\Gamma = 10$ (SC) and $U/\Gamma = 20$ (LM), respectively. In the LM regime the absence of Kondo screening is signalized by a gapped spectral function.

for $U < U_c$ (SC) the spectrum is characterized by the low-energy Kondo resonance, while for $U > U_c$ the spectrum presents a gap at the Fermi energy, signalizing the absence of magnetic screening of the spin on the impurity site.

In comparison with the previous results obtained with the conventional Gutzwiller wave function [245], the g-GW improves the impurity phase diagram by reducing the overestimated values of the critical interaction $U_c(r)$. The g-GW gives a much more realistic description of the LM regime, which in the conventional Gutzwiller is described by an isolated magnetic impurity completely decoupled from the metallic host. Indeed, as one can see from the top panel of Fig. 3.5, despite a vanishing quasiparticle residue in the LM regime (bottom panel of Fig. 3.5), g-GW is characterized by a non-zero average value of the double occupancy on the impurity site. This additional feature could enrich the out of equilibrium dynamics analyzed with the conventional Gutzwiller approach in Ref. [245]. A non-vanishing hybridization with the high-energy bath levels induces additional relaxation channels that may drive the nonequilibrium evolution towards a stationary state even in the regime of the strong interactions.

3.4 The Mott transition in the single-band Hubbard model

The conventional Gutzwiller approximation applied to the half-filled Hubbard model predicts a continuous Mott metal-to-insulator transition, the so-called *Brinkman-Rice scenario* [38], characterized by vanishing spectral weight at the Fermi level and diverging effective mass. In spite of its simplicity, the approach is a powerfull tool for extracting the Landau parameters [24, 93, 235, 279, 280] of strongly correlated Fermi liquids [165, 211] and it captures the main ingredients of the Mott transition that are confirmed by more accurate DMFT calculations [94]. The main drawback of the Gutzwiller approach is the poor description of the Mott insulator. Indeed, within this approximation, the insulating state is described by a collection of single

electrons frozen on each lattice sites. Remarkably, the g-GW captures both the (low-energy) quasiparticle bands and the (high-energy) Hubbard bands within the same theoretical framework. In order to show this striking result we apply the g-GW to the single-band Hubbard model [111, 119, 140], which is described by the Hamiltonian:

$$H = -\frac{t}{\sqrt{\mathbf{Z}}} \sum_{\langle i,j \rangle} \sum_{\sigma} \left(d^{\dagger}_{i\sigma} d_{j\sigma} + \text{H.c.} \right) + U \sum_{i} \left(n_{i\uparrow} - \frac{1}{2} \right) \left(n_{i\downarrow} - \frac{1}{2} \right), \tag{3.60}$$

where $\langle i, j \rangle$ means nearest-neighbor bonds, and $\mathbf{Z}$ is the lattice coordination number that must be sent to $+\infty$ to ensure a variational character. This model contains the basic elements that identify the physics of strongly correlated electrons systems: the kinetic energy of the electrons, the interaction between them and the static ionic potential and the electron-electron interaction at the minimal level. Despite its apparent simplicity, no exact solution of this model is known in dimension $d > 1$ [78, 173]. The physics of this model is the object of an intense investigation by means of analytical and numerical methods [231]. The Hubbard model is able to describe the Mott transition from a metallic state to a correlated insulator, as we already discussed in Chapter 1. The proximity to such transition is universally recognized to be an essential ingredient for the many unexpected properties (e.g. high-T_c-superconductivity) which characterize the strongly correlated electron systems [19, 27, 169].

In the following we present the numerical computations obtained with g-GW on a Bethe lattice, whose density of state, in the limit $\mathbf{Z} \to +\infty$, is given by

$$\rho(\epsilon) = \frac{2}{\pi W^2} \sqrt{W^2 - \epsilon^2} \theta(W - |\epsilon|) \tag{3.61}$$

where W is the half-bandwidth, $W = 2t$. Referring to the formulation presented in Section 3.2.2, we shall assume a translational invariant ground state, that implies a site-independent embedded impurity wave function:

$$|\psi(i)\rangle = |\psi\rangle, \tag{3.62}$$

in the paramagnetic sector (i.e. $SU(2)$ spin-rotations invariance):

$$\Delta_{a\sigma,b\sigma'}(i) = \delta_{\sigma\sigma'} \Delta_{ab}, \; R_{\sigma,a\sigma'}(i) = \delta_{\sigma\sigma'} R_a, \; V_{a\sigma,\sigma'}(i) = \delta_{\sigma\sigma'} V_a, \tag{3.63}$$

where we split the spin $\sigma = \uparrow, \downarrow$ and the orbital $a = 1, \cdots, N$ indices. Moreover, we require that the variational wave function is invariant under the particle-hole transformation C_σ, that acts on the embedded impurity model in Eq. (3.50) as

$$C_\sigma : \left(d_\sigma \to d^{\dagger}_{\sigma} \cup \prod_{a} \left(c_{a\sigma} \to -c^{\dagger}_{C_a\sigma} \right) \right) \tag{3.64}$$

while for the quasiparticle lattice model (3.22) reads:

$$c_{ia} \to (-1)^{R_i} c^{\dagger}_{iC_a}, \tag{3.65}$$

where $(-1)^{R_i}$ can be either ± 1 depending on the parity of the lattice site i, and in Eqs. (3.64) and (3.65) a and C_a are particle-hole conjugated bath levels. We notice that the particle-hole symmetry (3.64-3.65) implies that the single-particle density matrix satisfies the relation:

$$\Delta_{ab} = \delta_{ab} - \Delta_{C_b C_a}, \tag{3.66}$$

where a and b are particle-hole conjugated to C_a and C_b, respectively. Similar relations hold for the matrix of Lagrange multipliers

$$\lambda_{ab} = -\lambda_{C_b C_a}, \quad \lambda^c_{ab} = -\lambda^c_{C_b C_a} \tag{3.67}$$

and

$$R^*_a R_b = R^*_{C_b} R_{C_a}. \tag{3.68}$$

Finally, The expectation value per site E of the Hamiltonian (3.60) on the variational wave function (3.1) can be written as a functional of $|\psi\rangle$ as shown in Eq. (3.33). The Slater determinant $|\Psi_*\rangle$ is the ground state of the auxiliary non-interacting Hamiltonian

$$H_* = \sum_{ab=1}^{3} \sum_{\sigma} \sum_{\mathbf{k}} c^\dagger_{\mathbf{k}\, a\sigma} \left(\epsilon_{\mathbf{k}} R^*_a R_b + \mu_{ab} \right) c_{\mathbf{k}\, b\sigma} \,, \tag{3.69}$$

where the dispersion relation reads

$$\epsilon_{\mathbf{k}} = -\frac{t}{2\sqrt{\mathbf{Z}}} \sum_{j}^{\text{n.n. of } i} e^{i\mathbf{k}\cdot(R_i - R_j)}, \tag{3.70}$$

and the sum over j is extended only to the nearest neighbors of i.

The optimization of the g-GW Lagrangian (3.33) is performed by using the iterative scheme presented in Section 3.2.3, considering $N = 3$ auxiliary orbitals. Then, in order to analyze the effect of additional levels we consider the variational ghost-Gutzwiller solution for $N = 5$. In particular, we compare $N = 3, 5$ and DMFT results to determine the improvement in the description of the ground state properties of the metallic and the Mott insulating phases provided by an enlarged number of subsidiary levels. Before entering the discussion, we present the results obtained for $N = 3$. Fig. 3.8 shows the evolution of the g-GW total energy and the wave function renormalization factors R_a (3.18) as a function of the Hubbard interaction strength U/W for $N = 3$. Our ground state energy is shown in comparison with the DMFT one, the latter is obtained by using exact diagonalization as impurity solver with 7 bath levels [44, 49]. The agreement between g-GW and DMFT is quantitatively noteworthy. In particular, the g-GW wave function enables us to account for the coexistence region of the Mott and metallic phases, which is not captured by the standard Gutzwiller. Solid blue line in the top panel of Fig. 3.8 shows the energy of the Mott insulator, while solid red line is the one corresponding to the metallic solution. We notice that the Mott insulator exists only above a critical value of the interaction U_{c1}, below which the only stable solution is the metal, light red region in Fig. 3.8. In the intermediate white region, the metastable Mott insulator coexists with the stable metal. Finally, at the critical value U_{c2} the metallic solution merges continuously into the insulating solution and for $U > U_{c2}$ the system is a pure Mott insulator, depicted as the blue region in the top panel of Fig. 3.8. The values of the boundaries of the coexistence region, $U_{c1}/W \simeq 1.85$ and $U_{c2}/W \simeq 2.88$, are slightly underestimated with respect to DMFT predictions, $U_{c1}/W \simeq 2.39$ and $U_{c2}/W \simeq 2.94$ [95]. Moreover, in Fig. 3.9 we report the ground state kinetic, potential and total energy contributions comparing the DMFT results with the g-GW technique.

Approaching the Mott transition from the metallic side, we find that $R_1 = R_3 \to 1/\sqrt{2}$ and $R_2 \to 0$, see bottom panel of Fig. 3.8. Just like in DMFT, the Mott transition is characterized by the vanishing hybridization between the impurity and the bath level at the Fermi energy,

$$Q_2 = \langle \psi | c^\dagger_{2\sigma} d_\sigma | \psi \rangle \to 0, \tag{3.71}$$

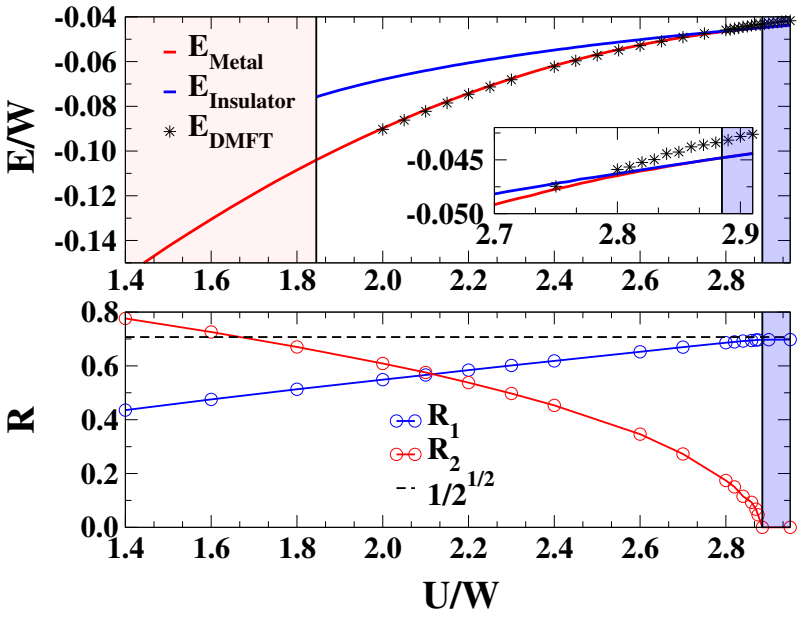

Figure 3.8: Top panel: total energy E per site vs. U, in units of the half-bandwidth W, for the stable metal and metastable insulator solutions, red and blue lines, respectively. The starred symbols are obtained from DMFT calculations using exact diagonalization as impurity solver with 7 bath levels instead of the $N = 3$ as in the variational g-GW. In the light red region only the metallic solution exists, while in the blue one the system is a pure Mott insulator. Intermediate white region is characterized by the coexistence of the two solutions. Bottom panel: renormalization parameters $R_1 = R_3$ and R_2. We note that the Mott transition is signalized by disappearance of R_2, while $R_1 = R_3$ approach the value $\sqrt{1/2}$ from below.

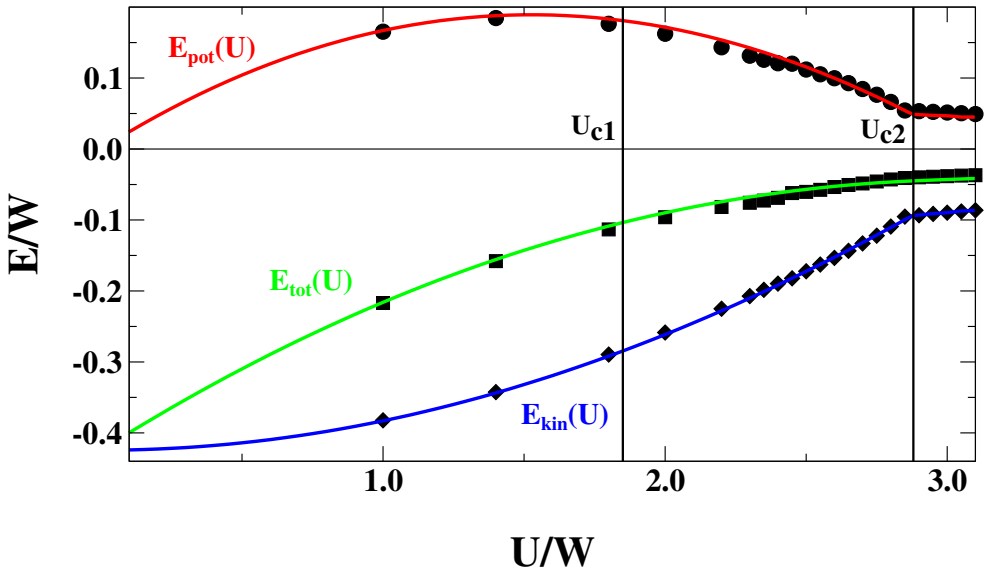

Figure 3.9: Red, blue and green solid lines represent the potential, kinetic and total energy contribution, respectively, computed with g-GW for $N = 3$. Black points are DMFT data obtained using exact diagonalization as impurity solver with 7 bath levels. Vertical black lines report the values of U_{c1} and U_{c2}.

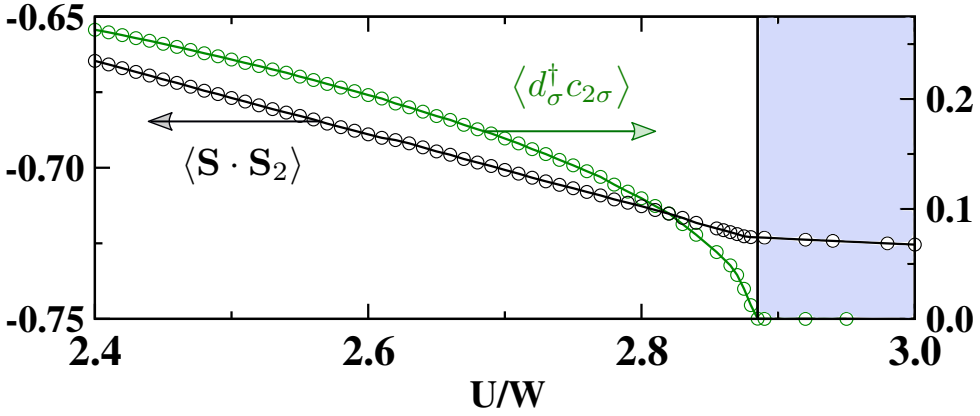

Figure 3.10: Expectation value $\langle\psi|\mathbf{S}\cdot\mathbf{S}_2|\psi\rangle$ of the spin correlation between the impurity and the level 2. Note that $\langle\psi|\mathbf{S}\cdot\mathbf{S}_2|\psi\rangle$ increases in absolute value with U, and is continuous across the Mott transition, despite the vanishing expectation value $\langle\psi|d^\dagger_\sigma c_{2\sigma}|\psi\rangle$ of the hybridization, also shown. In the light blue region the metallic solution is destroyed, $\langle\psi|d^\dagger_\sigma c_{2\sigma}|\psi\rangle = 0$, and only the Mott insulator exists.

see Fig. 3.10. In the insulating phase, the wave function $|\psi\rangle$ thus factorizes into a spin-1/2 wave function $|\phi_\sigma\rangle$ for the impurity and the auxiliary levels 1 and 3, with the spin mostly localized on the impurity since 1 and 3 are far from the chemical potential, and a spin-1/2 wave function $|\varphi_\sigma\rangle$ of the decoupled singly-occupied level 2. However, due to Eqs. (3.13) and (3.18) that determine both Hamiltonian H_* in (3.22) and its ground state, the variational wave function with lowest energy is actually the singlet combination

$$|\psi\rangle = (|\phi_\uparrow\rangle \times |\varphi_\downarrow\rangle - |\phi_\downarrow\rangle \times |\varphi_\uparrow\rangle)/\sqrt{2} \tag{3.72}$$

lying at $\sim J/8 = W^2/8U$ below the triplet[3]. In other words, despite level 2 is not hybridized with the impurity, it remains entangled with the latter in the optimized wave function. This result is shown Fig. 3.10 where we plot, as a function of U around the Mott transition, the expectation value $\langle\psi|\mathbf{S}\cdot\mathbf{S}_2|\psi\rangle$, where $\mathbf{S}$ and $\mathbf{S}_2$ are the spin operators of the impurity and the level 2, respectively. We note that this quantity is continuous across the Mott transition and approaches the spin-singlet limit $-3/4$ at large U. This wave function evidently describes a pure state that cannot be interpreted as the ground state of an Anderson impurity model. Indeed, the spin entanglement between $|\phi_\sigma\rangle$ and $|\varphi_\sigma\rangle$ can only be rationalized through an effective antiferromagnetic exchange between level 2 and the remaining sites of the impurity model, which is not a one-body potential. The above result, Eq. (3.72), turns out to be of fundamental importance. Indeed, as we will explain in Section 4.5, it allows us to capture the physics of the Mott transition in photoexcited semiconductors. Before entering the argument, we would like to conclude by analyzing the effect of two additional bath levels on the g-GW description of the metal and Mott insulator.

Fig. 3.11 shows the ground state energy and double occupancy of the metallic solution as a function of U/W. As expected, by enlarging the number of variational parameters the ground state energy of the metallic solution improves. A closer look at the inset of Fig. 3.11 shows that the value of U_{c2}/W increases from $\simeq 2.88$ for $N = 3$ to $\simeq 2.9$ for $N = 5$, second value being closer to the DMFT prediction [95]. The lower panel of Fig. 3.11 depicts the enhancement of the double occupancy by increasing N from $N = 3$ up to $N = 5$. The additional levels are located close to

[3] In the large-U Mott insulating regime the variational wave function can be obtained analytically for $N = 3$, we refer the interested reader to Section A.2 for detailed calculations.

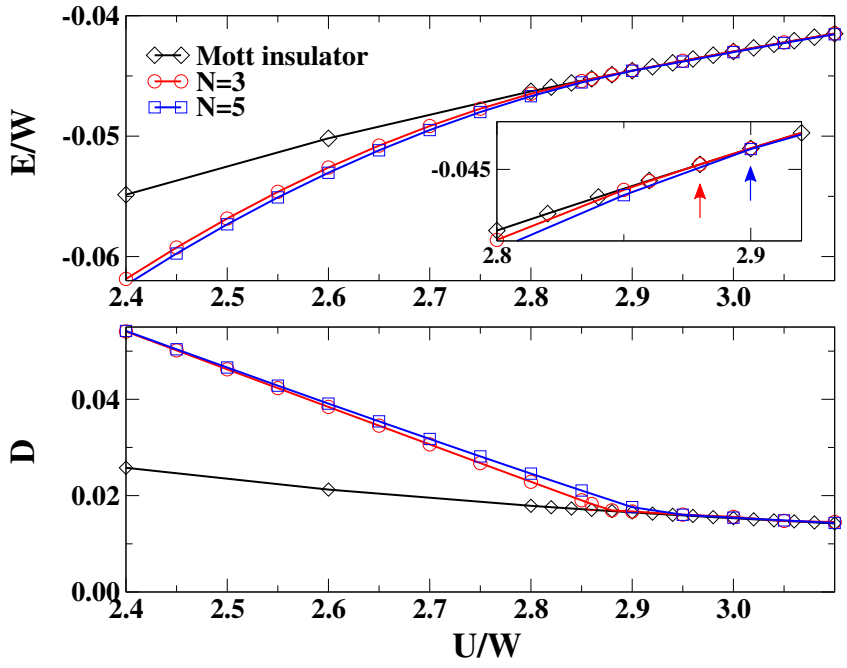

Figure 3.11: Ground state energy and double occupancy as a function of U/W. Top panel: Red and blue lines represent the energy of the metallic solution computed with $N = 3$ and $N = 5$ bath levels, respectively. Instead, black line is the Mott insulator energy computed for $N = 3$. A closer look at the critical region is shown in the inset, where red and blue arrows point out the different values of U_{c2} for $N = 3, 5$. Bottom panel: Red and blue lines represent the double occupancy of the metallic solution computed with $N = 3$ and $N = 5$ bath level respectively. The black line represents the Mott insulating state.

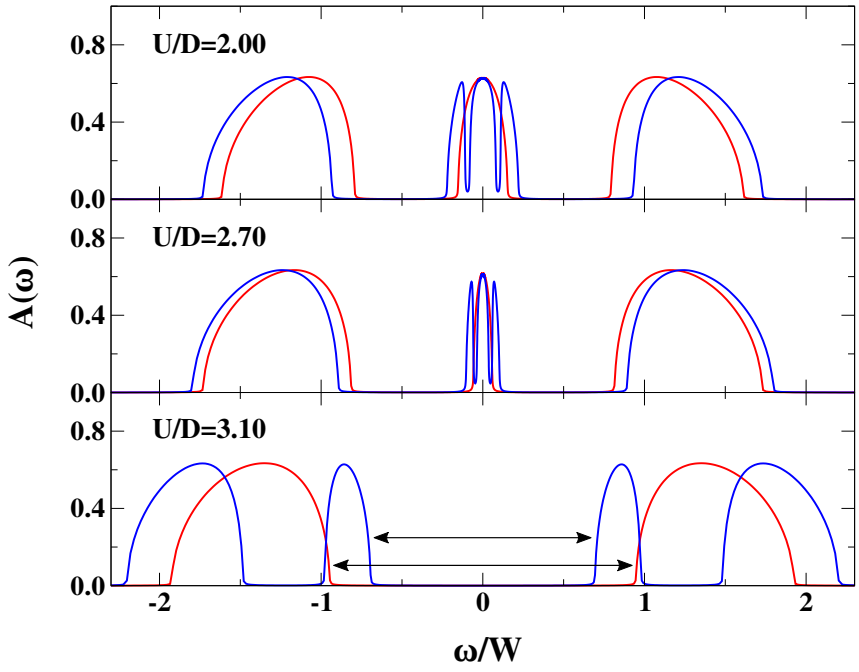

Figure 3.12: Evolution of the density of states of the correlated metal for different values of U/W. Red and blue lines represent the equilibrium g-GW spectral function computed with $N = 3$ and $N = 5$ bath levels, respectively.

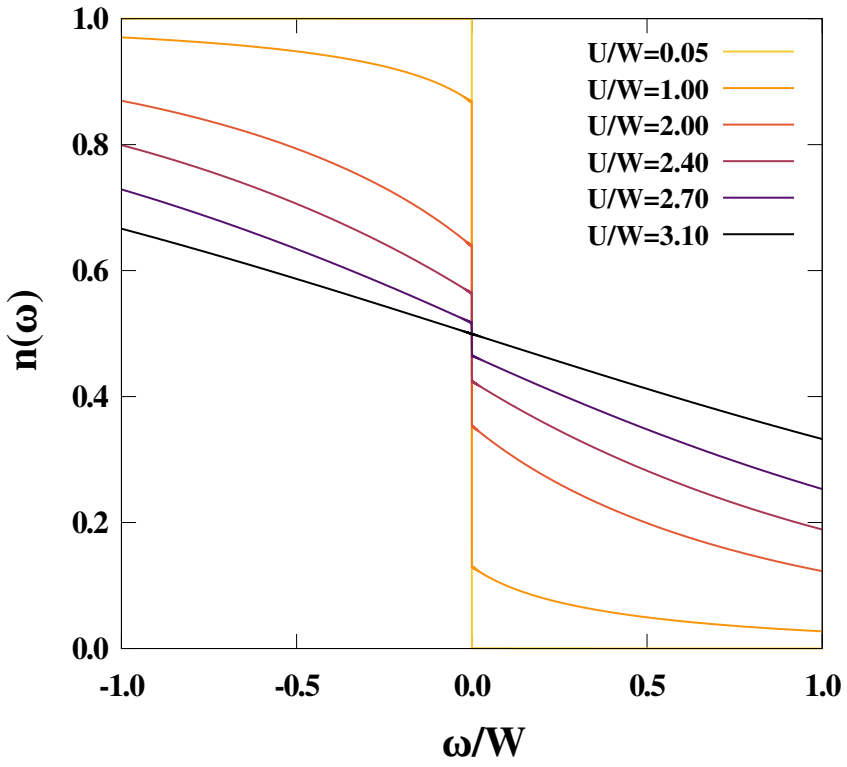

Figure 3.13: Interacting distribution function $n(\omega)$ computed with $N = 5$ bath levels. The jump gives the fraction of excitations of the interacting systems, which can be described in terms of effective free particles.

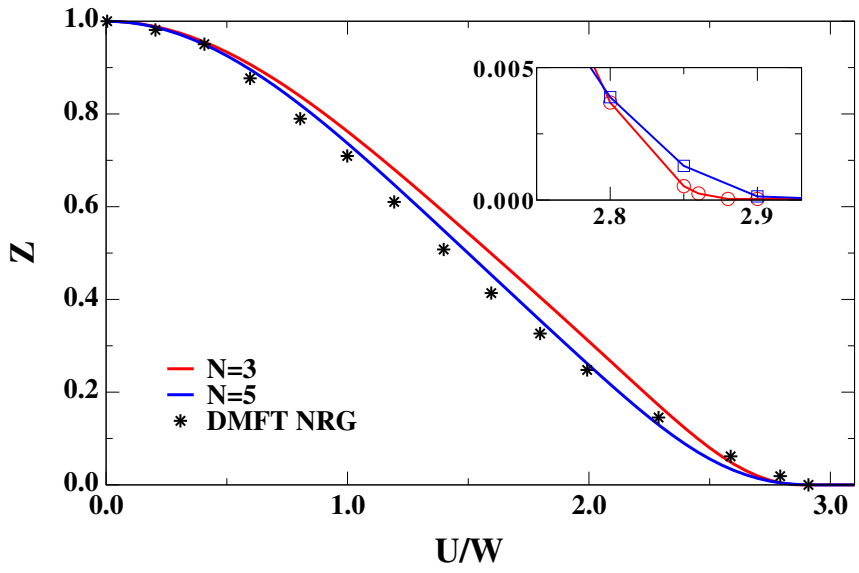

Figure 3.14: Red and blue lines represent the quasiparticle residue Z as a function of U/W for $N = 3, 5$, respectively. Black stars are DMFT data taken from [41]. The inset shows the region close to the spinodal point U_{c2}/W of the metallic solution.

the Fermi energy in the metallic phase. This feature is displayed in Fig. 3.12 where we compare the spectral function[4] for $N = 3, 5$ computed at different values of the interaction. On the other hand, in the insulating regime $U > U_{c2}$ the lower and upper Hubbard bands split, giving rise to two different high-energy spectral features. It is interesting to notice that the Hubbard gap becomes smaller as the number of bath level increases. This tendency suggests that the spinodal point for the Mott insulator U_{c1}/W increases by increasing N, and it eventually reaches a converged value for $N \gg 1$. Finally, in Fig. 3.13 we show the g-GW quasiparticle distribution function, which is defined in Eq. (A.23) of Appendix A.4, for different values of U/W and $N = 5$. Remarkably, the method describes the quasiparticles close to the Fermi level and high-energy charge excitations. By increasing the interaction the discontinuity at the Fermi level decreases and eventually vanishes above the critical interaction U_{c2}, $U \geq U_{c2}$. This behavior is shown in Fig. 3.14, where we plot Z as a function of U/W comparing the g-GW results for $N = 3, 5$ with DMFT ones. The agreement between g-GW and DMFT is quantitatively remarkable, and becomes better by increasing N.

3.5 Conclusions and perspectives

In this chapter, we present the formulation of the g-GW approach for a generic multi-band Hubbard model, neglecting superconductive correlations. The variational wave function is characterized by the addition of auxiliary fermionic degrees of freedom and allows describing not only the low-energy quasiparticles but also the high-energy Hubbard bands due to incoherent charge fluctuations. The improvement with respect to the conventional Gutzwiller wave function is outstanding. We underline that the g-GW is much richer than the standard Gutzwiller wave function and, on the other hand, less numerically expensive than DMFT, which makes the method more likely applicable to realistic simulations. Moreover, the flexibility of the g-GW allows us to apply the variational approach both to single-impurity and lattice models.

The application of the method to the SIAM improves the estimation of the Kondo temperature with respect to the conventional Gutzwiller (Fig. 3.2), which is however still overestimated for $N = 3$. It is interesting to look at the scaling of the Kondo temperature obtained by increasing the number of bath levels N. This future project will shed light on the role of the parameter N, that is expected to play a similar role of the bond dimension in matrix-product states [217, 236] or the number of "hidden" variables in neural networks states [50] and, therefore, related to the amount of entanglement in the variational wave function. Fig. 3.3 shows that the addition of subsidiary degrees of freedom allows removal of the magnetic instability that characterizes the conventional Gutzwiller solution of the SIAM (discussed in detail in Section C.4).

An ideal test for our approach, we study the quantum phase transition between the screened (SC) regime and the local magnetic moment (LM) one occurring in the pseudogap SIAM. In comparison with the conventional Gutzwiller, the method with $N = 3$ improves substantially the impurity phase diagram 3.6. In the LM regime the valence fluctuation peaks in the spectral function (blue line in Fig. 3.7) are broaden due to the residual effective coupling of the impurity with the high-energy levels of the bath. Correspondingly, the LM phase is characterized by a non vanishing value of the double occupancy on the impurity site. As already observed at the end of Section 3.3.1, this additional feature could enrich the out of equilibrium dynamics analyzed with the conventional Gutzwiller approach in Ref. [245].

Finally, we apply the approach to describe the Mott transition in the single-band Hubbard model. As expected from previous results for the impurity models, the g-GW reproduces not

[4] For more details on the single-particle spectral function within the g-GW, we refer the interested readers to Appendix A, Section A.3.

only the low-energy quasiparticle excitations, but also the Hubbard bands (see Fig. 3.12). It is important to remark that the approach allows us to capture the coexistence between the Mott insulator and the metal, which is not described by the conventional Gutzwiller technique. The comparison with more accurate DMFT, displayed in Figs. 3.8 and 3.9, shows an excellent agreement even for a relatively small number of auxiliary sites, $N = 3$. Finally, we investigate the variational results by increasing the number of subsidiary site up to $N = 5$. Interestingly, the estimations of the end points of the coexistence region and the quasiparticle residue improve by increasing the number of subsidiary sites, see Figs. 3.11 and 3.14. This result poses a question about the limit of $N \gg 1$. In particular, one may argue that the variational g-GW solution approaches the exact DMFT result [95] for $N \to \infty$. To clarify the connection between these methods we believe that a detailed analysis of the variational g-GW results as a function of N is required.

4

Exciton Mott transition in photoexcited semiconductors

The dissociation of excitons into a liquid of holes and electrons in photoexcited semiconductors, despite being one of the first recognized examples of a Mott transition, still defies a complete understanding, especially regarding the nature of the transition, which is found continuous in some cases and discontinuous in others. Here we consider an idealized model of photoexcited semiconductors that can be mapped onto a spin-polarised half-filled Hubbard model. Our phase diagram reproduces most of the phenomenology of those systems and uncovers the key role of the exciton binding energy in determining the nature of the exciton Mott transition. We find indeed that the transition changes from discontinuous to continuous as the binding energy increases. Moreover, we uncover a rather anomalous electron-hole liquid phase next to the transition, which still sustains excitonic excitations despite being a degenerate Fermi liquid of heavy mass quasiparticles. We tackle the problem with the ghost-Gutzwiller variational wave function introduced in Chapter 3.

4.1 Introduction

The transition between an exciton gas (EG) and an electron-hole liquid (EHL) in photoexcited semiconductors (PES) above the exciton condensation temperature is since long known [39, 198, 234] to realize an almost ideal Mott transition [196], i.e., a metal-insulator transition driven by interaction and not accompanied by any symmetry breaking. Away from the critical region, in the regime of small density of electron-hole excitations, most of the photoexcited carriers are bound in excitons (EG) that propagate as chargeless particles in the semiconductor. In the opposite regime of large concentration of photoexcited pairs, where the Coulomb interaction is strongly screened, the system is a plasma of free carriers (EHL), that, differently from the EG, exhibits a finite current to an applied electric field. Hence, we expect at first glance to observe, in the intermediate regime, a phase transition analogous to the liquid-gas one where, as the density of electron-hole pair increases, the gas of excitons gradually dissociates into an unbound liquid of electrons and holes. It is important to remark that the different electrical characteristics of the insulating EG and the metallic EHL complicate the interpretation of experimental results by introducing the intriguing possibility of a metal-insulator Mott transition separated from the

liquid-gas one. Nevertheless and despite the great progresses in the theoretical understanding of the Mott transition, several aspects remain puzzling; in the first place the nature of the transition. On one hand, the liquid-gas analogy suggests that, as the number of photoexcited electron-hole pairs increases, a gradual crossover between the two phases takes place via the formation, within the EG, of liquid droplets that grow till the system transforms entirely into an EHL, just like in any phase-separation scenario of a first-order transition. However, the concurrent growth of screening might lead to an avalanche effect [234] and thus to an abrupt transition into the EHL. This scenario could reveal itself either by the existence of a Mott transition distinct from the gas-liquid one, as Landau and Zeldovich originally proposed for liquid mercury [164], or through a bistability [254].

In view of the revived interest in the physics of excitons, the solution of the basic yet open issues in the exciton Mott transition cannot be further delayed. The scope of this Chapter is just putting together some pieces of that puzzle. For that purpose, we consider an idealized model of PES that can be mapped onto a half-filled repulsive Hubbard model at finite spin polarization, where the fully polarized state, a trivial insulator, maps onto the unexcited semiconductor, and each spin flip corresponds to adding one electron and one hole in the conduction and valence bands, respectively. In turns, the insulator-metal Mott transition reached at large enough Hubbard U upon decreasing spin polarization translates into the EG-EHL transition on increasing the density of photoexcited electron-hole pairs. We find that such Mott transition can be either continuous or discontinuous, in the sense specified above, depending on the strength of U, which translates into the magnitude of the exciton binding energy, in good agreement with experiments.

Before presenting our theoretical results, we shall review some experimental studies on the EG-EHL transition in PES. Furthermore, we discuss some recent cutting-edge experiments on monolayer transition metal dichalcogenides (TMDs). This new class of materials with high control and tunability, for instance through interfaces with light sources, promises to be a fruitful future platform for condensed matter theory, somewhat similar to graphene and ultracold atoms [281].

4.2 Controversial experimental evidences

Experimentally, the nature of the transition, which can be studied by photoluminescence or optical absorption, is till now rather controversial. There are, indeed, evidences of two distinct transitions [264–266], as well as of a bistable behavior [13, 254, 270], but also of a gradual transition [141, 146, 239, 271].

To the latter scenario belongs the experimental observations in Ref. [141] where they study photoexcited 80 Å $In_xGa_{1-x}As$ quantum well (QW), with a low indium content of $x = 5\%$ grown by molecular-beam epitaxy. This QW is embedded in the middle of a GaAs layer. The sample is optically excited by means of laser pulses at a photon energy of 1.57 eV corresponding to 80 meV above the QW band gap. Figure 4.1 shows photoluminescence spectra integrated from 130 to 180 ps after excitation, using various excitation powers. At low excitation density, $n_{\text{e-h}} < 1 \times 10^{10} cm^{-2}$, we can easily distinguish the free-carrier luminescence appearing at the band gap 1490 meV and, separated by the exciton binding energy of $E_{\text{ex}} = 6.5$ meV below the band gap, the $1s$ exciton resonance. Moreover, we notice that the free-carrier contribution displays an exponential decrease to higher energy corresponding to a Boltzmann distribution of the carriers in the bands. The relative magnitude of the exciton and free-carrier luminescence components remains approximately constant in the density range of the first two spectra. At higher pair densities (between $2 \times 10^{10} cm^{-2}$ and $1 \times 10^{11} cm^{-2}$) the exciton as well as the

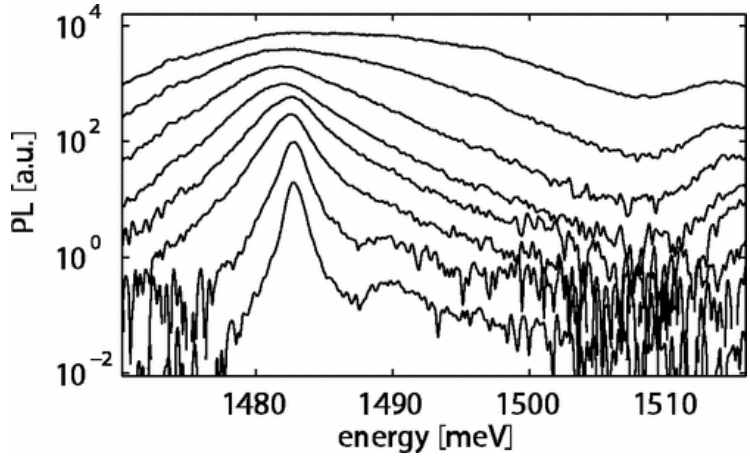

Figure 4.1: Photoluminescence spectra for different excitation powers integrated between 130 and 180 ps after excitation. The free-carrier luminescence threshold is located at the band gap 1490 meV and the $1s$ exciton contribution around 6.5 meV below the band gap. Peak intensities are equally spaced for improved readability. The carrier densities are (from lower to upper curve): $n_{\text{e-h}} = 1.6{\times}10^9 cm^{-2}, 7.8{\times}10^9 cm^{-2}, 2.3{\times}10^{10} cm^{-2}, 4.7\times10^{10} cm^{-2}, 7.8\times10^{10} cm^{-2}, 1.6\times10^{11} cm^{-2}, 3.1\times10^{11} cm^{-2}$, and $6.2\times10^{11} cm^{-2}$. Adapted from Ref. [141].

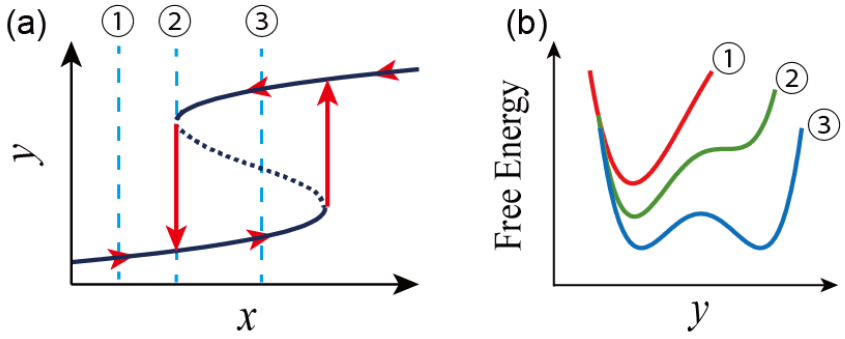

Figure 4.2: Schematic picture of a bistable system. (a) Output y as a function of input x. (b) Free energy at each cut in Fig. (a). Adapted from Ref. [254].

continuum luminescence progressively broaden masking the onset of band-to-band transitions. However, the spectra in this pair density regime still display an excitonic resonance revealed by the nonexponential high-energy tail. At higher density (above $1.6\times10^{11} cm^{-2}$) the excitonic resonance completely disappears, evidenced by an exponential high-energy photoluminescence tail which is the signature of the emission of a nondegenerate EHL. Therefore, the Mott transition is manifested by a gradual enhancement from an exciton-dominated population to an unbound electron-hole pair population as the pair density $n_{\text{e-h}}$ increases.

On the contrary, the bistable transition implies an abrupt transition from the EG to the EHL at the critical Mott density of electron-hole pairs. To clarify the concept of bistability we report in Fig. 4.2 panel (a) the function $y(x)$, which exhibits a bistable region as a function of the control parameter x. The bistable system has one thermodynamically unstable branch between two stable branches, and the transition from one branch to another one is accompanied by a hysteresis behavior, like in any ordinary liquid-gas transition where the control parameter is the applied pressure. As one can clearly see from Fig. 4.2 panel (a), the Maxwell construction is not allowed and the system jumps discontinuously to the stable branch. The correspondent

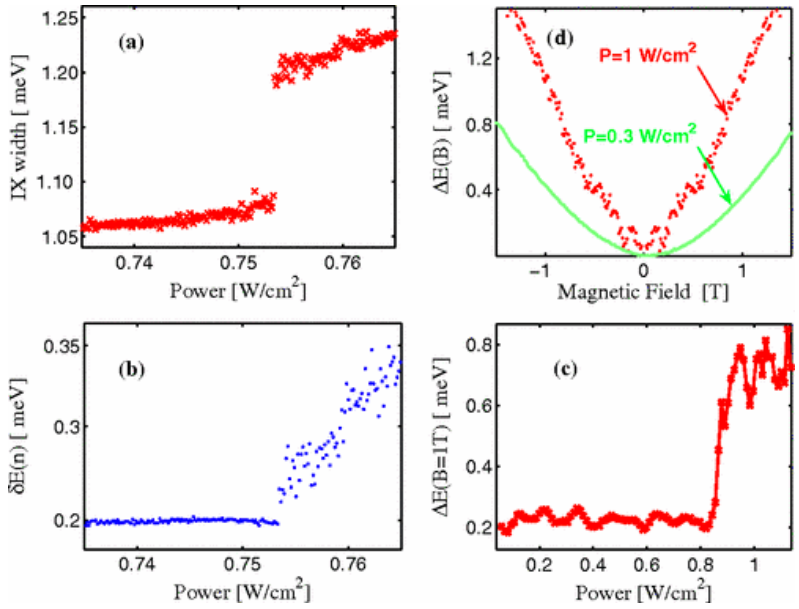

Figure 4.3: The PL properties for excitation in both wells $E_L > E_{NW}$ at temperature $T = 1.5$ K. (a) The linewidth, (b) the PL energy shift, and (c) the diamagnetic coefficient as a function of the power density. (d) The diamagnetic shift at two power levels, below and above the transition. Adapted from Ref. [270].

free energy is reported in Fig. 4.2 panel (b) and shows the presence of two stable solutions in the intermediate region. This scenario is observed in Ref. [270], where a sample made by coupled QWs is arranged in an $n^+ - i - n^+$ structure grown by molecular beam epitaxy on a semi-insulating GaAs substrate. The i region consists of two GaAs QWs of different width, 7 and 10 nm, separated by a 5 nm $Al_{0.28}GaAs$ barrier and surrounded by two AlGaAs spacer layers. Moreover, an electric field of 24 kV/cm was applied in a direction perpendicular to the QWs, such that the electron level in the wide well is higher than that of the narrow well. By a laser pulse with energy $E_L > E_{NW}$ electron-hole pairs are excited both in the narrow and wide wells, such that direct (within the same well) and indirect (among different wells) excitons can be formed. Fig. 4.3 panel (a) shows the photoluminesce linewidth, which changes from 1.0 meV to 1.2 meV at the critical power density of 0.75W/cm^2. The different nature of the phases across the abrupt transition are probed by measuring the diamagnetic response to an applied magnetic field B as reported in Fig. 4.3 panel (d). At large power density $P = 1.0\text{W/cm}^2$ the system is composed by free-carriers in Landau orbitals and, thus, characterized by a diamagnetic energy shift linear in the magnetic field, $\Delta E(B) = \hbar\omega_c/2 \propto B$. Conversely, for low electron-hole pairs density $P = 0.3\text{W/cm}^2$, the system is an EG, which is characterized by $\Delta E = \alpha B^2\langle r^2\rangle \propto B^2$ [40], where $\langle r^2\rangle$ is the average value of the exciton radius squared.

Differently from the precedent experiments, in Refs. [264–266] authors observe a double phase transition. They find out that at low temperature, starting from the low density EG, a liquid-gas transition to an excitonic condensed phase occurs, and then, as the total density of pairs is raised, the condensed phase undergoes a first-order Mott transition into droplets of EHL. The experimental results agree with the prediction proposed by Landau and Zeldovich in the seminal paper [164] that suggests the presence of two critical points, one for the liquid-gas transition and the other for the metal-to-insulator one. However, the theoretical description of this interesting scenario requires to include spacial correlations in the variational wave function and goes beyond the scope of our work.

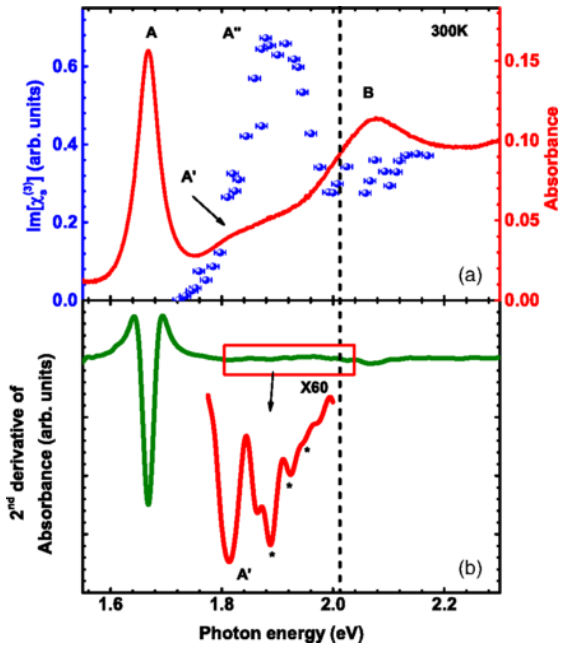

Figure 4.4: Top panel: Linear absorption (red line, right axis) and two-photon photoluminescence excitation spectrum (blue symbols, left axis) measured on monolayer WSe_2 at room temperature. Lower panel: Second-order numerical derivative of the linear absorption spectrum of (a). Black dashed line denotes the band gap energy of 2.02 eV. In addition to the lowest energy exciton states, labeled as A (1.65 eV) and B (2.08 eV) (located at the two non equivalent lattice points K and K'), the spectra present additional features whose detailed description is given in Ref. [115]. Adapted from Ref. [115]

Yet despite this fact, our theoretical calculations allow obtaining a phase diagram that reproduces most of the phenomenology observed in the previous experimental results and uncovers the key role of the exciton binding energy in determining the nature of the exciton Mott transition. Before entering the discussion, we shall present in the next Section an overview on the exciton physics in monolayer TMD.

4.2.1 Exciton Mott transition in monolayer TMD

The exciton physics in semiconductors has been given a new lease of life by monolayer TMD [71, 282, 283, 289, 290]. TMDs are semiconducting layered van der Waals crystals characterized with hexagonal lattice structure that are attracting an ever increasing attention for the potential technological impact of their electronic and optical properties. In the single layer limit, they exhibit an indirect-to-direct band gap transition due to the lack of interlayer interaction [283, 289]. Interestingly, the reduced screening results in a significantly enhanced Coulomb energy. This yields large exciton binding energies of several hundred meV [115, 219, 274], together with other multiparticle excitations, such as trions, and biexcitons. Top panel of Fig. 4.4 shows the linear absorption (red line) of monolayer WSe_2 in the energy range 1.5 – 2.2 eV, which is characterized by the presence of two prominent exciton peaks at 1.65 eV and 2.08 eV. Remarkably, the measured exciton binding energy is $E_{ex} = 0.37$ eV, which is about an order of magnitude larger than that in III-V semiconductor quantum wells and renders the exciton excited states observable even at room temperature. The direct band gap of monolayer TMDs and their large exciton binding energy make them potentially interesting candidates for various applications in optics and optoelectronics [200]. Furthermore, the two direct gaps located at K and K' are characterized

by different orbital polarization, which allow pumping selectively one of the two valley by exciting the sample with circularly polarized light [132, 171, 181, 260]. This phenomenon offers fascinating opportunities to realize novel phenomena and emerging applications, often referred to as valleytronics.

The dynamics of photoexcited electron-hole pairs in monolayer TMD has been investigated in many experiments, see, e.g., Refs. [29, 54, 61, 131, 222, 241, 262, 269]. At low excitation density, there is a consensus that both the excitons and the electronic gap red shift [61, 222, 262] signalize an important contribution of Coulomb repulsion in the semiconducting state of TMD. At higher excitation densities, where the EG-EHL transition is expected to happen, the situation is less clear. Reflectance measurements in WS_2 [54] irradiated by an ultrashort laser pulse show a gradual bleaching of the exciton absorption peak and, at lower energies, a loss of reflectance that is attributed [54] to an EHL phase with a more than 20% reduction of the gap. The coexistence of both signals indicates phase separation, and thus a continuous transformation from the EG to the EHL. On the contrary in Ref. [29], time-resolved photoluminescence in MoS_2 during a long 500 ns pulse photoexcitation reveals, at low pump fluence, the aforementioned red shift and a broadening of the exciton emission peak, which, above a threshold fluence, suddenly turns into a much broader and five times more intense emission peak, centred 200 meV below. This behaviour is rather suggestive of a discontinuous transition, unlike what observed in WS_2 [54]. Surprisingly, photoluminescence stops right after the 500 ns pump pulse [29], which can be interpreted as if the system undergoing a transformation from direct to indirect gap semiconductor, possibly driven by lattice expansion. All this suggests that photoexcited TMD may show rather interesting properties, especially because of the important role played by Coulomb repulsion.

4.3 The Model

In Fig. 4.5 we describe schematically a PES in the simple case of a direct-gap single-valley semiconductor. A laser pulse excites electrons across the gap, thus leaving behind holes in the valence band and creating electrons in the conduction one (panel (a)). If the electron-hole (e-h) recombination time is long enough, a quasi-stationary local-equilibrium state sets in (panel (b)) at finite densities of electrons, n_{e}, and holes, n_{h}, which, at low temperature, are equal to the density $n_{\text{e-h}}$ of photoexcited e-h pairs, i.e., $n_{\mathrm{e}} = n_{\mathrm{h}} = n_{\text{e-h}}$. Some of them bind together and form excitons, that we depict in Fig. 4.5 as e-h pairs connected by strings, while others remain unbound. Such quasi-stationary state can be probed either by absorption or photoluminescence, blue and red light beams in panel (c). Specifically, the system can absorb light by creating additional e-h pairs above an absorption edge shifted by the presence of already existing particles and holes, or, at lower energy, through intra-exciton transitions [136]. Photoluminescence is expected to arise by the radiative recombination both of unbound e-h pairs and of excitons. These two processes emit at different frequencies, and thus the corresponding emission intensities give a measure of the relative populations of bound and unbound e-h pairs. When the gap is instead indirect, light absorption and emission must be accompanied by emission of phonons to compensate the momentum mismatch.

The quasi-stationary state in the simple case shown in Fig. 4.5 can be described by the Hamiltonian

$$H = \sum_{\mathbf{k}\sigma} \left(\epsilon_{h\mathbf{k}}\, h^{\dagger}_{\mathbf{k}\sigma}\, h_{\mathbf{k}\sigma} + \epsilon_{e\mathbf{k}}\, e^{\dagger}_{\mathbf{k}\sigma}\, e_{\mathbf{k}\sigma} \right) + \sum_{\mathbf{q}} \frac{U(\mathbf{q})}{2V} \left(\rho_{h\,\mathbf{q}} - \rho_{e\,\mathbf{q}} \right) \left(\rho_{h\,-\mathbf{q}} - \rho_{e\,-\mathbf{q}} \right), \tag{4.1}$$

at fixed and equal densities of particles and holes, $n_{\mathrm{e}} = n_{\mathrm{h}} = n_{\text{e-h}}$. The operators $h^{\dagger}_{\mathbf{k}\sigma}$ and $e^{\dagger}_{\mathbf{k}\sigma}$

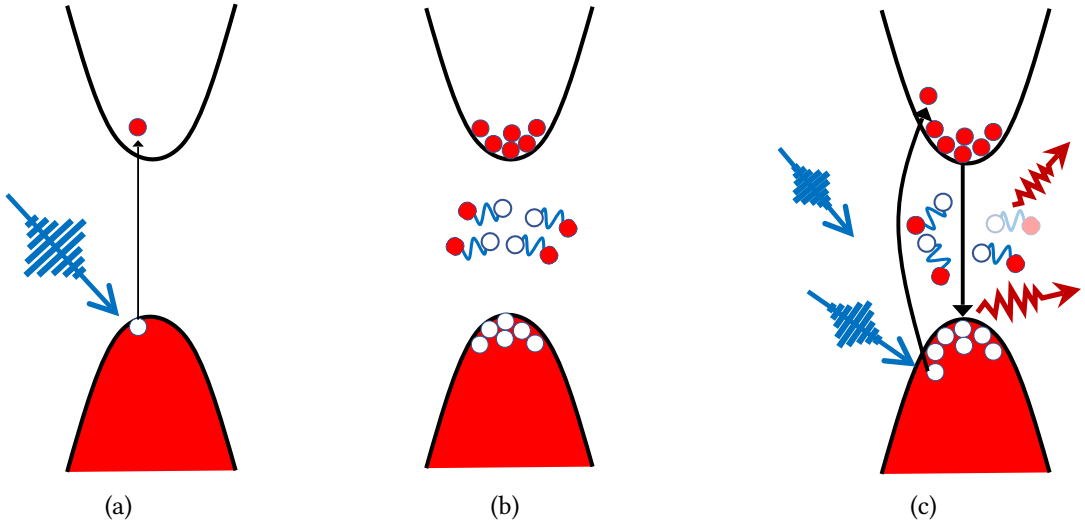

Figure 4.5: Photoexcitation of a semiconductor by a laser pulse. (a) A semiconductor initially at equilibrium is shot by a laser pulse. (b) A transient quasi-stationary local equilibrium state is established with excitons in the gap, and electron and holes in the conduction and valence bands, respectively. (c) Such local equilibrium state can be probed by optical absorption of light, blue beams, which either transfers additional electrons across the gap, above an absorption edge blue shifted by the presence of other electrons and holes, or excites internal states of the exciton. Alternatively, photoluminescence can be used as probe, red beams, which corresponds to radiative recombination either of bound or unbound electron-hole pairs.

create, respectively, a hole in the valence band, with energy cost $\epsilon_{h\mathbf{k}}$, and an electron in the conduction one, with energy cost $\epsilon_{e\mathbf{k}}$, both with momentum $\mathbf{k}$ and spin σ. $U(\mathbf{q})$ is the Coulomb interaction screened by all bands except the valence and conduction ones, while $\rho_{h\,\mathbf{q}}$ and $\rho_{e\,\mathbf{q}}$ the densities at momentum $\mathbf{q}$ of holes and electrons, which have opposite charges. Because of our assumption of quasi-stationarity, we do not include in (4.1) the recombination processes, so that n_e and n_h are both conserved.

In order to single out the interaction physics, we consider here an idealized modelling, discussed, e.g., in Ref. [213], obtained by further simplifying the Hamiltonian (4.1). First, since the e-h Coulomb binding is primarily a charge effect, we ignore the spin, and thus assume spinless holes and particles. Second, we neglect the effective mass difference between valence and conduction bands, assuming $\epsilon_{h\mathbf{k}} = \epsilon_{e\mathbf{k}} \equiv \epsilon_{\mathbf{k}}$, and, for simplicity, take the latter as the dispersion relation of a tight-binding model with nearest neighbour hopping, which is also quadratic in the small-$\mathbf{k}$ regime pertinent to low density. Finally, we replace the long-range Coulomb interaction $U(\mathbf{q})$ by a short range Hubbard-like term U constant in $\mathbf{q}$, so that the Hamiltonian (4.1) transforms into

$$H = \sum_{\mathbf{k}\sigma} \epsilon_{\mathbf{k}} \left(h^\dagger_{\mathbf{k}} h_{\mathbf{k}} + e^\dagger_{\mathbf{k}} e_{\mathbf{k}} \right) - U \sum_i n_{e\,i}\, n_{h\,i} - \mu \sum_i \left(n_{e\,i} + n_{h\,i} \right), \tag{4.2}$$

where $n_{h(e)\,i}$ is the local density at site i of holes(electrons), and the chemical potential μ is such as to fix $\langle n_{h\,i} \rangle = \langle n_{e\,i} \rangle = n_{\text{e-h}}$, where $n_{\text{e-h}} \ll 1$ is the density of photoexcited e-h pairs. We remark that the model (4.2) can describe the same physics of (4.1) only if U is large enough to create bound states below the two-particle continuum, which play the role of the excitons in the original system[1]. The simplified Hamiltonian (4.2) can be mapped onto a standard repulsive

[1] In the limit case of a single pair of e-h excitations the critical U for the bound state formation can be computed exactly, we refer to Section B.1 for more details.

Hubbard model

$$H = \sum_{\mathbf{k}} \sum_{\sigma} \epsilon_{\mathbf{k}}\, d^{\dagger}_{\mathbf{k}\sigma}\, d_{\mathbf{k}\sigma} + U \sum_{i} n_{i\uparrow}\, n_{i\downarrow} - h \sum_{i} \left(n_{i\uparrow} - n_{i\downarrow}\right), \tag{4.3}$$

through the particle-hole transformation C_{ph}:

$$C^{\dagger}_{\text{ph}}\, e_i\, C_{\text{ph}} = d_{i\downarrow}, \quad C^{\dagger}_{\text{ph}}\, h_i\, C_{\text{ph}} = (-1)^{R_i} d^{\dagger}_{i\uparrow}, \tag{4.4}$$

where $(-1)^{R_i}$ can be either -1 or $+1$ depending on the parity of the lattice site i. Clearly the tight-binding part of the simplified Hamiltonian (4.2) is invariant under the transformations generated by C_{ph}, while the interaction part changes its sign. Thus, the model in Eq. (4.2) is mapped to the repulsive one (4.3). At equilibrium, the empty lattice of e-h pairs is mapped to the:

$$C_{\text{ph}}|0\rangle = \prod_{i} d^{\dagger}_{i\uparrow}|0\rangle$$

which is the fully spin polarized half-filled band state. In this context each e-h pair corresponds to a spin-flip excitation $\uparrow \rightarrow \downarrow$. The particle-hole transformation (4.4) affects the e-h number operator in a non-trivial way,

$$\sum_{i} C^{\dagger}_{\text{ph}} \left(e^{\dagger}_i e_i + h^{\dagger}_i h_i - 1\right) C_{\text{ph}} = \sum_{i} \left(d^{\dagger}_{i\downarrow} d_{i\downarrow} - d^{\dagger}_{i\uparrow} d_{i\uparrow}\right),$$

and relates pair and magnetization densities

$$2n_{\text{e-h}} - 1 = -m \rightarrow n_{\text{e-h}} = \frac{1+m}{2}. \tag{4.5}$$

Moreover, the unbalance between the electron in conduction band and the holes in the valence one transforms under (4.4) as:

$$\sum_{i} C^{\dagger}_{\text{ph}} \left(e^{\dagger}_i e_i - h^{\dagger}_i h_i\right) C_{\text{ph}} = \sum_{i} \left(d^{\dagger}_{i\downarrow} d_{i\downarrow} + d^{\dagger}_{i\uparrow} d_{i\uparrow} - 1\right),$$

which by assuming a compensated semiconductor, $\langle n_{ei}\rangle = \langle n_{hi}\rangle$, implies the half-filling condition:

$$\langle n_{i\uparrow}\rangle + \langle n_{i\downarrow}\rangle = 1. \tag{4.6}$$

It follows that the model (4.2) with a fixed $n_{\text{e-h}}$ maps to a repulsive model at half-filling with a fixed magnetization $m = 1 - 2n_{\text{e-h}}$, which can be enforced by the Lagrange multiplier h playing the role of a fictitious Zeeman field. Finally, we observe that the Hamiltonian (4.3) is invariant under the particle-hole transformation:

$$C^{\dagger}\, d_{i\sigma}\, C = (-1)^{i} \sigma d^{\dagger}_{i\bar{\sigma}} \tag{4.7}$$

where $\sigma = +1$ for spin $\uparrow$ and -1 for $\downarrow$. Thus, spin $\uparrow$ and $\downarrow$ observables of the repulsive model (4.3) are not independent but are related by the unitary transformation (4.7).

Therefore, the physics of PES can be captured by the half-filled repulsive Hubbard model at fixed, and large if $n_{\text{e-h}} \ll 1$, magnetization m, provided all assumptions above are valid. Indeed, the Hamiltonian (4.3) is expected to display several phases in one to one correspondence to those of PES [48, 123, 172, 195]: a low-temperature canted antiferromagnetic insulator, which translates into a phase of condensed excitons, and high temperature magnetized Mott insulating and metallic phases, which correspond to the EG and EHL, respectively. In particular, the EG,

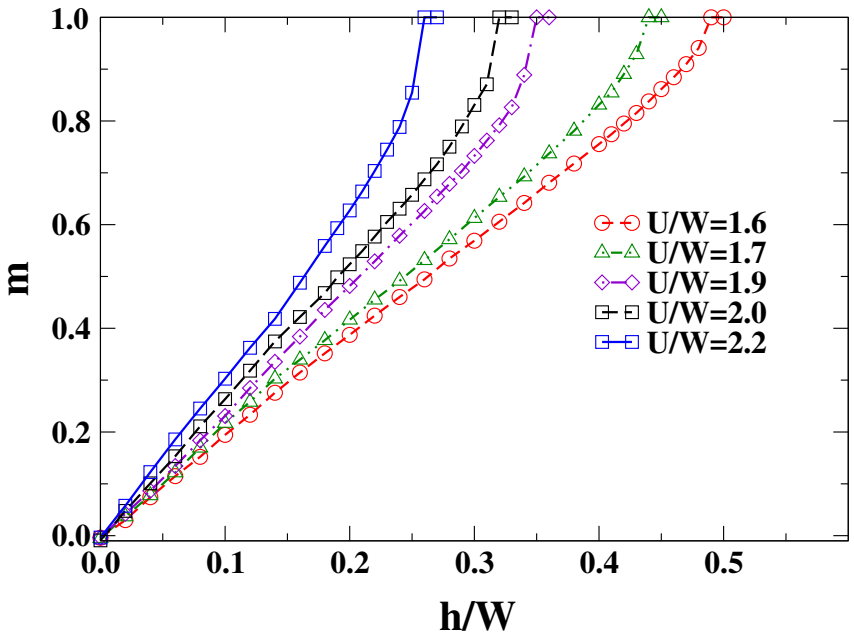

Figure 4.6: Magnetization m vs. h for increasing values of U/W, obtained by DMFT using exact diagonalization at zero temperature with 8 bath sites, and a semicircular density of states of width $2W$. In the large U regime relevant to PES, we always find, upon increasing h, a first order transition from a partially polarized metal to a fully polarized insulator.

composed by bound electron and hole pairs, corresponds to a set of incoherent singlet bound states in the background of a spin ↑ polarized system. On the other hand, the EHL, characterized by a non-vanishing fraction of unbounded e-h pairs, is a strongly spin ↑ polarized solution where a fraction of ↑ and ↓ electrons are deconfined excitations free to propagate on the lattice.

In this chapter we study the zero temperature stability of variational solutions assuming that it is representative of finite temperature (i.e. the entropic contribution does not spoil the physical picture).

4.4 The Method

The Hamiltonian (4.3) is ideally suited to DMFT [95]. However, earlier results on the simple half-filled repulsive Hubbard model in a Zeeman field [30, 48, 145, 160, 294] show some differences in the nature of the transition, despite an overall agreement on the main features of the phase diagram. In particular, in the large $U \gg h$ regime pertinent to PES, the Mott transition is always found to be of the first order, but Refs. [160] and [48] predict a transition between a partially polarized metal and a partially polarized insulator, while Refs. [30] and [294] report a transition between a partially polarized metal and a fully polarized insulator, and no evidence of a partially polarized insulator. We also performed a zero-temperature DMFT calculation using exact diagonalization as impurity solver, and we could not stabilize a partially polarized insulator, see the magnetization m vs. h shown in Fig. 4.6, in agreement with [30] and [294].

The reason for this discordance can be readily traced back to the iterative scheme employed to solve DMFT, which fails to converge when forcing the translational symmetry and the residual $U(1)$ spin-rotational symmetry around the z-axis parallel to h, both of which are instead spontaneously broken in the true canted antiferromagnetic ground state. In DMFT, assuming a semicircular density of states (DOS) and forcing the aforementioned symmetries, the

lattice model (4.3) is mapped onto an Anderson impurity model (AIM), where the spin-resolved hybridization function with the bath, $\Gamma_\sigma(\epsilon)$ (defined in Eq. (3.53)), is self-consistently determined by the single-particle DOS of the impurity, $A_\sigma(\epsilon)$ [95] – which in turn must correspond to the local DOS of the lattice model – through the equation

$$\Gamma_\sigma(\epsilon) = \frac{\pi W^2 A_\sigma(\epsilon)}{4}\,, \tag{4.8}$$

where W is the half-bandwidth. Let us consider the iterative solution of Eq. (4.8) at $h \ll W, U$ in the Mott insulating regime, which translates into an AIM whose hybridisation function $\Gamma(\epsilon) = \Gamma_\uparrow(\epsilon) + \Gamma_\downarrow(\epsilon)$ has a gap of order U at the chemical potential. This implies that, at any iteration i, the hybridization function is obtained by the impurity DOS at the previous iteration, $\Gamma_\sigma^{(i)}(\epsilon) = W^2 A_\sigma^{(i-1)}(\epsilon)/4$, and thus acquires the same spin polarisation. Since in this regime the impurity is characterized by a diverging local magnetic susceptibility, $\chi_{\rm loc} \to \infty$, and the impurity-bath hybridization entails an effective antiferromagnetic coupling at a given iteration the spin of the impurity will be polarized in the opposite direction of that of the bath, thus opposite to the same impurity at the previous iteration. The reversal of the impurity spin from an iteration to the next one is unavoidable when $\Gamma(\epsilon)$ is gapped, unless h is large enough to prevail over the effective antiferromagnetic coupling with the bath and thus align the impurity spin parallel to it. If so, at the next iteration also the bath will be aligned with h, and the iterations will converge to a trivial solution where both bath and impurity are fully spin polarized along h, which is evidently eigenstate of the AIM. In other words, the iterative procedure in the Mott insulating phase either oscillates between solutions of opposite spin or, for h above a threshold, it converges to a trivial solution that represents a fully spin-polarized insulator, in accordance with our calculations and Refs. [30] and [294], or, in the language of PES, to the equilibrium state without photoexcited e-h pairs.

The lack of convergence at small h, which prevents the stabilization of a partially polarized insulator and simply signalizes the tendency to form an antiferromagnetic state, can be formally avoided by choosing a convergence criterium only within the same-parity iterations, i, $i+2$, …, and, at the end, assuming as impurity DOS, $A_\sigma(\epsilon)$, the average of those at even and odd iterations [48]. This choice is equivalent to assume a mixed state, despite the temperature is zero, where the partial spin polarization of the Mott insulator results from a statistical ensemble of pure states, with the impurity spin polarized in opposite directions. Since the impurity spin polarization maps in DMFT into the lattice magnetization, m, which, in turn, translates into $1-2n_{\text{e-h}}$ in the language of PES, see Eq. (4.5). Hence, such statistical ensemble of states with $1-2n_{\text{e-h}} = m \sim +1$ and $1-2n_{\text{e-h}} = m \sim -1$ actually describes a rather strange, and not very physical, phase-separated exciton Mott insulator, where the bound e-h pairs are circumscribed within a finite portion of the system, $n_{\text{e-h}} \sim 1$, while they are almost absent in the rest, $n_{\text{e-h}} \sim 0$. This result would not change when solving, still iteratively, the DMFT self-consistency equation (4.8) at small but finite temperatures [160].

4.4.1 The variational g-GW applied to PES

We emphasize once more that the issue here is the iterative implementation of DMFT when forcing symmetries that are instead spontaneously broken in the true ground state. For instance, we would not expect to find the same unsatisfactory results in a direct routinely constrained optimization of the DMFT functional [154], which however has never been implemented to the best of our knowledge. A less accurate approach, but equally free of the problems outlined before, would be the minimization of the expectation value of the Hamiltonian on a constrained

variational wave function, forced to be invariant under the aforementioned symmetries. In what follows we shall adopt just this variational approach.

The main difficulty in this context is finding a variational wave function that can faithfully describe a Mott insulator. This is the case of the g-GW, that we present in Chapter 3. The wave function (3.1) is simple and bears close similarity to DMFT. Indeed, as proved in Section 3.2.2, the variational parameters $\lambda_{\Gamma\gamma}(i)$ can be associated to the components $\psi(i;\Gamma,\gamma)$ of a wave function $|\psi(i)\rangle = \sum_{\Gamma\gamma} \psi(i;\Gamma,\gamma)\,|\Gamma_i\rangle\times|\gamma_i\rangle$ that describes an impurity at site i coupled to a bath of N spinfull levels. The analogy with DMFT is thus self-evident.

Hereafter, in order to enforce translationally symmetry and the $U(1)$ symmetry under spin rotation around the z-axis, we shall assume that $|\Psi_*\rangle$ is translationally invariant, $|\psi(i)\rangle = |\psi\rangle$, $\forall\, i$, and that both wave functions are eigenstates of the total z-component of the spin S^z. As shown in Section 3.4, where we apply the g-GW to describe the paramagnetic Mott transition in the half-filled Hubbard model, symmetry conditions naturally reduce the number of independent variational parameters.

We apply the g-GW approach to study the model (4.3) on a Bethe lattice with infinite coordination, which corresponds to a semicircular tight-binding DOS (3.61). We choose to work with $N = 3$ subsidiary orbitals, which, as shown in Section 3.4, provide already very accurate ground state properties in comparison with DMFT. Moreover, we treat all components $\psi(\Gamma,\gamma)$ of the wave function describing the quantum impurity coupled to the bath of $N = 3$ levels as free variational parameters, apart from the normalization and the constraints imposed by spin $U(1)$ and particle-hole symmetries. This means that we adopt the optimization scheme in Section 3.2.3 and we do not require $\psi(\Gamma,\gamma)$ to be a ground state of an auxiliary Anderson impurity model, i.e., an interacting impurity hybridized with a non-interacting bath, an unnecessary requirement which would lead to the same problems of the DMFT iterative solution.

The expectation value per site E of the Hamiltonian (4.3) at $h = 0$ on the variational wave function (3.1) can be written as a functional of $|\psi\rangle$ that only depends parametrically on the magnetization m, and reads [163]

$$E\left[|\psi\rangle, m\right] = \frac{1}{V}\,\langle\Psi_*|H_*|\Psi_*\rangle + U\,\langle\psi|n_\uparrow\, n_\downarrow|\psi\rangle\,, \tag{4.9}$$

where V is the number of sites, and n_σ the spin-σ occupation number of the impurity. The Slater determinant Ψ_* is the ground state of the non-interacting Hamiltonian

$$H_* = \sum_{ab=1}^{3}\sum_{\sigma}\sum_{\mathbf{k}} c^\dagger_{\mathbf{k}a\sigma}\Big(\epsilon_{\mathbf{k}} R^*_{\sigma,a\sigma}\, R_{\sigma,b\sigma} + \mu_{ab,\sigma}\Big)c_{\mathbf{k}b\sigma}\,, \tag{4.10}$$

where the Lagrange multipliers $\mu_{ab,\sigma}$ in (4.10) enforce the constraint in Eq. (3.13), while the parameters $R_{\sigma,a\sigma}$ are defined in Eq. (3.18). The energy functional $E\left[|\psi\rangle, m\right]$ in (4.9) must be minimized with respect to $|\psi\rangle$, which is subjected to the constraints fixing the density to 1 and m to the desired value $1 - 2n_{\text{e-h}}$, i.e.,

$$\langle\psi|n_\uparrow + n_\downarrow|\psi\rangle = 1\,, \quad \langle\psi|n_\uparrow - n_\downarrow|\psi\rangle = 1 - 2n_{\text{e-h}}\,. \tag{4.11}$$

In the following Section we consider the case relevant for PES. Starting by recalling the crucial result obtained in Section 3.4 we report the form of the impurity wave function to describe PES. Then, we present our phase diagram and we conclude by stressing the important role of the exciton binding energy in the EG to EHL Mott transition in PES.

4.5 Exciton Mott transition in PES

In the Mott insulating regime $U > U_{c2}$, where valence fluctuations from the low energy site are vanishing, measured by R_2 as can be seen in bottom panel of Fig. 3.8, the saddle-point impurity wave function is a singlet combination, reported in Eq. (3.72), between the low energy site and the remaining sites of the embedded model. Remarkably, this result highlights the spin-liquid like character of the Mott insulator, which despite being paramagnetic posses singlet short-range correlations in its ground state. The above result, which in the large-U regime is analytically proved in Section A.2 of the Appendix A, naturally suggests how to construct a good trial insulating wave function with fixed impurity magnetization m:

$$|\psi\rangle = \cos\phi\,|\phi_\uparrow\rangle \times |\varphi_\downarrow\rangle - \sin\phi\,|\phi_\downarrow\rangle \times |\varphi_\uparrow\rangle, \tag{4.12}$$

with $\cos 2\theta \simeq m$. This wave function (4.12) evidently describes a pure state that cannot be interpreted as the ground state of an Anderson impurity model. Indeed, the spin entanglement between $|\phi_\sigma\rangle$ and $|\varphi_\sigma\rangle$ can only be rationalized through an effective antiferromagnetic exchange between the low energy level and the remaining levels of the impurity model, which is not a one-body potential. It is interesting to notice that in the large-U regime the variational wave function (4.12) allows us to recover the expected $t - J$ model result. Moreover, it allows us to obtain exact predictions on the EG in the regime of large-U and small densities, which are particularly relevant for systems characterized by large binding energies, e.g. monolayer TMDs. We refer the interested reader to Section B.2 where detailed analytical calculations are performed.

Let us consider the phase diagram of the Hamiltonian (4.3) as a function of its parameters, i.e., the number of photoexcited e-h pairs $n_{\text{e-h}}$ and the exciton binding energy E_{ex}, with the half-bandwidth W as the unit of energy. We choose these parameters because they are directly connected with physical properties that can be measured in experiments on PES. From the mapping in Eq. (4.5), we can relate the $n_{\text{e-h}}$ with the magnetization m of a repulsive Hubbard model in the presence of an external magnetic field. On the contrary, the binding energy E_{ex} in PES is not directly related to the short-range Hubbard U, since the latter is just meant to mimic the role of the long-range Coulomb interaction in binding electrons and holes into excitons. This implies that the model Hamiltonian (4.3) must have in common with PES the existence of exciton states.

In the present case of a semicircular DOS (3.61), whose square root behavior at the edges reproduces that one found at the bottom or top of a band in three dimensions, the on-site interaction U must exceed a threshold to produce a bound state, unlike long-ranged Coulomb repulsion. Its binding energy E_{ex} can be calculated exactly solving the problem of a single e-h pair, see Section B.1. However, for consistency with the calculation at $n_{\text{e-h}} > 0$, we determine E_{ex} by the variational optimisation in the limit $n_{\text{e-h}} \to 0$. In the top panel of Fig. 4.7 we show for the model Hamiltonian (4.3) the single particle DOS of a spin down electron in the Mott insulator at almost full polarization, $m = 0.98$, which, through Eq. (4.4), corresponds to the DOS of an electron in the conduction band within the EG phase at $n_{\text{e-h}} = 0.01$, as well as, since we assumed particle-hole symmetry, to the DOS of a hole in the valence band. We note at positive energies, i.e., above the chemical potential of the quasi stationary local equilibrium state in Fig. 4.5 (c), the continuum of empty states in the conduction band, and at negative energy a very narrow peak that accommodates all the $n_{\text{e-h}} = 0.01$ density of photoexcited electrons. This peak evidently corresponds to the exciton, and its distance from the bottom of the conduction band defines the binding energy E_{ex}, whose dependence on U is shown in the bottom panel of Fig. 4.7. Only when $E_{\text{ex}} > 0$, i.e., $U/W > U_{\text{ex}}/W \simeq 1.5$, the model Hamiltonian (4.3) can be used to describe the physics of PES. In the language of the repulsive Hubbard model (4.3), the exciton peak below the chemical potential and the broad continuum above translate into the lower and

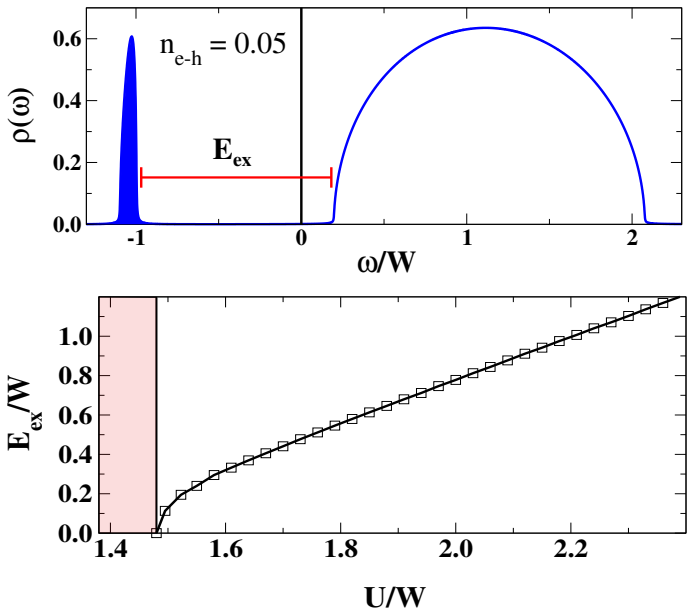

Figure 4.7: Top panel: density of states (DOS) of an electron in the conduction band at $U/W = 2.4$ with a density $n_{\text{e-h}} = 0.05$ of photoexcited electron holes pairs. The narrow peak at negative frequency, the occupied side of the spectrum, corresponds to the filled exciton state, whereas the conduction band at positive frequency is empty. Such DOS thus describes an exciton gas, and allows extracting a exciton binding energy E_{ex} through the distance of the exciton peak from the bottom of the conduction band, which is shown as function of U/W in the bottom panel. Note that a finite E_{ex} requires U/W above a threshold $\simeq 1.5$. The region below that threshold, in light red, is therefore not representative of PES.

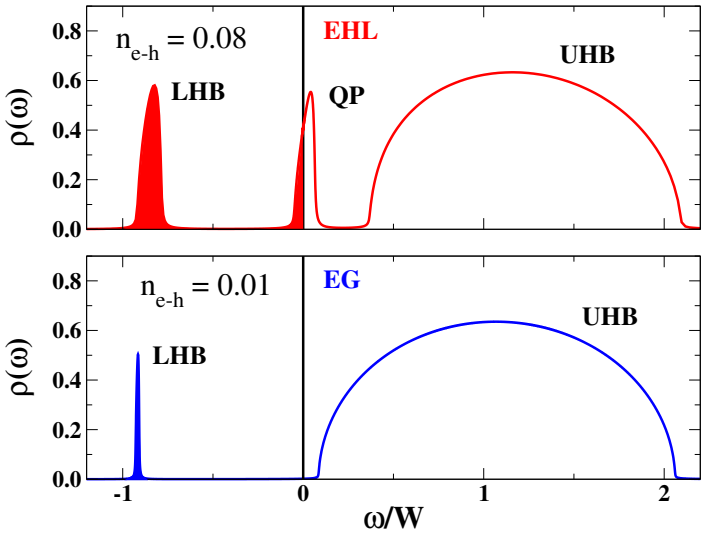

Figure 4.8: Density of states (DOS) for a spin down particle corresponding to an electron in the conduction band, as well as a hole in the valence one. Top: DOS in the metallic EHL solution at $U/2t = 2.2$, which corresponds to $E_{\text{ex}}/2t \simeq 0.9$, and $n_{\text{e-h}} = 0.08$. Bottom: same quantity in the EG Mott insulator at the same value of U but smaller $n_{\text{e-h}} = 0.01$. In the language of the repulsive Hubbard model, the features associated with lower and upper Hubbard bands are indicated by LHB and UHB, respectively. Note that they both survive also in the correlated metal phase, top panel, despite the emergence of quasiparticles narrowly peaked at the Fermi energy.

upper Hubbard bands, respectively, while the threshold value U_{ex} is actually the limit of the Mott insulator spinodal value of interaction, so-called U_{c1} [95], when the magnetization $m \to 1$.

Before discussing in detail the phase diagram, it is worth to hightlight the properties that characterize the EHL as opposed to the EG. In Fig. 4.8 we show the DOSs of an electron in the conduction band, or a hole in the valence one, in a representative EHL solution at $E_{ex}/W \simeq 0.9$ and $n_{e\text{-}h} = 0.08$, top panel, in contrast to a representative EG one at the same $E_{ex}/W \simeq 0.9$ but at smaller $n_{e\text{-}h} = 0.01$, bottom panel. We note in the EHL phase, top panel, still clearly visible Hubbard bands, the lower one (LHB) corresponding to the exciton, and the upper (UHB) to the incoherent contribution of the conduction (for the electron) and valence (for the hole) bands. In addition, a narrow quasiparticle peak emerges at the chemical potential, which distinguishes the EHL DOS in the top panel from the EG one in the bottom panel. The finite gap between the quasiparticle peak and the UHB is most likely an artefact of the use of a small bath ($N = 3$). We expect that further bath levels would fill that gap by small spectral weight. Nonetheless, the correlated metal feature of a coherent quasiparticle peak distinct from the UHB incoherent background should persist.

Our ground state calculation does not allow us to easily compute the two-particle response functions associated to the optical absorption and luminescence. However, the DOS shown in the top panel of Fig. 4.8 suggests that the optical spectrum of the EHL should still display exciton signatures, which have been indeed observed experimentally [104, 255, 271], and predicted theoretically [179]. Moreover, the narrow width of the quasiparticle peak suggests an anomalous strongly correlated EHL metal, also not in disagreement with experiments [255].

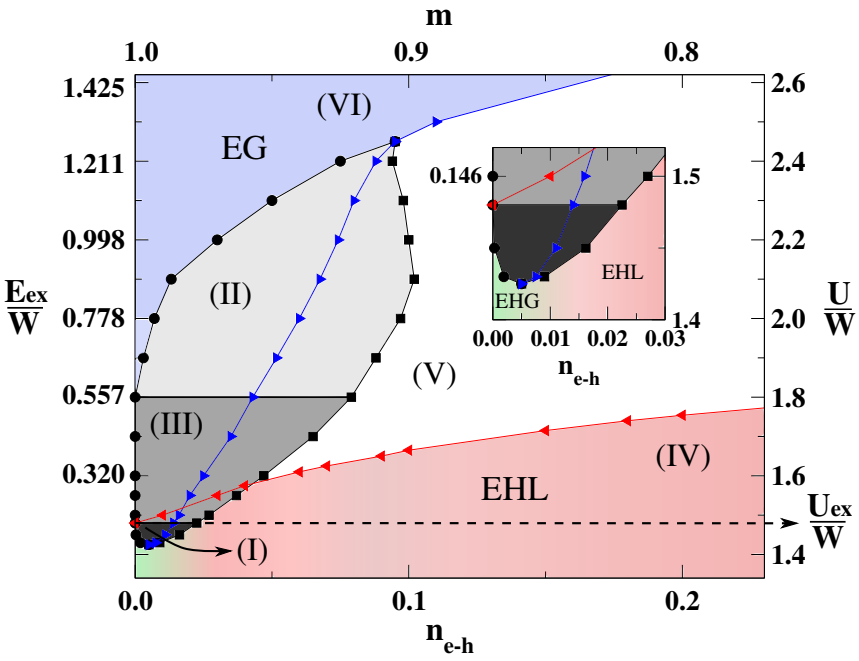

Figure 4.9: Phase diagram as function of the exciton binding energy E_{ex} and the density $n_{e\text{-}h}$ of photoexcited e-h pairs, left y and bottom x axes, respectively, or, equivalently, $U/2t$ and magnetization $m = 1 - 2n_{e\text{-}h}$, right y and top x axes, respectively. In red we plot the insulator spinodal line, while in blue the metal one. The different regions, labeled from (I) to (VI) are discussed in the text. The inset shows a zoom of the phase-diagram around region (I).

Let us now discuss the phase diagram, which is shown in Fig. 4.9 as a function of the exciton

Brief description of the phase diagram in Fig. 4.9	
region	description
(VI)	regime of small $n_{\text{e-h}}$, stable EG
(IV)	regime of large $n_{\text{e-h}}$, stable EHL
(I)	phase separation between the EHG and the EHL
(II)	phase separation between the EG and the EHL
(III)	bistability region between the EG and the EHL
(V)	the metastable EG coexists with the stable EHL

Table 4.1: Summary of different regions in the PES phase diagram displayed in Fig. 4.9.

binding energy E_{ex} and the density of photoexcited e-h pairs $n_{\text{e-h}}$. For completeness, we also show the values of magnetization m and interaction U that correspond to $n_{\text{e-h}}$ and E_{ex} in the repulsive Hubbard model (4.3) and we summarize the main information in Table 4.1. The red curve in that figure corresponds to the spinodal line above which an EG solution exists, which is also the spinodal $U_{c1}(m)$ of the Mott insulator [154] in the repulsive model (4.3), and becomes for $m \to 1$ the threshold value U_{ex} in Fig. 4.7. On the contrary, the blue curve is the spinodal line above which the EHL becomes unstable, and thus only the EG exists, which is the metal spinodal $U_{c2}(m)$ in the repulsive model (4.3).

Considering instead the different phases in Fig. 4.9, in the dark region (I) for very small $n_{\text{e-h}}$, which is zoomed in the inset and, strictly speaking, is not pertinent to PES since $U < U_{\text{ex}}$, we find phase separation between two metallic phases, one liquid (EHL) at larger $n_{\text{e-h}}$, and the other gaseous (EHG), at smaller $n_{\text{e-h}}$. The two phases merge at a second order critical point. In the light grey region (II) above $E_{\text{ex}}/W \simeq 0.557$, now relevant to PES, we instead find phase separation between an EG and an EHL. In the top panel of Fig. 4.10 we plot the chemical potential obtained from the energy per site E and $n_{\text{e-h}}$ through $\mu = -\partial E/\partial n_{\text{e-h}}$, together with the common tangent construction. It follows that for $n_{\text{e-h}} \in [0.05, 0.095]$ the system phase separates into an EG at low density $n_{\text{e-h}} = 0.05$ and an EHL at larger density $n_{\text{e-h}} = 0.095$.

On the contrary, within the intermediate region (III) (dark grey in the phase diagram Fig. 4.9) a common-tangent construction is not possible, see bottom panel of Fig. 4.10. This may suggest a bistable behavior with a sudden transformation of the EG into the EHL, which has been invoked [254] to explain some experimental evidences [255], even though we cannot exclude a numerical artifact since the variational optimization is hard at very low $n_{\text{e-h}}$.

In region (IV), below $U_{c1}(m)$, only the EHL is stable. On the contrary, in region (V), white in the figure, we find coexistence between a stable EHL and a metastable EG. Finally, in region (VI), blue in the figure, only the EG is stable. We find that the transition line separating (V) and (VI) has a second order character. We note that in the language of the repulsive Hubbard model (4.3), this second order line persists down to $m = 0$, while, for the reasons outlined in Section 4.4, DMFT calculations find a continuous transition only at $m = 0$, and a discontinuous one at any $m \neq 0$ [30, 48, 160, 294].

The phase diagram in Fig. 4.9 has been obtained at zero temperature forcing all symmetries of the Hamiltonian (4.3), and should be representative of the one above the exciton condensation temperature with the caveat that the character of all transition lines, and the size of the stability domain of each phase might change when accounting for entropy effects. Let us therefore discuss the possible effect of a finite temperature. Since the exciton peak in Fig. 4.8 presumably carries more entropy than the quasi-particle peak [95], it is most likely that the second order line separating regions (V) and (VI) transforms into a first order transition accompanied by phase

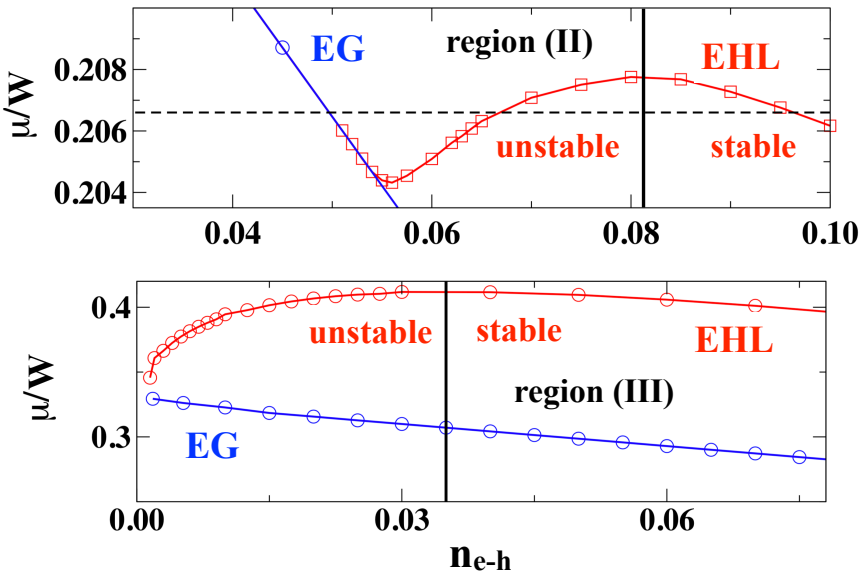

Figure 4.10: Top panel: phase separation at $E_{ex}/W \simeq 1$, region (II) in Fig. 4.9. We plot the chemical potential extracted by E vs. $n_{e\text{-}h}$ for both EHL (red line) and EG (blue line) solutions. The vertical line indicate the EHL spinodal value of $n_{e\text{-}h}$, below which this phase is not stable anymore. The dotted line corresponds to the common tangent construction, which implies that for $n_{e\text{-}h} \in [0.05, 0.095]$ the system phase separates into an EG at $n_{e\text{-}h} = 0.05$ and an EHL at $n_{e\text{-}h} = 0.095$. Bottom panel: bistability at $E_{ex}/W \simeq 1$, region (III) in Fig. 4.9. Here the behavior of the chemical potential of the EHL (red line) and EG (blue line) solutions does not allow a common tangent construction.

separation, i.e., a gradual transfer of charges from the EG phase to the EHL one as $n_{e\text{-}h}$ increases that simply extends region (II) to higher values of $n_{e\text{-}h}$.

On the other hand, we cannot exclude that, if the bistability in region (III) is true and not due to numerical issues, it might survive at finite temperature, nor that, at the border between regions (I) and (III), a discontinuous exciton Mott transition appears besides the gaseous-liquid transition EHG $\rightarrow$ EHL.

4.6 Conclusions

Despite its extreme simplicity, the spin-polarized half-filled repulsive Hubbard model shows a rather rich phase diagram in Fig. 4.9 with phase transitions that, upon translation in the language of semiconductors at finite density of photoexcited electron-hole pairs, bear strong similarities with the transitions from an exciton gas to an electron-hole liquid observed in those systems, among the earliest known realizations of Mott transitions. In particular, taking into account finite temperature entropy effects not included in our calculation, the phase diagram in Fig. 4.9 encompasses a first order exciton Mott transition that almost everywhere is accompanied by phase separation, thus implying a continuous transformation of the exciton gas into the electron-hole liquid. However, within a small region in the phase diagram at low exciton binding energy, we also find bistability, which would correspond to a sudden transformation of the exciton gas into the electron-hole liquid without phase-separation. We mentioned that experimentally there are both evidences of continuos exciton Mott transitions, i.e., phase separation [54, 141, 146, 239], as well as of discontinuous ones [13, 29, 254, 255, 264–266, 270]. The discriminant parameter might well be the exciton binding energy E_{ex}, as we do find, since a discontinuous transition is mostly observed in bulk semiconductors, while a continuous one in confined geometries, like

quantum wells, where E_{ex} is supposedly larger due to the smaller screening of the Coulomb interaction. Transition metal dichalcogenides seem to constitute an exception to this rule. In spite of their large exciton binding energy, they have been shown to display either a continuous transition [54] after an ultrashort laser pulse, or a discontinuous one [29] under continuous-wave photoexcitation, although we cannot exclude that the different photoexcitation processes are responsible of the different outcomes.

We conclude this Section remarking that the electron-hole liquid that we find is rather unconventional, see the single-particle density of states shown in the top panel of Fig. 4.8, since it still displays excitonic signatures despite being a degenerate Fermi liquid of holes and electrons. This is in contrast with the expectation that the exciton binding energy should vanish at the transition. Moreover, we find that the effective mass of the unbound electrons and holes is quite large, as clear from the narrow width of the coherent peak at the chemical potential. In the EHL we observe the characteristic red-shift of the bottom of the e-h continuum, displayed in the top panel of Fig. 4.8, where the low-energy quasiparticle peak crosses the vertical black line which defines the band gap of the semiconductor. Conversely, in the EG, bottom panel of Fig. 4.8, we observe the blue-shift of the e-h continuum. These features have been observed experimentally [255].

5

The time-dependent ghost-Gutwiller wave function

By means of the Dirac-Frenkel variational principle we employ the ghost-Gutzwiller wave function, introduced in Chapter 3, to describe the out of equilibrium dynamics of isolated quantum systems. We present the method for a generic multi-orbital system, neglecting, like in the equilibrium case, superconducting correlations. The method is able to access the full out of equilibrium dynamics also far from the linear response regime. In the out of equilibrium case, the additional degrees of freedom introduce dephasing channels that suppress the coherent oscillations observed in the conventional Gutzwiller dynamics. Despite this remarkable improvement, the ghost-Gutzwiller dynamics lacks dissipative channels to describe the system flowing towards a steady state. We apply the method to the single-band lattice Hubbard model and we benchmark our results with the more accurate DMFT. The goal of this Chapter is not a new characterization of the dynamical phase transition, but rather a benchmark of the novel time-dependent ghost-Gutzwiller with respect to DMFT and conventional Gutzwiller.

5.1 Introduction

Recent years have seen enormous experimental progress in preparing, controlling and probing strongly interacting quantum systems in different nonequilibrium regimes [43, 96]. These developments have triggered a set of fundamental questions concerning dynamics, dissipation, transport and the approach to thermal equilibrium in quantum many-body systems [74, 223]. Furthermore, nonequilibrium experiments provide additional information that are complementary to those attainable by studying the matter at equilibrium [28]. For instance, the possibility of selectively exciting specific degrees of freedom in correlated materials opens the way to create novel metastable states, that cannot be reached via thermodynamic transformations [51].

The interplay between the equilibrium energy scales of the problem and the time dynamics makes the theoretical description of the nonequilibrium evolution of strongly correlated systems extremely challenging. A powerful and numerically inexpensive approach to tackle these problems is the time-dependent Gutzwiller variational wave function (t-GW) [81], which has been applied to study the evolution of strongly correlated lattice problems in many circumstances

[161, 184, 215, 243, 247, 253]. However, as a consequence of the mean-field like character of the approach, the time-dependent Gutzwiller dynamics is dominated by coherent oscillations and lacks dissipative channels to describe the system flowing towards a steady state.

The aim of this Chapter is presenting the time-dependent ghost-Gutzwiller wave function (t-g-GW), that enriches the conventional Gutzwiller out of equilibrium evolution of driven quantum systems by introducing additional degrees of freedom. We will show that the method is able to access the full nonequilibrium dynamics also far beyond the linear response regime discussed in Ref. [82]. In particular a nice feature of the t-g-GW is its ability of treating on equal footing the dynamics of both low-energy quasiparticles and high-energy incoherent excitations, which are commonly referred as Hubbard bands. A particularly interesting fact emerging from the time-dependent extension of the g-GW is that in the weak-coupling regime dynamics the additional degrees of freedom introduce dephasing processes that suppress the coherent oscillations observed in the t-GW, and eventually lead to a quasi-stationary regime. However, in contrast to Ref. [191], we do not find any relaxation to a thermal state for long times. In this respect we believe that, as already observed in the equilibrium case, the number N of subsidiary degrees of freedom may strongly influence the out of equilibrium dynamics and introduce, in the regime of $N \gg N_{\rm phys}$, relaxation to a thermal state. In the strong coupling limit the dynamics is characterized by the coherent oscillations with the period $\sim 2\pi\hbar/U$, in agreement with Refs. [72, 73, 247, 248], that signalizes the freezing of double-occupancies dynamics due to the absence of the elastic channel to decay [151, 238].

Our calculations of the single-band Hubbard model, which are benchmarked against the time-dependent DMFT [20, 72, 73], show that the t-g-GW dynamics quantitatively improves the t-GW results [247, 248] and allows us to describe coherent oscillations as well as dephasing processes.

5.2 Time-dependent ghost-Gutzwiller wave function

We shall assume that both the Slater determinant as well as the Gutzwiller projectors are time-dependent, hence:

$$|\Psi_G(t)\rangle = \prod_i \mathcal{P}_i(t)|\Psi_*(t)\rangle. \tag{5.1}$$

The Slater determinant $|\Psi_*(t)\rangle$ is characterized by $2N \geq 2M$ spinful orbitals, while

$$\mathcal{P}_i(t) = \sum_{\Gamma\gamma} \lambda_{\Gamma\gamma}(t,i)|\Gamma_i\rangle\langle\gamma_i| \tag{5.2}$$

is a linear map at site i, parametrized by the time-dependent variational parameters $\lambda_{\Gamma\gamma}(t,i)$, from the local $2N$-orbital Hilbert space, spanned by the states $|\gamma_i\rangle$, to the physical orbital local space, spanned instead by $|\Gamma_i\rangle$. We recall that $2N$ is the number of physical spinful orbitals, and $2M$ is the number of the auxiliary ones. Adopting the same notation used in Chapter 3, we remind that c_{ia}, $a = 1, \cdots, 2N$, are the fermionic operators of the N spinful orbitals per each site i in the enlarged Hilbert space, while $d_{i\alpha}$, $\alpha = 1, \cdots, 2M$, denote the operators of the physical spinful orbitals. Clearly, for $N = M$ the approach reduces to the conventional time-dependent Gutzwiller [247, 248]. The Dirac-Frenkel principle, which can be interpreted as the extension of the variational principle out of equilibrium, allows the approximation of the Schrödinger dynamics of an interacting system with the equations of motion for $\lambda_{\Gamma\gamma}(t,i)$ and $|\Psi_*(t)\rangle$, obtained at the saddle point, $\delta S = 0$, of the Gutzwiller action:

$$S\left[\Psi_G(t)\right] = \int dt\, \langle\Psi_G(t)|\, i\partial_t - H(t)\,|\Psi_G(t)\rangle = \int dt\, \mathcal{L}(t)\,, \tag{5.3}$$

where $H(t)$ is the time-dependent version of the multi-band Hubbard model in Eq. (3.2) and $\mathcal{L}(t)$ is the ghost-Gutzwiller Lagrangian. Following Section 3.2.2, we associate the time-dependent variational parameters $\lambda_{\Gamma\gamma}(t,i)$ to the components $\psi(t,i;\Gamma,\bar{\gamma})$ of an impurity wave function and we express the average value of the local observables in terms of $|\psi(t,i)\rangle$.

Like in the conventional t-GW, the time-dependent expectation values of the local and non-local operators, defined in Section 3.2.1, can be computed analytically in the infinite-coordination lattices [81] provided that the Gutzwiller constraints (3.5) are satisfied at any time:

$$\langle\psi(t,i)|\psi(t,i)\rangle = 1, \tag{5.4}$$

$$\langle\psi(t,i)|c_{ib}c_{ia}^{\dagger}|\psi(t,i)\rangle = \langle\Psi_*(t)|c_{ia}^{\dagger}c_{ib}|\Psi_*(t)\rangle \equiv \Delta_{ab}(t,i), \quad \forall\, a,b. \tag{5.5}$$

As long as Eqs. (5.4) and (5.5) are satisfied the expressions for the wave function renormalization factors and the average of local in Eqs. (3.18) and (3.31) hold and, thus, the average value of $H(t)$ will have the same expression as in Eq. (3.21), i.e.:

$$E(t) = \sum_i \langle\psi(t,i)|H_i(t)|\psi(t,i)\rangle + \langle\Psi_*(t)|H_*(t)|\Psi_*(t)\rangle \tag{5.6}$$

where $H_*(t)$, defined in Eq. (3.22), becomes time-dependent since $R(t,i)$ in Eq. (3.18) depends on time. Finally, the term with the time derivative in Eq. (5.3) can be rewritten as [81]

$$i\langle\Psi_G(t)|\partial_t\Psi_G(t)\rangle = i\sum_i \langle\psi(t,i)|\partial_t\psi(t,i)\rangle + i\langle\Psi_*(t)|\partial_t\Psi_*(t)\rangle \tag{5.7}$$

and the ghost-Gutzwiller Lagrangian (5.3) reads:

$$\begin{aligned}\mathcal{L}(t) =& i\sum_i \langle\psi(t,i)|\partial_t\psi(t,i)\rangle + i\langle\Psi_*(t)|\partial_t\Psi_*(t)\rangle \\ &- \sum_i \langle\psi(t,i)|H_i(t)|\psi(t,i)\rangle - \langle\Psi_*(t)|H_*(t)|\Psi_*(t)\rangle \\ &+ \sum_i \sum_{ab=1}^{2N} \left[\mu_{ab}(i)\left(\langle\psi(t,i)|c_{ib}c_{ia}^{\dagger}|\psi(t,i)\rangle - \langle\Psi_*(t)|c_{ia}^{\dagger}c_{ib}|\Psi_*(t)\rangle\right)\right].\end{aligned} \tag{5.8}$$

In the previous expression $\mu_{ab}(i)$ stands for the matrix of Lagrange multipliers such to satisfy the Gutzwiller constraints in Eq. (5.5). It is important to notice that even in the presence of subsidiary degrees of freedom the Lagrange multipliers $\mu_{ab}(i)$ are time independent since the Gutzwiller constraint is preserved during the time evolution. In other words, provided that Eq. (5.5) is satisfied at $t = 0$, and Eq. (5.4) is enforced by construction, then the constraint is automatically satisfied by the saddle point solution of the action (5.3) at any time $t \geq 0$. This important result can be easily proved for the g-GW by following the same line of reasoning presented in Ref. [82].

The saddle-point condition:

$$\frac{\delta S}{\delta\langle\psi(t,i)|} = 0, \quad \frac{\delta S}{\delta\langle\Psi_*(t)|} = 0$$

gives the equations of motion:

$$i\partial_t|\psi(t,i)\rangle = \left(H_i(t) - \sum_{ab=1}^{2N}\mu_{ab}(i)c_{ib}c_{ia}^{\dagger}\right)|\psi(t,i)\rangle + \frac{\delta}{\delta\langle\psi(t,i)|}\langle\Psi_*(t)|H_*(t)|\Psi_*(t)\rangle, \tag{5.9}$$

and

$$i\partial_t|\Psi_*(t)\rangle = \left(H_*(t) + \sum_i \sum_{ab=1}^{2N} \mu_{ab}(i) c_{ia}^\dagger c_{ib}\right)|\Psi_*(t)\rangle. \tag{5.10}$$

As it can be appreciated from Eqs. (5.9) and (5.10), within the t-d-GW the electron dynamics is described by the Schrödinger equation of the Slater determinant $|\Psi_*(t)\rangle$ which is self-consistently coupled to the evolution of the embedded model $|\psi(t,i)\rangle$. Compared with the standard Gutzwiller dynamics, the addition of subsidiary degrees of freedom provides a more realistic description of the evolution of a strongly-correlated systems, which is characterized by the coexistence of different time scales associated with the low- and high-energy excitations. Furthermore, the hybridization of the physical orbital $d_{i\alpha}$ with the electron bath c_{ia} provides energy exchange mechanisms that suppresses the mean-field like coherent oscillations observed in the t-GW.

Given the initial conditions $|\psi(t=0,i)\rangle$ and $|\Psi_*(t=0)\rangle$, that solve the equilibrium g-GW problem in Section 3.2.3, the solution of the system of coupled equations can be obtained by a standard 4th order implicit Runge-Kutta method [35]. In particular, Eq. (5.9) consists of the evolution of the independent amplitudes $\psi(t,i,\Gamma,\gamma)$ of the embedded wave function $|\psi(t,i)\rangle$[1]. For what concerns the Slater determinant, we mention that for translationally invariant systems the evolution of $|\Psi_*(t)\rangle$ (5.10) can be recast in terms of the Heisenberg dynamics of the single-particle density matrix:

$$\langle n_{\mathbf{k}ab\sigma}(t)\rangle \equiv \langle\Psi_*(t)|c_{\mathbf{k}a\sigma}^\dagger c_{\mathbf{k}b\sigma}|\Psi_*(t)\rangle. \tag{5.11}$$

Therefore, the strategy for the solution of the Gutzwiller dynamics corresponds to the evolution of $\langle n_{\mathbf{k}ab\sigma}(t)\rangle$ for each $\mathbf{k}$ point in the Brillouin zone, that, summed over the $\mathbf{k}$ space, at any instant of time determines the hybridization amplitudes between the impurity $d_{i\alpha}$ and the bath c_{ia}.

We conclude by noting that the t-g-GW approach presented in this Section allows us to study the out of equilibrium dynamics of a generic lattice model in the absence of superconductive correlations. Furthermore, we observe that the stationary equilibrium problem, presented in Section 3.2.3, is obtained by substituting the expressions:

$$|\psi(t,i)\rangle = e^{-i\Lambda t}|\psi(i)\rangle, \quad |\Psi_*(t)\rangle = e^{-i\Lambda_* t}|\Psi_*\rangle, \tag{5.12}$$

in Eqs. (5.9) and (5.10). In the following we consider the specific example of the interaction quench dynamics of the repulsive single-band Hubbard model. This problem has already been studied with DMFT in [72, 73] and with conventional Gutzwiller in [247, 248]. Therefore, we had a possibility to benchmark our method.

5.3 Application to the half-filled Hubbard model

We now apply the above formalism to the simple case of a single-band Hubbard model at half-filling, where each lattice site hosts a single orbital $M = 1$ and the physical degree of freedom α reduces to the spin projection $\sigma = \uparrow, \downarrow$ along the quantization axis. The analysis allows us to compare the results obtained with our time-dependent variational approach together with the previous studies on the dynamics of the single-band Hubbard model [72, 191, 247]. We will show that with our approach we can recover known results, but also find additional features that are missing from the conventional Gutzwiller evolution.

[1]The number of amplitudes $\psi(t,i,\Gamma,\gamma)$ grows exponentially with the dimension of the embedded impurity model. To reduce the number of Eqs. of motion it is important to implement the symmetries inherited from the lattice model directly on $|\psi(t,i)\rangle$.

We consider the dynamics of the single-band Hubbard model induced by a time-dependent interaction $U(t)$:

$$H(t) = -\frac{t}{\sqrt{\mathbf{Z}}} \sum_{\langle i,j \rangle} \sum_{\sigma} \left(d^{\dagger}_{i\sigma} d_{j\sigma} + \text{H.c.} \right) + U(t) \sum_{i} \left(n_{\uparrow} - \frac{1}{2} \right) \left(n_{\downarrow} - \frac{1}{2} \right), \tag{5.13}$$

where $\langle i, j \rangle$ stands for the nearest-neighbor bonds on a Bethe lattice, and $\mathbf{Z}$ is the lattice coordination number that must be sent to $+\infty$ such that the calculations are truly variational. Analogously to the equilibrium case, we use the Bethe lattice density of state $\rho(\epsilon) = \theta(W - |\epsilon|) 2\sqrt{W^2 - \epsilon^2}/\pi W^2$, where W is the half-bandwidth. We study the Hamiltonian (5.13), assuming that during the evolution the time dynamics preserves the translational symmetry:

$$|\psi(t, i)\rangle = |\psi(t)\rangle, \quad \forall\, i, \tag{5.14}$$

and does not induce any magnetization (i.e. $SU(2)$ spin-rotations invariance):

$$\Delta_{a\sigma,b\sigma'}(t) = \delta_{\sigma\sigma'} \Delta_{ab}(t), \; R_{\sigma,a\sigma'}(t) = \delta_{\sigma\sigma'} R_a(t), \tag{5.15}$$

where we separate the spin $\sigma = \uparrow, \downarrow$ and the orbital $a = 1, \cdots, N$ indices. Furthermore, the invariance of the embedded and the effective tight-binding $H_*(t)$ lattice model, under the particle-hole symmetries (3.64) and (3.65), reduces the number of independent entries of the single-particle density matrix:

$$\Delta_{ab}(t) = \delta_{ab} - \Delta_{C_b C_a}(t),$$

where a and b are particle-hole conjugated to C_a and C_b, respectively. Similar relations hold for the elements of the Lagrange multipliers matrix and wave function renormalization factors:

$$\mu_{ab} = -\mu_{C_b C_a}, \quad R^*_a(t)\, R_b(t) = R^*_{C_b}(t)\, R_{C_a}(t).$$

The embedded wave function $|\psi(t)\rangle$, invariant under the symmetry transformations in (3.64) and (3.65), lives in the subspace characterized by the quantum numbers

$$Q = N - N_{\text{sites}} = 0, \quad S^z = (N_{\uparrow} - N_{\downarrow})/2 = 0,$$

where $N_{\sigma} = d^{\dagger}_{\sigma} d_{\sigma} + \sum_{a=1}^{N} c^{\dagger}_{a\sigma} c_{a\sigma}$ is the operator that counts the total number of electrons with spin σ, $N = N_{\uparrow} + N_{\downarrow}$ and N_{sites} is the number of bath levels plus the impurity site $N_{\text{sites}} = N_{\text{levels}} + 1$. Within the subspace (5.3) the $|\psi(t)\rangle$ reads:

$$|\psi(t)\rangle = \sum_{n} \frac{1}{\sqrt{g_{\gamma(n)}}}\, s_n\, \psi_{\gamma(n)}(t)\, |n\rangle \tag{5.16}$$

where n runs over the many-body states of the subspace (5.3), $|n\rangle$ describes an embedded impurity model configuration, $g_{\gamma(n)}$ is a degeneracy factor that counts the number of different configurations $\{|n_1\rangle, \cdots, |n_l\rangle\}$ characterized by the same weight $|\psi_{\gamma(n)}|$. Therefore, the corresponding amplitudes $\psi_{\gamma(n)}$ may differ only for the sign factor, that we denote as s_n. We notice that the parametrization in Eq. (5.16) implies that the normalization condition (5.4) reads:

$$\langle \psi(i) | \psi(i) \rangle = \sum_{\gamma} |\psi_{\gamma}(t)|^2,$$

where we sum only the independent amplitudes of the impurity wave function. In terms of the amplitudes ψ_γ the Eq. (5.9) takes the form:

$$\begin{aligned} i\partial_t \psi_{\gamma_n}(t) =& \frac{\partial}{\partial \psi^*_{\gamma_n}(t)} \sum_{ml} \frac{g_{\gamma_n}}{\sqrt{g_{\gamma_m} g_{\gamma_l}}} s_m s_l \psi^*_{\gamma_m}(t) \psi_{\gamma_l}(t) \langle m| \left(H_i(t) - \sum_\sigma \sum_{ab=1}^{N} \mu_{ab} c_{ib\sigma} c^\dagger_{ia\sigma} \right) |l\rangle \\ &+ \frac{g_{\gamma_n}}{V} \sum_{\mathbf{k}\sigma} \epsilon_{\mathbf{k}} \sum_{ab=1}^{N} \langle n_{\mathbf{k}ab\sigma}(t) \rangle \frac{\partial}{\partial \psi^*_{\gamma_n}(t)} \left[R^*_a(t) R_b(t) \right], \end{aligned} \tag{5.17}$$

where we have performed the Fourier transform of $H_*(t)$, whereas $\langle n_{\mathbf{k}ab\sigma}(t) \rangle$ is the quasiparticle distribution in momentum space defined in Eq. (5.11). The latter quantity evolves according to the Heisenberg equation

$$i\partial_t \langle n_{\mathbf{k}ab\sigma}(t) \rangle = \sum_{c=1}^{N} \Big(\mathscr{H}_*(t,\mathbf{k})_{bc} \langle n_{\mathbf{k}ac\sigma}(t) \rangle - \mathscr{H}_*(t,\mathbf{k})_{ca} \langle n_{\mathbf{k}cb\sigma}(t) \rangle \Big), \tag{5.18}$$

where

$$\mathcal{H}_*(t) = \sum_{\mathbf{k}\sigma} \vec{\Psi}^\dagger_{\mathbf{k}\sigma} \cdot \mathscr{H}_*(t,\mathbf{k}) \cdot \vec{\Psi}_{\mathbf{k}\sigma},$$

with

$$\mathscr{H}^*(t,\mathbf{k})_{ab} = \epsilon_{\mathbf{k}} R^*_a(t) R_b(t) + \mu_{ab},$$

and $\vec{\Psi}_{\mathbf{k}\sigma} = (c_{\mathbf{k}1\sigma}, \cdots, c_{\mathbf{k}N\sigma})^T$. In the following we analyze the solution of the Eqs. (5.17) and (5.18) considering the case of a sudden change of the Hubbard U on-site interaction.

5.4 Quench dynamics

We now turn to the application of the formalism to discuss the out of equilibrium evolution in the half-filled single band Hubbard model (5.13). Among different nonequilibrium protocols we consider one of the most popular, the evolution under a sudden change of the Hamiltonian parameters, i.e. quantum quench. This protocol corresponds to prepare the system in the many-body variational ground state $|\Psi_i\rangle$ of the Hubbard model with initial interaction $U(t \leq 0) = U_i$, then for times $t > 0$ the state evolves under an Hamiltonian characterized by a value of the local interaction different from the initial one $U(t > 0) = U_f \neq U_i$.

The improved characterization of the Mott insulator, provided by the g-GW variational wave function, allows us to describes the time-dependent dynamics taking as initial condition both the metallic and the Mott insulating solutions, the latter not being accessible by the conventional time-dependent Gutzwiller wave function. However, in order to make a clear comparison with pre-existing results [72, 73, 247, 248], we focus our analysis by considering as initial condition a correlated metal $U_i < U_{c2}$ which is evolved by quenching the local interaction $U_f > U_i$. Under these circumstances the dynamics is characterized by the presence of a dynamical critical point U_c^d that splits the evolution in three different regimes of weak $U_f < U_c^{\rm dyn}$, intermediate $U_f \sim U_c^{\rm dyn}$ and strong $U_f > U_c^{\rm dyn}$ quenches. In order to characterize the dynamics in the different regimes, we focus on three physical quantities, namely the double occupancy $D(t) = \langle \psi(t) | d^\dagger_{i\uparrow} d_{i\uparrow} d^\dagger_{i\downarrow} d_{i\downarrow} | \psi(t) \rangle$, the quasiparticle residue $Z(t)$ and the discrete Fourier transform (DFT) of $D(t)$.

5.4.1 Weak quenches

For weak quantum quenches the t-g-GW evolution of the double occupancy $D(t)$ is shown in Fig. 5.1 **(a)** and its discrete Fourier transform (DFT) in Fig. 5.1 **(b)** in comparison with the t-GW results

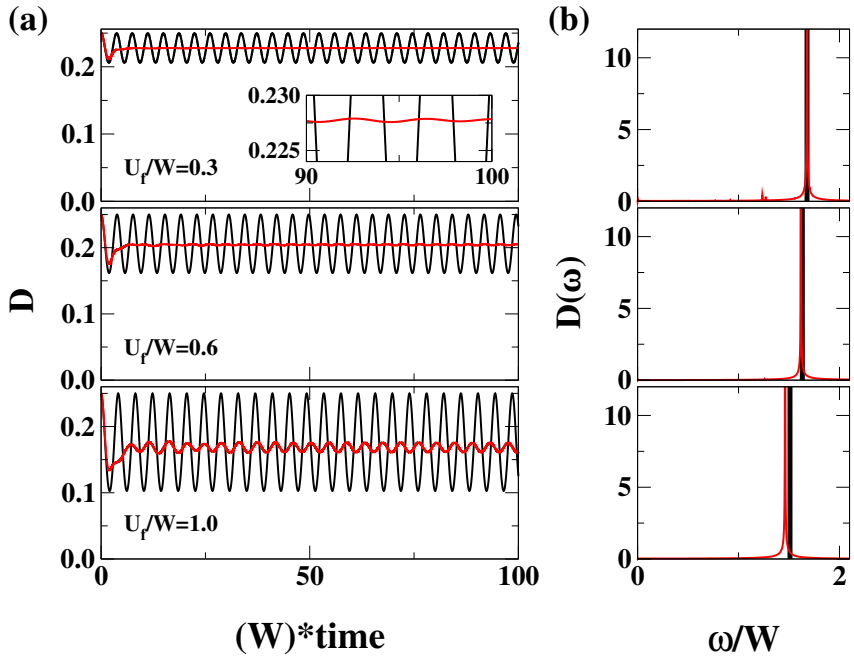

Figure 5.1: Double occupancy as a function of time for different values of U_f taking as initial condition the ideal Fermi gas $U_i/W = 0$. Black and red lines represent the standard GW and g-GW results, respectively. Panel **(a)** shows $D(t)$ for $U_f/W = 0.3, 0.6$ and 1.0 plotted from top to bottom. Panel **(b)** we plot the DFT of the double occupancy for the same values of U_f.

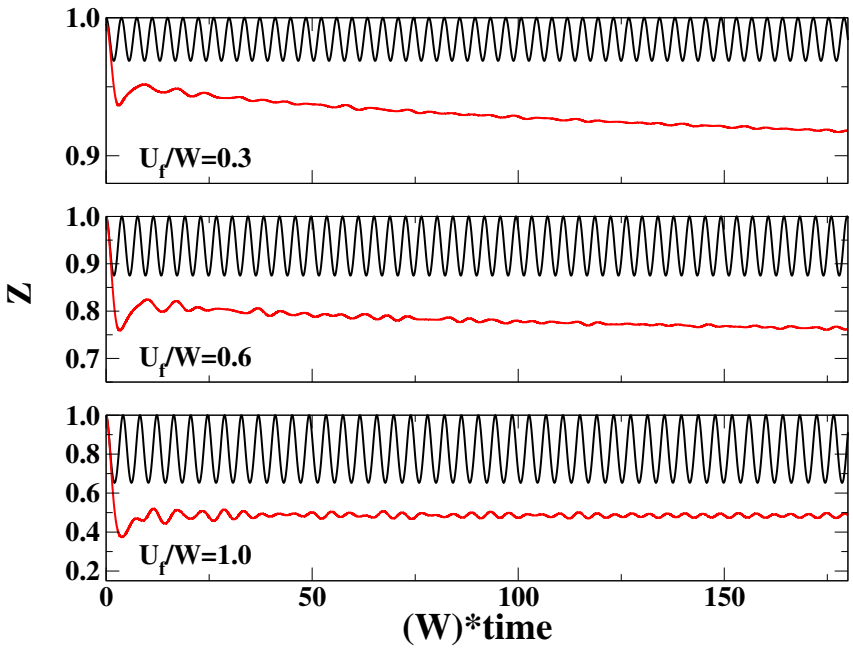

Figure 5.2: Quasiparticle residue as a function of time for different values of U_f starting from the ideal Fermi gas $U_i/W = 0$. Black and red lines represent the standard GW and g-GW results, respectively. $Z(t)$ is computed for the following values $U_f/W = 0.3, 0.6$ and 1.0.

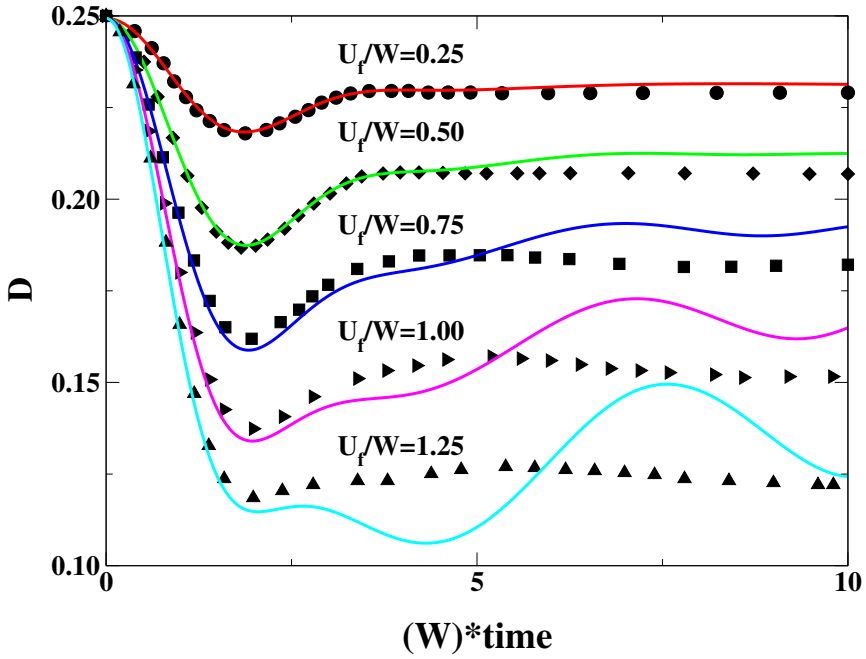

Figure 5.3: Double occupancy as a function of time in the weak quenches regime. Different lines correspond to t-g-GW, while black points are DMFT results for $U_i/W = 0$ and different values of U_f/W. DMFT data are taken from Ref. [73].

[247, 248]. Interestingly, the auxiliary fermionic degrees of freedom introduced in the g-GW wave function provide dephasing mechanisms that reduce the amplitude of the oscillations, with respect to the t-GW dynamics, in the regime large times. By increasing the value of U_f/W, from top to bottom of Fig. 5.1 **(a)**, we observe that the amplitude of the residual oscillations increases due to the excess of injected energy that the system is not able to dissipate. The DFT of the double occupancy $D(t)$ time series is shown in Fig. 5.1 **(b)**. Remarkably, the signal is dominated by a single mode whose frequency is close to the one observed in the standard t-GW, which is represented by the black solid vertical line. Moreover, we notice that the frequency of the mode is decreasing as the value of the interaction increases from $U_f/W = 0.3$ to $U_f/W = 1.0$. On the other hand, the evolution of the quasiparticle residue $Z(t)$, in Fig. 5.2, shows deviations from the results obtained with the standard t-GW. For $U_f/W = 0.3, 0.6$ we observe the tendency of the time-dependent evolution to approach the thermal regime, characterized by a vanishing renormalization factor $Z(t \to \infty) = 0$. However, the time scale associated to the thermalization process is much longer than the estimate made in [191], i.e. $\tau_{\text{therm}} \sim \hbar W^3/8U^4$.

In Fig. 5.3 we compare the dynamics of the double occupancies $D(t)$ obtained both with t-g-GW and DMFT [72, 73]. Instead, Fig. 5.4 shows the comparison between the evolution of the quasiparticle residue factor $Z(t)$ computed with t-g-GW and DMFT. At short times we observe a good agreement between the two different approaches. However, at larger times we notice deviation from the DMFT dynamics due to the residual oscillations characteristic for the t-g-GW at $N = 3$. We expect that the amplitude of the oscillations reduce by increasing the number of bath levels N.

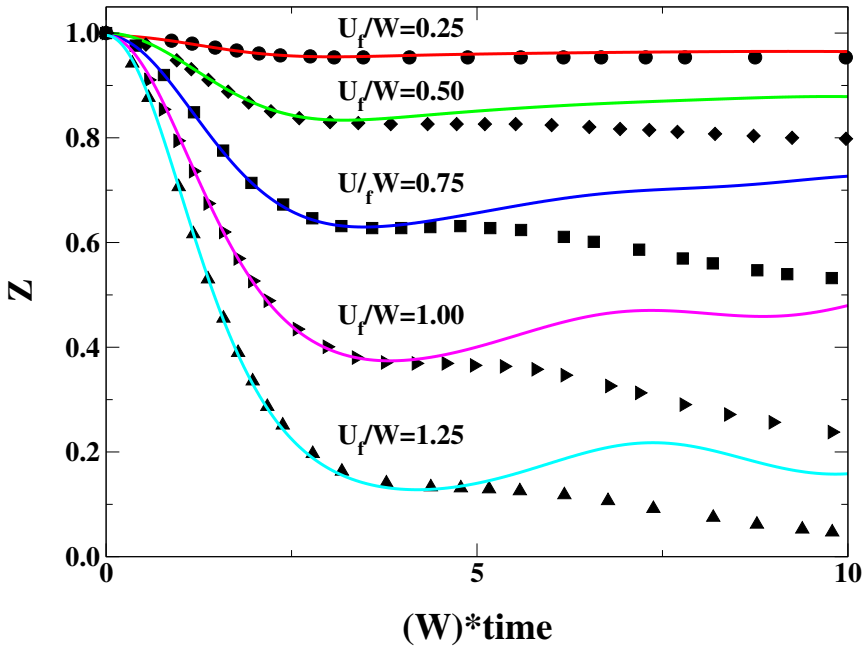

Figure 5.4: Quasiparticle residue as a function of time in the weak quenches regime. Different lines correspond to t-g-GW, while black points are DMFT results for $U_i/W = 0$ and different values of U_f/W. DMFT data are taken from Ref. [73].

5.4.2 Strong quenches

For quenches at large U_f, above the dynamical critical interaction $U_c^{\rm dyn}$, the evolution is characterized by coherent oscillations with period $\sim 2\pi\hbar/U_f$ both in $D(t)$ and $Z(t)$. This behavior is easy to understand in the limit of large quenching, $W/U_f \to 0$, where the evolution operator takes the form $\prod_i e^{iU_f(n_{i\uparrow}-1/2)(n_{i\downarrow}-1/2)t}$. For any finite value of the ratio W/U_f we expect to observe damping of the periodic oscillations induced by hopping processes. Figs. 5.5 and 5.6 shows the comparison between standard GW and t-g-GW dynamics. The comparison between the t-g-GW evolution and DMFT is shown in Figs. 5.7 and 5.8, where we plot double occupancy and quasiparticle weight as a function of time. Figs. 5.7 and 5.8 show that as the value of U_f increases, the evolution given by the t-g-GW is closer to the exact dynamics obtained in DMFT. Despite the reduction of the amplitude of the oscillations with respect to the standard GW dynamics, relaxation processes are missing in the g-GW dynamics and the long time evolution is dominated by the presence of persistent oscillations.

5.4.3 Intermediate quenches and dynamical phase diagram

In this Section we consider the regime of intermediate quenches close to the dynamical critical point $U_c^{\rm dyn}$, that, as shown in Fig. 5.10, we find to be located in the interval $U_c^{\rm dyn} \simeq [1.62, 1.65]$[2]. This regime is characterized by the critical slowing down of the dynamics, and, correspondingly, by the presence of a low energy mode in the $D(t)$ oscillations. Therefore, the system undergoes a dynamical phase transition that separates the two different regimes of strong and weak quenches.

[2]We notice that for numerical reasons the time-evolution of the ghost-Gutzwiller wave function does not allow us to find a precise value for the critical U, but rather an interval where the critical point is located.

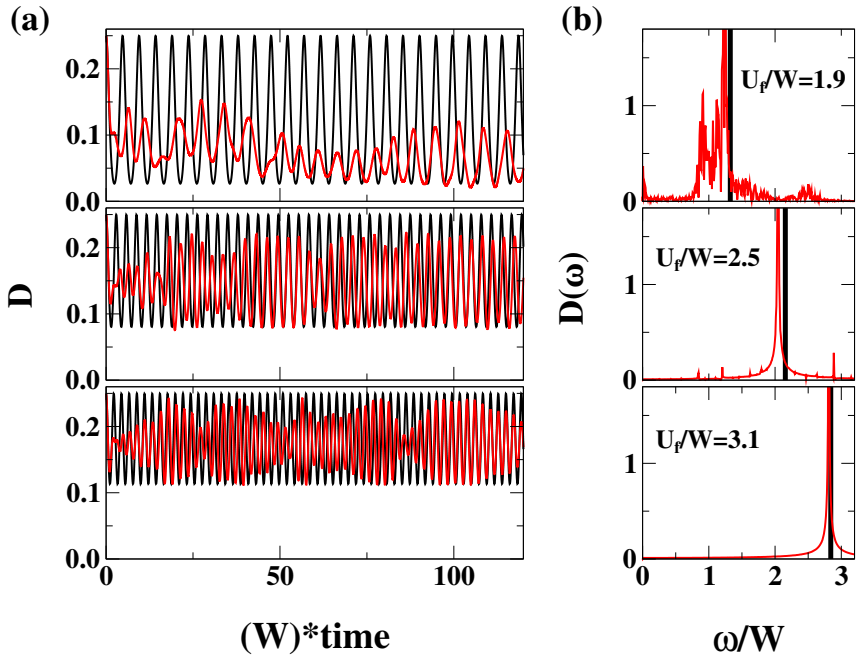

Figure 5.5: Double occupancy as a function of time for different values of U_f starting from the weakly interacting regime $U_i/W = 0$. Black and red lines represent the standard GW and g-GW results, respectively. Panel **(a)** shows the evolution of the double occupancy for the values of the interaction $U_f/W = 1.9, 2.5$ and 3.1. Panel **(b)** displays the DFT of $D(t)$ for the same values of the interaction.

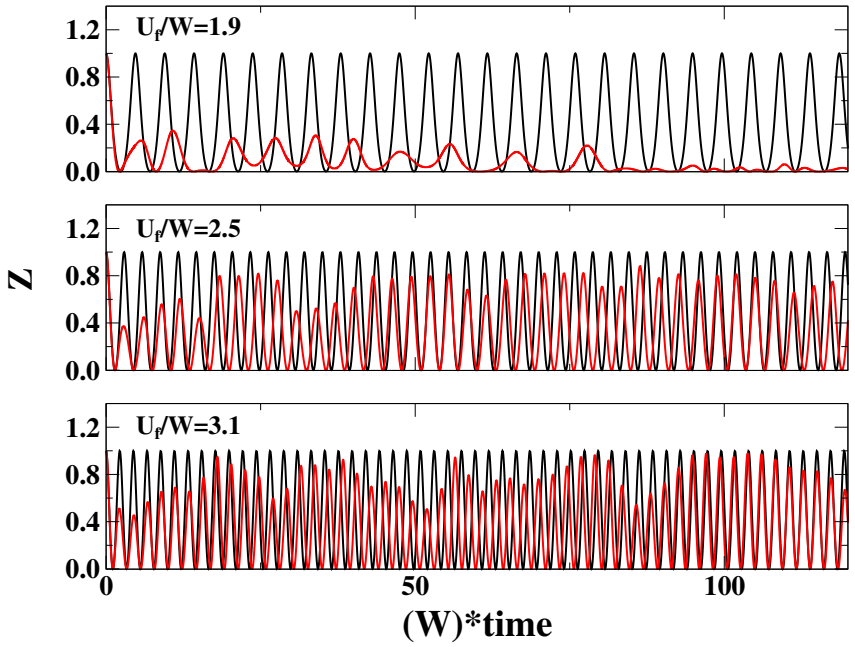

Figure 5.6: Quasiparticle residue as a function of time for different values of U_f starting from the weakly interacting regime $U_i/W = 0$. Black and red lines represent the standard GW and g-GW results, respectively. In this case the values of the final interaction are $U_f/W = 1.9, 2.5$ and 3.1.

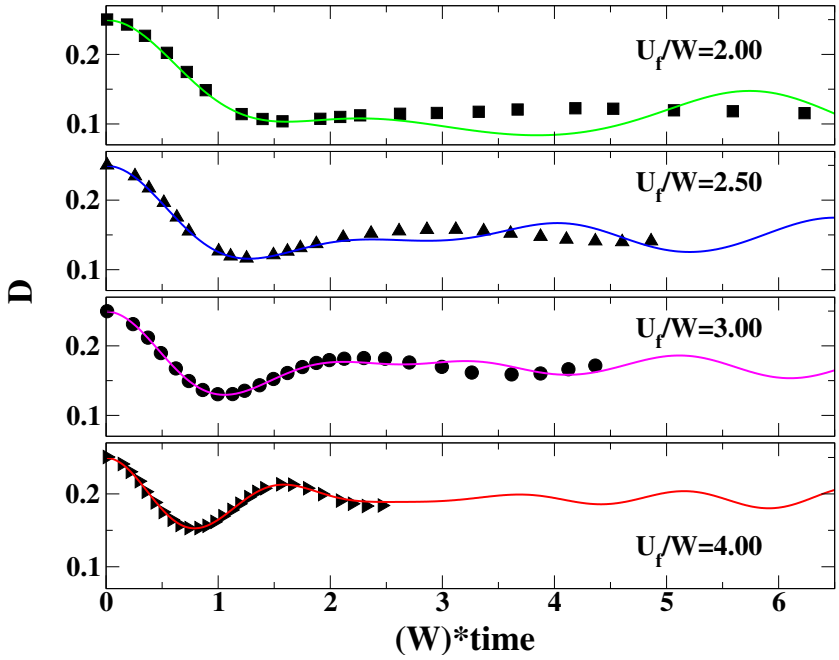

Figure 5.7: Double occupancy as a function of time in the strong quenches regime. Solid lines correspond to t-g-GW results, while black points represent DMFT data taken from [73].

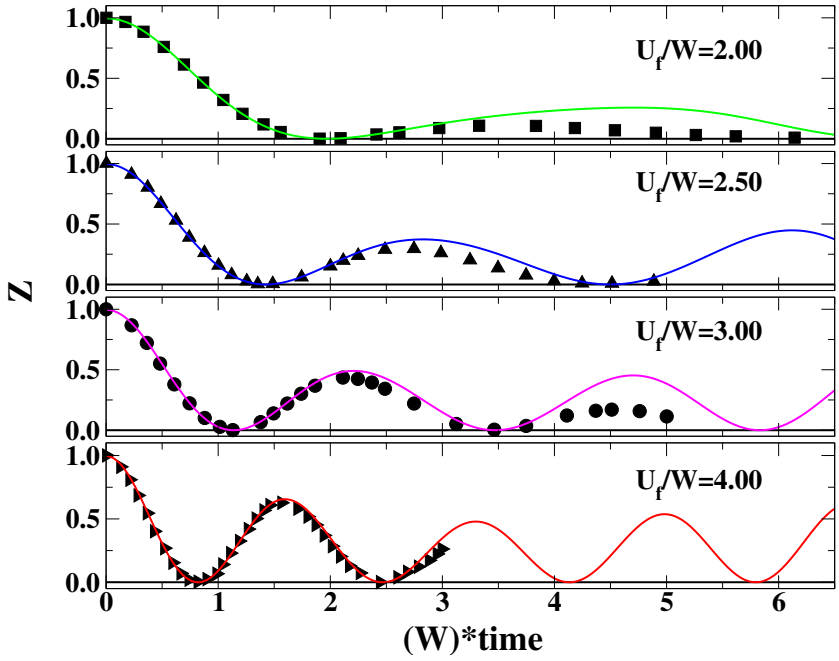

Figure 5.8: Quasiparticle residue as a function of time in the strong quenches regime. Solid lines correspond to t-g-GW results, while black points represent DMFT data taken from [73].

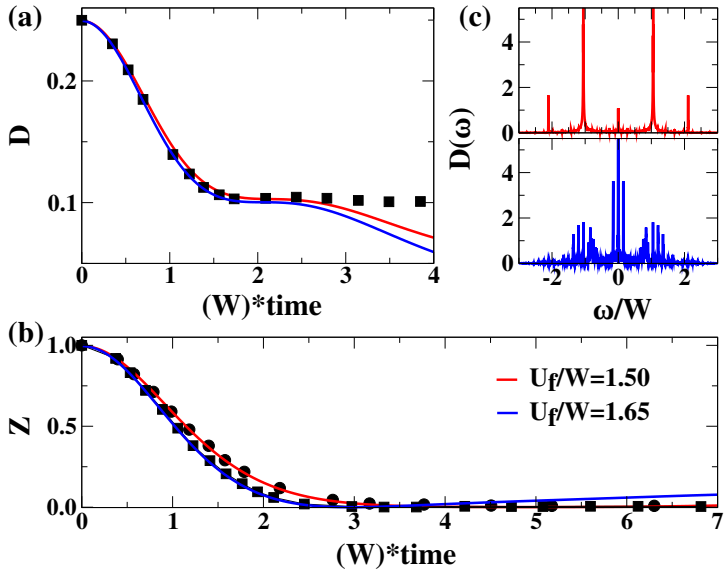

Figure 5.9: Comparison between t-g-GW (solid lines) and DMFT (black dots) results, taken from [73], for $U_f/W = 1.5, 1.65$. Panel **(a)** shows the evolution of the double occupancy. Panel **(b)** depicts the quasiparticle residue $Z(t)$. Finally, in panel **(c)**, we report the DFT of $D(t)$.

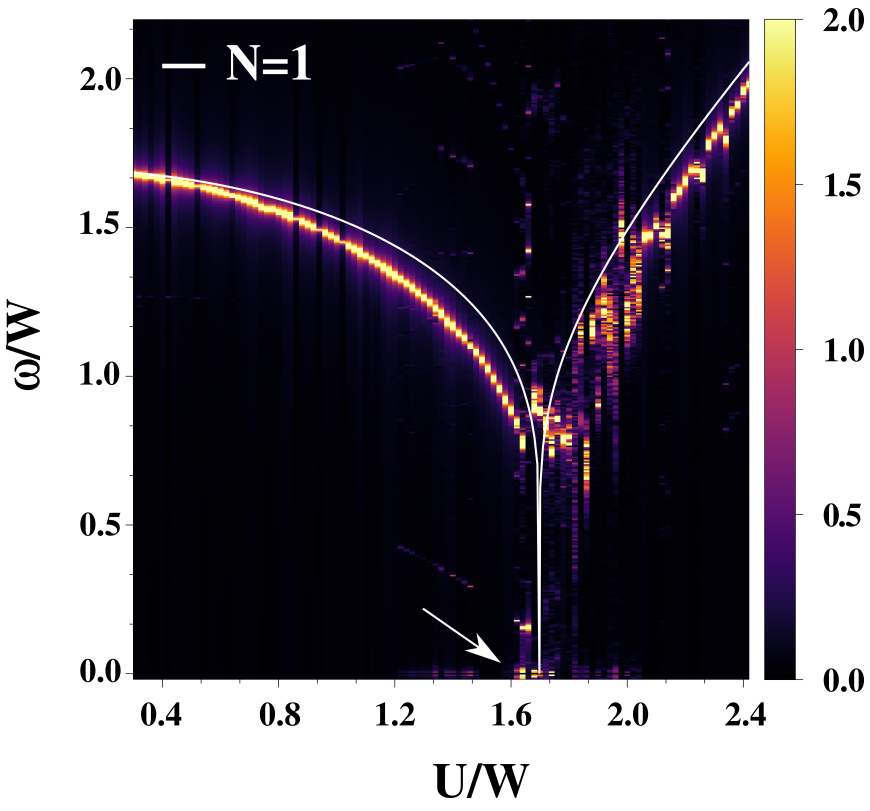

Figure 5.10: Fourier transform of the double occupancy for different values of the quench interaction U_f/W. The presence of a finite spectral weight $|D(\omega)|$ with vanishing frequency characterizes the dynamical critical point, indicated by the white arrow.

In Fig. 5.9 panel **(a)** and **(b)** we compare the t-g-GW dynamics of the double occupancy and the quasiparticle residue with DMFT results. The comparison with Figs. 5.7 and 5.8 points out the characteristic slowing down of the dynamics and the correspondent onset of a low-energy mode in the $D(t)$. Remarkably, even in the dynamical critical regime, we observe good agreement in the short time dynamics between t-g-GW and DMFT. However, differently from DMFT results, the coherent oscillations characterizing the t-g-GW dynamics are persistent and give rise to the spectral features shown in panel **(c)** of Fig. 5.9 for $U_f/W = 1.5$ and $U_f/W = 1.65$. We notice that in the critical region of the interaction quenches $U_f/W = 1.65$ the dynamics is a composed by a superpositions of several modes dominated by the zero frequency one, see panel **(c)** of Fig. 5.9.

Finally, we report in Fig. 5.10 the color map that shows the DFT of the double occupancy as a function of the quench interaction U_f. For weak quenches, the frequency ω_D of the double occupancy oscillations is close to the result obtained with the conventional Gutzwiller (solid white line). In the strong coupling regime, instead, we observe that the frequency of the oscillations approaches the atomic limit $\omega \sim U_f$, $U_f/W \geq 2$. Finally, in the intermediate regime we observe the presence of a dynamical critical point characterized by a vanishing value of the frequency of the double occupancy $D(t)$, namely $\omega_D \sim 0$. Our numerical calculations predict that $U_c^{\mathrm{dyn}}/W \simeq [1.62, 1.65]$, taking as initial state the ideal Fermi gas, that is not far from the value obtained with DMFT $U_c^{\mathrm{dyn}}/W \simeq 1.6$ [72, 73] .

5.5 Conclusions

We extend the ghost-Gutzwiller wave function to describe the out of equilibrium evolution of multi-band Hubbard models in the absence of superconductive correlations. To benchmark our method with DMFT and conventional Gutzwiller result we study the out of equilibrium dynamics in the single-band Hubbard model induced by a quench in the local interaction. The addition of subsidiary degrees of freedom in the Gutzwiller wave function provides a more accurate and complete description of the evolution of a strongly-correlated system, which is characterized by the coexistence of different time scales associated with low- and high-energy excitations. Differently from the conventional Gutzwiller results, the hybridization of the physical orbital $d_{i\sigma}$ with N, $N > 1$, bath levels c_{ia} provides energy exchange mechanisms that suppress the mean-field like coherent oscillations observed in the t-GW. However, as long as the number of bath levels is finite, the novel channels do not act as a reservoir that absorbs the excess of energy injected by the time-dependent perturbation and the system never reaches an asymptotic stationary state. We expect that numerical simulations with $N > 3$ would certainly improve the results presented in Section 5.4 by a further suppression of the residual oscillations.

6

Unbinding slave-spins in Anderson impurity models

In this Chapter we show that a generic single-orbital Anderson impurity model can be exactly mapped without any constraint onto a resonant level model coupled to two Ising variables, which reduce to one if the hybridization is particle-hole symmetric. It is interesting to notice that the mean-field slave-spin solution of the single-orbital Anderson impurity model (SIAM) is found to be stable to unphysical spontaneous magnetisation of the impurity, unlike the saddle-point solution in the standard slave-boson representation [81, 156]. Remarkably, the mean-field estimates of the Wilson ratio R_W and of the quasiparticle scattering amplitudes tend to the exact Nozières' local Fermi liquid result in the Kondo regime [194, 212, 214]. We discuss quantum fluctuations on top of the mean-field results and their contribution to the Green's function of the impurity electrons. The previous analysis allows us to employ the self-consistent mean-field slave-spin theory as an approximate impurity solver within the dynamical mean field theory (DMFT) [152].

6.1 Introduction

Within any approximate technique based on independent particles, as, e.g., Hartree-Fock, the electron's quantum numbers, i.e., its charge, spin, and, eventually, orbital component, are inevitably all entangled into the single-particle excitations. This is ultimately the reason why such independent-particle schemes fail in correlated electron systems where charge degrees of freedom are instead well separated in energy from spin and orbital ones.

An efficient and popular trick to disentangle the different degrees of freedom is to enlarge the Hilbert space adding auxiliary particles, *slaves* to the physical charge excitations. So far there exists a number of various implementations of such a technique, starting from the elder slave-boson theory [25, 58, 156] to more recent rotationally invariant slave-boson [126, 166], slave-spin [65, 120, 240] and slave-rotor [87] ones. Those auxiliary particles are bound by a product of local constraints that project the enlarged Hilbert space $\mathscr{H}_*$ onto the physical subspace $\mathscr{H}$, and concurrently the effective Hamiltonian H_* of the electrons plus the auxiliary particles onto the original electron-only one, H. As is common in such cases, H_* possesses a local gauge invariance that translates into local conserved quantities. The constraints simply fix the values

that those conserved quantities have in the physical subspace.

The big advantage of this apparently more cumbersome approach is that a mean-field decoupling of the electrons from the slave particles naturally provides the desired disentanglement of charge from all other degrees of freedom, hence allowing the access to phenomena like Mott localization [156] otherwise inaccessible by mean-field in the original electron-only representation.

The problem with the mean-field in slave-particle theories is that the constraints are only satisfied *on average*, which brings out unphysical gauge-symmetry breaking, i.e. mean-field solutions mixing the physical subspace with the non-physical one. There is actually an exception where the constraint is not required: a particle-hole (p-h) symmetric SIAM that is represented in terms of a resonant level coupled to a two-level system, one level corresponding to the singly occupied impurity and the other to the empty or doubly occupied impurity. Because of the p-h symmetry, the partition function within the physical subspace is equal to the one in the unphysical one, so that the former is just half of the partition function calculated in the whole enlarged Hilbert space without any restriction [248]. In this representation the constraint translates into a local Z_2 gauge symmetry, which is spontaneously broken at zero temperature [26] since the model effectively corresponds to a two-level system in a sub-ohmic bath [46]. Therefore, the symmetry breaking is here not a spurious result of mean field but a real feature of the model. Since a p-h symmetric Hubbard model in infinitely coordinated lattices maps within dynamical mean-field theory (DMFT) [95] just onto that same SIAM, one can show [248] that the free energy of the lattice model can be straightforwardly obtained by the corresponding one of its Z_2 slave spin representation [120, 240] without imposing any constraint. One outstanding consequence of such mapping is that the metallic phase of the Hubbard model translates into a phase where the local Z_2 gauge symmetry breaks spontaneously [121] whereas the symmetry is restored in the Mott insulator[1]. This mapping thus endows the Mott transition of a genuine order parameter. More recently, a similar trick of exploiting particle-hole symmetry to get rid of the local constraints was used [152] to derive a Landau-Ginzburg theory of the orbital-selective Mott transition in a two-band Hubbard model at half-filling.

In the next Section, we formulate the slave-spin mapping for a generic SIAM, showing that both local observables and Green's functions can be evaluated without any need of local constraints. Remarkably, this result extends to multi-orbital impurity model under certain assumptions on the form of the local interaction on the impurity site.

6.2 The model

In this Section we formulate the slave-spin mapping for a generic SIAM[2] where the tunnel-coupling amplitudes $V_{\mathbf{k}\sigma}$ are spin-dependent and nonsymmetric under $\epsilon \to -\epsilon$:

$$H = \sum_{\mathbf{k}\sigma} \left[\epsilon_{\mathbf{k}\sigma} \psi^\dagger_{\mathbf{k}\sigma} \psi_{\mathbf{k}\sigma} + \frac{V_{\mathbf{k}\sigma}}{\sqrt{V}} \left(d^\dagger_\sigma \psi_{\mathbf{k}\sigma} + \psi^\dagger_{\mathbf{k}\sigma} d_\sigma \right) \right] - \frac{U}{4}\,\Omega - \frac{\mu}{2}(n_\uparrow + n_\downarrow - 1) - \frac{h}{2}(n_\uparrow - n_\downarrow)\,, \qquad (6.1)$$

where d_σ is the annihilation operator of an electron state on the impurity, $n_\sigma = d^\dagger_\sigma d_\sigma$ is the corresponding density, while $\Omega = -(2n_\uparrow - 1)(2n_\downarrow - 1)$ and $n = n_\uparrow + n_\downarrow$. Despite a nonsymmetric $V_{\mathbf{k}\sigma}$, we can always assume, without loss of generality, a p-h symmetric spectrum $\epsilon_{\mathbf{k}\sigma}$, which implies the existence of a one-to-one correspondence between spin-dependent pairs of momenta,

[1] We notice that the spontaneous breaking of the discrete Z_2 gauge symmetry is possible only when the lattice coordination number is infinite [183].

[2] For more details on the SIAM we refer to Section 3.3.

$\mathbf{k}$ and $\mathbf{p} = C_\sigma(\mathbf{k})$, such that $\epsilon_{\mathbf{k}\sigma} = -\epsilon_{\mathbf{p}\sigma}$. It is convenient to define for all $\mathbf{k}$ such that $\epsilon_{\mathbf{k}\sigma} < 0$ the following combinations:

$$\begin{aligned}\psi_{1\mathbf{k}\sigma} &= (\psi_{\mathbf{k}\sigma} + \psi_{C_\sigma(\mathbf{k})\sigma}) / \sqrt{2},\\ \psi_{2\mathbf{k}\sigma} &= (\psi_{\mathbf{k}\sigma} - \psi_{C_\sigma(\mathbf{k})\sigma}) / \sqrt{2},\end{aligned} \tag{6.2}$$

as well as tunnel-coupling amplitudes:

$$\begin{aligned}V_{1\mathbf{k}\sigma} &= (V_{\mathbf{k}\sigma} + V_{C_\sigma(\mathbf{k})\sigma}) / \sqrt{2},\\ V_{2\mathbf{k}\sigma} &= (V_{\mathbf{k}\sigma} - V_{C_\sigma(\mathbf{k})\sigma}) / \sqrt{2}.\end{aligned} \tag{6.3}$$

In terms of $\psi_{1(2)\mathbf{k}\sigma}$ and $V_{1(2)\mathbf{k}\sigma}$ the Hamiltonian (6.1) reads:

$$\begin{aligned}H(U,\mu,h,V_{2\uparrow},V_{2\downarrow}) = &\sum_\sigma \sum_{\mathbf{k}}^{\epsilon_{\mathbf{k}\sigma}<0} \epsilon_{\mathbf{k}\sigma}\left(\psi^\dagger_{1\mathbf{k}\sigma}\psi_{2\mathbf{k}\sigma} + \psi^\dagger_{2\mathbf{k}\sigma}\psi_{1\mathbf{k}\sigma}\right)\\ &+ \sum_\sigma \sum_{\mathbf{k}}^{\epsilon_{\mathbf{k}\sigma}<0} \sum_{a=1}^{2} \frac{V_{a\mathbf{k}\sigma}}{\sqrt{V}}\left(d^\dagger_\sigma \psi_{a\mathbf{k}\sigma} + \psi^\dagger_{a\mathbf{k}\sigma} d_\sigma\right)\\ &- \frac{U}{4}\Omega - \frac{\mu}{2}(n_\uparrow + n_\downarrow - 1) - \frac{h}{2}(n_\uparrow - n_\downarrow),\end{aligned} \tag{6.4}$$

where we simply denoted $V_{a\mathbf{k}\sigma}$ as $V_{a\sigma}$, and as it will stand in the following.

Under a spin-σ p-h transformation:

$$C_\sigma : \left\{ d_\sigma \to d^\dagger_\sigma \bigcup \prod_{\mathbf{k}} \left(\psi_{1\mathbf{k}\sigma} \to -\psi^\dagger_{1\mathbf{k}\sigma} \bigcup \psi_{2\mathbf{k}\sigma} \to \psi^\dagger_{2\mathbf{k}\sigma}\right)\right\}, \tag{6.5}$$

the Hamiltonian (6.4) changes as follows:

$$\begin{aligned}C^\dagger_\uparrow H(U,\mu,h,V_{2\uparrow},V_{2\downarrow})C_\uparrow &= H(-U,-h,-\mu,-V_{2\uparrow},V_{2\downarrow})\\ C^\dagger_\downarrow H(U,\mu,h,V_{2\uparrow},V_{2\downarrow})C_\downarrow &= H(-U,h,\mu,V_{2\uparrow},-V_{2\downarrow}),\end{aligned} \tag{6.6}$$

while $\epsilon_{\mathbf{k}\sigma}$ and $V_{1\mathbf{k}\sigma}$ are invariant. Since the partition function, defined as:

$$Z(U,\mu,h,V_{2\uparrow},V_{2\downarrow}) = \mathrm{Tr}\left[\exp\left(-\beta H(U,\mu,h,V_{2\uparrow},V_{2\downarrow})\right)\right] \tag{6.7}$$

is invariant under any unitary transformation, we have:

$$\begin{aligned}Z(U,\mu,h,V_{2\uparrow},V_{2\downarrow}) &= Z(-U,h,\mu,V_{2\uparrow},-V_{2\downarrow})\\ &= Z(-U,-h,-\mu,-V_{2\uparrow},V_{2\downarrow})\\ &= Z(U,-\mu,-h,-V_{2\uparrow},-V_{2\downarrow}).\end{aligned} \tag{6.8}$$

The previous identities will be used in the next Section, where we will get rid of the slave-particle projector from the evaluation of the SIAM partition function.

6.3 Mapping within the slave-spin representation

In the local magnetic moment regime, when U is by far the largest energy scale, the charge fluctuations are well-separated in energy from the spin ones. However, the Hamiltonian (6.4) lacks a clear separation between the charge and spin degrees of freedom which is desirable in

the large-U regime. To disentangle low and high-energy sectors, we enlarge the original Hilbert space $\mathscr{H}$ by adding two Ising variables $\boldsymbol{\tau}_\uparrow$ and $\boldsymbol{\tau}_\downarrow$:

$$|n\rangle \rightarrow |n\rangle \otimes |s\rangle_\uparrow \otimes |s\rangle_\downarrow,$$

where $|n\rangle$ describes the f_σ pseudofermion configurations $\{|0\rangle, |\uparrow\rangle, |\downarrow\rangle, |\uparrow\downarrow\rangle\}$ on the impurity site, while $|s\rangle_\sigma$ refers to the configuration of a two level quantum system $\{|+\rangle_\sigma, |-\rangle_\sigma\}$. Thus, in the enlarged Hilbert space $\mathscr{H}_*$ we introduce the two commuting operators:

$$\mathcal{P}_\uparrow = \tau^z_\uparrow (2n_\uparrow - 1), \qquad \mathcal{P}_\downarrow = \tau^z_\downarrow (2n_\downarrow - 1), \tag{6.9}$$

which have eigenvalues $p_\sigma = \pm 1$ and can therefore be regarded as *parity* operators. A representation of the physical Hilbert space is obtained by requiring the correspondence:

$$\begin{aligned} |0\rangle_\sigma &\equiv |n^f_\sigma = 0\rangle \otimes |\tau^z_\sigma = -1\rangle, \\ |1\rangle_\sigma &= d^\dagger_\sigma |0\rangle \equiv |n^f_\sigma = 1\rangle \otimes |\tau^z_\sigma = +1\rangle, \end{aligned} \tag{6.10}$$

which comprises all states of the enlarged Hilbert space $\mathscr{H}_*$ even under the parity transformations in Eq. (6.9), i.e. with $p_\sigma = +1$. The projector onto the physical subspace is thus

$$\mathbb{P} = \mathbb{P}_\uparrow \mathbb{P}_\downarrow = \frac{1}{4}\Big(1 + \mathcal{P}_\uparrow\Big)\Big(1 + \mathcal{P}_\downarrow\Big), \tag{6.11}$$

and corresponds to the operator equivalence

$$\tau^z_\sigma \equiv (2n_\sigma - 1), \tag{6.12}$$

which is just the slave-spin constraint [65]. From Eq. (6.10) we readily realize that in the physical subspace of the enlarged Hilbert space the original annihilation operator d_σ is replaced by:

$$d_\sigma = \tau^x_\sigma f_\sigma, \tag{6.13}$$

ensuring the anticommutation relations $\{d_\sigma, d^\dagger_{\sigma'}\} = \delta_{\sigma\sigma'}$. Plugging Eq. (6.13) in Hamiltonian (6.4) we obtain:

$$\begin{aligned} H_2(U, \mu, h, V_{2\uparrow}, V_{2\downarrow}) = \sum_\sigma \sum_{\mathbf{k}}^{\epsilon_{\mathbf{k}\sigma}<0} \Bigg[\epsilon_{\mathbf{k}\sigma} \left(\psi^\dagger_{1\mathbf{k}\sigma} \psi_{2\mathbf{k}\sigma} + \text{H.c.}\right) + \sum_{a=1}^{2} \tau^x_\sigma \frac{V_{a\mathbf{k}\sigma}}{\sqrt{V}} \left(f^\dagger_\sigma \psi_{a\mathbf{k}\sigma} + \text{H.c.}\right) \Bigg] \\ + \frac{U}{4} \tau^z_\uparrow \tau^z_\downarrow - \frac{\mu}{4}(\tau^z_\uparrow + \tau^z_\downarrow) - \frac{h}{4}(\tau^z_\uparrow - \tau^z_\downarrow), \end{aligned} \tag{6.14}$$

where we have used the constraint in Eq. (6.12) to rewrite the local Hamiltonian in terms of $\tau^z_\uparrow$ and $\tau^z_\downarrow$ only. The Hamiltonian in Eq. (6.14) commutes with $\mathbb{P}_\uparrow$ and $\mathbb{P}_\downarrow$, so that each eigenstate of H_2 can also be chosen as an eigenstate of $\mathbb{P}_\sigma$ with eigenvalues p_σ, $\sigma = \uparrow, \downarrow$. We notice that in the physical subspace of $\mathscr{H}_*$ there are several possible definitions of the original fermionic degree of freedom:

$$\tau^x_\sigma f_\sigma = \tau^-_\sigma f_\sigma = -i\tau^y_\sigma f_\sigma, \tag{6.15}$$

with $\tau^-_\sigma = \tau^x_\sigma - i\tau^y_\sigma$. The previous identity (6.15) allows us to rewrite the Hamiltonian as:

$$\begin{aligned} H_2(U, \mu, h, V_{2\uparrow}, V_{2\downarrow}) = \sum_\sigma \sum_{\mathbf{k}}^{\epsilon_{\mathbf{k}\sigma}<0} \Bigg[\epsilon_{\mathbf{k}\sigma} \left(\psi^\dagger_{1\mathbf{k}\sigma} \psi_{2\mathbf{k}\sigma} + \text{H.c.}\right) \\ + \tau^x_\sigma \frac{V_{1\mathbf{k}\sigma}}{\sqrt{V}} \left(f^\dagger_\sigma \psi_{1\mathbf{k}\sigma} + \psi^\dagger_{1\mathbf{k}\sigma} f_\sigma\right) \\ + i\tau^y_\sigma \frac{V_{2\mathbf{k}\sigma}}{\sqrt{V}} \left(f^\dagger_\sigma \psi_{2\mathbf{k}\sigma} - \psi^\dagger_{2\mathbf{k}\sigma} f_\sigma\right) \Bigg] \\ + \frac{U}{4} \tau^z_\uparrow \tau^z_\downarrow - \frac{\mu}{4}(\tau^z_\uparrow + \tau^z_\downarrow) - \frac{h}{4}(\tau^z_\uparrow - \tau^z_\downarrow). \end{aligned} \tag{6.16}$$

We shall prefer the previous expression of the slave-spin Hamiltonian, since here the role of the p-h symmetry transformation C_σ (6.6) is simply played by τ^x_σ. Indeed, the equivalences below hold straightforwardly:

$$\begin{aligned} H_2(-U,h,\mu,V_{2\uparrow},-V_{2\downarrow}) &= \tau^x_\downarrow H_2(U,\mu,h,V_{2\uparrow},V_{2\downarrow})\,\tau^x_\downarrow\,,\\ H_2(-U,-h,-\mu,-V_{2\uparrow},V_{2\downarrow}) &= \tau^x_\uparrow H_2(U,\mu,h,V_{2\uparrow},V_{2\downarrow})\,\tau^x_\uparrow\,,\\ H_2(U,-\mu,-h,-V_{2\uparrow},-V_{2\downarrow}) &= \tau^x_\uparrow\tau^x_\downarrow H_2(U,\mu,h,V_{2\uparrow},V_{2\downarrow})\,\tau^x_\downarrow\tau^x_\uparrow, \end{aligned} \tag{6.17}$$

so that, through Eq. (6.8), we find

$$\begin{aligned} Z(U,\mu,h,V_{2\uparrow},V_{2\downarrow}) &= \mathrm{Tr}\Big(\mathrm{e}^{-\beta H_2(U,\mu,h,V_{2\uparrow},V_{2\downarrow})}\,\mathbb{P}\Big)\\ &= \mathrm{Tr}\Big(\tau^x_\downarrow \mathrm{e}^{-\beta H_1(U,\mu,h,V_{2\uparrow},V_{2\downarrow})}\,\tau^x_\downarrow\,\mathbb{P}\Big)\\ &= \mathrm{Tr}\Big(\tau^x_\uparrow \mathrm{e}^{-\beta H_1(U,\mu,h,V_{2\uparrow},V_{2\downarrow})}\,\tau^x_\uparrow\,\mathbb{P}\Big)\\ &= \mathrm{Tr}\Big(\tau^x_\uparrow\tau^x_\downarrow \mathrm{e}^{-\beta H_1(U,\mu,h,V_{2\uparrow},V_{2\downarrow})}\,\tau^x_\downarrow\tau^x_\uparrow\,\mathbb{P}\Big). \end{aligned} \tag{6.18}$$

Since

$$1 = \mathbb{P} + \tau^x_\uparrow\mathbb{P}\,\tau^x_\uparrow + \tau^x_\downarrow\mathbb{P}\,\tau^x_\downarrow + \tau^x_\uparrow\tau^x_\downarrow\mathbb{P}\,\tau^x_\downarrow\tau^x_\uparrow\,, \tag{6.19}$$

it readily follows that

$$Z(U,\mu,h,V_{2\uparrow},V_{2\downarrow}) = \frac{1}{4}\,\mathrm{Tr}\Big(\mathrm{e}^{-\beta H_2(U,\mu,h,V_{2\uparrow},V_{2\downarrow})}\Big) = \frac{Z_2(U,\mu,h,V_{2\uparrow},V_{2\downarrow})}{4}\,. \tag{6.20}$$

Eq. (6.20) is our main result. It states that the partition function of the original impurity model (6.1) can be calculated *without any constraint* through the partition function of the model (6.16) that describes two resonant levels, one for each spin species, each coupled to an Ising variable, with the latter two coupled antiferromagnetically to each other by the U-term. The equivalence (6.20) allows us to compute the thermodynamic expectation values of the SIAM in the slave-spin representation without any constraint (we refer to Appendix C.1 for more details).

Similarly, it can also be shown that the average value of observables O, that commutes with C_σ, can be obtained in the the slave-spin representation without any constraint:

$$\langle O\rangle = \left\langle O^{SS}\right\rangle_2 \tag{6.21}$$

where the operator O^{SS} is now constructed out of operators $\{f_\sigma, \psi_{a\mathbf{k}\sigma}, \boldsymbol{\tau}_\sigma\}$ that act on the enlarged Hilbert space, and $\langle\cdots\rangle_2$ denotes the thermal average with the Boltzmann distribution of H_2 in Eq. (6.16):

$$\langle\cdots\rangle_2 = \mathrm{Tr}\left[\exp\left(-\beta H_2(U,\mu,h,V_{2\uparrow},V_{2\downarrow})\right)\cdots\right]/\mathrm{Tr}\left[\exp\left(-\beta H_2(U,\mu,h,V_{2\uparrow},V_{2\downarrow})\right)\right], \tag{6.22}$$

where the trace is extended to the enlarged Hilbert space $\mathscr{H}_*$. The proof of Eq. (6.21) is left to Section C.2 of the Appendix C.

Interestingly, also the physical single-particle Green's functions in the imaginary time τ of the impurity can be computed through the Green's functions of the composite operators $\tau^-_\sigma f_\sigma$ and $f^\dagger_\sigma\tau^+_\sigma$ in the slave-spin representation without constraints. In particular (details can be found in Appendix C Section C.3)

$$\begin{aligned} G_\sigma(\tau) &= -\left\langle T_\tau\left(d_\sigma(\tau)d^\dagger_\sigma(0)\right)\right\rangle\\ &= -2\left\langle T_\tau\left(\tau^-_\sigma(\tau)f_\sigma(\tau)f^\dagger_\sigma(0)\tau^+_\sigma(0)\right)\right\rangle_2, \end{aligned} \tag{6.23}$$

where $\tau^{\pm}_{\sigma} = \tau^{x}_{\sigma} \pm i\tau^{y}_{\sigma}$, the average $\langle \cdots \rangle_2$ is defined in Eq. (6.22) and time evolved operators reads:

$$\begin{aligned} f_{\sigma}(\tau) &= \mathrm{e}^{\tau H_2} f_{\sigma} \mathrm{e}^{-\tau H_2}, \\ \tau^{\pm}_{\sigma}(\tau) &= \mathrm{e}^{\tau H_2} \tau^{\pm}_{\sigma} \mathrm{e}^{-\tau H_2}, \end{aligned} \tag{6.24}$$

where $H_2 = H_2(U, \mu, h, V_{2\uparrow}, V_{2\downarrow})$. This result is not only useful by its own but also because it allows implementing DMFT [95, 121] in the slave-spin representation of Hubbard-like models in lattices with infinite coordination, which in some cases could be more convenient than working directly in the physical representation.

6.3.1 Charge-orbital decoupling: an equivalent representation

The Hamiltonian (6.16) lacks a clear separation between the charge and spin degrees of freedom which is desirable when the interaction U is large. The latter is coupled to the combination $\tau^{z}_{\uparrow}\tau^{z}_{\downarrow}$, which is therefore the actual operator that controls the large-U freezing of valence fluctuations. Since $\tau^{z}_{\uparrow}\tau^{z}_{\downarrow}$ is still an Ising variable, with value ± 1, we can exploit a convenient change of variables. Following Ref. [83] we define

$$\tau^{z}_{\uparrow}\tau^{z}_{\downarrow} = -\sigma^{z}, \tag{6.25}$$

and thus, consistently,

$$\begin{aligned} \tau^{z}_{\uparrow} &= \tau^{z}, & \tau^{z}_{\downarrow} &= -\tau^{z}\sigma^{z}, \\ \tau^{x}_{\uparrow} &= \tau^{x}\sigma^{x}, & \tau^{x}_{\downarrow} &= \sigma^{x}, \\ \tau^{y}_{\uparrow} &= \tau^{y}\sigma^{x}, & \tau^{y}_{\downarrow} &= -\tau^{z}\sigma^{y}. \end{aligned} \tag{6.26}$$

After this transformation Hamiltonian (6.16) changes into

$$\begin{aligned} H_2(U, \mu, h, V_{2\uparrow}, V_{2\downarrow}) = \sum_{\sigma} \sum_{\mathbf{k}}^{\epsilon_{\mathbf{k}\sigma}<0} \Bigg[& \epsilon_{\mathbf{k}\sigma}\left(\psi^{\dagger}_{1\mathbf{k}\sigma}\psi_{2\mathbf{k}\sigma} + H.c.\right) \\ & + \sigma^{x}(\tau^{x}\delta_{\sigma\uparrow} + \delta_{\sigma\downarrow}) \frac{V_{1\mathbf{k}\sigma}}{\sqrt{V}}\left(f^{\dagger}_{\sigma}\psi_{1\mathbf{k}\sigma} + H.c.\right) \\ & + i\,(\tau^{y}\sigma^{x}\delta_{\sigma\uparrow} - \tau^{z}\sigma^{y}\delta_{\sigma\downarrow}) \frac{V_{2\mathbf{k}\sigma}}{\sqrt{V}}\left(f^{\dagger}_{\sigma}\psi_{2\mathbf{k}\sigma} - H.c.\right)\Bigg] \\ & - \frac{U}{4}\sigma^{z} - \left[\frac{\mu}{4}(1-\sigma^{z}) + \frac{h}{4}(1+\sigma^{z})\right]\tau^{z}, \end{aligned} \tag{6.27}$$

where $\delta_{\sigma\sigma'}$ is the Kronecker delta.

The previous Hamiltonian notably simplifies when the nonsymmetric component of the tunnel-coupling amplitude is vanishing, $V_{2\mathbf{k}\sigma} = 0$. By following the same steps of Section 6.3 but in the reverse order we can reduce the number of Ising variables to one. To this aim we absorb the τ^{x} Ising variable inside the pseudofermion operator $f_{\uparrow}$ and, so, we reduce the dimension of the enlarged Hilbert space by a factor of two. Therefore, the slave-spin model involves a single auxiliary Ising variable and by using the operatorial identity $\tau^{z} = 2n_{\uparrow} - 1$ we obtain:

$$\begin{aligned} H_1(U, \mu, h) = \sum_{\sigma} \sum_{\mathbf{k}}^{\epsilon_{\mathbf{k}\sigma}<0} & \left[\epsilon_{\mathbf{k}\sigma}\left(\psi^{\dagger}_{1\mathbf{k}\sigma}\psi_{2\mathbf{k}\sigma} + H.c.\right) + \sigma^{x}\frac{V_{1\mathbf{k}\sigma}}{\sqrt{V}}\left(f^{\dagger}_{\sigma}\psi_{1\mathbf{k}\sigma} + H.c.\right)\right] \\ & - \frac{U}{4}\sigma^{z} - \left[\frac{\mu}{4}(1-\sigma^{z}) + \frac{h}{4}(1+\sigma^{z})\right](2n_{\uparrow} - 1), \end{aligned} \tag{6.28}$$

with the projector on the physical subspace:

$$\mathbb{P} = \frac{1 - \sigma^z \, (2n_\uparrow - 1) \, (2n_\downarrow - 1)}{2}. \tag{6.29}$$

Following the same line of reasoning of Section 6.3, it is possible to prove that the partition function of the SIAM in Eq. (6.1) with $V_{2\mathbf{k}\sigma} = 0$ can be computed *without any constraint* through the partition function of the model (6.28):

$$Z(U, \mu, h, 0, 0) = \frac{1}{2} \mathrm{Tr}\left(e^{-\beta H_1(U,\mu,h)}\right). \tag{6.30}$$

The latter identity (6.30), where the Hamiltonian H_1 is defined in Eq. (6.28), generalizes the result obtained in Ref. [248] to the case of a spin-dependent chemical potential shift applied on the impurity site and a p-h symmetric tunnel-coupling amplitude $V_{\mathbf{k}\sigma}$, i.e. $V_{\mathbf{k}\sigma}(\epsilon_\mathbf{k}) = V_{\mathbf{k}\sigma}(-\epsilon_\mathbf{k})$ or $V_{2\mathbf{k}\sigma} = 0$.

6.3.2 Extension to multi-orbital impurity models

The mapping in Section 6.3 can be straightforwardly extended to a multi-orbital impurity model with Hamiltonian

$$\begin{aligned} H = H_{\mathrm{imp}} + \sum_\sigma \sum_{\alpha=1}^{M} \sum_{\mathbf{k}}^{\epsilon_{\mathbf{k}\alpha\sigma}<0} \Big[& \epsilon_{\mathbf{k}\alpha\sigma} \left(\psi^\dagger_{1\mathbf{k}\alpha\sigma} \psi_{2\mathbf{k}\alpha\sigma} + H.c.\right) \\ & + V_{1\mathbf{k}\alpha\sigma}\left(d^\dagger_{\alpha\sigma} \psi_{1\mathbf{k}\alpha\sigma} + H.c.\right) \\ & + V_{2\mathbf{k}\alpha\sigma}\left(d^\dagger_{\alpha\sigma} \psi_{2\mathbf{k}\alpha\sigma} + H.c.\right) \Big], \end{aligned} \tag{6.31}$$

in the simple case where the isolated impurity Hamiltonian H_{imp} contains only the occupation numbers $n_{\alpha\sigma} = d^\dagger_{\alpha\sigma} d_{\alpha\sigma}$, where $\alpha = 1, \ldots, M$ is the orbital index, i.e., $H_{\mathrm{imp}} = H_{\mathrm{imp}}\left(\{n_{\alpha\sigma}\}\right)$, does not include Coulomb exchange terms. Moreover, we assume that the tunnel-coupling amplitude between the bath and the impurity is diagonal in the spin and the orbital indices. Analogously to Section 6.3 we define a generalized p-h transformation that involves the spin as well as the orbital degree of freedom:

$$C_{\alpha\sigma} : \left\{ d_{\alpha\sigma} \to d^\dagger_{\alpha\sigma} \bigcup \prod_{\mathbf{k}} \left(\psi_{1\mathbf{k}\alpha\sigma} \to -\psi^\dagger_{1\mathbf{k}\alpha\sigma} \bigcup \psi_{2\mathbf{k}\alpha\sigma} \to \psi^\dagger_{2\mathbf{k}\alpha\sigma}\right) \right\}. \tag{6.32}$$

Under this circumstance we can extend the slave-spin mapping to the multi-orbital by introducing an Ising variable $\boldsymbol{\tau}_{\alpha\sigma}$ for any spinful orbital on the impurity site and defining:

$$d_{\alpha\sigma} = \tau^x_{\alpha\sigma} f_{\alpha\sigma}, \tag{6.33}$$

where the equality holds in the physical subspace of the enlarged Hilbert, that is selected by the projector:

$$\mathbb{P}_{\alpha\sigma} = \frac{1 + \tau^z_{\alpha\sigma}(2n_{\alpha\sigma} - 1)}{2}. \tag{6.34}$$

We notice that the enlarged Hilbert space $\mathscr{H}_*$ is 2^{2M} larger than the original one. Therefore, we can exploit the p-h transformations in Eq. (6.32) for each orbital species and follow exactly the

same reasoning as in Section 6.3 to show that the partition function Z of the Hamiltonian (6.31) can be calculated as

$$Z = \left(\frac{1}{2}\right)^{2M} \mathrm{Tr}\left(\mathrm{e}^{-\beta H_{2M}}\right), \tag{6.35}$$

where the trace Tr extends over the enlarged Hilbert space and

$$\begin{aligned} H_{2M} = \sum_{\sigma} \sum_{\alpha=1}^{M} \sum_{\mathbf{k}}^{\epsilon_{\mathbf{k}\alpha\sigma}<0} \Big[& \epsilon_{\mathbf{k}\alpha\sigma}\left(\psi^{\dagger}_{1\mathbf{k}\alpha\sigma}\,\psi_{2\mathbf{k}\alpha\sigma} + H.c.\right) \\ & + \tau^{x}_{\alpha\sigma}\, V_{1\mathbf{k}\alpha\sigma}\left(f^{\dagger}_{\alpha\sigma}\,\psi_{1\mathbf{k}\alpha\sigma} + H.c.\right) \\ & + i\tau^{y}_{\alpha\sigma}\, V_{2\mathbf{k}\alpha\sigma}\left(f^{\dagger}_{\alpha\sigma}\,\psi_{2\mathbf{k}\alpha\sigma} - H.c.\right)\Big] \\ & + H_{\mathrm{imp}}\left(\{\tau^{z}_{\alpha\sigma}\}\right). \end{aligned} \tag{6.36}$$

The equivalence between the partition functions (6.35) allows us to compute the thermodynamic average values of a multi-orbital AIM in the slave-spin representation without any constraint. Remarkably, also the physical single-particle Green's functions of the impurity in our slave-spin theory is free from any constraint, and in imaginary time τ reads:

$$\begin{aligned} G_{\alpha\sigma}(\tau) &= -\left\langle T_{\tau}\left(d_{\alpha\sigma}(\tau)\, d^{\dagger}_{\alpha\sigma}(0)\right)\right\rangle \\ &= -2\left\langle T_{\tau}\left(\tau^{-}_{\alpha\sigma}(\tau)\, f_{\alpha\sigma}(\tau)\, f^{\dagger}_{\alpha\sigma}(0)\, \tau^{+}_{\alpha\sigma}(0)\right)\right\rangle_{2M}, \end{aligned} \tag{6.37}$$

where

$$\langle \cdots \rangle_{2M} = \frac{\mathrm{Tr}\left(e^{-\beta H_{2M}} \cdots\right)}{\mathrm{Tr}\left(e^{-\beta H_{2M}}\right)} \tag{6.38}$$

is the average over the enlarged Hilbert space.

6.4 A relevant application: mean-field solution of the SIAM

In order to appreciate the importance of a mapping without constraints, we perform the mean field-calculation of the impurity magnetic susceptibility χ_{imp} and charge compressibility κ_{imp} of a simple spin-$SU(2)$ invariant and p-h symmetric Anderson impurity model. The Hamiltonian is therefore the one from Eq. (6.4) at finite $h \gtrsim 0$ and $\mu \gtrsim 0$, with $V_{2\mathbf{k}\sigma} = 0$ and spin-independent $\epsilon_{\mathbf{k}\sigma} = \epsilon_{\mathbf{k}}$ and $V_{1\mathbf{k}\sigma} = V_{\mathbf{k}}$.
The mean-field approach to the conventional slave-boson representation of such Hamiltonian erroneously yields at large-U a negative $\chi_{\mathrm{imp}} < 0$, discussed in Section 3.3 (detailed calculations can be found in Section C.4 of the Appendix C), signalizing an instability of the paramagnetic solution towards spontaneous spin polarization [252]. This is the tangible evidence that imposing the constraint *on average* may lead to unphysical results.

Let us consider instead our mapping onto the equivalent Hamiltonians (6.27) and (6.28), which do not require any constraint to be imposed. The mean-field approach consists in approximating the ground-state wave function with a factorized one, a product of a fermionic $|\Psi_*\rangle$ part times an Ising one $|\chi\rangle$. We underline that this approximation is physically sound as long as the two subsystems are controlled by well-separated energy scales, otherwise we have no guarantee that the fluctuations beyond the mean-field are negligible. This is indeed realized in the model (6.27) when U is large. On the contrary, a sharp distinction is absent in the equivalent representation (6.16), where, after the mean-field decoupling, the Ising sector $(\boldsymbol{\tau}, \boldsymbol{\sigma}) = (\boldsymbol{\tau}_{\uparrow}, \boldsymbol{\tau}_{\downarrow})$ always contains

excitation energies within the resonant spectral width. Therefore, even though Eq. (6.16) is equivalent to Eq. (6.27), the mean-field approximation is, strictly speaking, only justified in the latter model and when U is large, which we shall consider hereafter.

Within mean-field applied to (6.28) the Ising degree of freedom is controlled by the Hamiltonian

$$H_*^\sigma = -\frac{U}{4}\sigma^z + \langle T\rangle_*\,\sigma^x - \frac{h-\mu}{2}\left\langle n_\uparrow - \frac{1}{2}\right\rangle_* \sigma^z, \tag{6.39}$$

where

$$\begin{aligned}\langle T\rangle_* &\equiv \langle\Psi_*|T|\Psi_*\rangle = \frac{1}{\sqrt{V}}\sum_{\mathbf{k}}\sum_{\sigma} V_k\left(\langle\Psi_*|f_\sigma^\dagger\psi_{\mathbf{k}\sigma}|\Psi_*\rangle + \text{c.c.}\right),\\ \langle n_\uparrow\rangle_* &\equiv \langle\Psi_*|n_\uparrow|\Psi_*\rangle = \langle\Psi_*|f_\uparrow^\dagger f_\uparrow|\Psi_*\rangle\end{aligned} \tag{6.40}$$

are expectation values in the variational fermionic wave function $|\Psi_*\rangle$. The ground state of the effective Ising model (6.39) is identified by

$$\begin{aligned}\langle\sigma^x\rangle_\chi &\equiv \sin\theta = \frac{\mathcal{B}_x/\mathcal{B}_z}{\sqrt{1+(\mathcal{B}_x/\mathcal{B}_z)^2}},\\ \langle\sigma^z\rangle_\chi &\equiv \cos\theta = \frac{1}{\sqrt{1+(\mathcal{B}_x/\mathcal{B}_z)^2}},\end{aligned} \tag{6.41}$$

where $\langle\cdots\rangle_\chi \equiv \langle\chi|\cdots|\chi\rangle$, and for convenience we have introduced the self-consistent field:

$$\boldsymbol{\mathcal{B}} = \left(-\langle T\rangle_*, 0, \frac{U}{4} + \frac{h-\mu}{2}\left\langle n_\uparrow - \frac{1}{2}\right\rangle_*\right). \tag{6.42}$$

The fermionic problem is thus reduced such to find the ground state of the Hamiltonian

$$H_*^f = \sum_{\mathbf{k}\sigma}\epsilon_{\mathbf{k}\sigma}\psi_{\mathbf{k}\sigma}^\dagger\psi_{\mathbf{k}\sigma} + \frac{1}{\sqrt{V}}\sum_{\mathbf{k}\sigma}\sin\theta V_{\mathbf{k}\sigma}\left(f_\sigma^\dagger\psi_{\mathbf{k}\sigma} + \psi_{\mathbf{k}\sigma}^\dagger f_\sigma\right) - \sum_\sigma\frac{\lambda_\sigma}{2}n_\sigma, \tag{6.43}$$

where

$$\lambda_\uparrow = h(1+\cos\theta) + \mu(1-\cos\theta), \quad \lambda_\downarrow = 0. \tag{6.44}$$

By performing straightforward calculations, that are summarized in the Section C.5 of Appendix C, the expectation values in Eq. (6.40) become

$$\langle T\rangle_* = 2\sum_\sigma\int d\omega\left(\omega + \frac{\lambda_\sigma}{2}\right)f(\omega)A_{f\sigma}(\omega)/\sin\theta, \tag{6.45}$$

$$\langle n_\uparrow\rangle_* = \int d\omega f(\omega)A_{f\uparrow}(\omega), \tag{6.46}$$

where $f(\omega) = 1/(e^\beta\omega + 1)$ and the f_σ pseudofermion spectral function reads:

$$A_\sigma^f(\omega) = \frac{1}{\pi}\frac{-\text{Im}\Sigma_{f\sigma}^R(\omega)}{\left[\omega + \lambda_\sigma/2 - \text{Re}\Sigma_{f\sigma}^R(\omega)\right]^2 + \text{Im}\Sigma_{f\sigma}^R(\omega)^2}. \tag{6.47}$$

In the latter expression the f_σ pseudofermion self-energy is given by:

$$\Sigma_{f\sigma}^R(\omega) = \sin^2\theta\int\frac{d\epsilon}{\pi}\frac{\Gamma(\epsilon)}{\omega - \epsilon + i0^+}. \tag{6.48}$$

Given the spectral properties of the bath, i.e. $\Gamma(\epsilon)$, Eqs. (6.45) and (6.46) provide the self-consistent fermionic field $\boldsymbol{\mathcal{B}}$, which depends on the ground state variational parameter θ. Therefore, we close the set of mean-field Eqs. and the ground state is obtained by solving

$$\sin\theta = \frac{\mathcal{B}_x(\theta)/\mathcal{B}_z(\theta)}{\sqrt{1+\left(\mathcal{B}_x(\theta)/\mathcal{B}_z(\theta)\right)^2}}, \tag{6.49}$$

which corresponds to a root-finding problem $g(\theta) = 0$ in a single angular variable.

Assuming that the half bandwidth W is much larger than the other energy scales (this limit is discussed in detail in Section C.4 of the Appendix C), the hybridization function $\Delta^R(\omega)$ with the bath can be approximated as

$$\Delta^R(\omega) \simeq -i\Gamma\theta(W-|\omega|).$$

In order to compute the charge and magnetic susceptibilities of the impurity we consider separately the effect of applying a chemical potential shift and a Zeeman term on the impurity site. Under these circumstances we have:

$$\langle T\rangle_* = -\frac{2\Gamma_*}{\pi\sin\theta}\left[2\log\frac{W}{\Gamma_*} + \log\frac{1}{\sqrt{1+\left[\epsilon\left(1\pm\sqrt{1-\Gamma_*/\Gamma}\right)/2\Gamma_*\right]^2}}\right]$$

and

$$\langle n_\uparrow\rangle_* - \frac{1}{2} = \frac{1}{\pi}\tan^{-1}\frac{\epsilon\left(1\pm\sqrt{1-\Gamma_*/\Gamma}\right)}{2\Gamma_*}$$

where the plus sign applies to $\epsilon = h$, while the minus relates to $\epsilon = \mu$, and $\Gamma_* = \Gamma\sin^2\theta$. It is more convenient to use Γ_* as the variational parameter said so, the saddle-point Eq. (6.49) becomes

$$1 = \frac{2\Gamma}{\pi}\sqrt{1-\frac{\Gamma_*}{\Gamma}}\frac{2\log W/\Gamma_* + \log\left\{1/\sqrt{1+\left[\epsilon\left(1\pm\sqrt{1-\Gamma_*/\Gamma}\right)/2\Gamma_*\right]^2}\right\}}{U/4 \pm \epsilon\arctan\left[\epsilon\left(1\pm\sqrt{1-\Gamma_*/\Gamma}\right)/2\Gamma_*\right]/2\pi}. \tag{6.50}$$

For large U the solution of Eq. (6.50) at $h,\mu \ll \Gamma_*$ reads:

$$\Gamma_*(h) \simeq \Gamma_*(0)\left(1-\frac{h^2}{4\Gamma_*^2(0)}\right), \quad \Gamma_*(\mu) \simeq \Gamma_*(0)\left(1+\frac{\mu^2}{64\Gamma^2}\right) \tag{6.51}$$

where $\Gamma_*(0) \simeq W\exp\left[-\pi U/16\Gamma\right]$ is the same in the slave-boson mean-field theory[3], and can be associated with the Kondo temperature T_K, though overestimated with respect to its actual value [26]. In the regime of small applied fields, the magnetization and the charge on the impurity site are:

$$m = \left\langle(1+\sigma^z)\left(n_\uparrow-\frac{1}{2}\right)\right\rangle_1 = \frac{4}{\pi\Gamma_*(0)}\frac{h}{2} + O\left(h^2\right), \tag{6.52}$$

and

$$q = \left\langle(1-\sigma^z)\left(n_\uparrow-\frac{1}{2}\right)\right\rangle_1 = \frac{\Gamma_*(0)}{4\pi\Gamma^2}\frac{\mu}{2} + O\left(\mu^2\right), \tag{6.53}$$

[3]We refer the interested reader to Section C.4 of the Appendix C for more details.

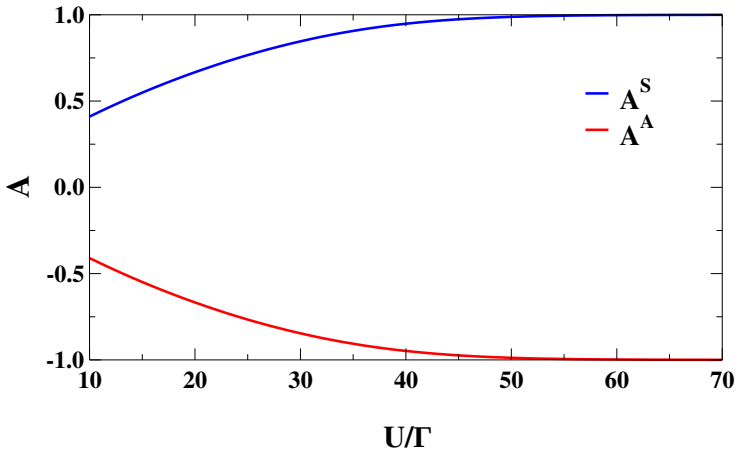

Figure 6.1: Numerical calculation of the symmetric A^S (blue line) and antisymmetric A^A (red line) quasiparticle scattering amplitudes. In the Kondo regime the values of A^S and A^A approach the exact result $A^S = -A^A = 1$. We emphasize that the universal values follow directly from the expression of the impurity charge and spin vertices in the slave-spin representation (6.28).

where the average $\langle \cdots \rangle_1$ is performed over the enlarged Hilbert space obtained by adding a single Ising variable. Therefore, the impurity contribution to the charge and spin susceptibilities becomes:

$$\chi_{\rm imp} = \frac{4}{\pi \Gamma_*(0)}, \tag{6.54}$$

and

$$\kappa_{\rm imp} = \frac{\Gamma_*(0)}{4\pi\Gamma^2} \simeq 0. \tag{6.55}$$

We emphasize that $\chi_{\rm imp}$ in Eq. (6.54) is positive, unlike in slave-boson mean-field theory. The impurity contribution to the specific heat at low temperature only comes from the fermionic degrees of freedom and reads explicitly

$$c_{\rm imp} \simeq \frac{2\pi^2}{3} \frac{T}{\pi \Gamma_*(0)}. \tag{6.56}$$

Hence, our simple calculation predicts a Wilson ratio at large U:

$$R_W = \frac{\chi_{\rm imp}/\chi^0_{\rm imp}}{c_{\rm imp}/c^0_{\rm imp}} = 2, \tag{6.57}$$

in agreement with the exact result in the Kondo regime [273]. We notice that in Eq. (6.57) $\chi^0_{\rm imp}$ and $c^0_{\rm imp}$ are non-interacting impurity quantities. According to Nozières' Fermi liquid description of the Kondo effect [212] (see also Ref. [189]),

$$\chi_{\rm imp} = 2\rho_* \left(1 - A^A\right), \quad \kappa_{\rm imp} = 2\rho_* \left(1 - A^S\right), \tag{6.58}$$

where $\rho_* = 1/\pi\Gamma_*(0) = Z\rho_0$ is the quasiparticle density of states at the chemical potential, as opposed to its bare value $\rho_0 = 1/\pi\Gamma$, with $Z = \sin^2\theta \ll 1$ the quasiparticle residue, while A^S and A^A are the quasiparticle scattering amplitudes in the symmetric (S) and antisymmetric (A) channels, respectively. The mean-field results, derived in Eqs. (6.52)-(6.53), and presented in Fig. 6.1, are thus compatible at large U with $A^S = -A^A = 1$, which, together with Eq. (6.56), are the bases of Nozières' local Fermi liquid theory of the Kondo effect [212]. This phenomenological

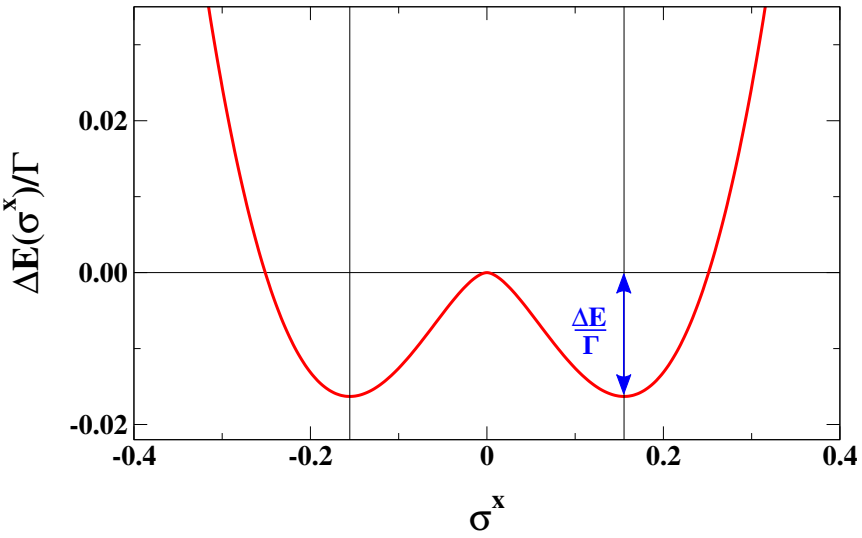

Figure 6.2: Mean-field energy measured with respect to the free magnetic moment (i.e. $\Gamma = 0$) as a function of $\langle\sigma^x\rangle$ for $U/W = 0.1$ and $\Gamma/W = 2.0 \times 10^{-3}$. The state at $\langle\sigma^x\rangle = 0$ corresponds to the local magnetic moment on the impurity site decoupled from the conduction electrons. The system gains energy by developing a finite $\langle\sigma^x\rangle$ that corresponds to a non magnetic state where the impurity spin is coupled in a singlet configuration with the conduction electron spin. We notice that the energy reveals two degenerate minima symmetric under the Z_2 parity transformation $\langle\sigma^x\rangle \to -\langle\sigma^x\rangle$. At zero temperature the ground state breaks spontaneously the Z_2 symmetry by choosing one of the two minima.

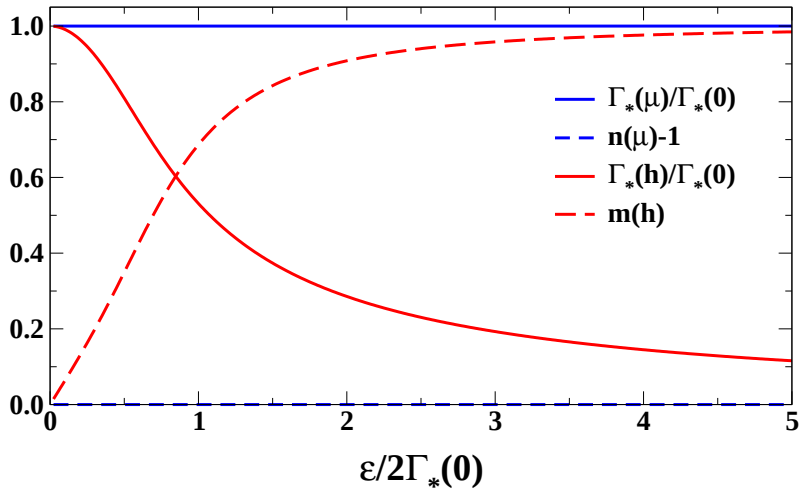

Figure 6.3: In red solid and dashed lines we plot the mean-field values of the effective hybridization width $\Gamma_*(h)/\Gamma_*(0)$ and magnetization $m(h)$ as a function of the applied magnetic field $\epsilon = h$. Whereas, in blue solid and dashed lines we plot the mean-field values of $\Gamma_*(\mu)/\Gamma_*(0)$ and $n(\mu) - 1$ as a function of a chemical potential shift. We notice that the response to an external chemical potential is strongly suppressed due to the missing $1/U$ corrections to the charge susceptibility. The parameters used are $U/W = 0.1$ and $\Gamma/W = 1.96 \times 10^{-3}$, which corresponds to $\Gamma_*(0)/W \simeq 4.01 \times 10^{-5}$.

theory has been successfully exploited in many contexts, not least to derive universal properties in transport across quantum dots [86, 100, 142, 193, 257]. We emphasize that the universal values in Eq. (6.58) simply follow from the expressions of the impurity charge and spin density vertices, the former proportional to $(1 - \sigma^z)$ and the latter to $(1 + \sigma^z)$, and the fact that, in the Kondo regime, σ^z is found to be $\sigma^z \simeq 1$ with negligible fluctuations. As a result, the mean-field solution, $\sigma^z \to \langle \sigma^z \rangle$, not only predicts the suppression of the charge compressibility and the enhancement of the magnetic one, but also captures the leading vertex corrections, remarkably. By contrast, the mean-field approximation does not allow one to recover the nonuniversal corrections to the Kondo regime, which are polynomials in $1/U$ for large U [118, 250]. These corrections are subleading in the spin susceptibility, but leading in the charge one (see Eq. (6.53)).

We conclude by mentioning that the model 6.28 can still be viewed as a dissipative two-level system [46] in a subohmic bath, as it was the case at $\epsilon = 0$ [26]. Each potential well corresponds to a value of $\sigma^x = \pm 1$, while σ^z induces quantum tunneling between the two wells. Localization inside one of the two minima, displayed in Fig. 6.2, is signalized by a finite expectation value of σ^x, and it also corresponds to spontaneous breakdown of the local Z_2 gauge symmetry $\sigma^x \to -\sigma^x$ and $f_\sigma \to -f_\sigma$. The Kondo temperature $T_K \sim \langle \sigma^x \rangle^2$ thus plays the role of a *bona fide* order parameter.

In this language, the field ϵ translates into an assisted tunneling that hampers localization but, at least within mean-field, cannot rule it out, as shown in Fig. 6.3 where we plot in red and blue the response of the system to an applied magnetic field and a chemical potential shift, respectively. We believe that the persistence of Z_2 gauge-symmetry breaking even in the presence of the assisted tunneling is a real feature of the model and not just an artifact of the method.

6.4.1 Self-consistent evaluation of the physical fermionic propagator

In this Section we show that within a simple conserving mean-field approximation we find an impurity spectral function that displays both the expected low-energy Kondo resonance and the high-energy valence fluctuations peaks. In order to provide a consistent description of the high-frequency feature one has to include RPA corrections in the Ising variable propagator.

For simplicity we present the self-consistent calculation of the physical fermions Green's function for the Hamiltonian (6.28) at $\mu = h = 0$. In this case we have:

$$G_\sigma(\tau) = -\left\langle T_\tau \left(d_\sigma(\tau) d_\sigma^\dagger(0) \right) \right\rangle = -\left\langle T_\tau \left(\sigma^x(\tau) f_\sigma(\tau) f_\sigma^\dagger(0) \sigma^x(0) \right) \right\rangle_1 \tag{6.59}$$

where $\langle \cdots \rangle_1$ is the average over the extended Hilbert space obtained by introducing a single Ising variable. The generalization to the generic case (6.16) is straightforward and can be found in Section 6.5.

The mean-field self-consistent calculation of the electron Green's function is based on representing the $\boldsymbol{\sigma}$-matrices by bilinear combinations of Fermi operators [1]:

$$\phi_\alpha^\dagger \, \sigma^i_{\alpha\beta} \, \phi_\beta = \hat{\sigma}^i, \tag{6.60}$$

where the upper index $i = 1, 2, 3$ denotes the Pauli matrices and the lower ones are $\alpha, \beta = \pm$. The fermion substitution Eq. (6.60) introduces two additional configurations $|0, 0\rangle$ and $|1, 1\rangle$ to the two dimensional Hilbert space of the $\boldsymbol{\sigma}$-matrices, which is composed by $|1, 0\rangle$ and $|0, 1\rangle$. The physical states satisfy the condition:

$$N = \phi_+^\dagger \phi_+ + \phi_-^\dagger \phi_- = 1. \tag{6.61}$$

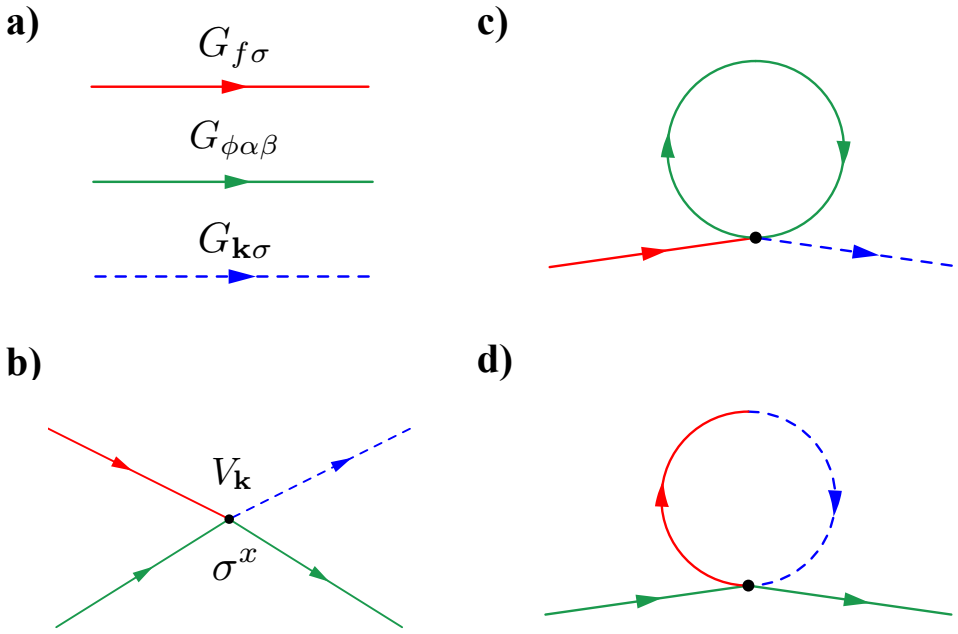

Figure 6.4: a) Bare Green's functions. **b)** Bare interaction. Hartree-Fock self-energy diagrams corresponding to the slave-spin mean-field approximation: **c)** elastic scattering between f_σ and $\psi_{\mathbf{k}\sigma}$ fermions renormalized by $\langle \phi^\dagger_\alpha \sigma^x_{\alpha\beta} \phi_\beta \rangle_\chi$, **d)** ϕ fermion self-energy determined by valence fluctuations induced by the hybridization operator T.

Remarkably, previous constraint can be implement exactly [147, 224] by introducing an imaginary chemical potential in the fermionic representation of the spin Hamiltonian:

$$H_\sigma \to H_f + i\pi N/2\beta$$

which results in a rigid shift of the fermionic Matsubara frequencies $i\epsilon_n = i\pi T(2n+1) \to i\pi T(2n+1/2)$. However, in the following we perform a zero temperature calculations, where the constraint (6.61) is automatically satisfied. Indeed, the unphysical configurations are excluded since physical quantities involve only averages of products of $\hat{\sigma}^i$, which have the property of giving zero when acting on the nonphysical states $|0,0\rangle$ and $|1,1\rangle$. In this representation, the hybridization term in Eq. (6.28) becomes the four-leg fermionic interaction vertex depicted in Fig. 6.4 **b)**. The Hartree-Fock approximation corresponds to the mean-field decoupling presented in Section 6.4 and is described by the self-energy diagrams in Figs. 6.4 **c)** and **d)**:

$$\begin{aligned} \Sigma_\phi &= \sigma^x \langle T \rangle_* , \\ \Sigma_{f\mathbf{k}} &= V_{\mathbf{k}} \left\langle \phi^\dagger_\alpha \sigma^x_{\alpha\beta} \phi_\beta \right\rangle_\chi , \end{aligned} \tag{6.62}$$

where the averages $\langle \cdots \rangle_*$ and $\langle \cdots \rangle_\chi$ are defined in Eqs. (6.40) and (6.41). Consistently with the Hartee-Fock approximation the physical fermion spectral function reads:

$$A_{d\sigma}(\omega) = \left\langle \phi^\dagger_\alpha \sigma^x_{\alpha\beta} \phi_\beta \right\rangle^2_\chi A_{f\sigma}(\omega) + \frac{1}{\pi} \int d\epsilon A_{f\sigma}(\omega - \epsilon) \mathrm{Im}\, \mathbf{\Pi}^R_{xx}(\epsilon) \left[f(\omega - \epsilon) + n(-\epsilon) \right] \tag{6.63}$$

where $f(\epsilon) = 1/(e^{\beta\epsilon}+1)$ and $n(\epsilon) = 1/(e^{\beta\epsilon}-1)$. We have extracted the condensate contribution from the two-particle correlation function:

$$\mathbf{\Pi}^R_{xx}(t-t') = -i\theta(t-t') \left\langle \left[\vec{\phi}^\dagger(t) \cdot \sigma^x \cdot \vec{\phi}(t), \vec{\phi}^\dagger(t') \cdot \sigma^x \cdot \vec{\phi}(t') \right] \right\rangle_1 \tag{6.64}$$

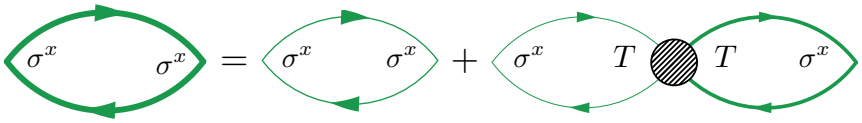

Figure 6.5: Random phase approximation (RPA) for the Π_{xx} two-particle correlation function.

where $\vec{\phi}^\dagger = \begin{pmatrix} \phi_+^\dagger & \phi_-^\dagger \end{pmatrix}$.

In a consistent scheme Hartree-Fock solution the evaluation of Π_{xx} includes quantum fluctuations obtained using the irreducible vertex, the latter is determined by the functional derivative of the self-energy. In our specific example, the bosonic operator $\hat{\sigma}^x$, i.e. the valence fluctuations, are directly coupled to the hybridization amplitude T, which implies the random phase resummation (RPA) displayed in Fig. 6.5:

$$\mathbf{\Pi}^R_{xx}(\omega) = \frac{\Pi^R_{xx}(\omega)}{1 - \Pi^R_{xx}(\omega)\chi^R_{TT}(\omega)}, \tag{6.65}$$

where Π_{xx} is the bare propagator:

$$\begin{aligned} \Pi^R_{xx}(\omega) &= -i \int \frac{d\epsilon}{2\pi} \mathrm{Tr}\left[\sigma^x G^R_\phi\left(\epsilon + \frac{\omega}{2}\right)\sigma^x G^A_\phi\left(\epsilon - \frac{\omega}{2}\right)\right] \\ &= \cos^2\theta\left(\frac{1}{\omega - \omega_0 + i0^+} - \frac{1}{\omega + \omega_0 + i0^+}\right), \end{aligned} \tag{6.66}$$

with ω_0 energy of the spin excitations $\omega_0 = U/2\cos\theta$, while

$$\chi^R_{TT}(t - t') = -i\theta(t - t')\left\langle [T(t), T(t')] \right\rangle_1 . \tag{6.67}$$

Performing the straightforward calculations we obtain:

$$\begin{aligned} \chi^R_{TT}(\omega) =& \frac{3U}{4\cos\theta} + \frac{4}{\sin^2\theta}\sum_\sigma \int dx f(x) A_{f\sigma}(x)\Bigg[\left(x + \frac{\omega}{2}\right)^2 G^R_{f\sigma}(x + \omega) \\ &+ \left(x - \frac{\omega}{2}\right)^2 G^A_{f\sigma}(x - \omega)\Bigg]. \end{aligned} \tag{6.68}$$

The d_σ electron spectral function in Eq. (6.63) is shown in the color map displayed in the top panel of Fig. 6.6, where we plot the evolution of the spectral features as a function of U/Γ. As the value of the interaction increases we observe a transfer of the spectral weight from the low-energy Kondo resonance, that becomes narrower, to the high-energy valence fluctuations peaks. It is interesting to notice that in the absence of the RPA corrections the width of high-energy features is Γ_*, i.e. the same as the low-energy quasiparticle peak. This unphysical result, that is a consequence of neglecting the RPA corrections, implies the narrowing of the high-energy spectral features in the large-U regime. To highlight the difference let us present in the bottom panel of Fig. 6.6 the spectral function obtained neglecting (red line) and including (black line) RPA corrections. We clearly see that the RPA allows us to reconstruct incoherent sidebands characterized by a width of the order of the bare hybridization Γ, centered around $\pm U/2$ and identified by the spectral weight $1 - \langle\sigma^x\rangle^2_\chi$. In this respect, a possible direction, worth exploring, is the analysis of the feedback of the RPA corrections on the self-consistent Eq. (6.50).

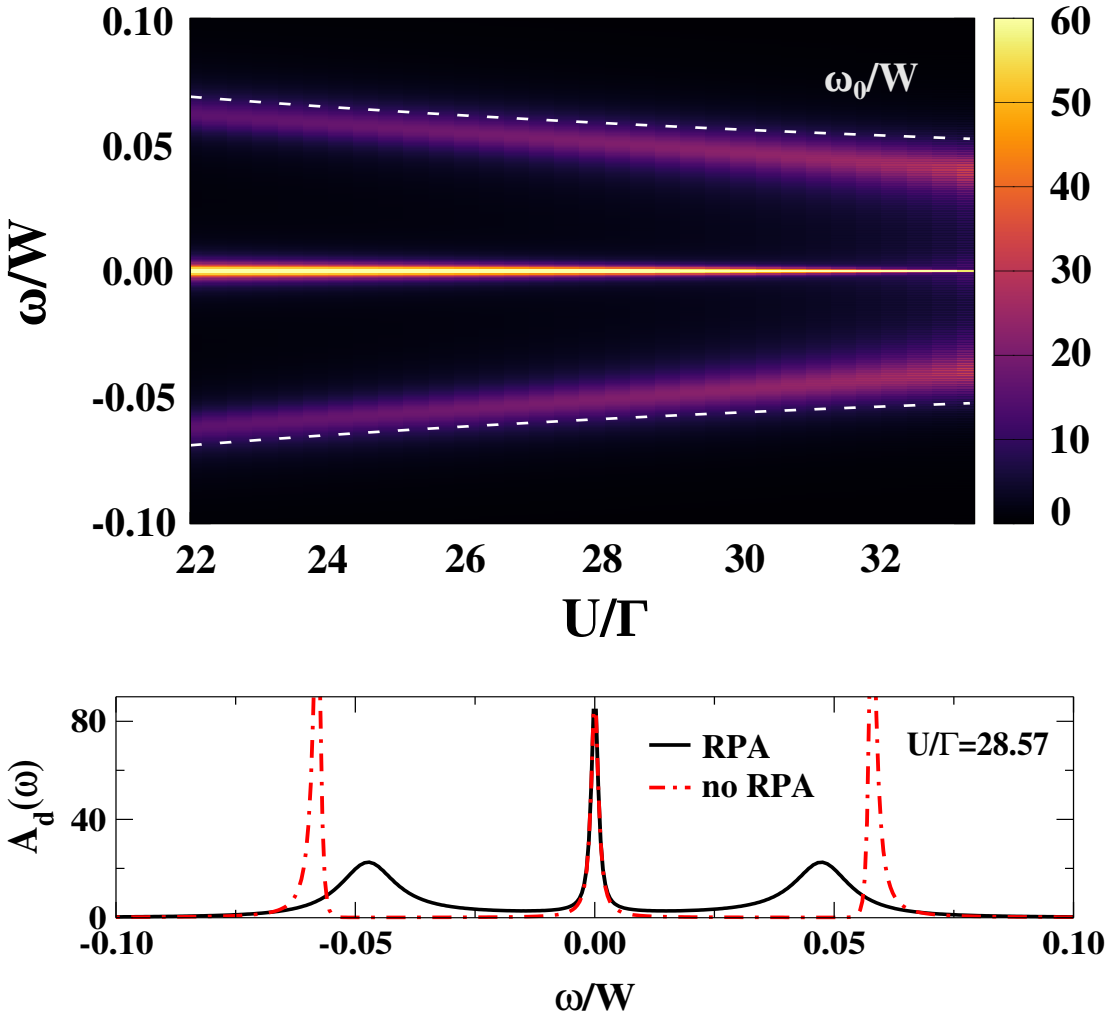

Figure 6.6: Top panel: evolution of the physical electron spectral function $A_d(\omega)$ as a function of U/Γ for $U/W = 0.1$ and different values of Γ/W obtained by performing the self-consistent mean-field calculation, see Eqs. (6.63) and (6.65). White dashed line corresponds to the charge fluctuations energy $\omega_0 = U/\cos\theta$. Bottom panel: $A_d(\omega)$ as a function of ω/W for $U/W = 0.1$ and $\Gamma/W = 3.5 \times 10^{-3}$, which corresponds to $\Gamma_*/W \simeq 8.8 \times 10^{-4}$. Black solid line is obtained including the RPA corrections, while the red dashed line is obtained plugging the bare propagator from Eq. (6.66) into Eq. (6.63).

6.5 Slave-spin as approximate impurity solver for DMFT

In this Section we present the self-consistent slave-spin theory applied as an approximate solver for DMFT calculations. Even though we will consider only the case of a single-band Hubbard model away from half-filling, the following results are easily generalizable to the case of a multi-band Hubbard model in the absence of Coulomb exchange interaction.

In DMFT we define the Weiss field as the bare Green's function of (6.1):

$$\mathcal{G}_\sigma^{-1}(z) = z - \Delta_\sigma(z),$$

where

$$\Delta_\sigma(z) = \int \frac{d\epsilon}{\pi} \frac{\Gamma(\epsilon)}{z-\epsilon}$$

is the hybridization function of the bath. It is important to remark that the properties of the dynamical bath are encoded in a single quantity, i.e. the hybridization amplitude $\Gamma_\sigma(\epsilon)$. Given a certain bath, $\Gamma_\sigma(\epsilon)$, we compute the single-particle Green's function of the model Hamiltonian (6.16):

$$G_\sigma^{-1}(z) = z - \Delta_\sigma(z) - \Sigma_\sigma(z),$$

with the aim of solving the DMFT self-consistency equation, that in the Bethe lattice reads:

$$\Gamma_\sigma(\omega) = \pi W^2 A_{d\sigma}(\omega)/4 \tag{6.69}$$

where W is the half-bandwidth.

In practice Eq. (6.69) is used in an iterative manner to update the spectral function of the bath degrees of freedom $\Gamma_\sigma^i(\omega) \to \Gamma_\sigma^{i+1}(\omega)$. DMFT self-consistency is reached when the distance between nearest neighbors $\Gamma_\sigma(\epsilon)$ is smaller than a fixed tolerance δ:

$$||\Gamma_\sigma^{i+1} - \Gamma_\sigma^i||_{L^1} = \int |\Gamma_\sigma^{i+1}(\omega) - \Gamma_\sigma^i(\omega)| d\omega < \delta. \tag{6.70}$$

In the following we consider a generic SIAM, which is the relevant case when we consider the single-band Hubbard lacking of any particle-hole symmetry. Given the tunnel-coupling amplitudes $V_{1\mathbf{k}\sigma}$ and $V_{2\mathbf{k}\sigma}$, introduced in Eq. (6.3), that depend on $\mathbf{k}$ only through $\epsilon_\mathbf{k}$, we define:

$$\Gamma_{ab\sigma}(\omega) = \pi\rho(\omega) V_{a\sigma}(\omega) V_{b\sigma}(\omega)/2.$$

Therefore, in terms of the hybridization function $\Gamma_\sigma(\epsilon)$ we have:

$$\Gamma_{11\sigma}(\epsilon) = \frac{\left(\sqrt{\Gamma_\sigma(\epsilon)} + \sqrt{\Gamma_\sigma(-\epsilon)}\right)^2}{4}, \quad \Gamma_{22\sigma}(\epsilon) = \frac{\left(\sqrt{\Gamma_\sigma(\epsilon)} - \sqrt{\Gamma_\sigma(-\epsilon)}\right)^2}{4}, \tag{6.71}$$

and

$$\Gamma_{12\sigma}(\epsilon) = \frac{\Gamma_\sigma(\epsilon) - \Gamma_\sigma(-\epsilon)}{4} = \Gamma_{21\sigma}(\epsilon), \tag{6.72}$$

such that $\Gamma_\sigma(\omega) = \Gamma_{11\sigma}(\epsilon) + \Gamma_{22\sigma}(\epsilon) + \Gamma_{12\sigma}(\epsilon) + \Gamma_{21\sigma}(\epsilon)$. Mean-field decoupling of Eq. (6.16) gives rise to two problems, an effective resonant level model:

$$H_*^f = H_b + \sum_\sigma \langle \tau_\sigma^x \rangle_\chi T_{1\sigma} + \sum_\sigma \langle \tau_\sigma^y \rangle_\chi J_{2\sigma}, \tag{6.73}$$

and a spin model:

$$H_*^\tau = \frac{U}{4}\tau_\uparrow^z \tau_\downarrow^z - \frac{\mu}{4}(\tau_\uparrow^z + \tau_\downarrow^z) - \frac{h}{4}(\tau_\uparrow^z - \tau_\downarrow^z) + \sum_\sigma \tau_\sigma^x \langle T_{1\sigma} \rangle_* + \sum_\sigma \tau_\sigma^y \langle J_{2\sigma} \rangle_*. \tag{6.74}$$

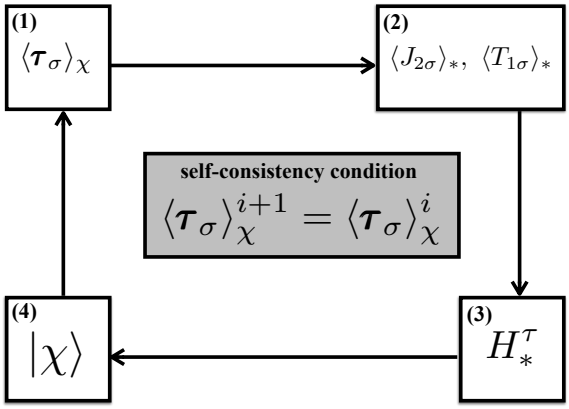

Figure 6.7: Schematic representation of the iterative procedure needed to reach the mean-field saddle-point. Convergence is reached when $\delta V_\sigma^i = 1 - \left|\langle \boldsymbol{\tau}_\sigma \rangle_\chi^{i+1} \cdot \langle \boldsymbol{\tau}_\sigma \rangle_\chi^{i}\right|$ is smaller than a given tolerance.

In Eq. (6.73) we have introduced:

$$T_{1\sigma} = \sum_{\mathbf{k}}^{\epsilon_{\mathbf{k}\sigma}<0} \frac{v_{1\mathbf{k}\sigma}}{\sqrt{V}} (f_\sigma^\dagger \psi_{1\mathbf{k}\sigma} + \text{H.c.})$$

and

$$J_{2\sigma} = i \sum_{\mathbf{k}}^{\epsilon_{\mathbf{k}\sigma}<0} \frac{v_{2\mathbf{k}\sigma}}{\sqrt{V}} (f_\sigma^\dagger \psi_{2\mathbf{k}\sigma} - H.c.),$$

that act on the Ising degrees like the x and y components of a self-consistent field, respectively. To determine the mean-field effect of the fermions on Ising degrees of freedom we have to compute the f pseudofermion Green's function; as usual the Dyson equation is:

$$G_{f\sigma}^{-1}(z) = z - \Sigma_{f\sigma}(z), \tag{6.75}$$

at mean-field level we have:

$$\Sigma_{f\sigma}(z) = \langle \tau_\sigma^x \rangle^2 \Delta_{11\sigma}(z) + \langle \tau_\sigma^y \rangle^2 \Delta_{22\sigma}(z), \tag{6.76}$$

where

$$\Delta_{ab\sigma}(z) = \int \frac{d\omega}{\pi} \frac{\Gamma_{ab\sigma}(\omega)}{z - \omega}. \tag{6.77}$$

For completeness we report the analytic expression of the average values $\langle T_{1\sigma} \rangle_*$ and $\langle J_{2\sigma} \rangle_*$ in Appendix C.6.

The numerical procedure for obtaining the slave-spin mean-field solution is described in Fig. 6.7. Given an initial configuration for the slave-spin degree of freedom $\langle \boldsymbol{\tau}_\sigma \rangle_\chi$ we compute the average quantities $\langle T_{1\sigma} \rangle_*$ and $\langle J_{2\sigma} \rangle_*$, that determine the effective magnetic field acting on the spin degrees of freedom $\boldsymbol{\tau}_\sigma$. Then, we find the ground state $|\chi\rangle$ of the updated spin Hamiltonian H_*^τ that allows us to obtain the expectation values $\langle \boldsymbol{\tau}_\sigma \rangle$. The mean-field solution is reached when the variation of $\delta V_\sigma^i = 1 - \left|\langle \boldsymbol{\tau}_\sigma \rangle_\chi^{i+1} \cdot \langle \boldsymbol{\tau}_\sigma \rangle_\chi^{i}\right|$ is smaller than a given tolerance.

Once the saddle-point solution is obtained, we compute the self-consistent d_σ fermions spectral function:

$$A_{d\sigma}(\epsilon) = 2\langle \chi | \tau_\sigma^- | \chi \rangle \langle \chi | \tau_\sigma^+ | \chi \rangle A_{f\sigma}(\epsilon) + 2 \int \frac{dx}{\pi} A_{f\sigma}(\epsilon - x) \text{Im} \mathbf{\Pi}_{-+,\sigma}^R(x) \left[f(\epsilon - x) + n(-x) \right], \tag{6.78}$$

where:

$$\mathbf{\Pi}^{R}_{-+,\sigma}(t-t') = -i\theta(t-t')\left\langle[\tau^{-}_{\sigma}(t),\tau^{+}_{\sigma}(t')]\right\rangle_{2}. \tag{6.79}$$

Following the same line of reasoning presented in Section 6.4.1, the evaluation of the $\Pi_{-+,\sigma}$ includes RPA corrections due to the low-energy pseudofermions coupled with the charge fluctuations on the impurity site.

The bare propagator of the Ising degrees of freedom can be easily computed as:

$$\Pi_{ab,\sigma}(z) = \sum_{n}^{n\neq 0}\left(\frac{\langle\chi|\tau^{a}_{\sigma}|\phi_n\rangle\langle\phi_n|\tau^{b}_{\sigma}|\chi\rangle}{z-\omega_{n0}} - \frac{\langle\phi_n|\tau^{a}_{\sigma}|\chi\rangle\langle\chi|\tau^{b}_{\sigma}|\phi_n\rangle}{z+\omega_{n0}}\right), \tag{6.80}$$

where $n=0$ refers to the ground state $|\chi\rangle$, while $n>0$ stands fo the excited states of the effective spin model H^{τ}_{*}. In this case the RPA corrections are more involved and take into account the coupling to the hybridization $T_{1\sigma}$ and the current $J_{2\sigma}$ operators. Diagrammatics calculations enable us to derive the equations for the RPA spin correlation functions (dropping the spin index σ and the frequency dependence):

$$\begin{aligned}
&\begin{pmatrix} \Pi^{-1}_{xx}\left(1-\Pi_{xx}\chi_{T_1T_1}-\Pi_{xy}\chi_{J_2T_1}\right) & -\Pi^{-1}_{xx}\Pi_{xy}\chi_{J_2J_2}-\chi_{T_1J_2} \\ -\chi_{T_1T_1}-\Pi^{-1}_{yx}\Pi_{yy}\chi_{J_2T_1} & \Pi^{-1}_{yx}\left(1-\Pi_{yy}\chi_{J_2J_2}-\Pi_{yx}\chi_{T_1J_2}\right)\end{pmatrix}\cdot\begin{pmatrix}\mathbf{\Pi}_{xx}\\ \mathbf{\Pi}_{yx}\end{pmatrix} = \begin{pmatrix}1\\1\end{pmatrix}, \\
&\begin{pmatrix} \Pi^{-1}_{xy}\left(1-\Pi_{xx}\chi_{T_1T_1}-\Pi_{xy}\chi_{J_2T_1}\right) & -\chi_{J_2J_2}-\Pi^{-1}_{xy}\Pi_{xx}\chi_{T_1J_2} \\ -\Pi^{-1}_{yy}\Pi_{yx}\chi_{T_1T_1}-\chi_{J_2T_1} & \Pi^{-1}_{yy}\left(1-\Pi_{yy}\chi_{J_2J_2}-\Pi_{yx}\chi_{T_1J_2}\right)\end{pmatrix}\cdot\begin{pmatrix}\mathbf{\Pi}_{xy}\\ \mathbf{\Pi}_{yy}\end{pmatrix} = \begin{pmatrix}1\\1\end{pmatrix},
\end{aligned} \tag{6.81}$$

where

$$\chi_{T_1T_1}(t) = -i\langle T_t(T_1(t)T_1)\rangle, \quad \chi_{J_2J_2}(t) = -i\langle T_t(J_2(t)J_2)\rangle,$$

and

$$\chi_{T_1J_2}(t) = -i\langle T_t(T_1(t)J_2)\rangle, \quad \chi_{J_2T_1}(t) = -i\langle T_t(J_2(t)T_1)\rangle.$$

Given ω, Eq. (6.81) is algebraic problem:

$$\hat{K}(\omega)\cdot\vec{\mathbf{\Pi}}(\omega) = \vec{1} \implies \vec{\mathbf{\Pi}}(\omega) = \hat{K}^{-1}(\omega)\cdot\vec{1},$$

which can be solved analytically through:

$$\begin{pmatrix} a & b \\ c & d\end{pmatrix} \to \frac{1}{ad-bc}\begin{pmatrix} d & -b \\ -c & a\end{pmatrix}.$$

Finally, the linear combination of the spin correlation functions, obtained by inverting Eq. (6.81):

$$\mathbf{\Pi}_{-+} = \frac{\mathbf{\Pi}_{xx}+\mathbf{\Pi}_{yy}+i\mathbf{\Pi}_{xy}-i\mathbf{\Pi}_{yx}}{4},$$

gives the RPA spectral function $\mathbf{\Pi}_{-+}$, giving us the possibility to compute self-consistently the second contribution in the right hand side of Eq. (6.78). Thus, by means of Eq. (6.78) we obtain the d_σ electrons spectral function, which allows, through Eq. (6.69), updating the bath $\Gamma_\sigma(\omega)$. The procedure is iterated up to the DMFT self-consistency (6.70) as displayed schematically in Fig. 6.8.

Before concluding let us note that the previous approach extends straightforwardly to the multi-orbital case (6.36) by simply introducing an additional index related to the orbital quantum number.

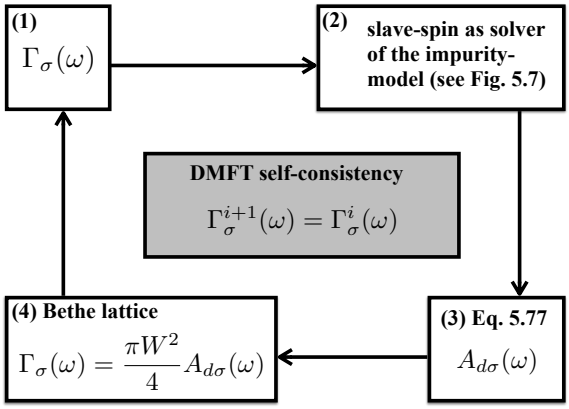

Figure 6.8: Schematic representation of the DMFT loop. The bath $\Gamma_\sigma(\omega)$ is updated by using the self-consistent slave-spin impurity Green's function.

6.6 Conclusions

In this Chapter we have shown that a generic SIAM can be mapped without any constraint onto a resonant level model coupled to two Ising spins, or just one in the simpler case when the hybridization with the bath is particle-hole symmetric. Remarkably, the slave-spin mapping can be directly generalized to the multi-orbital case within the assumptions of an impurity Hamiltonian that does not include Coulomb exchange terms.

In order to appreciate the importance of the mapping we show that the mean-field decoupling of electrons from the Ising variables is able to reproduce quite accurately the magnetic properties of the model even deep inside the large-U Kondo regime (Figs. 6.1 and 6.3), specifically, the finite susceptibility $\chi \sim 4/\pi T_K$ and Wilson ratio $R_W = 2$ [212, 214]. By comparison, in the same Kondo regime, conventional slave-boson mean-field theory yields a spin-polarized lowest-energy solution that unphysically breaks spin $SU(2)$ symmetry [252].

We also demonstrate that the single-particle Green's functions of the physical fermions can be calculated without constraints. This important result allows, for example, solving in the slave-spin representation a generic particle-hole nonsymmetric Hubbard model with DMFT. This could, in some cases, be more convenient than directly working within the physical Hilbert space, though smaller than the enlarged one, especially when one wants to prevent spontaneous symmetry breaking that usually accompanies a Mott transition. Indeed, the slave-spin Hamiltonian (6.28) is invariant under a particle-hole transformation acting on the fermions f_σ, despite the fact that the Hamiltonian of the physical electrons d_σ is not.

By introducing the Abrikosov representation of the 1/2 spin variable [1, 147, 224] we show that the slave-spin mean-field approach corresponds to a Hartee-Fock approximation. This convenient representation allows us to perform a self-consistent calculation of the single-particle physical fermions Green's function that, as shown in Fig. 6.6, reproduces both the Kondo resonance and the high-energy incoherent charge fluctuations peaks.

Finally, in Section 6.5, we present the slave-spin mean-field technique as approximate impurity solver for DMFT. Our proposal is a numerically inexpensive approach that allows studying the zero temperature properties of the multi-bands Hubbard models, where more accurate impurity solvers are extremely demanding.

7

Transport in quantum dots within the slave-spin technique

In this Chapter we study transport across a magnetic impurity by means of the constrained-free slave-spin technique formulated in Chapter 6. We prove that also the out of equilibrium evolution of quantum dot can be obtained in the slave-spin representation without any constraint on the enlarged Hilbert space. We formulate the slave-spin mean-field theory to study the evolution of a quantum dot driven out of equilibrium by an external perturbation. The method is able to access the full out of equilibrium dynamics also far from the linear response regime. Within a conserving mean-field approximation we find a conductance that displays not only the well-known zero-bias anomaly, $G = 2e^2/h$, but also the expected peak at bias of order U. Moreover, we apply the method to investigate the time-evolution of a quantum dot induced by a time-dependent electrochemical potential applied to the contacts. Similarly to the time-dependent Gutzwiller approximation, the mean-field slave-spin dynamics is able to capture dissipation in the leads, so that a steady-state is reached after a characteristic relaxation time.

7.1 Introduction

Originally observed in magnetic alloys [117], the Kondo effect [18, 153], which may be the simplest collective phenomena due to strong correlations, is now routinely realized in magnetic nanocontacts, either by real magnetic atoms and molecules [182, 218, 267] or artificial ones [23, 143], e.g. quantum dots. In these systems the Kondo effect reveals itself by the so-called zero-bias anomaly [60, 99, 101, 207]. It arises by the coupling between a single magnetic atom, such as cobalt, and the conduction electrons of an otherwise non-magnetic metal. Such an impurity typically behaves like a local moment that, due to spin exchange, forms a many-body spin singlet state with the itinerant electrons.

Unlike magnetic alloys, nanoscale Kondo systems can be driven out of equilibrium by applying charge or spin bias voltages across the devices [150]. In such a nonequilibrium situation, the interplay between the time dynamics and strong correlation effects makes the theoretical description extremely challenging. In order to address this problem, many innovative approaches have been developed, such as time-dependent numerical renormalization group [14–16], real

time Monte Carlo [246, 284], time-dependent density-matrix renormalization group [37, 249, 286], flow equation methods [88, 144, 272], perturbative renormalization group [139, 188, 210, 237, 251], time-dependent variational approaches [22, 161], slave-particle techniques [57, 69, 176, 228] and exact approaches [36, 185]. Despite the rich variety of methods, they often become numerically costly at long times, which limits their application to the short times evolution of simple models. Some semi-analytical approaches [57, 161] sacrifice the accuracy in order to access the full dynamics.

The nonequilibrium slave-spin technique for magnetic impurities presented in this Chapter belongs to the latter class of techniques. Following the same strategy presented in Section 6.3, we map, without any constraint, a SIAM, characterized by a particle-hole symmetric hybridization with the contacts, onto a resonant level model coupled to a single Ising variable. Remarkably, the mapping applies for the out of equilibrium dynamics and allows us to disentangle spin and charge dynamics, which are characterized by well-separated time-scales. In this representation, a simple self-consistent Hartree-Fock calculation is able to reproduce qualitatively the differential conductance of a single-orbital magnetic impurity both in the small and large bias regimes. Moreover, the slave-spin technique allows us to study the full time evolution of magnetic impurities coupled with metallic leads under a nonequilibrium protocol.

The plan of the Chapter is as it follows. We first introduce the model to describe a quantum dot coupled to two metallic contacts in Section 7.2. Then, in Section 7.3, we present the out of equilibrium extension of our slave-spin theory that allows computing the time-dependent average values without any constraint. In Section 7.4 we present the mean-field approximation for the out of equilibrium dynamics of a quantum dot. By assuming that the system relaxes after an initial transient, we present, in Section 7.5, the mean-field approximation for the nonequilibrium steady-state regime. To highlight the importance of the approach presented in this work, we devote the Section 7.6 to applications of the method to transport in quantum dots coupled to metallic contacts.

7.2 The slave-spin Hamiltonian for a quantum dot

A quantum dot is an artificial droplet of electron liquid with characteristic dimension ranging from nanometers to a few microns. The dot, which is often realized in semiconductors heterostructures, can be coupled to metallic contacts such to allow the electronic transport across the system. Applying a gate voltage it is possible to create configurations with an odd number of electrons, which are degenerate with respect to spin and typically in a spin-doublet state. The coupling with the contacts induces an effective magnetic exchange that, at temperature below T_K[1], removes the degeneracy and induces a collective state where the impurity magnetic moment is screened by the electrons of the contacts.

A minimal model, that in many circumstances describes the physics of quantum dots, is the SIAM (3.52). In the presence of two metallic contacts the model Hamiltonian reads:

$$H(t) = H_C(t) + H_{T,C}(t) + H_{\mathrm{D}}(t), \tag{7.1}$$

where the first term is the dot Hamiltonian

$$H_D = -\frac{U}{4}\Omega - \frac{V_g(t)}{2}(n-1) - \frac{h(t)}{2}(n_\uparrow - n_\downarrow),$$

[1]We have already encountered this important energy scale in the context of magnetic impurities in metals, see Sections 3.3 and 6.4.

where d_σ is the annihilation operator of an electron state on the quantum dot, $n_\sigma = d_\sigma^\dagger d_\sigma$ the corresponding density, while $\Omega = -(2n_\uparrow - 1)(2n_\downarrow - 1)$ and $n = n_\uparrow + n_\downarrow$. In Hamiltonian (7.2) U denotes the charging energy, while $V_g(t)$ the gate potential and $h(t)$ the Zeeman field, both time-dependent. The non-interacting right (R) and left (L) leads are represented by a free electron gas with half-bandwidth W

$$H_c = \sum_{a=L,R} \sum_{\mathbf{k}\sigma} (\epsilon_{\mathbf{k}} - \phi_a)\, \psi^\dagger_{a\mathbf{k}\sigma} \psi_{a\mathbf{k}\sigma}, \tag{7.2}$$

where ϕ_a is the electrochemical potential that fixes the number of electrons in each contact, $\phi_L = -\phi_R$. Finally, the tunnel-coupling between the contacts and the quantum dot is represented by:

$$H_{T,C}(t) = \sum_{a=L,R} \sum_{\mathbf{k}\sigma} \left(V_{a\mathbf{k}}(t)\, \psi^\dagger_{a\mathbf{k}\sigma}\, d_\sigma + H.c. \right) / \sqrt{V}, \tag{7.3}$$

where $V_{a\mathbf{k}}(t)$ is a time-dependent amplitude, and V is the number of $\mathbf{k}$ states. In this Chapter we limit the analysis to the symmetric case where $V_{L\mathbf{k}}(t)$, $V_{R\mathbf{k}}(t)$ do not depend on the spin and the channel quantum number, $V_{L\mathbf{k}}(t) = V_{R\mathbf{k}}(t) = V_{\mathbf{k}}(t)$. Furthermore, we assume a particle-hole symmetric bath, i.e. for any $\epsilon_{\mathbf{k}}$ there exist a $\mathbf{k}^*$ such that $\epsilon_{\mathbf{k}^*} = -\epsilon_{\mathbf{k}}$ and:

$$\Gamma(-\epsilon, t) = \Gamma(\epsilon, t),$$

where the time-dependent hybridization function reads:

$$\Gamma(\epsilon, t) = \sum_{\mathbf{k}} |V_{\mathbf{k}}(t)|^2 \delta(\epsilon - \epsilon_{\mathbf{k}})/V.$$

We observe that, by means of the results presented in Section 6.3, the slave-spin theory for the out of equilibrium dynamics of quantum dots can be generalized to more complicated situations, e.g. $V_L(t) \neq V_R(t)$ or multi-levels quantum dots.

Since the particle-hole transformation $C_{\sigma LR}$ will be important in the following, let us write

$$\left\{ d_\sigma \to d_\sigma^\dagger \bigcup \prod_{\mathbf{k}} \left(c_{L\mathbf{k}\sigma} \to -c^\dagger_{R\mathbf{k}^*\sigma} \bigcup c_{R\mathbf{k}\sigma} \to -c^\dagger_{L\mathbf{k}^*\sigma} \right) \right\} \tag{7.4}$$

that acts on the spin-σ electrons and mixes R and L contacts, leaving the chemical potential shift (7.2) invariant. Under such transformation the parameters of Hamiltonian (7.1) change as follows:

$$U \to -U, \quad V_g \to \mp h, \quad h \to \mp V_g, \tag{7.5}$$

where upper and lower signs refer to the action of $C_{\uparrow LR}$ and $C_{\downarrow LR}$, respectively.

By using the mapping presented in Section 6.3.1, considering the case of a particle-hole symmetric hybridization function, the dot Hamiltonian (7.1) can be written in the slave-spin representation as an effective resonant level model coupled to a single Ising variable:

$$H_1(t) = H_C + \sigma^x H_{T,C}(t) + H_D(t), \tag{7.6}$$

where H_C remains unaltered, $H_{T,C}(t)$ is obtained by replacing the electron d_σ with the pseudofermion f_σ, while the dot Hamiltonian takes the same form as in Eq. (6.28) but with time-dependent parameters:

$$H_D(t) = -\frac{U}{4}\sigma^z - \frac{h(t)}{4}(1 + \sigma^z)(2n_\uparrow - 1) - \frac{V_g(t)}{4}(1 - \sigma^z)(2n_\uparrow - 1). \tag{7.7}$$

We remind that the representation of the electron annihilation operator in terms of the slave-spin and the pseudofermion operator is $d_\sigma = \sigma^x f_\sigma$. The model Hamiltonian (7.6) is equivalent to the dot Hamiltonian (7.1) providing that the enlarged Hilbert space is projected at any time t in the physical subspace by the projector $\mathbb{P}$ defined in Eq. (6.29).

Remarkably, the time-dependent evolution of the quantum dot, Eq. (7.1), can be obtained from the auxiliary model in Eq. (7.6) without any constraint on the enlarged Hilbert space. The proof of this equivalence follows the same steps of the equilibrium case, see Section 6.3. However, we consider valuable to show, in the next Section, the possibility to remove the constraint in the time-dependent average value of physical operators. In particular, since our aim is to study the charge transport across the junction, we are going to prove the previous statement by considering the charge current operator, that, in terms of the original fermions d_σ, is defined as:

$$I_Q(t) = \frac{I_L(t) - I_R(t)}{2}, \tag{7.8}$$

where the current $I_a(t)$ reads

$$I_a(t) = i\,[H(t), N_a(t)] = -i \sum_{\mathbf{k}\sigma} \left(V_{\mathbf{k}}(t)\, \psi^\dagger_{a\mathbf{k}\sigma}\, d_\sigma - \text{H.c.} \right) / \sqrt{V}$$

with N_a number operator in lead a and $a = L, R$. Performing the slave-spin mapping the latter quantity becomes

$$I_Q(t) = \sigma^x \frac{I_L(t) - I_R(t)}{2} = \sigma^x I^f_Q, \tag{7.9}$$

where the I_L and I_R are obtained by replacing d_σ with f_σ.

Before moving on, we introduce the Glazman-Raikh rotation [99]:

$$\begin{pmatrix} \psi_{1\mathbf{k}\sigma} \\ \psi_{2\mathbf{k}\sigma} \end{pmatrix} = \frac{1}{\sqrt{2}} \begin{pmatrix} 1 & 1 \\ 1 & -1 \end{pmatrix} \begin{pmatrix} \psi_{L\mathbf{k}\sigma} \\ \psi_{R\mathbf{k}\sigma} \end{pmatrix}. \tag{7.10}$$

The previous unitary transformation is particularly convenient to study the transport across quantum dots. Indeed, it is easy to realize that the anti-symmetric combination of the electron states in the leads $\psi_{2\mathbf{k}\sigma}$ is decoupled from the impurity, while the symmetric combination $\psi_{1\mathbf{k}\sigma}$ remains coupled to d_σ, see Eq. (7.3). Thus, the Kondo screening involves only the $\psi_{1\mathbf{k}\sigma}$ variables. On the other hand, the current operator (7.8) is expressed in terms of $\psi_{2\mathbf{k}\sigma}$ only.

7.3 Fate of the slave-spin constraint in the evolution

Without losing generality, we assume the model in Eq. (7.1) placed at time $t = 0$ in thermal equilibrium at temperature $T = 1/\beta$:

$$\rho(U, V_g, h) = \frac{e^{-\beta H(U,V_g,h)}}{Z(U, V_g, h)},$$

where $Z(U, V_g, h) = \text{Tr}\left(e^{-\beta H(U,V_g,h)}\right)$ and the impurity is decoupled from the contacts $V_{\mathbf{k}}(0) = 0$. For $t > 0$ we let the system to evolve by suddenly changing the coupling between the dot and the leads: $V_{\mathbf{k}}(t > 0) = V_{\mathbf{k}}$. We note that the initial distribution may include a chemical potential bias between the L and R contacts. The average current flowing across the dot is:

$$I_Q(t; U, V_g, h) = \text{Tr}\left[\rho(U, V_g, h) U^\dagger(t, 0; U, V_g, h) I_Q U(t, 0; U, V_g, h)\right],$$

where U is the unitary time evolution operator:

$$U(t,0;U,V_g,h) = T_t\left[\exp\left(-i\int_0^t dt' H(t',U,V_g,h)\right)\right].$$

Since the trace is invariant under similarity transformations and $C^\dagger_{\downarrow LR}$ commutes with I_Q, Eq. (7.5) implies:

$$I_Q(t;U,V_g,h) = I_Q(t;-U,h,V_g),$$

and

$$I_Q(t;U,V_g,h) = \frac{I(t;U,V_g,h) + I_Q(t;-U,h,V_g)}{2}. \tag{7.11}$$

Within the slave-spin representation the initial equilibrium distribution is described by

$$\rho_1(U,V_g,h) = \frac{e^{-\beta H_1(U,V_g,h)}}{Z(U,V_g,h)},$$

and the average value of the current reads

$$I_Q(t;U,V_g,h) = \mathrm{Tr}\left[\rho_1(U,V_g,h)\, U_1^\dagger(t,0;U,V_g,h)\,\sigma^x\, I_Q\, U_1(t,0;U,V_g,h)\,\mathbb{P}\right],$$

where the trace is on the enlarged Hilbert space, $\mathbb{P}$ (6.29) is the projector in the physical subspace and U_1 is the time evolution operator generated by $H_1(t)$. In the slave-spin representation (7.6) the role of the particle-hole symmetry transformation $C_{\downarrow LR}$ is simply played by σ^x:

$$\begin{aligned} I_Q(t;-U,h,V_g) &= \mathrm{Tr}\left[\rho_1(-U,h,V_g)\, U_1^\dagger(t,0;-U,h,V_g)\,\sigma^x\, I_Q^f\, U_1(t,0;-U,h,V_g)\,\mathbb{P}\right] \\ &= \mathrm{Tr}\left[\rho_1(U,V_g,h)\, U_1^\dagger(t,0;U,V_g,h)\,\sigma^x\, I_Q^f\, U_1(t,0;U,V_g,h)\,\sigma^x\,\mathbb{P}\,\sigma^x\right]. \end{aligned}$$

Eq. (7.11) implies:

$$\begin{aligned} 2I_Q(t;U,V_g,h) =& \mathrm{Tr}\left[\rho_1(U,V_g,h)\, U_1^\dagger(t,0;U,V_g,h)\,\sigma^x\, I_Q^f\, U_1(t,0;U,V_g,h)\,\mathbb{P}\right] \\ &+ \mathrm{Tr}\left[\rho_1(U,V_g,h)\, U_1^\dagger(t,0;U,V_g,h)\,\sigma^x\, I_Q^f\, U_1(t,0;U,V_g,h)\,\sigma^x\,\mathbb{P}\,\sigma^x\right]. \end{aligned}$$

Since $1 = \mathbb{P} + \sigma^x\,\mathbb{P}\,\sigma^x$, it readily follows that:

$$I_Q(t;U,V_g,h) = \mathrm{Tr}\left[\frac{e^{-\beta H_1(U,V_g,h)}}{Z_1(U,V_g,h)}\, U_1^\dagger(t,0;U,V_g,h)\,\sigma^x\, I_Q^f\, U_1(t,0;U,V_g,h)\right], \tag{7.12}$$

where we have used the equivalence in Eq. (6.30), $Z_1(U,V_g,h) = 2Z(U,V_g,h)$. Eq. (7.12) states that the time-dependent average value of the current flowing across the impurity (7.8) can be computed in the slave-spin representation (7.6) without any constraint.

Following the same idea, the previous result extends to any time-dependent average of physical observables, that commutes with $C_{\downarrow LR}$, and holds for any nonequilibrium protocol. Hence, the out of equilibrium evolution of the observables, commuting with $C_{\downarrow LR}$ (7.1), can be obtained within the slave-spin representation (7.6) without projecting out unphysical configurations introduced by the mapping.

7.4 Time-dependent mean-field equations

In this Section we present the mean-field approximation to describe the out of equilibrium evolution of a driven quantum dot. Within the slave-spin mapping the dynamics of the model (7.1) is described by the time-dependent Schrödinger equation:

$$i\partial_t|\Psi(t)\rangle = H_1(t)|\Psi(t)\rangle, \tag{7.13}$$

where $|\Psi(t)\rangle$ describes the collective state of the resonant level model coupled to the Ising degree of freedom, and at $t = 0$ the system is placed in the ground state configuration $|\Psi(0)\rangle$ of the initial Hamiltonian Eq. (7.6).

The mean-field slave-spin approach consists in approximating the time-dependent wave function $|\Psi(t)\rangle$ with the direct product of a fermionic part $|\Phi(t)\rangle$ times a spin one $|\chi(t)\rangle$:

$$|\Psi(t)\rangle = |\chi(t)\rangle \times |\Phi(t)\rangle. \tag{7.14}$$

We stress again that the previous approximation becomes accurate as we approach the local moment regime, i.e. $U/\Gamma \gg 1$, where the two subsystems are characterized by well-separated energy scales. This is indeed the regime we consider hereafter.

The dynamics of the interacting model (7.1) is, thus, reduced to the evolution of a spin degree of freedom:

$$\partial_t\langle\sigma^i(t)\rangle = -2\,\epsilon_{ijk}\,\mathcal{B}_j(t)\,\langle\sigma^k(t)\rangle, \tag{7.15}$$

where ϵ_{ijk} is the Levi-Civita tensor in three dimensions and $\boldsymbol{\mathcal{B}}(t)$ is the self-consistent time-dependent fermionic field:

$$\boldsymbol{\mathcal{B}}(t) = \left(-\langle H_{T,C}(t)\rangle\,, 0, \frac{U}{4} + \frac{h(t) - V_g(t)}{2}\left\langle n_\uparrow(t) - \frac{1}{2}\right\rangle\right).$$

Eq. (7.15) is coupled with the Schrödinger equation of the Slater determinant $|\Phi(t)\rangle$:

$$i\partial_t|\Phi(t)\rangle = H^f_*(t)|\Phi(t)\rangle, \tag{7.16}$$

where $H^f_*(t)$ is

$$H^f_*(t) = H_C + \langle\sigma^x(t)\rangle\, H_{T,C}(t) - \sum_\sigma \frac{\lambda_\sigma(t)}{2} n_\sigma, \tag{7.17}$$

and

$$\lambda_\uparrow(t) = V_g(t)(1 - \langle\sigma^z(t)\rangle) + h(t)(1 + \langle\sigma^z(t)\rangle), \quad \lambda_\downarrow = 0.$$

For a given initial configuration, $|\Psi(0)\rangle = |\chi(0)\rangle \times |\Phi(0)\rangle$, Eqs. (7.15) and (7.16) allow us to study the dynamics of the original correlated model in terms of the evolution of a spin 1/2 coupled with a time-dependent resonant level model. As observed in Section 7.3, we emphasize that the nonequilibrium evolution of the Hamiltonian (7.1) can be obtained in the slave-spin representation without any need of local constraints, that project out unphsyical configurations introduced by the mapping.

The dynamical Eqs. (7.15) and (7.16) are similar but not equivalent to the ones obtained applying the conventional time-dependent Gutzwiller approximation (t-GA) [245] to the AIM [161]. In this regard, the evolution of the time-dependent Gutzwiller parameters resembles the dynamics of the spin variable, while the bath $\psi_{a\mathbf{k}\sigma}$ and the pseudofermion f_σ degrees of freedom evolve under the time-dependent self-consistent Hamiltonian (7.17).

For large time, namely after the transient, we assume that, due to the coupling with infinite contacts, the solution of Eqs. (7.15) and (7.16) thermalizes to a steady-state. In order to describe the asymptotic regime we develop, in the next Section, the nonequilibrium stationary mean-field approach.

7.5 Mean-field for the nonequilibrium steady-state

Without losing generality, we shall assume that at $t = 0$ the contacts are disconnected from the dot but in the presence of a finite bias, so that they are distributed according to:

$$\langle \psi^\dagger_{L(R)\mathbf{k}\sigma} \psi_{L(R)\mathbf{k}\sigma} \rangle = f_{L(R)}(\epsilon_\mathbf{k}) = f(\epsilon_\mathbf{k} \mp \phi/2), \tag{7.18}$$

where ϕ is the voltage difference applied to the contacts and $f(\epsilon)$ is the Fermi-Dirac distribution function. Once the tunnel-coupling (7.3) is turned on, a time-dependent current starts to flow across the junction according to Eqs. (7.15) and (7.16). For large time, $t \to \infty$, we assume that the system described by the ground-state $|\Psi(t)\rangle$ reaches a stationary state

$$|\Psi(t)\rangle \to |\Psi\rangle_{st}, \tag{7.19}$$

characterized by a constant current. We show in the following, Section 7.6, that Eq. (7.19) is a justified assumption.

The stationary mean-field approach assumes a factorized steady-state wave function:

$$|\Psi\rangle_{st} = |\chi\rangle_{st} \times |\Phi\rangle_{st}, \tag{7.20}$$

where $|\Phi\rangle_{st}$ is the fermionic part and $|\chi\rangle_{st}$ the spin one. We observe that even though the approximation (7.20) looks similar to the mean-field decoupling performed at equilibrium in Appendix 6.4, the two different wave functions are conceptually different. As we will see, the stationary state $|\Psi\rangle_{st}$ is characterized by a distribution function that is different from the equilibrium one (Fermi-Dirac). In order to capture this feature we work in the framework of the Keldysh technique, that is briefly introduced in Appendix D.1.

At stationarity, the pseudospin degree of freedom is controlled by the Hamiltonian:

$$H^*_\sigma = -\boldsymbol{\mathcal{B}} \cdot \boldsymbol{\sigma}, \tag{7.21}$$

where, for convenience, we have introduced the effective self-consistent field:

$$\boldsymbol{\mathcal{B}} = \left(-\langle H_{T,C} \rangle_{st}, 0, \frac{U}{4} + \left(h - V_g\right) \left\langle n_\uparrow - \frac{1}{2} \right\rangle_{st} \right), \tag{7.22}$$

and $\langle \cdots \rangle_{st} = \langle \Phi | \cdots | \Phi \rangle_{st}$. By defining $\langle \boldsymbol{\sigma} \rangle_{st} = (\sin\theta, 0, \cos\theta)$, the steady-state ground-state $|\Psi\rangle_{st}$ is obtained by solving the self-consistent equation:

$$\tan\theta = \mathcal{B}_x / \mathcal{B}_z, \tag{7.23}$$

where $\mathcal{B}_x$ explicitly reads:

$$\mathcal{B}_x = -\sqrt{\frac{2}{V}} \sum_\mathbf{k} \sum_\sigma \left(V_\mathbf{k} \left\langle \psi^\dagger_{1\mathbf{k}\sigma} f_\sigma \right\rangle_{st} + V^*_\mathbf{k} \left\langle f^\dagger_\sigma \psi_{1\mathbf{k}\sigma} \right\rangle_{st} \right), \tag{7.24}$$

while $\mathcal{B}_z$ contains:

$$\langle n_\uparrow \rangle_{st} = \langle f^\dagger_\uparrow f_\uparrow \rangle_{st}. \tag{7.25}$$

We notice that fermionic averages (7.24) and (7.25) are computed on the steady-state of the stationary Hamiltonian:

$$H^f_* = H_c + \sin\theta\, H_{T,C} - \sum_\sigma \frac{\lambda_\sigma}{2} n_\sigma \tag{7.26}$$

where

$$\lambda_\uparrow = h(1+\cos\theta) + V_g(1-\cos\theta), \quad \lambda_\downarrow = 0.$$

Eq. (7.24) requires the evaluation of the lesser Green's function $G^<_{1\mathbf{k}f\sigma}(t,t) = i\langle f^\dagger_\sigma(t)\psi_{1\mathbf{k}\sigma}(t)\rangle$, which, by means of the Dyson's equation, can be expressed in terms of the dressed Green's function of the f_σ pseudofermions and the free Green's function of the contacts. Instead, Eq. (7.25) can be expressed in terms of the pseudofermions Green's function only. By performing the straightforward calculations, that are summarized in Appendix D, Section D.3, we obtain:

$$\mathcal{B}_x = -\frac{2}{\sin\theta}\sum_\sigma \int d\epsilon(\epsilon+\lambda_\sigma) f_{\rm neq}(\epsilon) A_{f\sigma}(\epsilon), \tag{7.27}$$

$$\langle n_\uparrow\rangle_{st} = \int d\epsilon f_{\rm neq}(\epsilon) A_{f\uparrow}(\epsilon), \tag{7.28}$$

where the nonequilibrium distribution on the impurity is $f_{\rm neq}(\epsilon) = (f_L(\epsilon)+f_R(\epsilon))/2$ and the spectral function $A_{f\sigma}(\epsilon)$ is equivalent to Eq. (6.47) with the only difference that the self-energy $\Sigma^{R/A}_{f\sigma}(\omega)$, in Eq. (6.48), is multiplied by a factor of 2 counting the presence of the two different contacts.

Given the spectral properties of the contacts, the bias ϕ and the external fields applied to the quantum dot Eqs. (7.27) and (7.28) give an analytic expressions for the effective magnetic field $\mathcal{B}$, which depends on the steady-state average $\langle\sigma^x\rangle_{st}$. The steady-state variational problem is obtained by solving:

$$\tan\theta = \frac{\mathcal{B}_x(\theta)}{\mathcal{B}_z(\theta)}. \tag{7.29}$$

Even though numerically equivalent to the equilibrium problem, it contains the nonequilibrium properties of the steady-state $|\Psi\rangle_{st}$.

Before concluding the Section, we observe that the nonequilibrium steady-state self-consistent Eq. (7.29) is similar but not equivalent to the one obtained with the out of equilibrium Gutzwiller approach for quantum dots [161]. This feature has been already observed at equilibrium in Section (6.4), where the slave-spin allowed the removal of the magnetic instability observed in the Gutzwiller approach. Furthermore, in comparison with the latter approach, the slave-spin method has the advantage of permitting one to use the machinery of quantum field theory, i.e. Wick's theorem, to improve mean-field results by including fluctuations.

7.6 Two relevant applications

To highlight the importance of our formulation here we consider the simple case of a quantum dot with $V_g = h = 0$, and we take the wide-band limit (WBL). Moreover, we will firstly analyze the steady-state regime by computing the nonequilibrium ground-state and the differential conductance as a function of the voltage applied to the contacts. Then, we will study the out of equilibrium evolution induced by a slowly varying time-dependent voltage.

7.6.1 The steady-state solution in the wide-band limit

Initially, we assume the dot disconnected by the leads, which are placed at two different chemical potential $\pm\phi/2$, hence their initial distribution function is described by Eq. (7.18). Once the tunneling amplitude is turned on, after the initial transient, the steady-state Hamiltonian (7.21) is characterized by the self-consistent magnetic field:

$$\boldsymbol{\mathcal{B}} = (-\langle H_{T,C}\rangle_{st}, 0, U/4)\,.$$

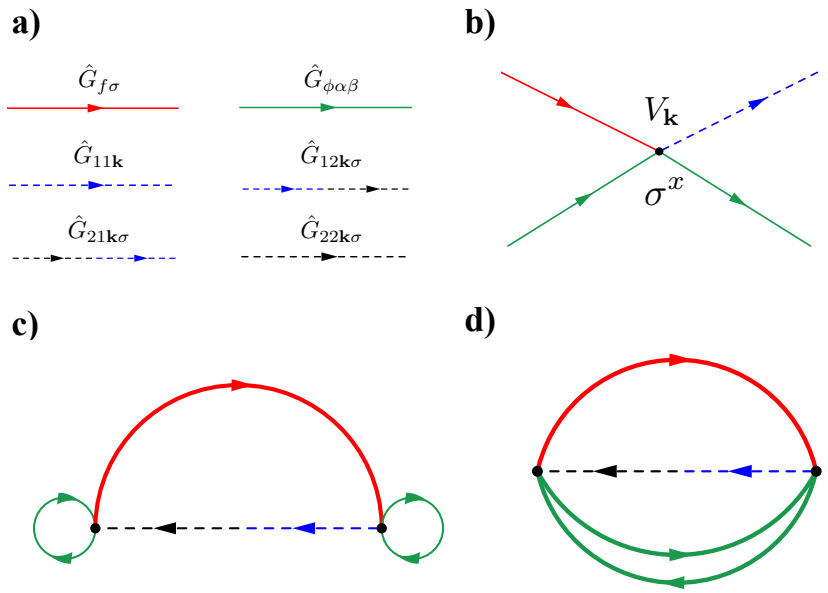

Figure 7.1: a) Bare Green's functions. **b)** Bare interaction. **c)** $\langle \phi^\dagger_\alpha \sigma^x_{\alpha\beta} \phi_\beta \rangle_{st} \langle I^f_Q \rangle_{st}$ contribution to the current. **d)** Self-consistent correction due to valence fluctuations.

In the WBL (C.25) the f_σ electron self-energy reduces to

$$\Sigma^R_{f\sigma}(\omega) = -i2\Gamma \sin^2\theta, \tag{7.30}$$

and

$$\mathcal{B}_x = \frac{4\Gamma_*}{\pi \sin\theta} \log \frac{D}{\sqrt{\Gamma_*^2 + \phi^2/4}}, \tag{7.31}$$

where Γ_* is the renormalized hybridization amplitude $\Gamma_* = 2\Gamma \sin^2\theta$ and Γ the bare one. The steady-state variational ground-state is obtained by solving the self-consistent Eq. (7.29). For large U, and for $\phi \ll \Gamma$, the solution reads:

$$\Gamma_*(\phi) \simeq \Gamma_*(0) - \frac{\phi^2}{8\Gamma_*(0)}, \tag{7.32}$$

where $\Gamma_*(0)$ is the equilibrium renormalized hybridization function in Eq. (6.51). As shown in Eq. (7.32) the effect of an external voltage ϕ, in the regime of $\phi \ll \Gamma$, is to reduce the equilibrium value of the renormalized hybridization $\Gamma_*(0)$. Moreover, the mean-field steady-state breaks spontaneously the Z_2 gauge symmetry by choosing one of the two degenerate minima $\langle \sigma^x \rangle_{st} \neq 0$, as already observed in the equilibrium case analyzed in Section 6.4.

At the steady-state variational minimum we can compute the average value of the current:

$$\langle I_Q \rangle_{st} = -\frac{i}{\sqrt{2V}} \sum_{\mathbf{k}\sigma} \left(\langle V_{\mathbf{k}} \psi^\dagger_{2\mathbf{k}\sigma} \sigma^x f_\sigma \rangle_{st} - c.c. \right) \tag{7.33}$$

that involves the two-particle correlation function $G^<_{x\cdot 2\mathbf{k}\sigma}(t,t') = i\langle \psi^\dagger_{2\mathbf{k}\sigma}(t') \sigma^x(t) f_\sigma(t) \rangle_{st}$. The self-consistent evaluation of the current (7.33) can be conveniently performed by means of the Abrikosov fermions. As already shown in Section 6.4.1, in this representation the slave-spin mean-field theory corresponds to the Hartee-Fock decoupling and allows us to identify the electron self-energies that, through the Bethe-Salpeter equation, determine the corrections that

are included in the two-particle correlation functions. In terms of Abrikosov fermions ϕ_α, defined in Eq. (6.60), the average value of the current reads:

$$\begin{aligned}\langle I_Q\rangle_{st} &= -\frac{i}{\sqrt{2V}}\sum_{\mathbf{k}\sigma}\left(V_{\mathbf{k}}\langle\,\psi^\dagger_{2\mathbf{k}\sigma}\,\phi^\dagger_\alpha\,\sigma^x_{\alpha\beta}\,\phi_\beta\,f_\sigma\rangle_{st}-\text{c.c.}\right)\\ &= -\frac{2}{\sqrt{2V}}\sum_{\mathbf{k}\sigma}\text{Re}\,\left[V_{\mathbf{k}}\,G^<_{x\cdot 2\mathbf{k}\sigma}(t,t)\right].\end{aligned} \tag{7.34}$$

Consistently with the slave-spin mean-field decoupling the current has two contributions, Figs. 7.1 **c)** and **d)**:

$$\langle I_Q\rangle_{st} = \langle\phi^\dagger_\alpha\,\sigma^x_{\alpha\beta}\,\phi_\beta\rangle_{st}\langle I^f_Q\rangle_{st} + \langle\delta I^f_Q\rangle_{st} \tag{7.35}$$

where the former, $\langle I^f_Q\rangle_{st}$, involves only the low-energy pseudofermion degree of freedom, and can be obtained by straightforward calculations summarized in Appendix D.3. Here, we report the final result:

$$\langle I^f_Q\rangle_{st} = 2\Gamma_*(\phi)\frac{2e}{h}\arctan\left(\frac{e\phi}{2\Gamma_*(\phi)}\right), \tag{7.36}$$

where e is the elementary charge and h the Planck's constant. Instead, the latter term in Eq. (7.35) takes into account the contribution of valence fluctuations and can be expressed as

$$\langle\delta I^f_Q\rangle_{st} = -\frac{4\Gamma e}{h}\int d\omega\,(f_L(\omega)-f_R(\omega))\,\text{Re}\,\mathcal{K}(\omega) \tag{7.37}$$

where the kernel $\mathcal{K}(\omega)$ is given by:

$$\mathcal{K}(\omega) = \int\frac{d\epsilon}{2\pi}\Big[\mathbf{\Pi}^<_{xx}(\epsilon)\,G^R_f(\omega-\epsilon)+\mathbf{\Pi}^R_{xx}(\epsilon)\,G^R_f(\omega-\epsilon)+\mathbf{\Pi}^R_{xx}(\epsilon)\,G^<_f(\omega-\epsilon)\Big],$$

and $\mathbf{\Pi}_{xx}$ is the ϕ fermion $\sigma^x-\sigma^x$ correlation function introduced in Eq. 6.64 for the equilibrium case. The spin correlation function $\mathbf{\Pi}_{xx}$ satisfies the Dyson's Eq. in Fig. 6.5 that for the different Keldysh components reads:

$$\mathbf{\Pi}^{R/A}_{xx}(\omega) = \frac{1}{\left[\Pi^{R/A}_{xx}(\omega)\right]^{-1}-\Sigma^R_{xx}(\omega)}, \tag{7.38}$$

and

$$\mathbf{\Pi}^<_{xx}(\omega) = \mathbf{\Pi}^R_{xx}(\omega)\Sigma^<_{xx}(\omega)\mathbf{\Pi}^A_{xx}(\omega), \tag{7.39}$$

where $\hat{\Sigma}_{xx} = \hat{\chi}_{TT}$. For more details we refer the interested reader to Appendix D.3. The self-energies appearing in Eqs. (7.38) and (7.39) are obtained by contracting the four-leg vertex in Fig. 7.1 **b)**. Specifically, the self-energy $\Sigma_{xx}(\omega)$ allows us to reconstruct the incoherent side bands characterized by a width of the order of the bare hybridization Γ and centered around $\pm U/2$ as shown in Fig. 6.6.

Numerical integration of Eq. (7.37) enables us to compute the differential conductance

$$G(\phi) = \frac{d\langle I\rangle_{st}}{d\phi},$$

which is shown in Fig. 7.2. We observe two distinct contributions: (i) the well-known zero-bias anomaly which derives from the Kondo peak at the Fermi level and controls the low-bias behavior and (ii) an incoherent peak, which mainly contributes to the large bias features of the conductance.

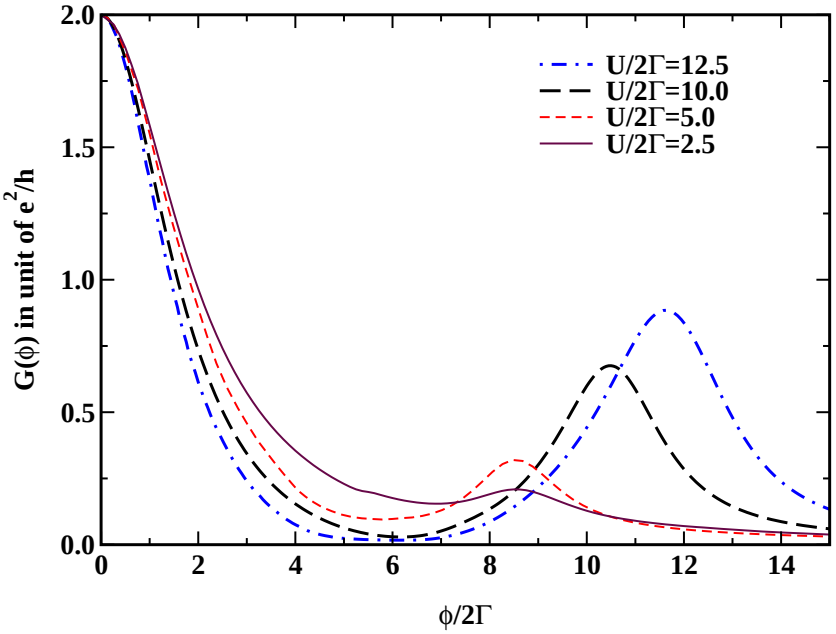

Figure 7.2: Differential conductance as a function of the applied voltage $\phi/2\Gamma$ for $U/W = 0.1$ and different values of 2Γ.

In order to compare our result $G(\phi)$ with the universal behavior of the conductance in the Kondo regime, obtained with renormalization group approach in Refs. [225, 257], we expand $\langle I_Q \rangle_{st}$ around $\phi/\Gamma \ll 1$ obtaining:

$$G(\phi) = \frac{2e^2}{h}\left[1 - \frac{1}{4}\left(\frac{\phi}{\Gamma_*(0)}\right)^2\right]. \tag{7.40}$$

In agreement with our self-consistent Hartree-Fock approximation, Eq. (7.40) reproduces exactly the ϕ^2 contribution given by the phase shift, while it neglects the contribution from the residual scattering among low-energy quasiparticles [212]. We believe that, in the slave-spin representation, the latter contribution arises from vertex corrections that are not included in the self-consistent mean-field theory.

7.6.2 Adiabatic dynamic induced by a time-dependent voltage

In the presence of a time-dependent voltage between the source and the drain contacts the single-particle energies become time-dependent: $\epsilon_k \to \epsilon_k - \phi_a(t)$ (here a label refers to the left L or right R lead) [130]. Starting, at $t = 0$, from an equilibrium configuration characterized by $\phi_L = \phi_R = 0$ ($N_L = N_R$) and a finite tunneling amplitude $V_{\mathbf{k}}$, we consider the evolution induced by a time-dependent electrochemical potential:

$$\phi_L(t) = \theta(t)\phi\frac{1 - e^{-t/t^*}}{2}, \quad \phi_R(t) = -\phi_L(t), \tag{7.41}$$

where t^* is the characteristic time scale of the external perturbation, ϕ is the asymptotic value of the voltage and $\theta(t)$ is the Heaviside step function such that $\phi_L(t) = 0$ for $t \leq 0$. To simplify the

calculations we consider the WBL (C.25). Hence, eq. (7.15) becomes:

$$\begin{aligned}\partial_t\langle\sigma^x(t)\rangle &= U\langle\sigma^y(t)\rangle/2,\\ \partial_t\langle\sigma^y(t)\rangle &= -2\langle H_{T,C}(t)\rangle\langle\sigma^z(t)\rangle - U\langle\sigma^x(t)\rangle/2,\\ \partial_t\langle\sigma^z(t)\rangle &= 2\langle H_{T,C}(t)\rangle\langle\sigma^y(t)\rangle,\end{aligned} \tag{7.42}$$

where the time-dependent average value of the hybridization is given by:

$$\langle H_{T,C}(t)\rangle = 2\sqrt{\frac{2}{V}}\sum_{\mathbf{k}\sigma}\mathrm{Re}\left(V_{\mathbf{k}}\langle\psi^\dagger_{1\mathbf{k}\sigma}(t)\, f_\sigma(t)\rangle\right). \tag{7.43}$$

The dynamics of the slave-spin variable (7.42) is coupled to the evolution of the fermionic degrees of freedom $\langle H_{T,C}(t)\rangle$, that evolve under the time-dependent effective resonant level model:

$$H^f_*(t) = H_C(t) + \langle\sigma^x(t)\rangle\, H_{T,C}.$$

The solution of the time-dependent problem is obtained by integrating Eq. (7.42) and the Heisenberg evolution of the single-particle density matrix $\langle\psi^\dagger_{1\mathbf{k}\sigma}(t)\, f_\sigma(t)\rangle$, which gives the self-consistent field acting of the slave-spin degrees of freedom. However, under the assumption of a slowly varying external perturbation, i.e. $t^*T_K \gg 1$, it is possible to obtain the solution of the dynamics (7.42) by performing a controlled expansion around the quasistatic approximation. To this aim we notice that Eq. (7.43) can be written as:

$$\begin{aligned}\langle H_{T,C}(t)\rangle &= \frac{2}{\langle\sigma^x(t)\rangle}\sum_\sigma \mathrm{Im}\left[\int dt_1\, \Sigma^<_{f\sigma}(t,t_1)\, G^A_{f\sigma}(t_1,t)\right]\\ &= \frac{2}{\langle\sigma^x(t)\rangle}\sum_\sigma \mathrm{Im}\left[\int \frac{d\epsilon}{2\pi}\, \Sigma^<_{f\sigma}(t,\epsilon)\star G^A_{f\sigma}(t,\epsilon)\right],\end{aligned} \tag{7.44}$$

where in the last passage we perform the Wigner transform (D.4) and $\star$ is the Moyal product:

$$\star = \exp\left[i\frac{\overleftarrow{\partial}_\epsilon\overrightarrow{\partial}_t - \overleftarrow{\partial}_t\overrightarrow{\partial}_\epsilon}{2}\right],$$

for more details we refer to Appendix D.4. Under the assumption of $\phi(t)$ slowly varying function of time, i.e. $t^*T_K \gg 1$, we can assume that the temporal inhomogeneity is weak and only lowest-order terms in the variation are kept, the so-called gradient expansion [12, 229].

To the first-order in the temporal variation we have:

$$\begin{aligned}\langle H_{T,C}(t)\rangle &\simeq \frac{2}{\langle\sigma^x(t)\rangle}\mathrm{Im}\int\frac{d\epsilon}{\pi}\left[\Sigma^<_f(t,\epsilon)G^A_f(t,\epsilon) + \frac{i}{2}\left\{\Sigma^<_f(t,\epsilon), G^A_f(t,\epsilon)\right\}_{\epsilon,t}\right]\\ &= \langle H_{T,C}(t)\rangle^{(0)} + \langle H_{T,C}(t)\rangle^{(1)},\end{aligned} \tag{7.45}$$

where $\{f,g\}_{\epsilon,t} = \partial_\epsilon f\,\partial_t g - \partial_t f\,\partial_\epsilon g$, more details can be found in Appendix D.4.

The evolution of the pseudospin variable at zero order in the gradient expansion Eq. (7.45) is displayed in Fig. 7.3. In the limit of $t^*T_K \gg 1$ we observe, as expected, the quasistatic dynamics, i.e. the system follows the change of $\mu(t)$ adiabatically. However, for any smaller value of t^*T_K the evolution is characterized by persistent oscillations, that become, eventually, centered around the steady-state result represented by the solid black line.

It is interesting to observe that the first-order correction, given by the latter term in Eq. (7.45), introduces damping in Eq. (7.42) and the dynamics converge to the expected stationary regime. This is shown in Fig. 7.4, where we compare the time-dependent average value of the current obtained within the zero and first order in the gradient expansion.

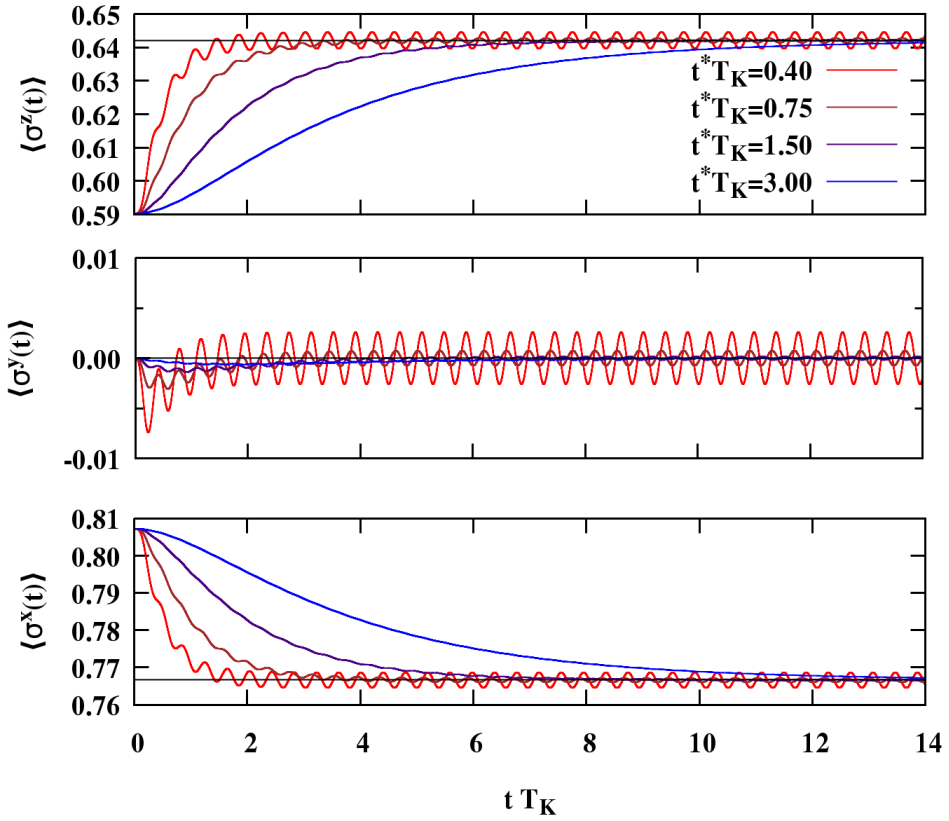

Figure 7.3: From top to bottom: evolution of $\langle\sigma^z(t)\rangle$, $\langle\sigma^y(t)\rangle$ and $\langle\sigma^x(t)\rangle$ as a function of $t\,T_K$ for several values of the external voltage time scale t^*, $U/W = 0.1$, $2\Gamma_0/U = 0.06$ and $\phi/U = 0.05$. Solid black line represents the steady-state result for the same set of parameters.

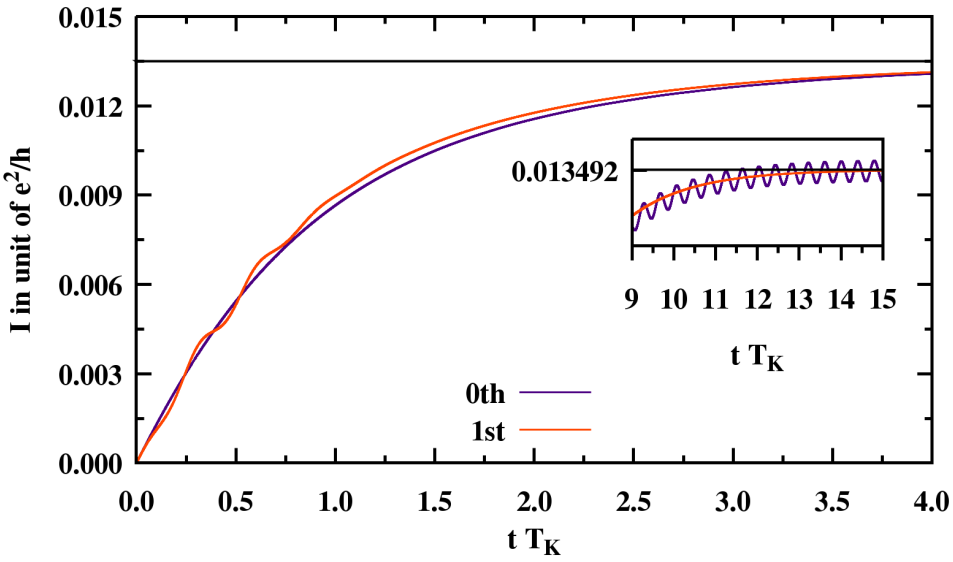

Figure 7.4: Time-dependent average value of the current as a function of $t\,T_K$ for $t^*T_K = 1.5$, $U/W = 0.1$, $2\Gamma_0/U = 0.06$ and $\phi/U = 0.05$. Orange and purple lines represent the evolution of the current obtained within the first and zeroth order in the gradient expansion. As shown from the inset, the first order corrections to the quasistatic approximation introduce relaxation processes that suppress the residual oscillations.

7.7 The slave-spin mapping for coupled quantum dots

We consider the problem of two quantum dots coupled via a tunneling amplitude (double quantum dot). Besides the energy scale $\Gamma(\epsilon)$ the model is characterized by an additional parameter $t_\perp$ that competes against the Kondo screening, see Fig. 7.5. A rich phase diagram emerges out of this competition, which is characterized by a crossover regime that separates the phase in which the impurity magnetic moments are quenched by Kondo screening from that in which the quenching is due to the antiferromagnetic coupling generated via superexchange processes [7, 135, 149].

We can model the double quantum dot as a two impurity Anderson model

$$\begin{aligned} H(U_1,U_2,\mu_{1\sigma},\mu_{2\sigma},t_{\perp\sigma},\Delta_{\perp\sigma}) = &\sum_{i=1}^{2}\left[\sum_\sigma\left(H_C^{i\sigma}+H_{T,C}^{i\sigma}-\mu_{i\sigma}\rho_{i\sigma}\right)+\frac{U_i}{4}\rho_{i\uparrow}\rho_{i\downarrow}\right] \\ &-\sum_\sigma t_{\perp\sigma}\left(d_{1\sigma}^\dagger d_{2\sigma}+d_{2\sigma}^\dagger d_{1\sigma}\right) \\ &-\sum_\sigma \Delta_{\perp\sigma}\left(d_{1\sigma}^\dagger d_{2\sigma}^\dagger+d_{2\sigma}d_{1\sigma}\right) \end{aligned} \tag{7.46}$$

where for convenience, in addition to the normal tunneling $t_{\perp\sigma}$, we include also the superconductive pairing $\Delta_{\perp\sigma}$. Only at the end we will set $\Delta_{\perp\sigma} = 0$ to zero, $t_{\perp\uparrow} = t_{\perp\downarrow} = t_\perp$ and $U_1 = U_2 = U$. In Eq. (7.46) $H_C^{i\sigma}$ is defined in (7.2) where indices i and σ refer to the contact and the spin projection, $H_{T,C}^{i\sigma}$, defined in (7.3), describes the spin σ tunnel-coupling between the contact i and the respective quantum dot, $\rho_{i\sigma} = 2n_{i\sigma} - 1$ where $n_{i\sigma} = d_{i\sigma}^\dagger d_{i\sigma}$ is the number operator on the quantum dot. Moreover, we assume that the hybridization function $\Gamma(\epsilon)$ is even as a function of ϵ: $\Gamma(\epsilon) = \Gamma(-\epsilon)$. Before considering the slave-spin mapping, let us introduce the Majorana

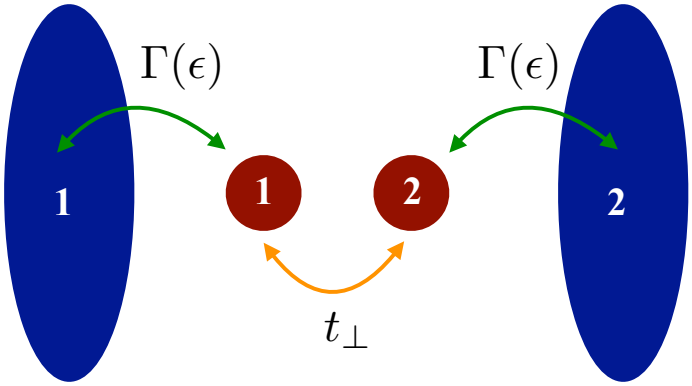

Figure 7.5: Two-impurity Anderson model. Each impurity is coupled to the respective metallic contact with hybridization function $\Gamma(\epsilon)$, where $\Gamma(\epsilon) = \Gamma(-\epsilon)$. We add a tunnel coupling amplitude between the dots.

fermions $\gamma_{i\sigma}$ and $\xi_{i\sigma}$:

$$d_{i\sigma} = \frac{\gamma_{i\sigma} + i\xi_{i\sigma}}{2}, \quad d^\dagger_{i\sigma} = \frac{\gamma_{i\sigma} - i\xi_{i\sigma}}{2},$$

such that the coupling between the two quantum dots can be written as:

$$\begin{aligned} T(t_{\perp\sigma}, \Delta_{\perp\sigma}) &= -\sum_\sigma t_{\perp\sigma}\left(d^\dagger_{1\sigma}d_{2\sigma} + d^\dagger_{2\sigma}d_{1\sigma}\right) - \sum_\sigma \Delta_{\perp\sigma}\left(d^\dagger_{1\sigma}d^\dagger_{2\sigma} + d_{2\sigma}d_{1\sigma}\right) \\ &= -i\sum_\sigma \left(\lambda_{1\sigma}\gamma_{1\sigma}\xi_{2\sigma} + \lambda_{2\sigma}\gamma_{2\sigma}\xi_{1\sigma}\right) = T(\lambda_{1\sigma}, \lambda_{2\sigma}) \end{aligned}$$

where $\lambda_{1\sigma} = (t_{\perp\sigma} - \Delta_{\perp\sigma})/2$ and $\lambda_2 = (t_{\perp\sigma} + \Delta_{\perp\sigma})/2$. We consider the particle-hole transformation $C_{i\sigma}$, defined as:

$$C_{i\sigma} : \left\{\left(d_{i\sigma} \to d^\dagger_{i\sigma}\right) \bigcup \prod_{\mathbf{k}} \left(\psi_{i\mathbf{k}\sigma} \to -\psi^\dagger_{i\mathbf{k}^*\sigma}\right)\right\}, \tag{7.47}$$

hence, by considering the spin orientation σ, we have

$$\begin{aligned} &C^\dagger_{1\sigma} H(U_1, U_2, \mu_{1\sigma}, \mu_{2\sigma}, \lambda_{1\sigma}, \lambda_{2\sigma}) C_{1\sigma} = H(-U_1, U_2, -\mu_{1\sigma}, \mu_{2\sigma}, \lambda_{1\sigma}, -\lambda_{2\sigma}), \\ &C^\dagger_{2\sigma} H(U_1, U_2, \mu_{1\sigma}, \mu_{2\sigma}, \lambda_{1\sigma}, \lambda_{2\sigma}) C_{2\sigma} = H(U_1, -U_2, \mu_{1\sigma}, -\mu_{2\sigma}, -\lambda_{1\sigma}, \lambda_{2\sigma}), \\ &C^\dagger_{2\sigma} C^\dagger_{1\sigma} H(U_1, U_2, \mu_{1\sigma}, \mu_{2\sigma}, \lambda_{1\sigma}, \lambda_{2\sigma}) C_{1\sigma} C_{2\sigma} = H(-U_1, -U_2, -\mu_{1\sigma}, -\mu_{2\sigma}, -\lambda_{1\sigma}, -\lambda_{2\sigma}), \end{aligned} \tag{7.48}$$

where, obviously, the component $-\sigma$ remains unchanged under particle-hole transformation $C_{i\sigma}$.

We introduce four Ising variables, one for each site i and spin σ configuration

$$\gamma_{i\sigma} = \tau^-_{i\sigma} f_{i\sigma} + \tau^+_{i\sigma} f^\dagger_{i\sigma}, \quad \xi_{i\sigma} = -i\tau^-_{i\sigma} f_{i\sigma} + i\tau^+_{i\sigma} f^\dagger_{i\sigma}, \tag{7.49}$$

where the physical subspace is selected by the projector operator:

$$\mathcal{P} = \prod_{i=1}^{2} \prod_{\sigma=\uparrow,\downarrow} \mathcal{P}_{i\sigma},$$

with

$$\mathcal{P}_{i\sigma} = \frac{1 + \tau^z_{i\sigma}\rho_{i\sigma}}{2}.$$

We can easily realize that different representations of the fermionic operators are allowed. Within the physical subspace we use this freedom to choose the representation where the role of the particle-hole transformation is simply played by $\tau^x_{i\sigma}$:

$$\gamma_{i\sigma} = \tau^x_{i\sigma}\,(f_{i\sigma} + f^\dagger_{i\sigma}), \quad \xi_{i\sigma} = -\tau^y_{i\sigma}\,(f_{i\sigma} + f^\dagger_{i\sigma}).$$

Within the previous representation the model Hamiltonian becomes:

$$\begin{aligned} H_*(U_1, U_2, \mu_{1\sigma}, \mu_{2\sigma}, \lambda_{1\,\sigma}, \lambda_{2\,\sigma}) = \sum_{i=1}^{2}\left[\sum_\sigma \left(H_C^{i\sigma} + \tau^x_{i\sigma}\, H_{T,C}^{i\sigma} - \mu_{i\sigma}\tau^z_{i\sigma}\right) + \frac{U_i}{4}\tau^z_{i\uparrow}\,\tau^z_{i\downarrow}\right] \\ + i\sum_\sigma \left(\lambda_{1\,\sigma}\tau^x_{1\sigma}\tau^y_{2\sigma} - \lambda_{2\sigma}\tau^x_{2\sigma}\tau^y_{1\sigma}\right)\gamma^f_{1\sigma}\gamma^f_{2\sigma} \end{aligned} \tag{7.50}$$

where $\gamma^f_{i\sigma} = f_{i\sigma} + f^\dagger_{i\sigma}$. Moreover, it is straightforward to prove that $\tau^x_{i\sigma}$ reproduces the same transformations (7.48) obtained by applying $C_{i\sigma}$ to the original Hamiltonian (7.46):

$$\begin{aligned} &\tau^x_{1\sigma}\, H(U_1, U_2, \mu_{1\sigma}, \mu_{2\sigma}, \lambda_{1\sigma}, \lambda_{2\sigma})\,\tau^x_{1\sigma} = H(-U_1, U_2, -\mu_{1\sigma}, \mu_{2\sigma}, \lambda_{1\sigma}, -\lambda_{2\sigma}), \\ &\tau^x_{2\sigma}\, H(U_1, U_2, \mu_{1\sigma}, \mu_{2\sigma}, \lambda_{1\sigma}, \lambda_{2\sigma})\,\tau^x_{2\sigma} = H(U_1, -U_2, \mu_{1\sigma}, -\mu_{2\sigma}, -\lambda_{1\sigma}, \lambda_{2\sigma}), \\ &\tau^x_{2\sigma}\tau^x_{1\sigma}\, H(U_1, U_2, \mu_{1\sigma}, \mu_{2\sigma}, \lambda_{1\sigma}, \lambda_{2\sigma})\,\tau^x_{1\sigma}\tau^x_{2\sigma} = H(-U_1, -U_2, -\mu_{1\sigma}, -\mu_{2\sigma}, -\lambda_{1\sigma}, -\lambda_{2\sigma}). \end{aligned} \tag{7.51}$$

This result allows us to remove the constraint from the evaluation of the partition function. Indeed,

$$Z(U_1, U_2, \mu_{1\sigma}, \mu_{2\sigma}, \lambda_{1\sigma}, \lambda_{2\sigma}) = \mathrm{Tr}\left[e^{-\beta H}\right] = \mathrm{Tr}\left[e^{-\beta H_*}\prod_{i=1}^{2}\prod_{\sigma=\uparrow,\downarrow}\mathcal{P}_{i\sigma}\right], \tag{7.52}$$

where we omit the Hamiltonian parameters to lighten the notation. By using the invariance of the trace under the unitary transformations and the results in (7.48) and (7.51), we can obtain:

$$Z(U_1, U_2, \mu_{1\sigma}, \mu_{2\sigma}, \lambda_{1\sigma}, \lambda_{2\sigma}) = \frac{1}{16}\mathrm{Tr}\left[e^{-\beta H_*}\right]. \tag{7.53}$$

Thus, we conclude that thermodynamic properties of the double quantum dot problem ($U_i = U, \lambda_{i\sigma} = t_\perp/2, \mu_{i\sigma} = 0$) can be obtained by studying the equivalent slave-spin Hamiltonian:

$$H_* = \sum_{i=1}^{2}\left[\sum_\sigma \left(H_C^{i\sigma} + \tau^x_{i\sigma}\, H_{T,C}^{i\sigma}\right) + \frac{U}{4}\tau^z_{i\uparrow}\,\tau^z_{i\downarrow}\right] + i\frac{t_\perp}{2}\sum_\sigma \left(\tau^x_{1\sigma}\tau^y_{2\sigma} - \tau^x_{2\sigma}\tau^y_{1\sigma}\right)\gamma^f_{1\sigma}\gamma^f_{2\sigma} \tag{7.54}$$

once again without any constraint on the enlarged Hilbert space $\mathscr{H}_*$. An interesting feature of the slave-spin model (7.54) is that the tunneling $t_\perp$ couples only the real components of the complex pseudofermions $f_{1\sigma}$ and $f_{2\sigma}$. This result resembles the physics observed in the two channel Kondo model where half of the impurity degree of freedom remains disentangled and gives rise to a finite entropy at zero temperature [5, 75]. Despite the absence of superconductive correlations in the original model (7.46), we notice that the slave-spin representation (7.54) presents superconductive pairing $\sim \left(f^\dagger_{1\sigma}f^\dagger_{2\sigma} + f_{2\sigma}f_{1\sigma}\right)$. We conclude by observing that Hamiltonian (7.54) is symmetric under the Z_2 transformation $\tau^z_{i\sigma}\rho_{i\sigma}$.

To start our analysis let us check if the slave-spin model reproduces correctly the atomic limit, $\Gamma(\epsilon) = 0$.

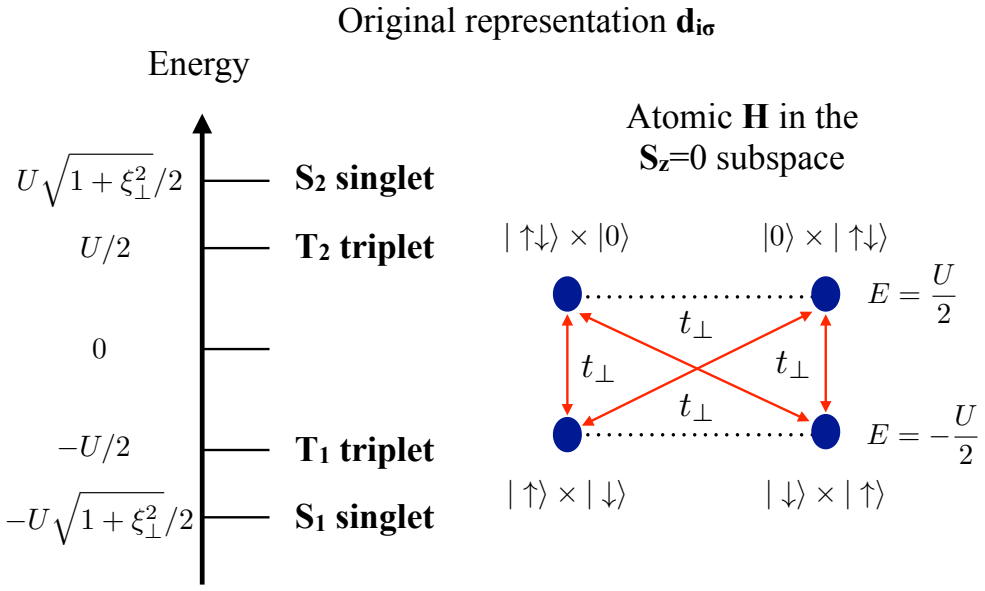

Figure 7.6: In the absence of the bath the model reduces to the H_2 molecule. We report the tunnel processes connecting different configurations on the double quantum dots and the spectrum of the subspace characterized by $S^z = 0$ and vanishing charge $Q = \sum_\sigma \sum_{i=1}^2 n_{i\sigma} - 2 = 0$.

7.7.1 The atomic limit: the H_2 molecule

In the absence of hybridization with the contacts the Hamiltonian (7.54) reduces to:

$$H_* = \frac{U}{4}\sum_{i=1}^{2} \tau_{i\uparrow}^z \tau_{i\downarrow}^z + i\frac{t_\perp}{2}\sum_\sigma \left(\tau_{1\sigma}^x \tau_{2\sigma}^y - \tau_{2\sigma}^x \tau_{1\sigma}^y\right)\gamma_{1\sigma}^f \gamma_{2\sigma}^f \tag{7.55}$$

and in the following we will show that the model (7.55) reproduces the characteristic spectrum shown in Fig. 7.6.

In the original representation, see Fig. 7.6, the ground state is invariant under the inversion $1 \leftrightarrow 2$ is a singlet $S^2 = 0$ and reads:

$$|GS\rangle = \frac{1}{2}\sqrt{1+\frac{1}{\sqrt{1+\xi_\perp^2}}}\left(d_{1\uparrow}^\dagger d_{2\downarrow}^\dagger + d_{2\uparrow}^\dagger d_{1\downarrow}^\dagger\right)|0\rangle + \frac{1}{2}\sqrt{1-\frac{1}{\sqrt{1+\xi_\perp^2}}}\left(d_{1\uparrow}^\dagger d_{1\downarrow}^\dagger + d_{2\uparrow}^\dagger d_{2\downarrow}^\dagger\right)|0\rangle\,, \tag{7.56}$$

with energy $E_{gs} = -U\sqrt{1+\xi_\perp^2}/2$, where $\xi_\perp = 4t_\perp/U$. We observe that $\gamma_{1\sigma}^f \gamma_{2\sigma}^f$ commutes with the slave-spin Hamiltonian and does not have any quantum dynamics. By assuming that the inversion symmetry $1 \leftrightarrow 2$ is preserved we define:

$$J_\perp(\sigma) = -i\frac{t_\perp}{2}\left\langle \gamma_{1\sigma}^f \gamma_{2\sigma}^f \right\rangle,$$

and the effective spin model reduces to:

$$H_*^\tau = \frac{U}{4}\sum_{i=1}^{2} \tau_{i\uparrow}^z \tau_{i\downarrow}^z - 2i\sum_\sigma J_\perp(\sigma)\left(\tau_{1\sigma}^+ \tau_{2\sigma}^- - \tau_{2\sigma}^- \tau_{1\sigma}^+\right). \tag{7.57}$$

In the regime of $U > t_\perp$, we can easily realize that the low-energy configurations are:

$$\{|+,-\rangle \times |+,-\rangle, |+,-\rangle \times |-,+\rangle, |-,+\rangle \times |+,-\rangle, |-,+\rangle \times |-,+\rangle\}.$$

We clearly observe that the two configurations in the middle are coupled by the $J_\perp(\sigma)$ to the high-energy configurations $\{|+,+\rangle\times|-,-\rangle, |-,-\rangle\times|+,+\rangle\}$. It is convenient to define the symmetric and antisymmetric combinations:

$$\begin{aligned} |\varphi_{S/A}\rangle &= \frac{|+,-\rangle\times|-,+\rangle \pm |-,+\rangle\times|+,-\rangle}{\sqrt{2}}, \\ |\eta_{S/A}\rangle &= \frac{|+,+\rangle\times|-,-\rangle \pm |-,-\rangle\times|+,+\rangle}{\sqrt{2}}. \end{aligned} \tag{7.58}$$

There are two different solutions depending on the value of $J_\perp(\sigma)$.

Spin-independent solution; Let us assume that the lambda σ parameter is spin independent, such that:

$$J_\perp(\sigma) = -\frac{t_\perp}{2}.$$

In this case $t_\perp$ couples the state $|\varphi_S\rangle$ to $|\eta_A\rangle$, while $|\varphi_A\rangle$ and $|\eta_S\rangle$ are eigenstates of the Hamiltonian (7.57) with energies $\pm U/2$ and correspond to the triplet configurations $T_{1/2}$. In the subspace of $|\varphi_S\rangle$ to $|\eta_A\rangle$ the Hamiltonian reads:

$$H_*^\tau = \begin{pmatrix} -U/2 & -2it_\perp \\ 2it_\perp & U/2 \end{pmatrix}.$$

The ground state is

$$|\chi_{gs}\rangle = i\sqrt{\frac{1}{2}+\frac{1}{2\sqrt{1+\xi_\perp^2}}}\,|\varphi_S\rangle + \sqrt{\frac{1}{2}-\frac{1}{2\sqrt{1+\xi_\perp^2}}}\,|\eta_A\rangle,$$

with energy

$$E_{gs} = -U\sqrt{1+\xi_\perp^2}/2.$$

Spin-dependent solution; Differently from the previous case, we consider a spin dependent:

$$J_\perp(\sigma) = -\frac{t_\perp}{2}\sigma.$$

In this case $|\varphi_S\rangle$ and $|\eta_A\rangle$ are eigenstates of (7.57) with energies $\pm U/2$, while $|\varphi_A\rangle$ and $|\eta_S\rangle$ are mixed by $t_\perp$:

$$H_* = \begin{pmatrix} -U/2 & 2it_\perp \\ -2it_\perp & U/2 \end{pmatrix}.$$

Thus, the ground state reads

$$|\chi_{gs}\rangle = -i\sqrt{\frac{1}{2}+\frac{1}{2\sqrt{1+\xi_\perp^2}}}\,|\varphi_A\rangle + \sqrt{\frac{1}{2}-\frac{1}{2\sqrt{1+\xi_\perp^2}}}\,|\eta_S\rangle,$$

with energy given by $E_{gs} = -U\sqrt{1+\xi_\perp^2}/2$.

Connection with average values of physical observables; Both spin-dependent and independent $J_\perp(\sigma)$ solve the atomic problem giving the same spectrum as the one obtained in the original representation[2], Fig. 7.6. In the slave-spin formalism the double occupancy operator $D = \sum_{i=1}^{2} n_{i\uparrow} n_{i\downarrow}$ reads:

$$\mathcal{D} = \sum_i \frac{(1+\tau^z_{i\uparrow})(1+\tau^z_{i\downarrow})}{4}. \tag{7.59}$$

Whilst, the bonding charge between the impurity sites, $K_\sigma = d^\dagger_{1\sigma} d_{2\sigma} + \text{H.c.}$, is given by:

$$\mathcal{K}_\sigma = -i\gamma^f_{1\sigma}\gamma^f_{2\sigma}(\tau^x_{1\sigma}\tau^y_{2\sigma} - \tau^y_{1\sigma}\tau^x_{2\sigma})/2.$$

It is straightforward to check that independently from the choice of $J_\perp(\sigma)$:

$$\langle \chi_{gs} | \mathcal{D} | \chi_{gs} \rangle = \frac{1}{2} - \frac{1}{2\sqrt{1+\xi^2_\perp}}, \tag{7.60}$$

and

$$\langle \chi_{gs} | \mathcal{K} | \chi_{gs} \rangle = \sum_\sigma \langle \chi_{gs} | \mathcal{K}_\sigma | \chi_{gs} \rangle = 2\frac{\xi_\perp}{\sqrt{1+\xi^2_\perp}}, \tag{7.61}$$

in agreement with the results obtained in the original representation.

7.7.2 Mean-field solution

In the opposite regime of vanishing tunneling, $t_\perp = 0$, and $\Gamma(\epsilon = 0) \neq 0$ the two quantum dots are decoupled and each is Kondo screened by the respective bath. From the previous calculations performed in Section 6.4 we know that the $T = 0$ equilibrium ground state is characterized by $\langle \tau^x_{i\sigma} \rangle \neq 0$ and breaks the $(Z_2)^4$ symmetry by choosing one of the 16 degenerate minima. The perturbation introduced by $t_\perp$ goes like $\sim \left(\tau^x_{1\sigma}\tau^y_{2\sigma} - \tau^y_{1\sigma}\tau^x_{2\sigma}\right)$ and, therefore, couples the different minima giving rise to a new ground state with lower energy. We expect that, by increasing $t_\perp$, the ground state solution would evolve smoothly from the asymptotic configuration of pure Kondo screening realized at $t_\perp = 0$, to the singlet one $t_\perp \gg \Gamma(\epsilon)$.

In spite of the absence of a clear hierarchy of energy scales between $\boldsymbol{\tau}_{i\sigma}$ and $f_{i\sigma}$ in Hamiltonian (7.54), we can look for the best mean-field ground state:

$$|\Psi\rangle = |\chi\rangle \times |\Phi\rangle$$

where $|\chi\rangle$ is the Ising part, while $|\Psi\rangle$ the fermionic one. The mean-field Hamiltonian for the Ising degrees of freedom reads:

$$H^\tau_* = \frac{U}{4}\sum_{i=1}^{2} \tau^z_{i\uparrow}\tau^z_{i\downarrow} - \sum_{i=1}^{2}\sum_\sigma \mathcal{B}_{i\sigma}\tau^x_{i\sigma} - \sum_\sigma J_\perp(\sigma)\left(\tau^x_{1\sigma}\,\tau^y_{2\sigma} - \tau^y_{1\sigma}\,\tau^x_{2\sigma}\right), \tag{7.62}$$

where:

$$\begin{aligned} &\mathcal{B}_{i\sigma} \equiv -\langle H^{i\sigma}_{T,C} \rangle, \\ &J_\perp(\sigma) \equiv -it_\perp \left\langle \gamma^f_{1\sigma}\gamma^f_{2\sigma} \right\rangle /2. \end{aligned} \tag{7.63}$$

The latter fermionic average values are determined by the effective resonant level-model

$$H^f_* = \sum_{i=1}^{2}\sum_\sigma \left[H^{i\sigma}_C + \langle \tau^x_{i\sigma} \rangle H^{i\sigma}_{T,C}\right] - i\sum_\sigma \lambda_\perp(\sigma)\,\gamma^f_{1\sigma}\,\gamma^f_{2\sigma}, \tag{7.64}$$

[2]Overall, considering spin σ and site i degrees of freedom there are 16 different equivalent representations and each of them reproduces the atomic spectrum.

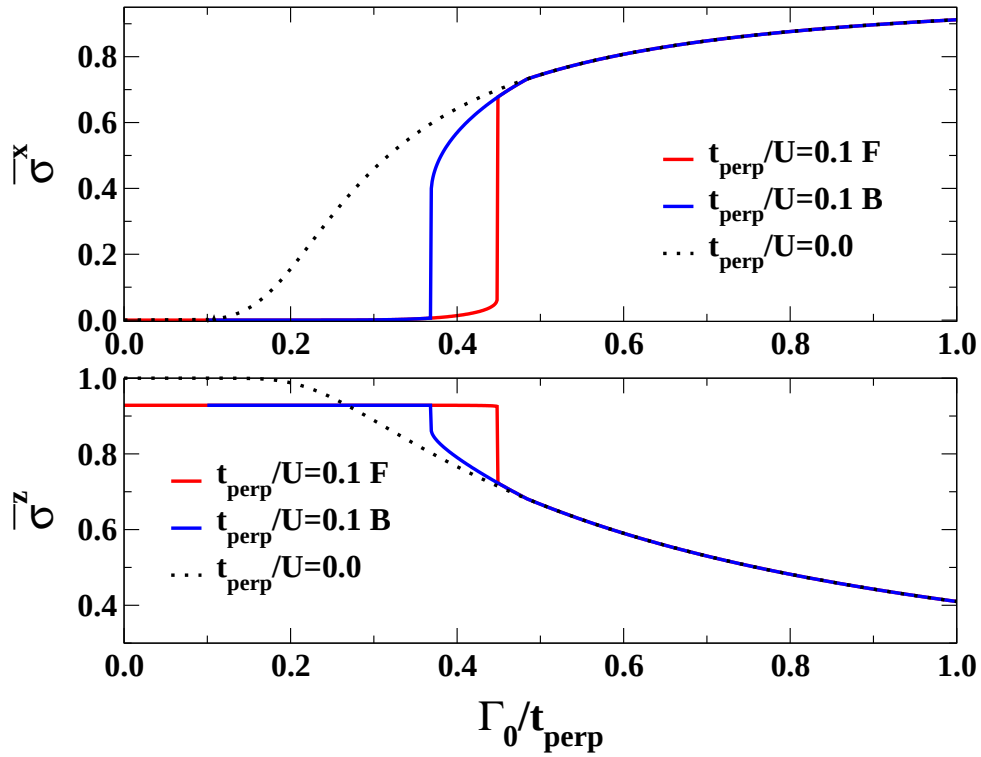

Figure 7.7: Top panel: the dotted black line represents $\langle\tau^x\rangle$ as a function of $\Gamma_0/t_\perp$ for a single dot. Blue and red lines describe $\langle\tau^x\rangle$ as a function of $\Gamma_0/t_\perp$ coming from large and small values of $\Gamma_0/t_\perp$, respectively. Bottom panel: the same as top panel but for $\langle\tau^z\rangle$.

where we have introduced the self-consistent coupling:

$$\lambda_\perp(\sigma) \equiv -\frac{t_\perp}{2}\left(\left\langle\tau^x_{1\sigma}\,\tau^y_{2\sigma}\right\rangle - \left\langle\tau^y_{1\sigma}\,\tau^x_{2\sigma}\right\rangle\right).$$

Assuming that the ground state solution does not break $1 \leftrightarrow 2$ symmetry and the $\langle\tau^x_{i\sigma}\rangle$ does not depend on i and σ, we find:

$$\begin{aligned}\left[\mathbf{G}^{\gamma\gamma}_\sigma(z)\right]^{-1} &= \frac{\sigma^0\left(i\epsilon - \langle\tau^x_\sigma\rangle^2\Delta(z)\right) - 2\sigma^y\lambda_\perp(\sigma)}{2},\\ \left[\mathbf{G}^{\xi\xi}_\sigma(z)\right]^{-1} &= \frac{\sigma^0\left(i\epsilon - \langle\tau^x_\sigma\rangle^2\Delta(z)\right)}{2},\end{aligned} \tag{7.65}$$

and $\mathbf{G}^{\xi\gamma}_\sigma(z) = \mathbf{G}^{\gamma\xi}_\sigma(z) = \mathbf{0}$. We notice that the Green's functions, written in terms of the Majorana fermions $\gamma^f_{i\sigma}$ and $\xi^f_{i\sigma}$, are 2×2 matrices in the site indices i, j, for instance:

$$G^{\gamma\gamma}_{ij,\sigma}(\tau) = -\left\langle T_\tau\left(\gamma^f_{i\sigma}(\tau)\,\gamma^f_{j\sigma}\right)\right\rangle.$$

After straightforward calculations we obtain:

$$\begin{aligned}\mathcal{B}_{i\sigma} = \mathcal{B}_\sigma &= -\frac{1}{2\langle\tau^x_\sigma\rangle}\int d\omega f(\omega)\left[\sum_{s=-1,+1}(\omega + 2s\lambda_\perp(\sigma))\,A_f(\omega+2s\lambda_\perp(\sigma)) + 2\omega A_f(\omega)\right],\\ J_\perp(\sigma) &= t_\perp\int d\omega\, f(\omega)\left[A_f(\omega-2\lambda_\perp(\sigma)) - A_f(\omega+2\lambda_\perp(\sigma))\right],\end{aligned} \tag{7.66}$$

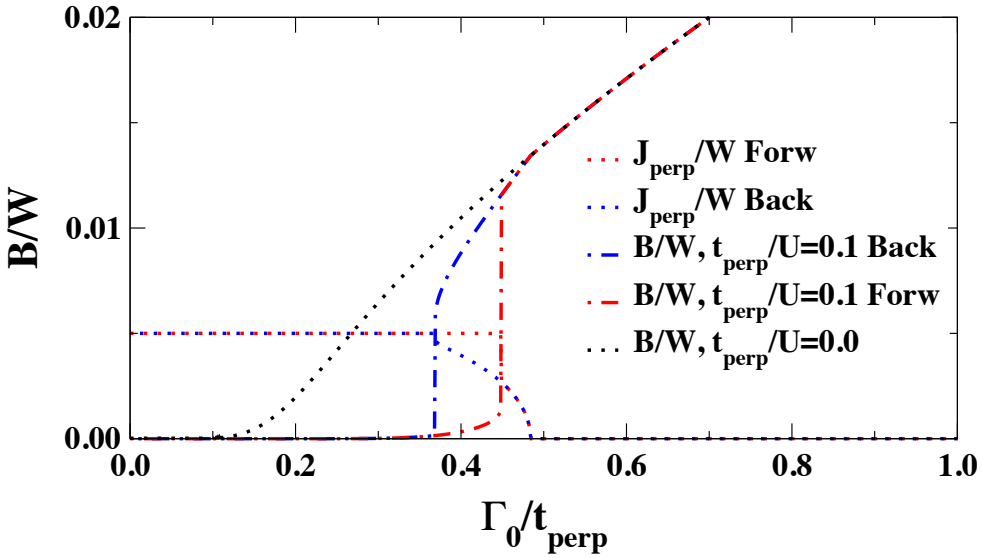

Figure 7.8: The dotted black line represents J/D as a function of Γ_0 in the absence of tunnel-coupling amplitude $t_\perp = 0$. Blue and red dashed lines describe $\mathcal{B}_\sigma/W$ as a function of $\Gamma_0/t_\perp$ coming from the Kondo screened phase (large $\Gamma_0/t_\perp$) and the singlet one (small $\Gamma_0/t_\perp$), respectively. Finally, blue and red dotted lines describe $J_\perp/D$ as a function of $\Gamma_0/t_\perp$.

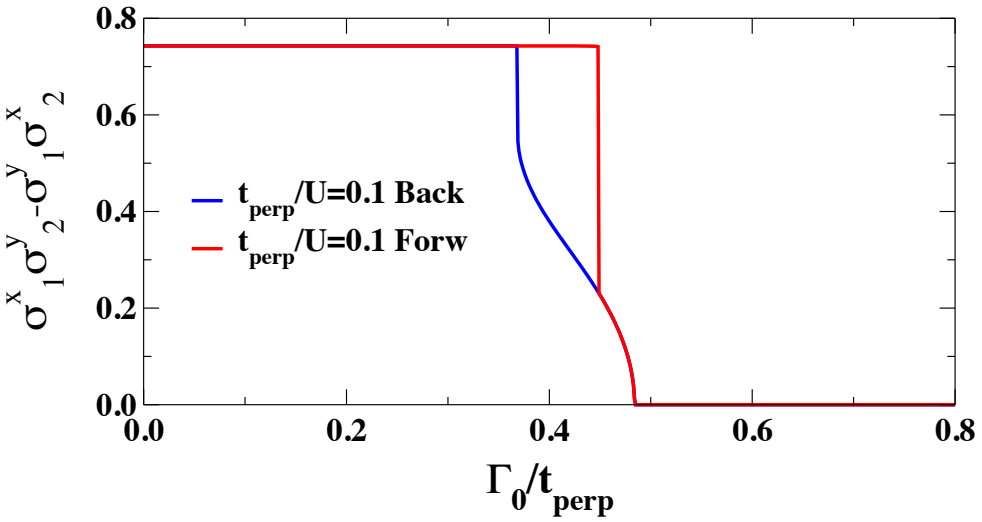

Figure 7.9: $\langle \tau_1^x \tau_2^y \rangle - \langle \tau_1^y \tau_2^x \rangle$ as a function of $\Gamma_0/t_\perp$. Blue and red lines are obtained coming from large (backward) and small (forward) values of $\Gamma_0/t_\perp$, respectively.

where we have introduced:

$$A_f(\omega) = -\frac{1}{2\pi i}\left[\frac{1}{\omega - \langle\tau^x\rangle^2\Delta^R(\omega)} - \frac{1}{\omega - \langle\tau^x_\sigma\rangle^2\Delta^A(\omega)}\right].$$

The numerical solution of the mean-field equations is obtained by proposing an initial value for $\mathcal{B}_\sigma$ and $J_\perp(\sigma)$, and then solving for the ground state the spin Hamiltonian (7.62). The spin ground state allows us to compute $\lambda_\perp(\sigma)$ and $\langle\tau^x_\sigma\rangle$ and, therefore, the updated values of $\mathcal{B}_\sigma$ and $J_\perp(\sigma)$ via Eq. (7.66). By iterating the procedure we evolve toward a fixed point that corresponds to the mean-field ground state.

Numerical results, obtained for a flat hybridization function $\Gamma(\omega) = \Gamma_0\theta(W - |\omega|)$, are shown in Figs. 7.7, 7.8 and 7.9. We notice that for $\Gamma_0/t_\perp > 1$ the ground state is Kondo screened and the two impurities are decoupled, signalized by a vanishing value of $\left\langle\tau^x_{1\sigma}\,\tau^y_{2\sigma}\right\rangle - \left\langle\tau^y_{1\sigma}\,\tau^x_{2\sigma}\right\rangle$ in Fig. 7.9. On the contrary, for $\Gamma_0/t_\perp \ll 1$ the solution is the singlet phase, where the two impurities are decoupled from the bath. We observe that in Fig. 7.8 we report the evolution of the effective coupling constants $J_\perp$ and $\mathcal{B}$ obtained by following the mean-field solution starting from the singlet phase (red lines) and Kondo screened one (blue lines).

The first order character is highlighted by the hysteresis cycle observed by following the mean-field solution starting from small and large values of $\Gamma_0/t_\perp$.

The slave-spin mean-field theory predicts a first order transition at a critical value of the ratio $\Gamma_0/t_\perp \sim 0.4$ for $U/W = 0.1$. A similar result was obtained with slave-boson mean-field theory, see Ref. [7].

7.8 Conclusions

We have shown that the out of equilibrium evolution of a quantum dot (7.1) can be studied in the slave-spin representation (7.6) without any constraint on the enlarged Hilbert space. The advantages of the new representation are twofold. On one side, we disentangle the charge and spin degrees of freedom. On the other side, we avoid the mean-field mixing of unphysical and physical subspaces, that affects the time evolution of other slave-particle techniques. In the steady-state regime the self-consistent Hartree-Fock decoupling is able to predict the properties of the model even deep inside the large-U Kondo regime. Specifically, the conductance shows both the known zero-bias anomaly but also the expected peak at bias of order U. Furthermore, we have extended the slave-spin approach to study the transient dynamics of a driven magnetic impurity. It is important to observe that the time-dependent slave-spin approach can be applied to study the dynamics in quantum dots for any nonequilbrium protocol, e.g. periodic driving, quantum quench, etc. For simplicity we apply the above method to study the dynamics induced by slowly varying chemical potential applied to the metallic contacts. After a characteristic time, which depends on the product $T_K\,t_*$ between T_K and the time scale of the external perturbation t_*, the dynamics relax to the nonequilibrium steady-state.

We mention that the technique, presented in this Chapter, can be applied to study the out of equilibrium of quantum dots with L and R leads characterized by different tunneling amplitude Γ_L and Γ_R by using the generalized mapping presented in Section 6.3. Moreover, it is also possible to study multi-orbital quantum dots by exploiting the mapping presented in Section 6.3.2.

The slave-spin has been further extended to the case of transport in a double quantum dots coupled via a tunnel amplitude $t_\perp$. Despite the promising form of the slave-spin Hamiltonian, preliminary equilibrium mean-field calculations predict a first order transition from the Kondo

screened phase to the singlet one. Higher order effects have to be included in order to reproduce the expected crossover behavior between the two phases.

8

Probing Majorana edge states by charge transport across a magnetic impurity

Motivated by recent experiments we consider transport across an interacting magnetic impurity coupled to the Majorana zero mode (MZM) observed at the boundary of a topological superconductor (SC). In the presence of a finite tunneling amplitude we observe hybridization of the MZM with the quantum dot, which is manifested by a half-integer zero-bias conductance $G_0 = e^2/2h$ measured on the metallic contacts. The low-energy feature in the conductance drops abruptly by crossing the transition line from the topological to the non-topological superconducting regime. Differently from the in-gap Yu-Shiba-Rosinov-like bound states, which are strongly affected by the on-site impurity Coulomb repulsion, we show that the MZM signature in the conductance is robust and persists even at large values of the interaction. Notably, the topological regime is characterized by a vanishing Fano factor induced by the MZM. We propose an experimental set-up to measure the conductance and the shot-noise in order to detect the topological properties of the superconducting wire and to distinguish the low-energy contribution of a MZM from other possible sources of zero-bias anomaly. Despite being interacting, the model is exactly solvable, which allows us to have an exact characterization of the charge transport properties of the junction.

8.1 Introduction

In a seminal paper [148], Kitaev pointed out the existence of electronic collective modes reminiscent of the Majorana fermions, speculated in 1937 by Ettore Majorana [180], in a simple many-body system: a one-dimensional (1D) chain of spinless fermions with a p-wave pairing. The key ingredient is the superconductive pairing induced in the 1D system by the proximity to a superconductive reservoir. Stimulated by this remarkable results, quasi 1D systems, hosting two or more Majorana zero modes (MZMs), have attracted both experimental [9, 62, 66, 79, 110, 116, 178, 199, 208, 293] and theoretical [90, 127, 216, 233] interest. One among them worth mentioning is the experiment in Ref. [62], where the authors studied semiconducting wires made of InAs, characterized by a strong spin-orbit coupling interaction, in proximity to an Al s-wave superconductor and in the presence of high magnetic fields. The confining electric field acting on the electrons in the wire induces the Rashba spin-orbit coupling (SOC),

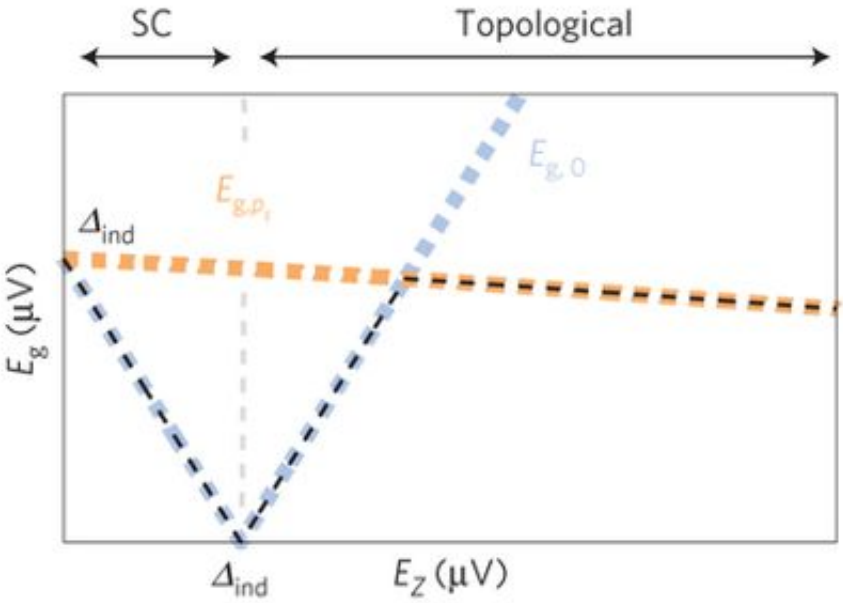

Figure 8.1: The evolution of the energy gap at $p = 0$ (dotted blue), at p_F (dotted yellow), and the overall energy gap (dashed black) with Zeeman energy, E_Z. Taken from [62].

that forms chiral states characterized by spin-orientation related to the momentum direction. The combined effect of the proximity induced pairing potential, the external magnetic field and the Rashba SOC produces an interesting phase diagram. As shown in Fig. 8.1 there is a critical magnetic field E_z where gap closes and the system enters in the topological phase. In correspondence of the topological region, the transport measurements show the presence of a zero bias anomaly which can be associated to Majorana zero modes (MZMs) at the edge of the wire.

From a quantum computing perspective MZMs can realize qubits, topologically protected against disorder, and local perturbations. Intrigued by the exciting possibility of manipulating, and realizing MZMs [10, 11, 204], theoretical studies focused on zero-bias and current measurement across a junction of metallic leads and topological superconductors (SCs) [3, 4, 55, 56, 85, 97, 113, 220], shot noise measurement [68, 98], interferometer measurement [67], persistent current in hybrid normal-superconducting rings [129, 202, 203, 221] and topological realization of the Kondo effect [32, 76, 77]. Recently, a new direction has emerged which explores the interplay between pure Majorana physics and electronic correlations [6, 52, 226, 227].

In this Chapter we fully characterize the electronic transport through a novel class of experimentally realizable systems [66, 293] which have recently attracted great interest for their easily realization and control. The MZM, emerging at the endpoint of a 1D semi-infinite wire with strong spin-orbit interaction (i.e. InAs wire) deposited on top of a s-wave SC and exposed to an external magnetic field, is coupled to an interacting magnetic impurity that can be used as a spectrometer. Hence, we probe the properties of the MZM though measurement of the current and the shot noise across the junction.

8.2 The Model Hamiltonian

To model the junction displayed in Fig. 8.2 we consider the Hamiltonian

$$H = H_{\text{imp}} + H_C + H_K + H_{T,C} + H_{T,K}, \tag{8.1}$$

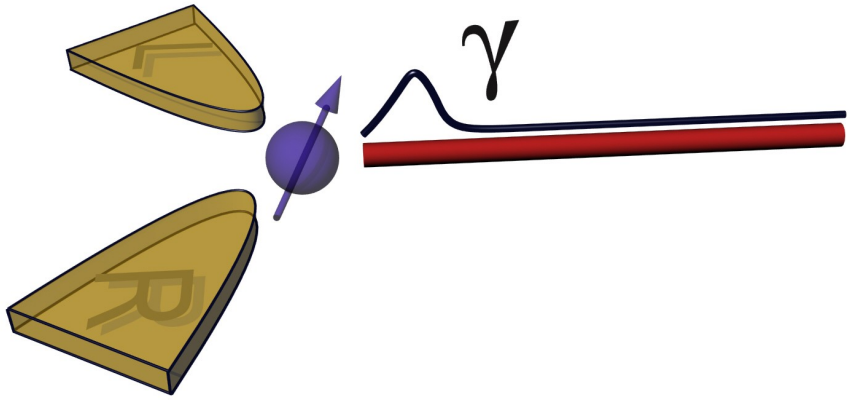

Figure 8.2: Sketch of a quantum dot coupled to two fully-polarized metallic leads and a semi-infinite topological p-wave SC hosting a MZM at its edge.

where

$$H_{\text{imp}} = -\frac{U}{4}\Omega_d - \frac{h}{2}\left(n_\uparrow^d - n_\downarrow^d\right) + \frac{\mu}{2}\left(n_\uparrow^d + n_\downarrow^d - 1\right) \tag{8.2}$$

is the dot Hamiltonian, with $n_\sigma^d = d_\sigma^\dagger d_\sigma$ the number operator on the impurity site and $\Omega_d = -(2n_\uparrow^d - 1)(2n_\downarrow^d - 1)$. In (8.2) U denotes the on-site interaction, μ the gate potential and h the Zeeman field applied on the dot level. The Hamiltonian of the semi-infinite Kitaev chain reads

$$H_K = \sum_{j=1}^{\infty}[(-tc_j^\dagger c_{j+1} + \Delta c_j c_{j+1} + \text{H.c.}) - \mu c_j^\dagger c_j] \tag{8.3}$$

where t is the hopping amplitude between nearest neighbor sites, Δ the p-wave superconducting pairing and μ the chemical potential of the wire. We notice that left (L) and right (R) metallic contacts are described by Hamiltonian (8.3) with $\Delta = 0$ and different electrochemical potentials $\mu_L = -\mu_R = \phi/2$. In our model both the Kitaev and the metallic chains are described by spinless particles. This is a reasonable assumption if one considers that topological SCs are realized in systems which are characterized by a strong spin-orbit coupling and large magnetic fields, and if we assume fully-polarized ferromagnetic contacts. In this regime the magnetic exchange between the impurity spin and the leads is suppressed and the low-energy physics is dominated by the coupling with the MZM [53, 122, 167, 261, 285]. The tunneling between the dot and the metallic contacts reads:

$$H_{T,C} = V_c \sum_{\alpha=L,R}\left(c_{1\alpha}^\dagger d_\uparrow + \text{H.c.}\right) \tag{8.4}$$

where V_c is the tunneling amplitude and $\alpha = L, R$. Finally, we consider the hybridization with the boundary site of the semi-infinite Kitaev chain:

$$H_{T,K} = -i\sum_j V_j \gamma_j \gamma_\uparrow^d, \tag{8.5}$$

where the sum extends to the semi-infinite Kitaev chain and we have introduced the Majorana operators $\gamma = c + c^\dagger$ and $\xi = -i(c - c^\dagger)$. The simple model in Eq. (8.5) allows us to study exactly the effect of correlations on the non-local Majorana edge state tunnel-coupled to an interacting quantum dot.

The interacting model is exactly solvable because the $d_\downarrow$ electrons are localized and $n_\downarrow^d$ can be treated as a Z_2 real number (= 0, 1). This property makes the Hamiltonian (8.1) an effective

quadratic model, where similarly to the Falicov-Kimball model (FKM) [84] the $\downarrow$ configuration is obtained by minimizing the ground-state energy of the $\uparrow$ degrees of freedom.

In the absence of metallic contacts, $V_c = 0$, the equilibrium properties of the model in Eq. (8.1) has been already studied in Ref. [258]. In this thesis we consider the charge transport properties of the junction obtained by measuring both the charge current and the shot noise. Before entering the discussion, we reshape the Hamiltonian into a convenient form. In particular we perform the gauge transformation:

$$\xi^{\eta}_{\uparrow} = \xi^{d}_{\uparrow}(1 - 2n^{d}_{\downarrow}), \quad \gamma^{\eta}_{\uparrow} = \gamma^{d}_{\uparrow}, \tag{8.6}$$

such that, in terms of $\gamma^{\eta}_{\uparrow}$ and $\xi^{\eta}_{\uparrow}$ fermions, the Hamiltonian (8.1) becomes:

$$\begin{aligned} H^{*} =& H_C + H_K - i\sum_j V_j \gamma_j \gamma^{\eta}_{\uparrow} - i\frac{U}{4}\gamma^{\eta}_{\uparrow}\xi^{\eta}_{\uparrow} - \frac{(\mu + h) - i(\mu - h)\gamma^{\eta}_{\uparrow}\xi^{\eta}_{\uparrow}}{4} q^{d}_{\downarrow} \\ &+ i\frac{V_c}{2}\sum_{\alpha=L,R}\left(\gamma^{\eta}_{\uparrow}\xi_{1\alpha} - q^{d}_{\downarrow}\xi^{\eta}_{\uparrow}\gamma_{1\alpha}\right). \end{aligned} \tag{8.7}$$

To avoid irrelevant complications we consider the case $\mu = h = 0$. Introducing the novel Dirac fermion $\eta_{\uparrow} = \gamma^{\eta}_{\uparrow} + i\xi^{\eta}_{\uparrow}$, the model Hamiltonian reads

$$H^{*} = H_C + H_K + \frac{1}{2}\sum_{\alpha=L,R}\left(\vec{\eta}^{\dagger}_{\uparrow}\cdot\hat{V}_c\cdot\vec{c}_{1\alpha} + \text{H.c.}\right) + \frac{1}{2}\sum_j\left(\vec{\eta}^{\dagger}_{\uparrow}\cdot\hat{V}_j\cdot\vec{c}_j + \text{H.c.}\right) - \frac{1}{2}\vec{\eta}^{\dagger}_{\uparrow}\cdot\frac{U}{2}\sigma^z\cdot\vec{\eta}_{\uparrow}, \tag{8.8}$$

where in the Nambu representation $\vec{\psi} = (\psi,\ \psi^{\dagger})^T$, $\hat{V}_j$ is the hybridization matrix between the dot and the j-th site of the Kitaev chain:

$$\hat{V}_j = iV_j\begin{pmatrix} 1 & 1 \\ 1 & 1 \end{pmatrix}, \tag{8.9}$$

and $\hat{V}_c$ couples the metallic contacts to the dot

$$\hat{V}_c = \frac{V_c}{2}\begin{pmatrix} (1 + q^{d}_{\downarrow}) & -(1 - q^{d}_{\downarrow}) \\ (1 - q^{d}_{\downarrow}) & -(1 + q^{d}_{\downarrow}) \end{pmatrix}. \tag{8.10}$$

To characterize the transport properties of the junction we compute the charge current, $I_Q = (I_L - I_R)/2$ with $I_\alpha = -i[N_\alpha, H]$, that in the new representation (8.6) reads:

$$I_Q = -i\frac{V_c}{4}\sum_{\alpha=L,R}\text{sign}(\alpha)\left[\gamma_{1\alpha}\gamma^{\eta}_{\uparrow} + q^{d}_{\downarrow}\xi_{1\alpha}\xi^{\eta}_{\uparrow}\right] \tag{8.11}$$

where $\text{sign}(L) = +1$ and $\text{sign}(R) = -1$, and the zero frequency limit of the I_Q fluctuations

$$S_Q = \int d(t - t')\frac{\langle\{\delta I_Q(t), \delta I_Q(t')\}\rangle}{2}, \tag{8.12}$$

with $\delta I_Q = I_Q - \langle I_Q\rangle$. In the following we study transport through the junction by performing calculations with Keldysh Green's function technique, see Appendix D or Refs. [114, 229], which we compare with the scattering matrix approach. For a detailed introduction to the latter technique we refer the interested reader to Refs. [34, 205, 209].

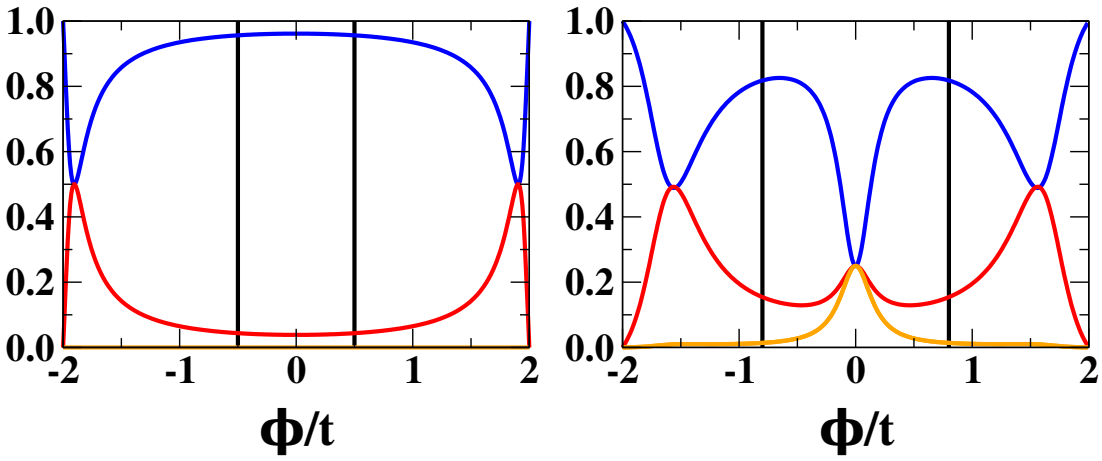

Figure 8.3: Scattering matrix coefficients for the system in Fig. 8.2 in the trivial regime (left panel) and in the topological one (right panel) at finite interaction $U/t = 1.6$. Blue: normal reflection; red: normal transmission, orange: Andreev reflection and crossed Andreev reflection. Vertical black lines show the "bulk" superconducting gap Δ_{gap}. The different scattering processes are summarized in Fig. 8.4.

8.3 Probing MZMs with charge conductance and shot noise

Experimental measurements of the charge conductance at the boundary of topological materials reveal the emergence of low-energy MZMs [9, 62, 66, 110, 178, 208, 293] and provide an experimental tool to detect topological transitions by studying surface states via scanning tunneling microscopy (STM) [70, 128, 170, 201, 244].

In this Section we present a detailed characterization of the low-energy signatures observed in the charge conductance and shot noise measurements that allows the classification of different regions of the Kitaev chain phase diagram. Despite being done on a toy model, the analysis may give physical insight in understanding the outgoing experiments where the effect of local on-site interaction cannot be neglected. We start by reporting the expression of the current flowing through the metallic contacts:

$$\langle I_Q \rangle = \frac{\pi e^2}{h} \int d\epsilon \bar{\rho}(\epsilon) \left(f_L(\epsilon) - f_R(\epsilon)\right) \text{ImTr}\left(\hat{\mathbf{T}}^A_{\eta\uparrow}(\epsilon)\right), \tag{8.13}$$

where $f_L(\epsilon) = f(\epsilon - \phi/2)$, $f_R(\epsilon) = f(\epsilon + \phi/2)$, Tr is the trace in the 2×2 Nambu space, $\hat{\mathbf{T}}^{R/A}(\epsilon)$ is the impurity transfer matrix

$$\hat{\mathbf{T}}^{R/A}(\epsilon) = \hat{V}_c^\dagger \cdot \hat{\mathbf{G}}^{R/A}_{\eta\uparrow}(\epsilon) \cdot \hat{V}_c, \tag{8.14}$$

and $\bar{\rho}(\epsilon)$ is the boundary density of states for the semi-infinite normal contacts (we refer to the Section E.3). The resulting value of the current is obtained by averaging over the spin $\downarrow$ configurations:

$$\langle\langle I_Q \rangle\rangle = \sum_{n^f_\downarrow = 0,1} p(n^f_\downarrow) \langle I_Q(n^f_\downarrow)\rangle, \tag{8.15}$$

where in the absence of any gate potential or Zeeman field on the quantum dot $p(0) = p(1) = 1/2$.

In the topological regime, the low-energy physics is governed by the in-gap states that emerge from the hybridization between the real and imaginary part of the spin up dot fermion and the MZM of the Kitaev chain. The coupling between $\gamma^d_\uparrow$ and γ_1 induces an energy splitting

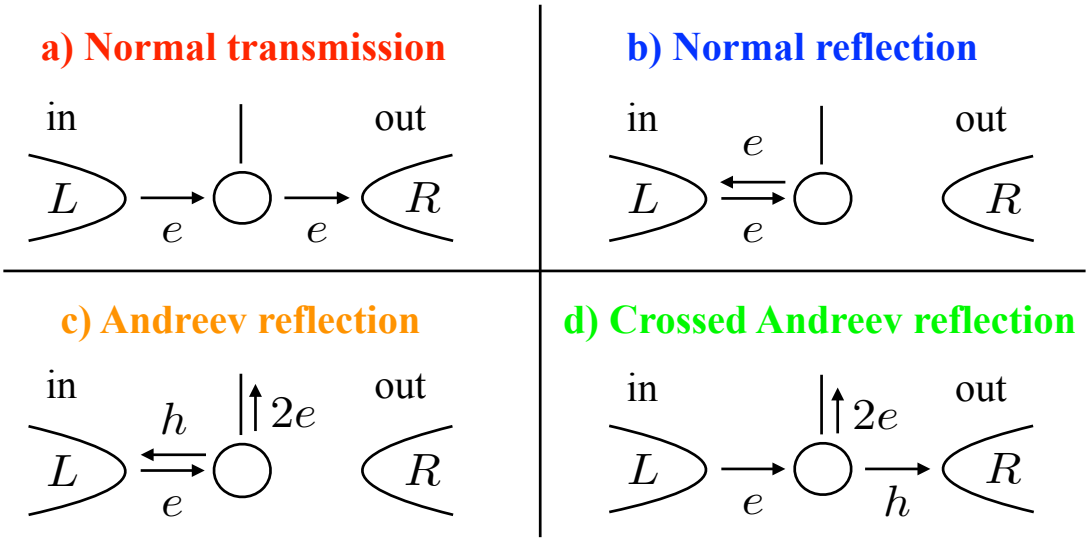

Figure 8.4: The electron, coming from the L contact, undergoes four different scattering processes at the interface with the quantum dot that is tunnel-coupled to the Kitaev chain. We notice that only the normal transmission and the Andreev reflection are responsible to a net charge variation between L and R contacts.

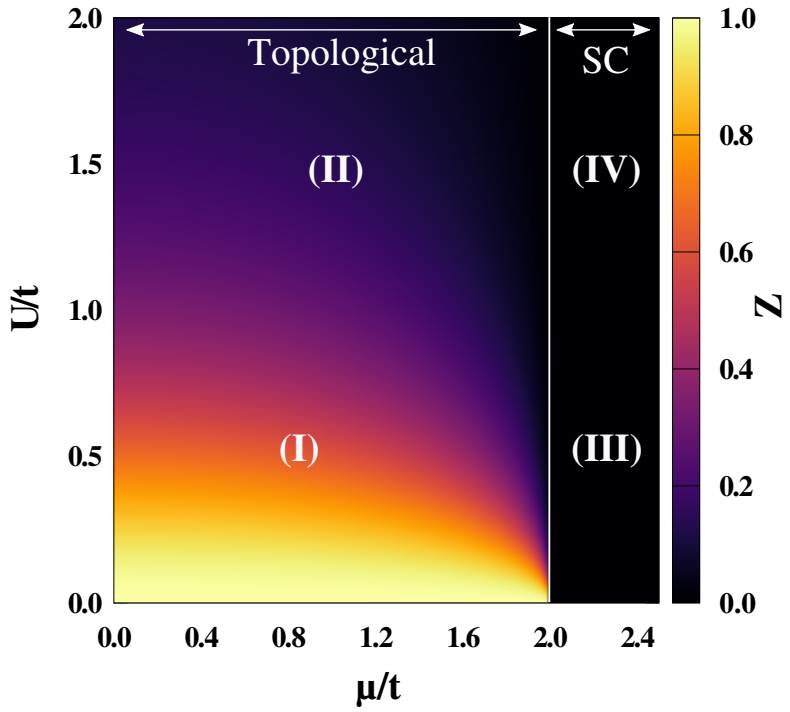

Figure 8.5: Quasiparticle residue Z of the low-energy MZM as a function of μ/t and U/t, for $\Delta/t = V/t = 0.4$. Symbols from (I) to (IV) characterize different charge transport behavior, see Fig. (8.8).

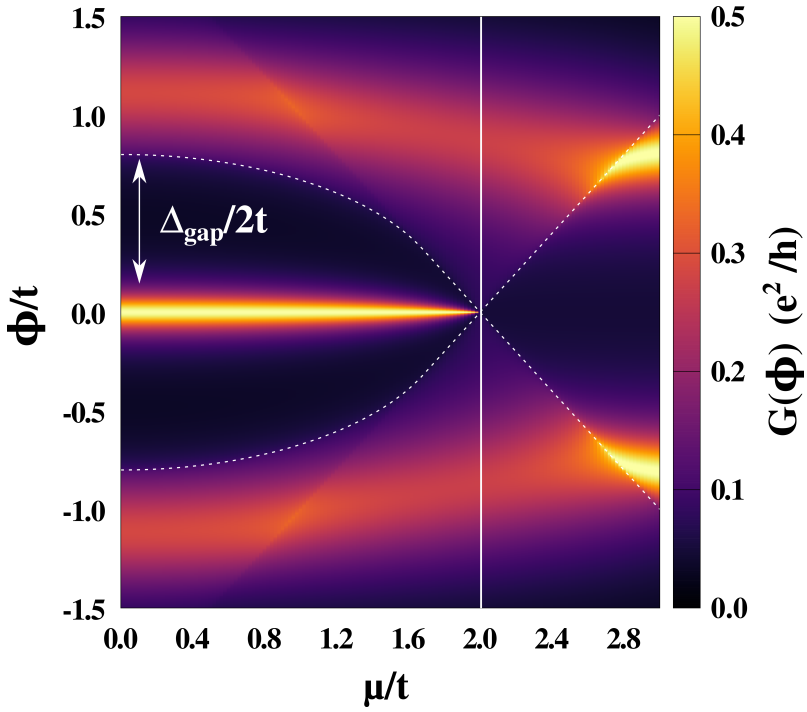

Figure 8.6: Evolution of the conductance $G(\phi)$ as a function of μ/t, for $U/t = 1.6$, $\Delta/t = V/t = 0.4$ and $V_c/t = 0.3$. Dashed white line shows the superconducting gap measured on the boundary site of the semi-infinite Kitaev chain. White vertical line corresponds to the topological transition.

$\sim V$, while the interaction on the dot generates an energy splitting $\sim U$ between $\gamma^d_\uparrow$ and $\xi^d_\uparrow$. The combined effect of the dot-Kitaev chain coupling and the interaction, on an odd number of MZMs, is to split the two of them by a term $\sim f(U, V)$ that eventually, for U strong enough, push them out from the superconducting gap. On the other hand, the third state is a topologically protected, and robust to the interaction, zero energy mode. In the trivial regime we have an even number of MZMs, no zero energy mode is preserved as any finite interaction induces a hybridization $\sim U$ between them.

These features can by easily detected resorting to the scattering matrix approach of Ref. [205, 209]. This technique allows us to interpret the transport properties of the system in terms of the scattering processes across the junction that are depicted schematically in Fig. 8.4. In the trivial regime (left panel of Fig. 8.3), the presence of massive in-gap modes suppresses low-energy scattering processes, so that the L and R contacts are disconnected in the large U/V_c limit (Coulomb blockade regime). On the contrary, in the topological regime (right panel of Fig. 8.3), the presence of the MZM keeps alive all the scattering processes at low-energy. The normal transmission (T), the Andreev reflection (A) and the crossed Andreev reflection (C) are equal to one fourth at any value of U and V. As a consequence, the charge current, I_Q, that measures the charge imbalance between left and right lead, is $\propto A + T \sim 1/2$ and the zero-bias conductance is reduced from e^2/h to $e^2/2h$, as already observed in previous studies [91, 167, 174, 175, 277]. Remarkably, the on-site local repulsion does not modify the result $e^2/2h$ while it affects the curvature of the low-bias conductance by renormalizing the MZM:

$$G(\phi) = \frac{\partial \langle I_Q \rangle}{\partial \phi} \simeq \frac{e^2}{2h}\left[1 - \left(\frac{\phi}{2\Gamma_c Z}\right)^2\right], \tag{8.16}$$

where $\Gamma_c = 2\pi\bar{\rho}(0)V_c^2$ is the hybridization with the metallic contacts, $\bar{\rho}(\omega)$ the boundary metallic

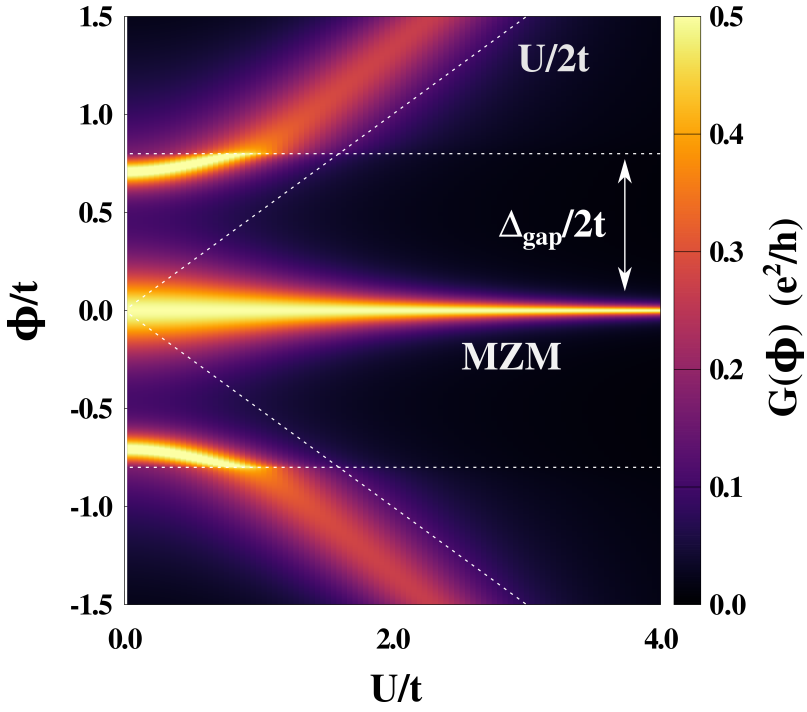

Figure 8.7: Influence of the interaction U/t on the conductance $G(\phi)$ for $\mu/t = 0.0$, $\Delta/t = V/t = 0.4$ and $V_c/t = 0.3$. Horizontal dashed lines show the width of the bulk superconducting gap Δ_{gap}.

density of states and Z the quasiparticle residue. The latter quantity is shown in the color map 8.5, where we analyze the evolution of Z in different regions of the phase diagram of the Kitaev chain. We stress that Eq. (8.16) is valid in the topological regime $|\mu| < 2t$ where the SC is topologically non-trivial and a MZM appears at the edge of the semi-infinite Kitaev chain. Conversely, in the region $|\mu| > 2t$ the MZM disappears and we enter in the Coulomb blockade regime where the zero-bias conductance is suppressed.

The topological transition is associated to a drastic variation of the conductance $G(\phi)$. Indeed, as shown in Fig. 8.6, by crossing the critical line, $\mu = 2t$, we observe a jump from $G_0 = e^2/2h$ in the topological region to $G_0 \simeq 0$ in the trivial one, which allows distinguishing the two different phases. Moreover, we notice that in the non-topological region, for $\mu/t \simeq 2.5$, the conductance presents coherent in-gap peaks attributable to Andreev bound states induced by the impurity, reminiscent of Yu-Shiba-Rosinov states [177, 242, 259]. The effect of the interaction on the $G(\phi)$ is shown in Fig. 8.7, where we report the evolution of the low-energy MZM and of the Yu-Shiba-Rosinov-like bound states as a function of U/t. Being non-topological, the latter features are strongly affected by the interaction, and indeed, as shown in Fig. 8.7, above a certain value of U/t they enter in the continuum of Cooper-pairs excitations of the SC. On the other hand, the contribution to the zero-bias conductance G_0 of the MZM is robust and persists for any value of U/t. The interaction renormalizes the coupling (8.9) between the dot and the MZM according to $V \to V\sqrt{Z}$, where Z the quasiparticle residue is displayed in Fig. 8.5, and enhances the curvature of the conductance close to the zero-bias anomaly (8.16).

We also compute the shot noise S_Q that at zero temperature reads:

$$S_Q = \frac{2\pi e^3}{h}\frac{\pi}{2}\int d\epsilon \bar{\rho}^2(\epsilon)\frac{f_L(\epsilon)-f_R(\epsilon)}{2}\text{Tr}\Big[\Big(\hat{\mathbf{T}}^R_{\eta\uparrow}(\epsilon)+\hat{\mathbf{T}}^A_{\eta\uparrow}(\epsilon)\Big)\cdot\Big(\hat{\mathbf{T}}^R_{\eta\uparrow}(\epsilon)+\hat{\mathbf{T}}^A_{\eta\uparrow}(\epsilon)\Big)\Big], \tag{8.17}$$

for more details we refer the interested reader to Appendix E Section E.5. Analogously to the

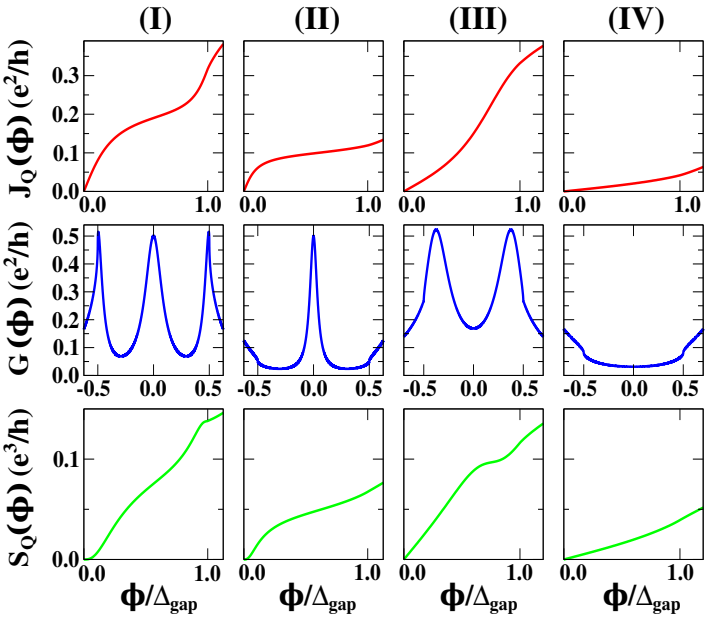

Figure 8.8: From top to bottom current $J(\phi)$, conductance $G(\phi)$ and shot noise $S_Q(\phi)$ as a function of the bias $\phi/\Delta_{\rm gap}$, where $\Delta_{\rm gap}$ is the bulk superconducting gap. Left side panels (I) and (II) describe different regions in the Topological SC phase: parameters are $U/t = 0.8,\ 2.0$, $V/t = 0.4$, $V_c/t = 0.3$ and $\mu/t = 0.0$ with bulk superconducting gap $\Delta_{\rm gap}/t = 1.6$. Right side panels (III) and (IV) describe different regions in the Trivial SC phase: parameters are $U/t = 0.8,\ 2.0$, $V/t = 0.4$, $V_c/t = 0.3$ and $\mu/t = 2.5$ with bulk superconducting gap $\Delta_{\rm gap}/t = 1.0$. In the topological phase (I) and (II) the zero-bias anomaly $e^2/2h$ shows the presence of a MZM, that is absent in the trivial-SC, regions (III) and (IV).

previous case, we perform the average over $\downarrow$ configurations

$$\langle S_Q \rangle = \sum_{n^f_\downarrow = 0,1} p(n^f_\downarrow) S_Q(n^f_\downarrow). \tag{8.18}$$

A complete characterization of the low-energy transport properties is given in Fig. 8.8, where we plot the current I_Q, the corresponding charge-conductance $G(\phi)$ and its fluctuations $S_Q(\phi)$ as a function of the applied bias. We notice that dependently on the region of the Kitaev phase diagram 8.5 we predict different low-energy response. In particular behavior (I) and (II) denote the presence of a MZM, while (III) and (IV) characterize the non-topological regime. Differently from (I) and (IV), regions (II) and (III) present additional in-gap bound states distinguished by sharp peaks in $G(\phi)$ away from the zero-bias anomaly.

We observe that an additional signature of the MZM is given by the low-bias behavior of the shot noise $S_Q(\phi)$, which is shown in the bottom panel of Fig. 8.8. Indeed, in the topological regime, for small bias, the shot noise goes like:

$$\langle S_Q \rangle \simeq \frac{e^3}{h} \frac{\phi^3}{24\,(\Gamma_c Z)^2} \left[1 - \frac{3}{10} \left(\frac{\phi}{\Gamma_c Z} \right)^2 \right], \tag{8.19}$$

while it becomes linear in the non-topological region, $S_Q \propto \phi$ for $|\mu| > 2t$. From the shot noise we compute the Fano factor

$$F = \left. \frac{S_Q}{J_B} \right|_{\phi=0} = q_{\rm e} \tag{8.20}$$

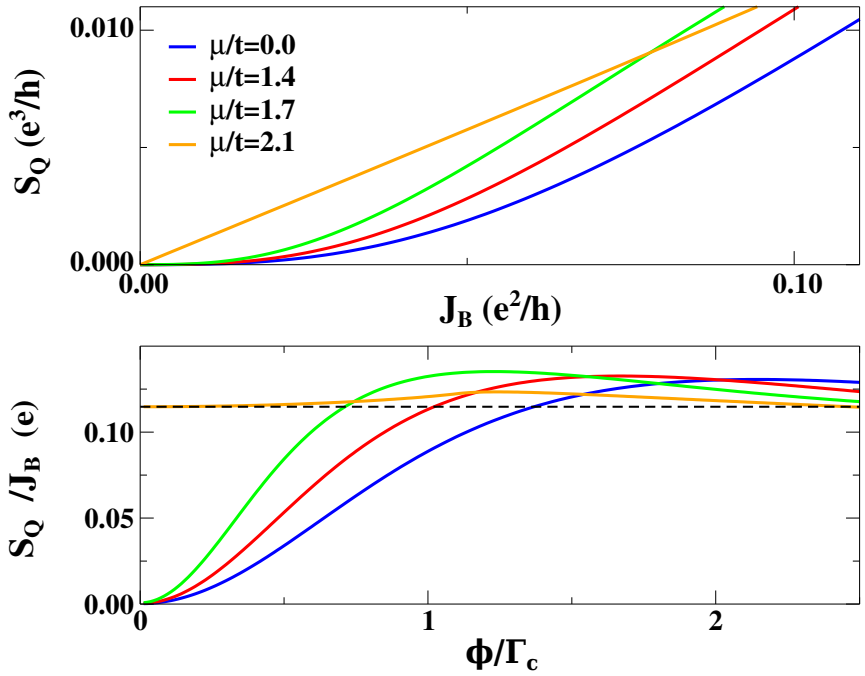

Figure 8.9: Top Panel: Shot noise $\langle S_Q \rangle$ as a function of the backscattering current J_B. Bottom panel: Ratio $\langle S_Q \rangle / J_B$ as a function of the bias ϕ measured in units of the hybridization with the metallic contacts $\Gamma_c/t = 2\pi\bar{\rho}(0)V_c^2/t = 0.18$. Dashed black line corresponds to Eq. (8.22). Different lines represent different values of the chemical potential of the Kitaev chain: $\mu/t = 0.0,\ 1.4,\ 1.7$ and 2.1. The other parameters are $V/t = \Delta/t = 0.4$, $V_c/t = 0.3$ and $U/\Gamma_c = 5.\bar{5}$.

which determines the charge of the elementary carriers [64]. In Eq. (8.20) we have introduced the backscattering current, defined as the deviation from the unitary transmission through the junction [256]:

$$J_B = \frac{e^2}{h}\phi - \langle\langle J_Q \rangle\rangle. \tag{8.21}$$

As a consequence of the small bias behavior of Eqs. (8.16) and (8.19), the topological regime $|\mu| < 2t$ is characterized by a vanishing Fano factor $F = 0$, independently from the value of the interaction U/t, as shown in the bottom panel of Fig. 8.9. On the other hand, in the non-topological region F is a function of U/t which becomes equal to 1 in the non-interacting limit $U/t \to 0$. In particular for $|\mu| > 2t$ we find:

$$F = \frac{(2\Gamma_c/U)^2}{1 + (2\Gamma_c/U)^2}. \tag{8.22}$$

Thus, experimental measurements of the shot noise give additional informations complementary to the characteristic zero-bias conductance $G_0 = e^2/2h$. Combined measurements of the conductance and the shot noise in the experimental set-up presented in Fig. 8.2 allow detecting the topological properties of the superconducting wire as well as distingishing the low-energy contribution of a MZM from other possible sources of zero-bias anomaly. We argue that the predicted behavior of the aforementioned observables persists even for a more realistic Hamiltonian, that presents a detailed description of the leads and of the quantum dot [53, 103, 167, 285]. A detailed analysis of this problem is left to future investigations.

8.4 Conclusions

We compute charge transport across a Majorana-Anderson model by measuring the charge current across the metallic contacts. The presence of a MZM is outlined by a fractional zero-bias conductance $e^2/2h$ that, as we have shown, is robust against the dot interaction. Additionally, for small values of the on-site repulsion, we find in-gap bound states that represent the only low-energy feature in the topologically trivial region of the phase diagram in Fig. 8.5. Furthermore, we find that the topological regime is characterized by a vanishing Fano factor induced by the tunnel-coupling with the MZM at the edge of the superconducting wire.

Our analysis gives a complete characterization of charge transport measurements that can experimentally detect the presence of MZM on the edge of real materials and, indirectly, allow reconstructing their topological phase diagram.

9 Conclusions and perspectives

In this thesis we introduce and explore two novel approaches for strongly correlated electron systems: the ghost-Gutzwiller wave function and the constraint-free slave-spin theory for impurity models. For the sake of clarity we summarize the main findings of this thesis in Sections 9.1 and 9.2, where, together with a brief description of the main methodological advances, we present the results obtained by applying these approaches to problems of current interest.

9.1 The ghost-Gutzwiller wave function

The ghost-Gutzwiller, presented in Chapter 3, extends the conventional Gutzwiller wave function by introducing subsidiary fermionic orbitals both in the local projector $\mathcal{P}$ and in the Slater determinant $|\Psi_*\rangle$. The novel method improves substantially the description of strongly correlated electron systems already for small number N of auxiliary states, $N = 3$.

For the single-level impurity Anderson model (SIAM) the method is able to describe not only the low-energy Kondo resonance but also the expected valence fluctuation peaks at $\pm U/2$. Furthermore, the variational estimation of the Kondo temperature T_K improves respect conventional Gutzwiller and slave-particle mean-field results, which is however still overestimated for $N = 3$. In this regard, it is interesting to look at the scaling of T_K as a function of $1/N$ and determine whether in the Kondo regime $\log T_K$ approaches the exact result $\sim -\pi U/8\pi$ for $N \gg 1$. This future project will shed light on the role of the parameter N, that is expected to play a similar role of the bond dimension in matrix-product states [217, 236] or the number of "hidden" variables in neural networks states [50] and, therefore, related to the amount of entanglement in the variational wave function.

The flexibility of the variational method makes it applicable to any quantum impurity problem. As an ideal test for our approach, we apply the method to the pseudogap SIAM that presents a quantum phase transition between the local moment (LM) and the Kondo screened phase (SC) [89, 102, 288]. The technique for $N = 3$ improves substantially the pseudogap SIAM phase diagram respect conventional Gutzwiller and slave-particles mean-field calculations. Differently from the latter approaches, where in the LM phase the impurity decouples from the electron bath, our variational technique predicts that the LM regime is characterized by a non vanishing value of the double occupancy on the impurity site and, correspondingly, by broadening of the

charge peaks at $\pm U/2$. This additional feature could enrich the out of equilibrium dynamics, analyzed with the conventional Gutzwiller approach in Ref. [245] by inducing relaxation towards a stationary state. In view of these promising results we are applying the variational method to the double quantum dots model, in order to determine whether the novel Gutzwiller wave function is able to capture the quantum critical point that separates the Kondo screened phase from the singlet one [134, 135].

The improvement in the variational description of impurity models opens the intriguing possibility of applying the g-GW as impurity solver for DMFT. In this respect, it is important to notice that the g-GW has the same numerical cost of exact diagonalization (ED) [44, 49]. However, in contrast to ED, which describes the impurity spectral function with a finite number of discrete peaks, the g-GW gives a continuous spectrum which is determined by optimizing the embedded impurity model. This feature may guarantee better physics of using ED as impurity solver at the same cost.

To highlight the importance of the novel Gutzwiller wave function we apply the method to the single-band lattice Hubbard model. Numerical results, obtained for $N = 3$ and $N = 5$, show that the approach allows the description of both the low-energy quasiparticles and the high-energy Hubbard bands. Furthermore, the estimation of the ground state energy, double occupancy and quasiparticle residue is not far from the results obtained with DMFT. This crucial result, originally presented in Ref. [163], highlights that the ghost Gutzwiller wave function is not only a powerful method to determine a variational estimation of the quasiparticle residue Z in the Fermi liquid regime but also gives a detailed description of the correlation-driven insulating phase. It is interesting to remark that the variational estimation of the spinodal points U_{c1} and U_{c2}, as well as the value of the quasiparticle residue Z improve by increasing the number of subsidiary degrees of freedom N. This result poses a question about the limit of $N \gg 1$, whether the variational g-GW solution approaches DMFT [95], that is exact in the infinite-coordination limit.

We underline that the ghost Gutzwiller wave function is simple and flexible enough to allow theorists to incorporate material-specific details into the calculations. Therefore, it can be exploited in combination with electronic structure calculations to provide more realistic description of correlated materials.

In this thesis we have faced, by means of the ghost Gutzwiller variational approach, two different problems of current interest.

- *Exciton Mott transition*

  The exciton Mott transition in photoexcited semiconductors is actually quite an old topic that goes back to the 1970's. Nonetheless, basic issues have remained unsolved in the huge literature that has appeared in the last decades on the theory of correlated systems and the Mott transition. In particular in some systems, the exciton Mott transition appears to be characterized by phase separation, like a liquid-gas transition, while in the others by a Mott transition distinct from the gas-liquid one [164], or through a bistability [254].

  The interest in the exciton physics of semiconductors has been recently boosted, mainly by the great potentials offered by monolayer transition metal dichalcogenides, see e.g. [281]. This revival is triggered also by the interest in exciton behavior under photoexcitation, not only in dichalcogenides, as, for instance, in Ref. [54], but also in more conventional semiconductors, see, e.g., Ref. [255].

  In light of this renewed interest, we decide to address the nature of the exciton Mott transition in Chapter 4. In particular, we consider a minimal model that, since the seminal work by Nozières and Schmitt-Rink, [213], is believed to capture the essential physics of the

exciton Mott transition, i.e., the half-filled single-band Hubbard model at fixed, and large, spin-polarization. Quite surprisingly, despite the half-filled single-band Hubbard model has been examined on every side by an incredible number of different state-of-the-art techniques, including the most sophisticated ones, yet the nature of the Mott transition at fixed spin-polarization remains controversial. We emphasize that, even though the model is ideally suited to DMFT, earlier results [30, 48, 145, 160, 294] show some differences in the nature of the transition. The reason of this discordance can be traced back to the iterative scheme employed to solve DMFT, which fails to converge in the regime of large-U and finite magnetization. For this reason we decide to use the novel Gutzwiller wave function approach that is free of the problem outlined before, which is discussed more in details in Section 4.4.

The results, that we present in Section 4.5 and summarized in Section 4.6, agree with experiments and allow identifying the key parameter that controls the nature of the transition: the magnitude of the exciton binding energy. Specifically, we find that for large exciton binding energies (small dielectric constant), the exciton Mott transition occurs as a gradual transition (liquid-gas). Hence we observe a coexistence region where, as the density of electron-hole pairs increases, the fraction of electron-hole droplets grows continuously till the formation of a finite spectral width at the Fermi level. Instead, in the regime of small exciton binding energies (large dielectric constant), the intermediate region is characterized by bistability with a sharp transition from the exciton gas to the electron-hole liquid.

- *Nonequilibrium dynamics*

  Recent years have seen enormous experimental progress in preparing, controlling and probing strongly interacting quantum systems in different nonequilibrium regimes. This led to the development of an entire new field of nonequilibrium quantum physics which aims to the control and manipulation of nonequilibrium matter.

  Motivated by the outstanding improvement observed at equilibrium, in Chapter 5 we extended the ghost-Gutzwiller wave function to describe the out of equilibrium evolution of multi-band Hubbard models in the absence of superconductive correlations. To benchmark our method with DMFT and conventional Gutzwiller result, in Section 5.4 we study the out of equilibrium dynamics in the single-band Hubbard model induced by a quench in the local interaction. The tunnel matrix elements connecting the physical orbital $d_{i\sigma}$ with N ($N > 1$) bath levels c_{ia} provides energy exchange mechanisms that suppress the mean-field like coherent oscillations observed in the conventional time-dependent Gutzwiller. However, as long as the number of bath levels is finite, the novel channels do not act as a reservoir that absorbs the excess of energy injected by the time-dependent perturbation and the system never reaches an asymptotic steady-state regime. We expect that $N > 3$ would certainly improve the results presented in Section 5.4 by a further suppression of the residual oscillations.

9.2 The Slave-spin theory

Concerning the slave-spin theory we have shown in Section 6.3 that a generic single-level Anderson impurity model (SIAM) can be mapped without any constraint onto a resonant level

model coupled to two Ising spins, or just one in the simpler case when the hybridization is particle-hole symmetric. The result straightforwardly applies to a generic multi-levels Anderson impurity model if the impurity Hamiltonian involves only the occupation numbers, i.e. it does not include Coulomb exchange terms, see Section 6.3.2. Moreover, the single-particle Green's functions of the physical electron can be calculated without any constraints. The latter result allows exploiting DMFT to study in the slave-spin representation particle-hole nonsymmetric multi-band Hubbard models in lattices with infinite coordination. In some cases this could be more convenient than directly working within the physical Hilbert space, though smaller, especially when one wants to prevent spontaneous symmetry breaking that usually accompanies a Mott transition, since the slave-spin Hamiltonian (6.28) is particle-hole symmetric in terms of the auxiliary fermions, despite the fact that the Hamiltonian of the physical electrons is not. Moreover, as already shown in Ref. [121], the slave-spin mapping endows the Mott transition of a genuine order parameter associated with the local Z_2 gauge symmetry. Thus, it allows to develop an equivalent of the Landau-Ginzburg energy functional for the Mott transition [152].

It is interesting to notice that by exploiting our novel slave-spin theory the mean-field solution of the single-orbital Anderson impurity model (SIAM) is found to be stable to unphysical spontaneous magnetisation of the impurity, unlike the saddle-point solution in the standard slave-boson representation [81, 156]. Remarkably, the mean-field estimate of the Wilson ratio R_{W} and the quasiparticle scattering amplitudes tend to the exact Nozières' local Fermi liquid result in the Kondo regime [194, 212, 214]. Moreover, we perform a self-consistent calculation of the single-particle physical fermions Green's function that reproduces both the Kondo resonance and the high-energy incoherent charge fluctuations peaks. The latter result allows to apply the self-consistent slave-spin mean-field theory as an approximate impurity solver within the DMFT.

The slave-spin mapping finds a direct application to transport in quantum dots. For this reason the method has been further extended to study the out of equilibrium evolution of quantum dots by employing the Keldysh Green's function approach. In particular we have considered two applications.

- *Transport in quantum dots*

  We have shown in Chapter 7 that the evolution of quantum dots can be described within the slave-spin representation without any need of local constraint on the enlarged Hilbert space. The advantages are twofold. On one side, we have disentangled high and low-energy degrees of freedom, by encoding the dynamics of the charge degrees of freedom in the Ising variables while the evolution of the low-energy ones in the effective resonant level model. On the other side, we avoided the mean-field mixing of unphysical and physical subspaces, that affects the time evolution of other slave-particle techniques.

  Furthermore, we have presented in Section 7.4 the time-dependent slave-spin mean-field theory that reduces the solution of the many-body Schrödinger equation to a set of equations that describe the evolution of the Ising variables coupled to the dynamics of the Slater determinant. It is important to observe that the time-dependent slave-spin approach can be applied to study the dynamics on a quantum dot for any nonequilbrium protocol, e.g. periodic driving, quantum quench, etc. For simplicity we apply in Section 7.6 the above method to study the dynamics induced by slowly varying chemical potential applied to the metallic contacts. After a characteristic time, which depends on the product $T_K\, t_*$ between T_K and the time scale of the external perturbation t_*, the dynamics relax to the nonequilibrium steady-state.

  In the steady-state regime, Section 7.6, the self-consistent Hartree-Fock decoupling is

able to predict the properties of the model even deep inside the large-U Kondo regime, specifically, the conductance shows both the known zero-bias anomaly but also the expected peak at bias of order U.

- *Slave-spin mapping for double quantum dots*

  In Section 7.7 we consider a double quantum dots model see Fig. 7.5. Each dot is coupled to the respective metallic contact, and the dots are connected via a tunnel-coupling $t_\perp$. At equilibrium this model shows a crossover between the Kondo screened phase and the unscreened one, where the magnetic moments on the quantum dots are coupled in a singlet configuration. The crossover becomes a quantum critical point in the large-U limit, when the tunnel-coupling $t_\perp$ can be approximated by an antiferromagnetic exchange $J_\perp$.

  Remarkably, even in the case of a finite $t_\perp$, we show in Section 7.7 that the thermodynamical properties computed within the slave-spin representation can be obtained without any need of constraints on the enlarged Hilbert space. Despite the promising form of the slave-spin Hamiltonian, preliminary equilibrium mean-field calculations predict a first order transition between the Kondo screened phase and unscreened one. In order to reproduce the expected crossover we are currently trying to go beyond mean-field approximation. In particular one possible direction, that we are considering, is performing degenerate perturbation theory around the $t_\perp = 0$ solution and generalizing the result for finite values of $t_\perp$. Once the equilibrium properties of the model are reproduced, we will proceed by considering the nonequilibrium transport across the double quantum dots.

In recent experiments [66, 293] a new direction has emerged which explores transport across an interacting magnetic impurity coupled to the edge of a 1D superconductive nanowire. It has been observed that, when the superconductor enters the topological regime, low-energy conductance measurements show zero-bias anomaly, that may signal the appearance of Majorana zero modes (MZM) at the boundary of a topological superconductor. To characterize the distinctive contribution given by the MZMs to electronic transport properties of the junction, we consider in Chapter 8 an idealized model that resembles the set-up realized in the aforementioned experiments. By performing calculations with both Keldysh Green's functions approach and Scattering matrix formalism we obtain that in addition to the well-known half-integer zero-bias conductance, the topological regime is characterized by a vanishing Fano factor $F = 0$, signature of the Majorana nature of the zero-bias anomaly. We argue that the predicted behaviors of the conductance and of the Fano factor persists even for realistic models, that include a more detailed description of the quantum dot and of the metallic leads.

Combined measurements of the conductance and the shot noise, in the experimental set-up analyzed in Refs. [66, 293], allow experiments to detect the topological properties of the superconducting wire and to distinguish the low-energy contribution of a Majorana zero mode from other possible sources of zero-bias anomaly.

A

Supplemental informations on the g-GW

In this Appendix we report some additional informations on the g-GW approach and an interesting calculation. In Section A.1 we show that average quantities computed as traces on the Gutzwiller projector $\hat{\phi}(i)$ can be expressed in terms of expectation values on the embedded wave function $|\psi(i)\rangle$. In the large-U regime, where charge fluctuations are negligible, the g-GW wave function can be computed exactly and provides a faithful description of the Mott insulator, see Section A.2. Finally, in Sections A.3 and A.4 we report the expression of the single-particle propagator and of the quasiparticle residue, respectively, in the g-GW approach.

A.1 Expectation values of the embedded model

Given the impurity wave function in Eq. (3.23) we are going show that identities in Eqs. (3.30), (3.31) and (3.32) hold.

Gutzwiller constraints; let us consider the norm of the wave function $|\psi(i)\rangle$:

$$\langle\psi(i)|\psi(i)\rangle = \sum_{\Gamma\gamma}\sum_{\Gamma'\gamma'} \delta_{\gamma\gamma'}\delta_{\Gamma\Gamma'}\phi^*(i)_{\Gamma\gamma}\phi(i)_{\Gamma\gamma} = \mathrm{Tr}\left(\phi^\dagger(i)\cdot\phi(i)\right). \tag{A.1}$$

The single-particle density matrix is:

$$\begin{aligned}\langle\psi(i)|c_{ib}c_{ia}^\dagger|\psi(i)\rangle &= \sum_{\Gamma\gamma}\sum_{\Gamma'\gamma'} \delta_{\Gamma\Gamma'}\,\phi^*(i)_{\Gamma\gamma'}\,\phi(i)_{\Gamma\gamma}\,\langle\gamma_i'|U_{\mathrm{PH}}^\dagger c_{ib}c_{ia}^\dagger U_{\mathrm{PH}}|\gamma_i\rangle e^{i\pi\left[N_\gamma(N_\gamma-1)-N_\gamma'(N_\gamma'-1)\right]/2}\\ &= \sum_{\Gamma\gamma}\sum_{\gamma'} \phi^*(i)_{\Gamma\gamma'}\,\phi(i)_{\Gamma\gamma}\left(\langle\gamma_i|c_{ia}^\dagger c_{ib}|\gamma_i'\rangle\right)^*\\ &= \mathrm{Tr}\left(\phi^\dagger(i)\cdot\phi(i)\cdot C_{ia}^\dagger\cdot C_{ib}\right),\end{aligned} \tag{A.2}$$

last equality follows from the fact that $\langle\gamma_i|c_{ia}^\dagger c_{ib}|\gamma_i'\rangle$ can be either 0 or ±1.

Average of a local bosonic operator; we consider the expectation value of the local (bosonic) operator O_i, which depends on the impurity degree of freedom only $O_i[\{d^\dagger_{i\alpha}\},\{d_{i\alpha}\}]$

$$\begin{aligned}\langle\psi(i)|O_i|\psi(i)\rangle &= \sum_{\Gamma\gamma}\sum_{\Gamma'\gamma'}\delta_{\gamma\gamma'}\,\phi^*(i)_{\Gamma'\gamma}\,\phi(i)_{\Gamma\gamma}\,\langle\Gamma'_i|O_i|\Gamma_i\rangle \\ &= \mathrm{Tr}\left(\phi^\dagger(i)\cdot O_i\cdot\phi(i)\right).\end{aligned} \tag{A.3}$$

Overlap matrix element; the hybridization between the impurity and the bath is determined by the average value

$$\begin{aligned}\langle\psi(i)|c^\dagger_{ia}d_{i\alpha}|\psi(i)\rangle &= \sum_{\Gamma\gamma}\sum_{\Gamma'\gamma'}\langle\gamma'|\times\langle\Gamma'|c_{ia}d_{i\alpha}|\Gamma\rangle\times|\gamma\rangle\phi^*_{\Gamma'\gamma'}(i)\phi_{\Gamma\gamma}(i)e^{i\pi\left[N_\gamma(N_\gamma-1)-N'_\gamma(N'_\gamma-1)\right]/2} \\ &= \sum_{\Gamma\gamma}\sum_{\Gamma'\gamma'}(-1)^{N_\gamma+N_\Gamma}\phi^*_{\Gamma'\gamma'}(i)\phi_{\Gamma\gamma}(i)\langle\gamma'|c_{ia}|\gamma\rangle\langle\Gamma'|d_{i\alpha}|\Gamma\rangle\end{aligned} \tag{A.4}$$

in the relevant cases we will consider in this work the coefficient $\phi_{\Gamma\gamma}$ is not vanishing if the half-filled condition is satisfied: $N_\Gamma + N_\gamma = N + M$. Moreover, we always consider an embedded impurity model composed by an even number of sites $N + M = 2n$, $n \in \mathbb{N}$. Thus,

$$\begin{aligned}\langle\psi(i)|c^\dagger_{ia}d_{i\alpha}|\psi(i)\rangle &= \sum_{\Gamma\gamma}\sum_{\Gamma'\gamma'}\phi^\dagger_{\gamma'\Gamma'}(i)\phi_{\Gamma\gamma}(i)\left(\langle\gamma|c^\dagger_{ia}|\gamma'\rangle\right)^*\langle\Gamma'|d_{i\alpha}|\Gamma\rangle \\ &= \mathrm{Tr}\left(C^\dagger_{ia}\cdot\phi^\dagger(i)\cdot D_{i\alpha}\cdot\phi(i)\right),\end{aligned} \tag{A.5}$$

where we have used the fact that $\langle\gamma|c^\dagger_{ia}|\gamma'\rangle$ is either 0 or ±1.

A.2 The analytical evaluation of the g-GW in the large-U regime

We present the analytical calculations of the g-GW for the deep Mott insulator solution ($U \gg U_{c2}$, where U_{c2} is the spinodal point for the correlated metal). In this regime the low-energy bath level does not contribute to valence fluctuations on the impurity site, $R_2 = 0$ see bottom panel of Fig. 3.8, and it is an effective spin degree of freedom. By physical reasons, based on the short-range singlet correlations that characterizes the Mott insulator, we consider a variational wave function where the low-energy spin is coupled in a singlet configuration to the remaining levels:

$$|\psi\rangle = \left(|\phi_\uparrow\rangle\times|\varphi_\downarrow\rangle - |\phi_\downarrow\rangle\times|\varphi_\uparrow\rangle\right)/\sqrt{2}$$

where $|\varphi_\sigma\rangle = |\sigma\rangle$, with $\sigma = \uparrow,\downarrow$, while $|\phi_\sigma\rangle$ describes the configuration of the remaining sites composing the embedded model that, for $N = 3$, is made by the impurity site and the high-energy levels. In the large-U regime charge fluctuation on the impurity site are strongly suppressed and the three site wave function $\phi(n;n_1,n_3)$, where n is the physical orbital configuration and n_a the bath site a configuration, $a = 1,3$, contains a leading component $\phi(\sigma;2,0)$, $\sigma = \uparrow,\downarrow$, in the subspace with total spin $S = 1/2$ and its z-component $S^z = \sigma$. Taking into account the next-to-leading configuration, we will further assume non-zero the components $\phi(0;2,\sigma)$ and $\phi(2;\sigma,0)$, which are generated by the hybridization between the physical orbital and the bath sites. Therefore, as shown in Fig. A.1, the three site trial wave function can be written as

$$|\phi_\sigma\rangle = \phi(\sigma;2,0)|\sigma;2,0\rangle + \phi(2;\sigma,0)|2;\sigma,0\rangle + \phi(0;2,\sigma)|0;2,\sigma\rangle.$$

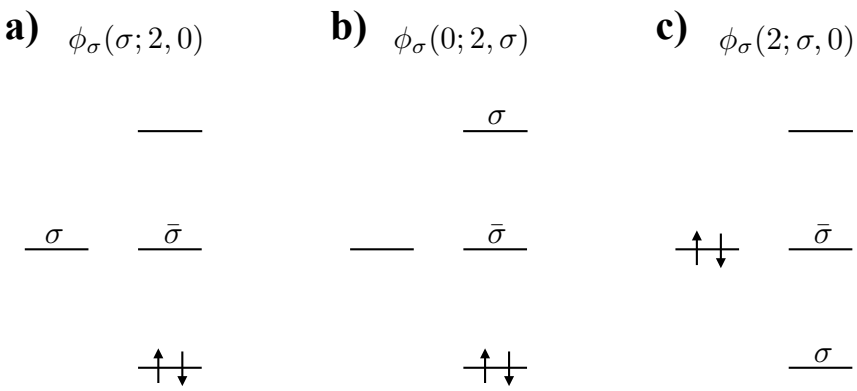

Figure A.1: Relevant configurations in the large-U regime. **a)** leading component $\phi(\sigma;2,0)$, while **b)** and **c)** are the next-leading amplitudes $\phi(2;\sigma,0)$ and $\phi(0;2,\sigma)$, respectively, which are generated by the hybridization between the impurity and the high-energy bath levels.

Normalization condition (3.13) implies:

$$\langle\psi|\psi\rangle = \frac{1}{2}\sum_{\sigma=\uparrow,\downarrow}\langle\phi_\sigma|\phi_\sigma\rangle = 1,$$

that is automatically satisfied by the following parametrization:

$$\begin{aligned}\phi(\sigma;2,0) &= \cos\theta,\\ \phi(2;\sigma,0) &= -\phi(0;2,\sigma) = \sin\theta/\sqrt{2},\end{aligned} \tag{A.6}$$

where we shall assume $\theta \sim 0$. It follows that $\Delta_{ab} = \langle\psi|c_b c_a^\dagger|\psi\rangle$ reads:

$$\hat{\Delta} = \begin{pmatrix} \sin^2\theta/4 & 0 & 0 \\ 0 & 1/2 & 0 \\ 0 & 0 & 1-\sin^2\theta/4 \end{pmatrix},$$

and

$$Q_1 = Q_3 = \frac{\sin\theta\cos\theta}{2\sqrt{2}},$$

while by construction $Q_2 = 0$. Therefore, for $\theta \sim 0$:

$$R_1 = R_3 = \frac{1}{\sqrt{2}} + O\left(\theta^2\right),$$

and thus the quasiparticle Hamiltonian reads:

$$H_* = -\frac{t}{2\sqrt{\mathbf{Z}}}\sum_{\langle ij\rangle\sigma}\left[\left(c_{i\,1\sigma}^\dagger + c_{i\,3\sigma}^\dagger\right)\left(c_{j\,1\sigma} + c_{j\,3\sigma}\right) + \text{H.c.}\right] + \frac{\mu}{2}\sum_{i\sigma}\left(c_{i\,1\sigma}^\dagger c_{i\,1\sigma} - c_{i\,3\sigma}^\dagger c_{i\,3\sigma}\right), \tag{A.7}$$

that naturally satisfies the condition on the occupation of the low-energy site $\langle\Psi_*|c_{i\,2\sigma}^\dagger c_{i\,2\sigma}|\Psi_*\rangle = 1/2$. The Lagrange multiplier μ is determined by imposing the constraint:

$$\langle\Psi_*|c_{i\,1\sigma}^\dagger c_{i\,1\sigma}|\Psi_*\rangle = \frac{1}{V}\sum_{\mathbf{k}} n_{11\sigma\mathbf{k}} = \frac{\sin^2\theta}{4},$$

where

$$\begin{aligned} n_{11(33)\sigma\mathbf{k}} &= \frac{1}{2} \mp \frac{1}{2} \frac{1}{\sqrt{1+\epsilon_{\mathbf{k}}^2/\mu^2}}, \\ n_{13(31)\sigma\mathbf{k}} &= -\frac{1}{2} \frac{\epsilon_{\mathbf{k}}/\mu}{\sqrt{1+\epsilon_{\mathbf{k}}^2/\mu^2}}, \end{aligned} \tag{A.8}$$

and $\epsilon_{\mathbf{k}}$ is defined in Eq. (3.70). In the large-U regime we expect $\mu \sim U$ and $\epsilon_{\mathbf{k}}/\mu \ll 1$:

$$\langle \Psi_* | c_{i\,1\sigma}^\dagger c_{i\,1\sigma} | \Psi_* \rangle \simeq \frac{1}{4V} \sum_{\mathbf{k}} \frac{\epsilon_{\mathbf{k}}^2}{\mu^2} \to \frac{\mu}{W} = \frac{1}{2\theta} + O(\theta),$$

where W is the half-bandwidth, $W = 2t$. Therefore, the kinetic energy per site is:

$$E_* = \frac{1}{2V} \sum_{\mathbf{k}} \sum_{\sigma} \epsilon_{\mathbf{k}} \left(n_{11\mathbf{k}\sigma} + n_{33\mathbf{k}\sigma} + n_{13\mathbf{k}\sigma} + n_{31\mathbf{k}\sigma} \right) = -W \left[\frac{\theta}{2} + O\left(\theta^3\right) \right],$$

and the average value of the Hubbard repulsion is:

$$U \langle \psi | n_\uparrow n_\downarrow | \psi \rangle = U \left[\frac{\theta^2}{2} + O\left(\theta^4\right) \right].$$

Finally, the variational energy reads:

$$E(\theta) = -W\frac{\theta}{2} + U\frac{\theta^2}{2},$$

and the saddle-point equation, $\partial_\theta E(\theta) = 0$, reads:

$$-\frac{W}{2} + U\theta = 0 \to \bar{\theta} = \frac{W}{2U},$$

and

$$\mu = U.$$

The ground-state energy is

$$E\left(\bar{\theta}\right) = -\frac{W^2}{8U} = -\frac{J}{8}, \tag{A.9}$$

the double occupancy reads:

$$\left\langle \psi\left(\bar{\theta}\right) \right| n_\uparrow n_\downarrow \left| \psi\left(\bar{\theta}\right) \right\rangle = \frac{W^2}{8U^2}$$

and

$$\left\langle \psi\left(\bar{\theta}\right) \right| \mathbf{S}_2 \cdot \mathbf{S} \left| \psi\left(\bar{\theta}\right) \right\rangle = -\frac{3}{4}\left(1 - \frac{W^2}{8U^2}\right).$$

Eq. (A.9) is, indeed, the correct ground state energy per site for $U/W \gg 1$, the limit in which the Hubbard model tends to the $t-J$ model:

$$H_{t-J} = \frac{J}{\mathbf{Z}} \sum_{\langle ij \rangle} \left(\mathbf{S}_i \cdot \mathbf{S}_j - \frac{1}{4} \right),$$

where $\mathbf{Z} \gg 1$. In this limit and for a paramagnetic wave function only the second term survives and $E_{t-J}/V = -J/8$. Furthermore, the dispersion relation of the high-energy auxiliary degrees of freedom is:

$$E_\pm(\mathbf{k}) = \frac{\epsilon_{\mathbf{k}}}{2} \pm \frac{U}{2} \sqrt{1 + \frac{\epsilon_{\mathbf{k}}^2}{U^2}},$$

and gives rise to the upper and lower Hubbard bands.

Before concluding, we notice that the trial wave function obtained by a triplet combination

$$|\psi\rangle = |\phi_\sigma\rangle \times |\varphi_\sigma\rangle$$

is separated by an energy gap $\Delta E_{\text{T-S}} = W^2/8U$ from the singlet ground-state. Indeed, by performing similar calculations to those presented before, it is straightforward to obtain that in the large-U regime the variational energy per lattice site reads

$$E_T(\theta) = \frac{U}{2}\theta^2 - W\theta^2 \rightarrow \bar{\theta} = 0.$$

A.3 Spectral properties of the physical electrons

The variational Hamiltonian H_* in Eq. (3.22) has rigorously no physical meaning but for the ground state properties. However, it is common [42, 109, 163] to interpret it as the Hamiltonian of the quasiparticles. Within such an assumption, the g-GW approximation can be regarded as a tool to extract low-energy quasiparticle and high-energy features. More precisely, suppose we already have the saddle-point values of $R_{\alpha a}(i)$ and $\lambda_{ab}(i)$, then under the assumption of translational invariant ground state the quasiparticle Hamiltonian reads

$$\mathcal{H}_* = \sum_{\mathbf{k}} \sum_{ab=1}^{2N} c^\dagger_{\mathbf{k}a}\, \mathcal{H}_*(\mathbf{k})_{ab}\, c_{\mathbf{k}b}, \tag{A.10}$$

with

$$\mathcal{H}_*(\mathbf{k})_{ab} = \left(\sum_{\alpha\beta=1}^{2M} R^\dagger_{a\alpha}\, \epsilon^{\alpha\beta}_{\mathbf{k}}\, R_{\beta b} + \lambda_{ab} \right), \tag{A.11}$$

and

$$\epsilon^{\alpha\beta}_{\mathbf{k}} = -\sum_{j}^{\text{n.n. } i} e^{-i\mathbf{k}\cdot(\mathbf{R}_j - \mathbf{R}_i)} \frac{t^{\alpha\beta}}{\sqrt{\mathbf{Z}}}, \tag{A.12}$$

where the sum extends only over nearest neighbors of i. The quasiparticle Green's function is a $2N \times 2N$ for any $\mathbf{k}$ point in the Brillouin zone and reads:

$$\mathcal{G}^{-1}(\mathbf{k}, z) = z\mathbf{1} - \mathcal{H}_*(\mathbf{k}), \tag{A.13}$$

where z is a complex variable. Within the g-GW approximation, the physical electron Green's function is given by:

$$G_{\alpha\beta}(\mathbf{k}, z) = \sum_{ab=1}^{2N} R_{\alpha a}\, \mathcal{G}_{\mathbf{k}ab}(\mathbf{k}, z)\, R^\dagger_{b\beta} \equiv \left[\frac{1}{z\mathbf{1} - \epsilon_{\mathbf{k}} - \mathbf{\Sigma}(z)} \right]_{\alpha\beta}, \tag{A.14}$$

where $\epsilon_{\mathbf{k}}$ is the $2M \times 2M$ matrix defined in Eq. (A.12). The momentum-resolved spectral function is:

$$A_{\alpha\beta}(\mathbf{k}, \omega) = -\frac{1}{\pi} \text{Im} G_{\alpha\beta}(\mathbf{k}, \omega + i0^+). \tag{A.15}$$

By summing over $\mathbf{k}$ we obtain the local spectral function

$$A_{\alpha\beta}(\omega) = \frac{1}{V} \sum_{\mathbf{k}} A_{\alpha\beta}(\mathbf{k}, \omega). \tag{A.16}$$

Before concluding the section, we present the single-particle Green's function of the impurity electrons of a generic single-level impurity model (we recall section 3.3 for an introduction to impurity models). By following the same assumptions used before, we can interpret the auxiliary degrees of freedom $c_{a\sigma}$ of the self-consistent g-GW RLM in Eq. (3.56) as the quasiparticle excitations of the correlated model. It readily follows:

$$\mathbf{G}_{c\sigma}(z) = \mathbf{G}^0_{c\sigma}(z) + \mathbf{G}^0_{c\sigma}(z) \cdot \mathbf{\Sigma}_{c\sigma}(z) \cdot \mathbf{G}_{c\sigma}(z), \tag{A.17}$$

where z is a complex variable, $\mathbf{G}_{c\sigma}(z)$ is the dressed $c_{a\sigma}$ fermions Green's function while $\mathbf{G}^0_{c\sigma}(z)$ is the bare one:

$$\left[\mathbf{G}^0_{c\sigma}(z)\right]^{-1} = z\mathbf{1} - \hat{\lambda}_\sigma. \tag{A.18}$$

Finally, the $c_{a\sigma}$ fermions self-energy in Eq. (A.17) reads:

$$\Sigma_{c\sigma ab}(z) = R^*_{\sigma,a\sigma}\, \Delta(z)\, R_{\sigma,b\sigma}, \tag{A.19}$$

where $\Delta(z)$ is the hybridization function, defined in Eq. (3.53) and evaluated at the complex frequency z. The solution of the Dyson's equation (A.17) is:

$$[\mathbf{G}_{c\sigma}(z)]^{-1} = \left[\mathbf{G}^0_{c\sigma}(z)\right]^{-1} - \mathbf{\Sigma}_{c\sigma}(z), \tag{A.20}$$

and allows computing the impurity fermion Green's function, that reads:

$$G_{d\sigma}(z) = \sum_{ab=1}^{N} R_{\sigma,a\sigma}\, G_{c\sigma ab}(z)\, R^*_{\sigma,b\sigma} = \frac{1}{\left(G^0_{d\sigma}(z)\right)^{-1} - \Sigma_{d\sigma}(z)}, \tag{A.21}$$

where $G^0_{d\sigma}(i\epsilon)$ includes the non-interacting local Hamiltonian and the hybridization with the metallic host.

Before concluding the section, we remark that in the g-GW the wave function renormalization matrix is a rectangular matrix $\hat{R}$ and, thus, is not invertible. Consequently, the g-GA lattice $\mathbf{\Sigma}(z)$ and impurity $\Sigma_{d\sigma}(z)$ self-energies in Eqs. (A.14) and (A.21) are not necessarily linear functions of the frequency z.

A.4 Low-energy Fermi liquid parameters: the quasiparticle residue

The Landau theory[1] for Fermi liquids asserts that in the vicinity of the Fermi surface $\mathbf{k} \simeq \mathbf{k}_F$, where the Fermi momentum is defined as $\epsilon_{\mathbf{k}_F} = 0$, the singular part of the Green's function reads [2, 211]:

$$G(\mathbf{k}, \omega) \simeq \frac{Z_{\mathbf{k}}}{\omega - \vec{v}(\mathbf{k}_F) \cdot (\mathbf{k} - \mathbf{k}_F) + i0^+ \mathrm{sign}(|\mathbf{k}| - |\mathbf{k}|_F)}. \tag{A.22}$$

The presence of low-energy coherent excitations induces a discontinuity of the fermionic distribution function:

$$n_{\mathbf{k}} = -i \int_{-\infty}^{\infty} \frac{d\omega}{2\pi} e^{i\omega 0^+} G(\mathbf{k}, \omega). \tag{A.23}$$

In particular, we have:

$$n_{\mathbf{k}_F^-} - n_{\mathbf{k}_F^+} = Z_{\mathbf{k}_F} \leq 1 \tag{A.24}$$

[1] We notice that the Landau theory holds for repulsive interaction among the electrons. In the presence of attraction between electrons the ground state is radically different from the that of the non-interacting Fermi gas.

where $\mathbf{k}_F^{\mp}$ indicates the limit $\mathbf{k} \to \mathbf{k}_F$ from below and above, respectively, the upper bound comes from the Pauli exclusion principle. In the case of the Fermi gas, the jump goes to unity. As anticipated, the jump gives the fraction of excitations of the interacting systems, which can be described in terms of effective free particles.

By applying the result in Eq. (A.23) to the g-GW approach we find that the quasiparticle residue in g-GW for a lattice model reads:

$$Z_{\alpha\beta} = n_{\alpha\beta}(\epsilon = \epsilon_F^-) - n_{\alpha\beta}(\epsilon = \epsilon_F^+), \tag{A.25}$$

where $\epsilon_F^{\mp}$ indicates the limit $\epsilon \to \epsilon_F$ from below and above, respectively, and

$$n_{\alpha\beta}(\epsilon) = \sum_{ab=1}^{2N} R^{\dagger}_{\alpha a} \left(\frac{1}{V} \sum_{\mathbf{k}} \delta(\epsilon - \epsilon_{\mathbf{k}}) \langle \Psi_* | c^{\dagger}_{\mathbf{k}a} c_{\mathbf{k}b} | \Psi_* \rangle \right) R_{b\beta}. \tag{A.26}$$

We remind that $c_{\mathbf{k}a}$ is the auxiliary fermion operator described by the quasiparticle Hamiltonian in Eq. (A.10). Finally, for impurity models the quasiparticle residue is obtained by exploiting the relation:

$$Z_{d\sigma} = \left. \frac{1}{1 - \partial_\omega \Sigma_{d\sigma}(\omega)} \right|_{\omega=0} \tag{A.27}$$

where

$$\Sigma_{d\sigma}(z) = z - \epsilon^d_\sigma - \Delta_\sigma(z) - G^{-1}_{d\sigma}(z), \tag{A.28}$$

and ϵ^d_σ is single-body on-site energy of the impurity fermion d_σ.

B

Details on the physics of photoexcited semiconductors

In this Appendix we report some useful calculations that allows a better understanding of Chapter 4. In Section B.1 we consider the simple example of a single e-h pair, where a simple calculation allow us to show that, in the presence an on-site attraction and for lattices in dimensions large than 2, a finite value of U is needed to form a bound state below the two-particle continuum. In Section B.2 we compute analytically the g-GW wave function for the exciton gas in the regime of large-U.

B.1 A single pair of e-h excitations: the critical U

In this section we perform a simple calculation that in lattices with large coordination $\mathbf{Z} \gg 1$ and in the presence of short-range attraction between e-h pairs $U > U_c$ in order to observe a bound state below the two-particle continuum. A single pair of e-h excitations is described by the wave function:

$$|\Psi_{\text{e-h}}(\mathbf{Q})\rangle = \sum_{\mathbf{k}} L(\mathbf{Q},\mathbf{k})\, e^{\dagger}_{\mathbf{k}}\, h^{\dagger}_{\mathbf{Q}-\mathbf{k}}|0\rangle \tag{B.1}$$

where the coefficients $L(\mathbf{Q},\mathbf{k})$ are obtained by looking for the eigenstates of the Hamiltonian (4.2). The secular Eq. reads:

$$L(\mathbf{Q},\mathbf{k}) = -\frac{U}{V}\sum_{\mathbf{p}} \frac{L(\mathbf{Q},\mathbf{p})}{E(\mathbf{Q}) - \epsilon_{\mathbf{k}} - \epsilon_{\mathbf{Q}-\mathbf{k}}}. \tag{B.2}$$

By defining:

$$J(\mathbf{Q}) = \frac{1}{V}\sum_{\mathbf{p}} L(\mathbf{Q},\mathbf{p}),$$

and summing over $\mathbf{k}$, Eq. (B.2) becomes:

$$1 = -\frac{U}{V}\sum_{\mathbf{k}} \frac{1}{E(\mathbf{Q}) - \epsilon_{\mathbf{k}} - \epsilon_{\mathbf{Q}-\mathbf{k}}},$$

whose solutions determine the eigenvalues of the e-h wave function (B.1). In particular, since we are interested to the ground state solution, we set $\mathbf{Q} = \mathbf{0}$ and we look the critical value of U where a bound state solution appear below the two-particle continuum:

$$1 + U \int d\epsilon \frac{\rho(\epsilon)}{E - 2\epsilon} = 0, \tag{B.3}$$

with $E < -2W$. For $\rho(\epsilon)$ given by the semicircular DOS in Eq. (3.61) we obtain $U_c = 1$. We notice that for cubic lattice structures $U_c = 0$ for dimensions $D = 1, 2$, while U_c is finite for $D > 2$.

B.2 The exciton gas in the large-U limit

In this section we perform an analytic calculation for the exciton gas in the limit of large-U and arbitrary density of e-h pairs. For convenience we perform the unitary transformation in Eq. (4.4) that translates the problem of a gas of bound e-h pairs in a magnetized Mott insulator. By following the same line of reasoning presented in Section A.2, the embedded impurity wave function is parametrized by the wave function in Eq. (4.12):

$$|\psi\rangle = \cos\phi\, |\phi_\uparrow\rangle \times |\varphi_\downarrow\rangle - \sin\phi\, |\phi_\downarrow\rangle \times |\varphi_\uparrow\rangle$$

where $|\varphi_\sigma\rangle = |\sigma\rangle$ describes the spin configuration on the low-energy site, and $|\phi_\sigma\rangle$ is parametrized by:

$$\begin{aligned}
\phi_\uparrow(\uparrow; 2, 0) &= \cos\theta, \\
\phi_\uparrow(2; \uparrow, 0) &= \frac{\sin\theta}{\sqrt{2}} \frac{\cos\phi_1}{\cos\phi}, \\
\phi_\uparrow(0; 2, \uparrow) &= -\frac{\sin\theta}{\sqrt{2}} \frac{\cos\phi_2}{\cos\phi},
\end{aligned} \tag{B.4}$$

and

$$\begin{aligned}
\phi_\downarrow(\downarrow; 2, 0) &= \cos\theta, \\
\phi_\downarrow(2; \downarrow, 0) &= \frac{\sin\theta}{\sqrt{2}} \frac{\sin\phi_1}{\sin\phi}, \\
\phi_\downarrow(0; 2, \downarrow) &= -\frac{\sin\theta}{\sqrt{2}} \frac{\sin\phi_2}{\sin\phi}.
\end{aligned} \tag{B.5}$$

We notice that Eq. satisfies the normalization condition (3.13). Moreover, the wave function (4.12) corresponds to mix the triplet $S^z = 0$ and the singlet component. The relevant components of the bath single-particle density matrix read:

$$\begin{aligned}
\Delta_{11\uparrow} &= \frac{\sin^2\theta \sin^2\phi_1}{2}, \\
\Delta_{11\downarrow} &= \frac{\sin^2\theta \cos^2\phi_1}{2}, \\
\Delta_{33\uparrow} &= 1 - \frac{\sin^2\theta \cos^2\phi_2}{2}, \\
\Delta_{33\downarrow} &= 1 - \frac{\sin^2\theta \sin^2\phi_2}{2},
\end{aligned} \tag{B.6}$$

while the impurity magnetization reads:

$$m = \langle\psi| d_\uparrow^\dagger d_\uparrow |\psi\rangle - \langle\psi| d_\downarrow^\dagger d_\downarrow |\psi\rangle = \cos 2\phi \cos^2\theta. \tag{B.7}$$

We notice that particle symmetry (4.7) implies $\Delta_{11\uparrow} = 1 - \Delta_{33\downarrow}$ and $\Delta_{11\downarrow} = 1 - \Delta_{33\uparrow}$, thus, from Eq. (B.6) it follows that $\phi_1 = \phi_2$. Therefore, the tunnel-coupling matrix elements are:

$$\langle\psi|c^\dagger_{1\uparrow}d_\uparrow|\psi\rangle = \langle\psi|c^\dagger_{3\downarrow}d_\downarrow|\psi\rangle = \cos\theta\sin\theta\sin\phi\sin\phi_1/\sqrt{2},$$
$$\langle\psi|c^\dagger_{1\downarrow}d_\downarrow|\psi\rangle = \langle\psi|c^\dagger_{3\uparrow}d_\uparrow|\psi\rangle = \cos\theta\sin\theta\cos\phi\cos\phi_1/\sqrt{2},$$

and

$$R_{1\uparrow} = R_{3\downarrow} = \cos\theta\sin\phi/\sqrt{1-\sin^2\theta\sin^2\phi_1/2} \simeq \sin\phi,$$
$$R_{1\downarrow} = R_{3\uparrow} = \cos\theta\cos\phi/\sqrt{1-\sin^2\theta\cos^2\phi_1/2} \simeq \cos\phi,$$

where we are assuming $\theta \sim 0$ since $U/W \gg 1$. The quasiparticle Hamiltonian is given by:

$$\begin{aligned}H_* = &-\frac{t}{\sqrt{\mathbf{Z}}}\sum_{\langle ij\rangle}\left[\left(\sin\phi\, c^\dagger_{i1\uparrow} + \cos\phi\, c^\dagger_{i3\uparrow}\right)\left(\sin\phi\, c_{i1\uparrow} + \cos\phi\, c_{i3\uparrow}\right) + \text{H.c.}\right]\\ &-\frac{t}{\sqrt{\mathbf{Z}}}\sum_{\langle ij\rangle}\left[\left(\cos\phi\, c^\dagger_{i1\downarrow} + \sin\phi\, c^\dagger_{i3\downarrow}\right)\left(\cos\phi\, c_{i1\downarrow} + \sin\phi\, c_{i3\downarrow}\right) + \text{H.c.}\right]\\ &+\frac{\mu+\epsilon}{2}\sum_i\left(c^\dagger_{i1\uparrow}c_{i1\uparrow} - c^\dagger_{i3\downarrow}c_{i3\downarrow}\right) + \frac{\mu-\epsilon}{2}\sum_i\left(c^\dagger_{i1\downarrow}c_{i1\downarrow} - c^\dagger_{i3\uparrow}c_{i3\uparrow}\right),\end{aligned}$$

and in $\mathbf{k}$ space becomes

$$\begin{aligned}H_* = &\sum_{\mathbf{k}}\vec{\Psi}^\dagger_{\mathbf{k}\uparrow}\cdot\left(\frac{\epsilon_{\mathbf{k}}}{2}\mathbf{1} - \cos 2\phi\frac{\epsilon_{\mathbf{k}}}{2}\sigma^z + \sin 2\phi\frac{\epsilon_{\mathbf{k}}}{2}\sigma^x + \frac{\mu}{2}\sigma^z + \frac{\epsilon}{2}\mathbf{1}\right)\cdot\vec{\Psi}_{\mathbf{k}\uparrow}\\ &+\sum_{\mathbf{k}}\vec{\Psi}^\dagger_{\mathbf{k}\downarrow}\cdot\left(\frac{\epsilon_{\mathbf{k}}}{2}\mathbf{1} + \cos 2\phi\frac{\epsilon_{\mathbf{k}}}{2}\sigma^z + \sin 2\phi\frac{\epsilon_{\mathbf{k}}}{2}\sigma^x + \frac{\mu}{2}\sigma^z - \frac{\epsilon}{2}\mathbf{1}\right)\cdot\vec{\Psi}_{\mathbf{k}\downarrow},\end{aligned}$$

where we have introduce the spinor $\vec{\Psi}_{\mathbf{k}\downarrow} = (c_{\mathbf{k}1\sigma}\ c_{\mathbf{k}3\sigma})^T$. The eigenvalues are:

$$E_{1(3)\uparrow}(\mathbf{k}) = \frac{\epsilon_{\mathbf{k}}+\epsilon}{2} \pm \frac{1}{2}\sqrt{(\mu - \cos 2\phi\,\epsilon_{\mathbf{k}})^2 + \sin^2 2\phi\,\epsilon^2_{\mathbf{k}}},$$
$$E_{1(3)\downarrow}(\mathbf{k}) = \frac{\epsilon_{\mathbf{k}}-\epsilon}{2} \pm \frac{1}{2}\sqrt{(\mu + \cos 2\phi\,\epsilon_{\mathbf{k}})^2 + \sin^2 2\phi\,\epsilon^2_{\mathbf{k}}},$$

while the eigenstates are:

$$f_{\mathbf{k}1\sigma} = \cos\frac{\theta_{\mathbf{k}\sigma}}{2}c_{\mathbf{k}1\sigma} + \sin\frac{\theta_{\mathbf{k}\sigma}}{2}c_{\mathbf{k}3\sigma},$$
$$f_{\mathbf{k}3\sigma} = \cos\frac{\theta_{\mathbf{k}\sigma}}{2}c_{\mathbf{k}3\sigma} - \sin\frac{\theta_{\mathbf{k}\sigma}}{2}c_{\mathbf{k}1\sigma},$$

where the angle $\theta_{\mathbf{k}\sigma}$ is given by:

$$\tan\theta_{\mathbf{k}\uparrow(\downarrow)} = \frac{\sin 2\phi\,\epsilon_{\mathbf{k}}}{\mu \mp \cos 2\phi\,\epsilon_{\mathbf{k}}}.$$

In the large-U regime we expect that the bands $3\uparrow$ and $3\downarrow$ are fully occupied while $1\uparrow$ and $1\downarrow$ orbitals are empty. It follows that the Gutzwiller constraints on the single-particle density matrix (3.13) become:

$$\frac{\Delta_{33\uparrow} - \Delta_{11\uparrow}}{2} = -\frac{1}{2V}\sum_{\mathbf{k}}\langle\Psi_*|\,\vec{\Psi}^\dagger_{\mathbf{k}\uparrow}\cdot\sigma^z\cdot\vec{\Psi}_{\mathbf{k}\uparrow}\,|\Psi_*\rangle\,,$$

and

$$\frac{\Delta_{33\downarrow}-\Delta_{33\uparrow}}{2}=\frac{1}{2V}\sum_{\mathbf{k}}\left(\langle\Psi_*|\,c^\dagger_{\mathbf{k}3\downarrow}c_{\mathbf{k}3\downarrow}\,|\Psi_*\rangle-\langle\Psi_*|\,c^\dagger_{\mathbf{k}3\uparrow}c_{\mathbf{k}3\downarrow}\,|\Psi_*\rangle\right).$$

In terms of the quasiparticles $f_{\mathbf{k}a\sigma}$ the latter Eq. reads:

$$\frac{\sin^2\theta\cos 2\phi_1}{2}=\frac{1}{V}\sum_{\mathbf{k}}\left(\cos^2\frac{\theta_{\mathbf{k}\uparrow}}{2}-\cos^2\frac{\theta_{\mathbf{k}\downarrow}}{2}\right)=0\implies\phi_1=\pi/4,\ \epsilon=0,$$

where the sum on the Brillouin zone vanishes because $\theta_{\mathbf{k}\uparrow}=-\theta_{\mathbf{k}+\mathbf{Q}\downarrow}$with $\mathbf{Q}=(\pi,\cdots,\pi)$. By expanding the former Eq. in $\epsilon_{\mathbf{k}}/\mu\ll 1$ and keeping terms up to $\epsilon^2_{\mathbf{k}}/\mu^2$, we obtain:

$$1-\frac{\sin^2\theta}{2}=\frac{1}{V}\sum_{\mathbf{k}}\left(1-\frac{1}{2}\sin^2 2\phi\frac{\epsilon^2_{\mathbf{k}}}{\mu^2}\right)\implies\mu=\frac{W}{2}\frac{\sin 2\phi}{\sin\theta}.$$

The average value of the kinetic energy reads:

$$\begin{aligned}E_*=&\frac{1}{V}\sum_{\mathbf{k}}\left(\epsilon_{\mathbf{k}}\cos 2\phi\cos\theta_{\mathbf{k}\uparrow}-\epsilon_{\mathbf{k}}\sin 2\phi\sin\theta_{\mathbf{k}\uparrow}\right),\\ \simeq&-\frac{\sin^2 2\phi}{\mu}\frac{1}{V}\sum_{\mathbf{k}}\epsilon^2_{\mathbf{k}}=-\frac{W}{2}\sin 2\phi\sin\theta.\end{aligned}$$

On the other hand, the energy contribution given by the on-site repulsion is:

$$U\langle\psi|n_\uparrow n_\downarrow|\psi\rangle=U\frac{\sin^2\theta}{2}.$$

Since the parametrization is meant to describe the large-U limit, we assume $\theta\ll 1$ so that Eq. (B.7) becomes

$$m\simeq\cos 2\phi,$$

and

$$E(\theta,m)\simeq-\frac{W}{2}\sqrt{1-m^2}\theta+\frac{U}{2}\theta,$$

where the magnetization m is regarded as a parameter fixed by the density of e-h excitations. Therefore, the optimization of the variational energy gives:

$$\partial_\theta E(\theta,m)=-\frac{W}{2}\sqrt{1-m^2}+U\theta=0\implies\bar\theta(m)=\frac{W}{2U}\sqrt{1-m^2}$$

and $\mu=U$. Finally, we obtain that the energy of the large-U Mott insulator in the presence of a finite magnetization reads:

$$E(\bar\theta,m)=-\frac{W^2}{8U}(1-m^2)=-\frac{J}{8}(1-m^2)$$

in agreement with the result predicted by the $t-J$ model in the presence of a finite magnetization:

$$E_{t-J}(m)\simeq\frac{1}{V}\frac{J}{\mathbf{Z}}\sum_{\langle ij\rangle}\left(\frac{m^4}{4}-\frac{1}{4}\right)=-\frac{J}{8}(1-m^2),$$

where $\mathbf{Z}\to\infty$.

In the context of the PES the previous result implies that the energy of the an EG, in the regime of small $n_{\text{e-h}}$, is:

$$E_{\text{EG}}(n_{\text{e-h}}) = -\frac{W^2}{2\,|U|} n_{\text{e-h}}(1 - n_{\text{e-h}}), \tag{B.8}$$

and its charge susceptibility κ is always larger than zero, $\kappa = 1/\partial^2_{n_{\text{e-h}}} E_{\text{EG}}(n_{\text{e-h}}) = |U|\,/W^2 > 0$. The exciton binding energy goes like:

$$E_{\text{ex}} = E_{1\downarrow}(\mathbf{0}) - E_{3\downarrow}(\mathbf{Q}) = |U| + O\left(\frac{W^2}{|U|}\right) \tag{B.9}$$

which signals the presence of strongly bound excitons. Furthermore, the area under the exciton spectral function $A_{\text{ex}}(\omega)$:

$$\int d\epsilon\, A_{\text{ex}}(\epsilon) = R^2_{3\downarrow} = \sin^2\phi = \frac{1-m}{2} = n_{\text{e-h}},$$

i.e. all the photoexcited carriers are bound pairs. Thus, the g-GW predicts that in the asymptotic limit of small densities and large on-site attraction (small dielectric constant) the e-h excitations bind to form a stable phase EG, that is characterized by the exciton binding energy (B.9), that grows linearly with the strength of the on site attraction, and the charge susceptibility $\kappa = |U|\,/W^2 \sim E_{\text{ex}}/W^2$ (B.8).

C

Details on the slave-spin technique

In this Appendix we present additional details on the slave-spin mapping in Chapter 6. In Section C.1 we show the consequences of Eq. (6.20). In Section C.2 we prove that certain observables can be computed in the enlarged slave-spin Hilbert space without any constraint. In Section C.3 we extend this result to the single-particle Green's function. The slave-boson instability respect to magnetic ordering is reported in Section C.4. In Section C.5 we report supplemental informations on the slave-spin mean-field theory reported in Section 6.4. Finally, in Section C.6 we present some additional results useful to exploit the slave-spin mean-field theory as approximate impurity solver for the DMFT.

C.1 Thermodynamic averages in the physical subspace

The equivalence between the partition functions (6.20) implies the following equalities.

Average value of the energy;

$$\langle H \rangle = -\partial_\beta \log [Z] = -\partial_\beta \log [Z_2/4] = \langle H_2 \rangle_2. \tag{C.1}$$

Average magnetization;

$$m \equiv \langle n_\uparrow - n_\downarrow \rangle = \frac{2}{\beta}\partial_h \log [Z] = \frac{2}{\beta}\partial_h \log [Z_2/4] = \left\langle \frac{\tau^z_\uparrow - \tau^z_\downarrow}{2} \right\rangle_2 . \tag{C.2}$$

Average occupation;

$$\rho \equiv \langle n_\uparrow + n_\downarrow - 1 \rangle = \frac{2}{\beta}\partial_\mu \log [Z] = \frac{2}{\beta}\partial_\mu \log [Z_2/4] = \left\langle \frac{\tau^z_\uparrow + \tau^z_\downarrow}{2} \right\rangle_2 . \tag{C.3}$$

Average value of the hybridization; in order to obtain the average value of the hybridization of the impurity fermion with the fermionic host we introduce two different parameters γ_a such that $V_{a\mathbf{k}\sigma} \to \gamma_a V_{a\mathbf{k}\sigma}$ and

$$H = H_{\text{bath}} + H_{\text{loc}} + \sum_{a=1,2} \gamma_a T_a, \tag{C.4}$$

where

$$T_1 = \sum_\sigma \sum_{\mathbf{k}}^{\epsilon_{\mathbf{k}\sigma}<0} \frac{V_{1\mathbf{k}\sigma}}{\sqrt{V}} \left(d_\sigma^\dagger \psi_{1\mathbf{k}\sigma} + \psi_{1\mathbf{k}\sigma}^\dagger d_\sigma \right),$$
$$T_2 = \sum_\sigma \sum_{\mathbf{k}}^{\epsilon_{\mathbf{k}\sigma}<0} \frac{V_{2\mathbf{k}\sigma}}{\sqrt{V}} \left(d_\sigma^\dagger \psi_{2\mathbf{k}\sigma} + \psi_{2\mathbf{k}\sigma}^\dagger d_\sigma \right). \tag{C.5}$$

Once the derivative respect to is performed we set the correspondent value to one, $\gamma_a = 1$.

$$\langle T_1 \rangle = -\frac{1}{\beta} \partial_{\gamma_1} \log\left[Z_2/4\right]\Big|_{\gamma_a=1} = \left\langle \sum_\sigma \sum_{\mathbf{k}}^{\epsilon_{\mathbf{k}\sigma}<0} \tau_\sigma^x \frac{V_{1\mathbf{k}\sigma}}{\sqrt{V}} \left(f_\sigma^\dagger \psi_{1\mathbf{k}\sigma} + \psi_{1\mathbf{k}\sigma}^\dagger f_\sigma \right) \right\rangle_2,$$
$$\langle T_2 \rangle = -\frac{1}{\beta} \partial_{\gamma_2} \log\left[Z_2/4\right]\Big|_{\gamma_a=1} = \left\langle \sum_\sigma \sum_{\mathbf{k}}^{\epsilon_{\mathbf{k}\sigma}<0} i\tau_\sigma^y \frac{V_{2\mathbf{k}\sigma}}{\sqrt{V}} \left(f_\sigma^\dagger \psi_{2\mathbf{k}\sigma} - \psi_{2\mathbf{k}\sigma}^\dagger f_\sigma \right) \right\rangle_2. \tag{C.6}$$

Average value of the energy variation of the bath; in this case we perform the substitution $\epsilon_{\mathbf{k}\sigma} \to \alpha_\sigma \epsilon_{\mathbf{k}\sigma}$ and:

$$\langle H_{\mathrm{bath},\sigma} \rangle = -\frac{1}{\beta} \partial_{\alpha_\sigma} \log\left[Z_2/4\right]\Big|_{\alpha_\sigma=1} = \left\langle \sum_{\mathbf{k}}^{\epsilon_{\mathbf{k}\sigma}<0} \epsilon_{\mathbf{k}\sigma} \left(\psi_{1\mathbf{k}\sigma}^\dagger \psi_{2\mathbf{k}\sigma} + \psi_{2\mathbf{k}\sigma}^\dagger \psi_{1\mathbf{k}\sigma} \right) \right\rangle_2. \tag{C.7}$$

In the previous Eqs. we have used the notation introduced in Eq. (6.22):

$$\langle \cdots \rangle_2 = \mathrm{Tr}\left[\exp\left(-\beta H_2(U,\mu,h,V_{2\uparrow},V_{2\downarrow})\right)\cdots\right] / \mathrm{Tr}\left[\exp\left(-\beta H_2(U,\mu,h,V_{2\uparrow},V_{2\downarrow})\right)\right]. \tag{C.8}$$

We conclude by remarking that higher order derivatives of the $\log[Z]$ respect conjugated fields give impurity thermodynamic susceptibilities, i.e. magnetic susceptibility χ_{imp}, charge compressibility κ_{imp}, etc.

C.2 Average values in the physical subspace

Let us consider a generic operator O that commutes with the p-h transformation in Eq. (6.6):

$$[O, C_\sigma] = 0. \tag{C.9}$$

Its average value on the impurity model (6.1) reads:

$$\langle O(U,\mu,h,V_{2\uparrow},V_{2\downarrow}) \rangle = \frac{\mathrm{Tr}\left[\mathrm{e}^{-\beta H(U,\mu,h,V_{2\uparrow},V_{2\downarrow})} O\right]}{\mathrm{Tr}\left[\mathrm{e}^{-\beta H(U,\mu,h,V_{2\uparrow},V_{2\downarrow})}\right]} = \frac{\mathrm{Tr}\left[\mathrm{e}^{-\beta H_2(U,\mu,h,V_{2\uparrow},V_{2\downarrow})} O^{SS} \mathbb{P}\right]}{\mathrm{Tr}\left[\mathrm{e}^{-\beta H(U,\mu,h,V_{2\uparrow},V_{2\downarrow})}\right]} \tag{C.10}$$

where the operator O^{SS} is now constructed out of operators $\left\{ f_\sigma, \psi_{a\mathbf{k}\sigma}, \tau_\sigma^i \right\}$ that act on the enlarged Hilbert space, the latter Tr is extended to the enlarged Hilbert space $\mathscr{H}_*$ and the projector $\mathbb{P}$ (6.11) filters out the physical subspace where H_2 (6.16) is equivalent to the SIAM in Eq. (6.1). From Eq. (C.9) it readily follows:

$$\begin{aligned} \langle O(U,\mu,h,V_{2\uparrow},V_{2\downarrow}) \rangle &= \langle O(U,-h,-\mu,-V_{2\uparrow},V_{2\downarrow}) \rangle, \\ &= \langle O(-U,h,\mu,V_{2\uparrow},-V_{2\downarrow}) \rangle, \\ &= \langle O(U,-\mu,-h,-V_{2\uparrow},-V_{2\downarrow}) \rangle. \end{aligned} \tag{C.11}$$

Since the action of C_σ in the enlarged Hilbert space is implemented by τ^x_σ we have:

$$\begin{aligned}\langle O(U,\mu,h,V_{2\uparrow},V_{2\downarrow})\rangle =& \frac{1}{4\mathrm{Tr}\left[\mathrm{e}^{-\beta H(U,\mu,h,V_{2\uparrow},V_{2\downarrow})}\right]}\Big\{\mathrm{Tr}\left[\mathrm{e}^{-\beta H_2(U,\mu,h,V_{2\uparrow},V_{2\downarrow})}O^{SS}\mathbb{P}\right]\\ &+\mathrm{Tr}\left[\mathrm{e}^{-\beta H_2(U,\mu,h,V_{2\uparrow},V_{2\downarrow})}\tau^x_\uparrow O^{SS}\mathbb{P}\tau^x_\uparrow\right]\\ &+\mathrm{Tr}\left[\mathrm{e}^{-\beta H_2(U,\mu,h,V_{2\uparrow},V_{2\downarrow})}\tau^x_\downarrow O^{SS}\mathbb{P}\tau^x_\downarrow\right]\\ &+\mathrm{Tr}\left[\mathrm{e}^{-\beta H_2(U,\mu,h,V_{2\uparrow},V_{2\downarrow})}\tau^x_\uparrow\tau^x_\downarrow O^{SS}\mathbb{P}\tau^x_\downarrow\tau^x_\uparrow\right]\Big\}.\end{aligned} \tag{C.12}$$

Being invariant respect C_σ, it implies that in the slave-spin representation $\tau^x_\sigma O^{SS}\tau^x_\sigma = O^{SS}$. Finally, by using Eq. (6.19) we obtain:

$$\langle O\rangle = \frac{\mathrm{Tr}\left[\mathrm{e}^{-\beta H_2}O^{SS}\right]}{4\mathrm{Tr}\left[\mathrm{e}^{-\beta H}\right]} = \langle O\rangle_2, \tag{C.13}$$

where we drop the indices referring to the Hamiltonian parameters.

C.3 Single-particle Green's functions in the physical subspace

In the original representation, the impurity single-particle Green's functions in imaginary time are defined through:

$$\begin{aligned}G_\sigma(\tau) =& -\langle T_\tau\left(d_\sigma(\tau)d^\dagger_\sigma(0)\right)\rangle = -\frac{\theta(\tau)}{Z}\mathrm{Tr}\left(e^{-\beta H}e^{\tau H}d_\sigma e^{-\tau H}d^\dagger_\sigma\right)\\ &+\frac{\theta(-\tau)}{Z}\mathrm{Tr}\left(e^{-\beta H}d^\dagger_\sigma e^{\tau H}d_\sigma e^{-\tau H}\right),\end{aligned} \tag{C.14}$$

where the Hamiltonian $H = H(U,\mu,h,V_{2\uparrow},V_{2\downarrow})$ and the partition function $Z = Z(U,\mu,h,V_{2\uparrow},V_{2\downarrow})$. Through the action of the particle-hole transformations $C_\uparrow$ and $C_\downarrow$, and exploiting the invariance of the trace under a unitary transformation, one readily find the following relationships between the Green's functions in Matsubara frequencies $i\epsilon$:

$$\begin{aligned}G_\uparrow(i\epsilon;U,\mu,h,V_{2\uparrow},V_{2\downarrow}) &= G_\uparrow(i\epsilon;-U,h,\mu,V_{2\uparrow},-V_{2\downarrow}) = G_\uparrow(-i\epsilon;-U,-h,-\mu,-V_{2\uparrow},V_{2\downarrow})\\ &= G_\uparrow(-i\epsilon;U,-\mu,-h,-V_{2\uparrow},-V_{2\downarrow}),\\ G_\downarrow(i\epsilon;U,\mu,h,V_{2\uparrow},V_{2\downarrow}) &= G_\downarrow(i\epsilon;-U,-h,-\mu,-V_{2\uparrow},V_{2\downarrow}) = G_\downarrow(-i\epsilon;-U,h,\mu,V_{2\uparrow},-V_{2\downarrow})\\ &= G_\downarrow(-i\epsilon;U,-\mu,-h,-V_{2\uparrow},-V_{2\downarrow}).\end{aligned} \tag{C.15}$$

Because of Eq. (C.15) we define the physical Green's function as:

$$\begin{aligned}G_\uparrow(i\epsilon;U,\mu,h,V_{2\uparrow},V_{2\downarrow}) &\equiv \frac{G_\uparrow(i\epsilon;U,\mu,h,V_{2\uparrow},V_{2\downarrow}) + G_\uparrow(i\epsilon;-U,h,\mu,V_{2\uparrow},-V_{2\downarrow})}{2},\\ G_\downarrow(i\epsilon;U,\mu,h,V_{2\uparrow},V_{2\downarrow}) &\equiv \frac{G_\downarrow(i\epsilon;U,\mu,h,V_{2\uparrow},V_{2\downarrow}) + G_\downarrow(i\epsilon;-U,-h,-\mu,-V_{2\uparrow},V_{2\downarrow})}{2}.\end{aligned} \tag{C.16}$$

In the slave spin representation, the physical Green's functions can be alternatively obtained using the slave-spin Hamiltonian in Eq. (6.16) through the following expressions:

$$\begin{aligned}G_\sigma(\tau) =& -\frac{\theta(\tau)}{Z}\mathrm{Tr}\left(e^{-\beta H_2}e^{\tau H_2}\tau^-_\sigma f_\sigma e^{-\tau H_2}f^\dagger_\sigma\tau^+_\sigma\mathbb{P}_\uparrow\mathbb{P}_\downarrow\right)\\ &+\frac{\theta(-\tau)}{Z}\mathrm{Tr}\left(e^{-\beta H_2}f^\dagger_\sigma\tau^+_\sigma e^{\tau H_2}\tau^-_\sigma f_\sigma e^{-\tau H_2}\mathbb{P}_\uparrow\mathbb{P}_\downarrow\right),\end{aligned} \tag{C.17}$$

where Z is the partition function of the physical system, the slave-spin operators $\tau^{\pm}_{\sigma} = \tau^{x}_{\sigma} \pm i\tau^{y}_{\sigma}$, and $\mathbb{P}_{\sigma}$ is the projector on the physical subspace of the enlarged Hilbert space $\mathscr{H}_{*}$:

$$\mathbb{P}_{\sigma} = \frac{1}{2}\left(1 + \tau^{z}_{\sigma}(2n_{\sigma} - 1)\right). \tag{C.18}$$

We remind that $\tau^{x}_{\sigma}\mathbb{P}_{\sigma}\tau^{x}_{\sigma} = \bar{\mathbb{P}}_{\sigma} = \mathbf{1} - \mathbb{P}_{\sigma}$. Noticing that given σ and $\bar{\sigma} = -\sigma$:

$$\begin{aligned}
\mathrm{Tr}\left(e^{-\beta H}e^{\tau H}d_{\sigma}e^{-\tau H}d^{\dagger}_{\sigma}\right) &= \mathrm{Tr}\left(C^{\dagger}_{\bar{\sigma}}e^{-\beta H}C_{\bar{\sigma}}C^{\dagger}_{\bar{\sigma}}e^{\tau H}C_{\bar{\sigma}}d_{\sigma}C^{\dagger}_{\bar{\sigma}}e^{-\tau H}C_{\bar{\sigma}}d^{\dagger}_{\sigma}\right) \\
&= \mathrm{Tr}\left(e^{-\beta C^{\dagger}_{\bar{\sigma}}HC_{\bar{\sigma}}}e^{\tau C^{\dagger}_{\bar{\sigma}}HC_{\bar{\sigma}}}d_{\sigma}e^{-\tau C^{\dagger}_{\bar{\sigma}}HC_{\bar{\sigma}}}d^{\dagger}_{\sigma}\right) \\
&= \mathrm{Tr}\left(e^{-\beta\tau^{x}_{\bar{\sigma}}H_2\tau^{x}_{\bar{\sigma}}}e^{\tau\tau^{x}_{\bar{\sigma}}H_2\tau^{x}_{\bar{\sigma}}}\tau^{-}_{\sigma}f_{\sigma}e^{-\tau\tau^{x}_{\bar{\sigma}}H_2\tau^{x}_{\bar{\sigma}}}f^{\dagger}_{\sigma}\tau^{+}_{\sigma}\mathbb{P}_{\sigma}\mathbb{P}_{\bar{\sigma}}\right) \\
&= \mathrm{Tr}\left(e^{-\beta H_2}e^{\tau H_2}\tau^{-}_{\sigma}f_{\sigma}e^{-\tau H_2}f^{\dagger}_{\sigma}\tau^{+}_{\sigma}\mathbb{P}_{\sigma}\bar{\mathbb{P}}_{\bar{\sigma}}\right).
\end{aligned} \tag{C.19}$$

By using the definition in Eq. (C.15) and the previous result (C.19) we get rid of the projector on the opposite spin species $\mathbb{P}_{\bar{\sigma}}$:

$$\begin{aligned}
G_{\sigma}(\tau) = &-\frac{\theta(\tau)}{2Z}\mathrm{Tr}\left(e^{-\beta H_2}e^{\tau H_2}\tau^{-}_{\sigma}f_{\sigma}e^{-\tau H_2}f^{\dagger}_{\sigma}\tau^{+}_{\sigma}\mathbb{P}_{\sigma}\right) \\
&+\frac{\theta(-\tau)}{2Z}\mathrm{Tr}\left(e^{-\beta H_2}f^{\dagger}_{\sigma}\tau^{+}_{\sigma}e^{\tau H_2}\tau^{-}_{\sigma}f_{\sigma}e^{-\tau H_2}\mathbb{P}_{\sigma}\right).
\end{aligned} \tag{C.20}$$

We then observe that the operators $\tau^{-}_{\sigma}f_{\sigma}$ and $f^{\dagger}_{\sigma}\tau^{+}_{\sigma}$ are by definition vanishing in the unphysical subspace of the enlarged Hilbert space $\mathscr{H}_{*}$. It follows that the projector $\mathbb{P}_{\sigma}$ is unnecessary and the Green's function reads

$$\begin{aligned}
G_{\sigma}(\tau) &= -\frac{\theta(\tau)}{2Z}\mathrm{Tr}\left(e^{-\beta H_2}e^{\tau H_2}\tau^{-}_{\sigma}f_{\sigma}e^{-\tau H_2}f^{\dagger}_{\sigma}\tau^{+}_{\sigma}\right) + \frac{\theta(-\tau)}{2Z}\mathrm{Tr}\left(e^{-\beta H_2}f^{\dagger}_{\sigma}\tau^{+}_{\sigma}e^{\tau H_2}\tau^{-}_{\sigma}f_{\sigma}e^{-\tau H_2}\right), \\
&= -2\left\langle T_{\tau}\left(\tau^{-}_{\sigma}(\tau)f_{\sigma}(\tau)f^{\dagger}_{\sigma}(0)\tau^{+}_{\sigma}(0)\right)\right\rangle_{2}
\end{aligned} \tag{C.21}$$

where the thermal average:

$$\langle\cdots\rangle_{2} = \frac{\mathrm{Tr}\left(e^{-\beta H_2}\cdots\right)}{\mathrm{Tr}\left(e^{-\beta H_2}\right)} \tag{C.22}$$

is performed without constraints.

C.4 Slave-boson mean field in a magnetic field

The mean-field approximation within the paramagnetic sector of the slave-boson representation of an Anderson impurity model is long since known [25, 33, 58, 206, 232]. However the mean-field results allowing for spontaneous magnetization of the impurity are not as widely known. It was mentioned in Ref. [252] that at large U the actual lowest-energy mean-field solution is magnetic, though no details were presented. For this reason and in relation to the results presented in the thesis (Sections 3.3 and 6.4) we think it is worth to give here all details of such calculation. It is known that the slave-boson mean-field theory in the consistent formulation of Kotliar and Ruckenstein [156] is equivalent to the conventional Gutzwiller [92], so we shall use the latter technique, for which we refer to Ref. [81] for details.

Within the conventional Gutzwiller the variational energy reads

$$E(\theta, m) = E_{*}(\theta, m) - \frac{U}{4}\cos\theta - \frac{h}{2}m, \tag{C.23}$$

where $E_*(\theta, m)$ is the lowest expectation value of the effective resonant level Hamiltonian

$$H_* = \sum_{\mathbf{k}\sigma}\Big[\epsilon_{\mathbf{k}\sigma}\,\psi^\dagger_{\mathbf{k}\sigma}\,\psi_{\mathbf{k}\sigma} + R(\theta,m)\,\frac{V_{\mathbf{k}}}{\sqrt{V}}\Big(c^\dagger_\sigma\,\psi_{\mathbf{k}\sigma} + \psi^\dagger_{\mathbf{k}\sigma}\,c_\sigma\Big)\Big] - \frac{h_*(\theta,m)}{2}\,(n_\uparrow - n_\downarrow - m)\ , \tag{C.24}$$

where $h_*(\theta, m)$ is the Lagrange multipliers that selects the subspace of wave functions $|\Psi_*\rangle$ such that $\langle\Psi_*|n_\uparrow - n_\downarrow|\Psi_*\rangle = m$. In the following we consider the regime of small magnetization. In particular, we perform an expansion of the variational energy $E(\theta, m)$ in m keeping terms up to m^2. Moreover, in order to make the calculations as simple as possible we consider a flat hybridization function $\Gamma(\omega) = \Gamma\theta(W - |\epsilon|)$ and we take the wide band-width limit (WBL), i.e. the half bandwidth W of the metallic host much larger than the other energy scales. In the WBL the hybridization function in Eq. (3.53) becomes:

$$\Delta^R(\omega) = -i\Gamma\theta(W - |\epsilon|) - \frac{\Gamma}{2\pi}\log\left[\frac{(\omega - W)^2 + 0^+}{(\omega + W)^2 + 0^+}\right] \simeq -i\Gamma\theta(W - |\omega|). \tag{C.25}$$

The tunnel-coupling amplitude $V_{\mathbf{k}}$ is renormalized downwards by the quantity

$$\begin{aligned} R(\theta,m) &= \frac{1}{\sqrt{1-m^2}}\ \sin\frac{\theta}{2}\left[\sqrt{\cos^2\frac{\theta}{2} + m}\ +\ \sqrt{\cos^2\frac{\theta}{2} - m}\ \right] \\ &\simeq \sin\theta\left[1 + \frac{1}{2}\,m^2\,\frac{\cos\theta\,(2+\cos\theta)}{(1+\cos\theta)^2}\right] \\ &\equiv \sin\theta\left(1 + \frac{\rho(\theta)}{2}\,m^2\right) \end{aligned} \tag{C.26}$$

where the second expression is the expansion for $\cos^2\theta/2 \gg m$ to the second order in m. We define the effective hybridization width

$$\Gamma_*(\theta,m) = R(\theta,m)^2\,\Gamma \simeq \Gamma_*(\theta)\Big(1 + \rho(\theta)\,m^2\Big), \tag{C.27}$$

with $\Gamma_*(\theta) = \Gamma\sin^2\theta$, being Γ its bare value (C.25). Once fixed the value of the magnetization, the effective field $h_*(\theta, m)$ in Eq. (C.24) is the solution of the equation:

$$m = \langle\Psi_*|n_\uparrow - n_\downarrow|\Psi_*\rangle = \int d\epsilon\, f(\epsilon)\Big[A^*_\uparrow(\epsilon) - A^*_\downarrow(\epsilon)\Big] \tag{C.28}$$

where $f(\epsilon) = 1/(e^{\beta\epsilon} + 1)$ and the quasiparticle spectral function $A^*_\sigma(\epsilon)$ reads:

$$A^*_\sigma(\epsilon) = \frac{1}{\pi}\,\frac{\Gamma_*(\theta,m)}{(\epsilon + \sigma h_*(\theta,m)/2)^2 + \Gamma^2_*(\theta,m)}, \tag{C.29}$$

with $\sigma = \pm 1$. By performing the integral in Eq. (C.28) we obtain:

$$m = \frac{2}{\pi}\,\tan^{-1}\frac{h_*(\theta,m)}{2\Gamma_*(\theta,m)}\,, \tag{C.30}$$

which, at small m, is simply

$$h_*(\theta,m) \simeq \pi\,\Gamma_*(\theta)m. \tag{C.31}$$

By defining E_0 the energy of the metallic host in the absence of the impurity the variational

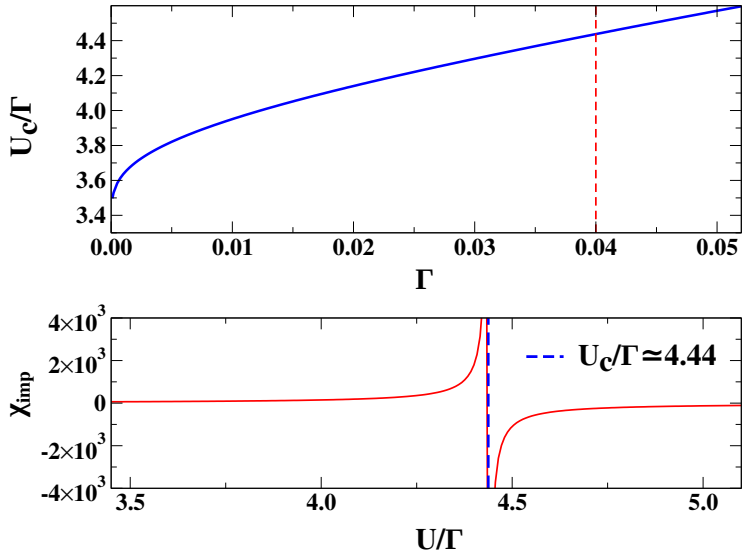

Figure C.1: Top panel: blue line is the critical interaction U_c above which the lowest energy mean-field solution is magnetic, in units of the bare hybridization width Γ. Lower panel: impurity magnetic susceptibility computed for $\Gamma/W = 0.04$ (red dashed line in the top panel) as a function of U/Γ. The energy unit is the cutoff $W = 1$.

energy is readily found to be

$$E(\theta, m) = E_0 - 2\,\frac{\Gamma_*(\theta,m)}{\pi}\,\ln\frac{eW}{\sqrt{h_*(\theta,m)^2/4+\Gamma_*(\theta,m)^2}} - \frac{U}{4}\cos\theta - \frac{h}{2}m\,, \tag{C.32}$$

and has to be minimized with respect to θ and m. Our aim is to study at $h = 0$ the stability of the $m = 0$ solution towards developing a spontaneous magnetization $m \ll 1$. Expanding the energy we find

$$\begin{aligned} E(\theta,m) &\simeq E_0 - 2\,\frac{\Gamma_*(\theta)}{\pi}\left(1+\rho(\theta)\,m^2\right)\left[\ln\frac{eW}{\Gamma_*(\theta)} - \frac{1}{2}\ln\left(1+2\rho(\theta)\,m^2+\frac{\pi^2}{4}m^2\right)\right] - \frac{U}{4}\cos\theta \\ &\simeq E_0 - 2\,\frac{\Gamma_*(\theta)}{\pi}\,\ln\frac{eW}{\Gamma_*(\theta)} - \frac{U}{4}\cos\theta + 2\,\frac{\Gamma_*(\theta)}{\pi}\,m^2\left\{\frac{\pi^2}{8} - \rho(\theta)\,\ln\frac{W}{\Gamma_*(\theta)}\right\}. \end{aligned} \tag{C.33}$$

The paramagnetic solution is stable as long as the expression $\Xi(\theta)$ in the curly bracket is positive at the saddle point value $\theta = \theta_*$ with $m = 0$, which satisfies

$$\frac{4\Gamma}{\pi}\,\cos\theta_*\,\ln\frac{W}{\Gamma_*(\theta_*)} = \frac{U}{4}\,. \tag{C.34}$$

It follows that

$$\Xi(\theta_*) = \frac{\pi^2}{8} - \rho(\theta_*)\,\frac{\pi U}{16\Gamma\,\cos\theta_*} > 0, \tag{C.35}$$

is the stability condition respect to the development of a spontaneous magnetization:

$$\chi_{\rm imp} = \left.\frac{\partial m}{\partial\,(h/2)}\right|_{h=0} = \frac{\pi}{2\Gamma_*(\theta_*)\Xi(\theta_*)} \tag{C.36}$$

where $\chi_{\rm imp}$ is the thermodynamic magnetic susceptibility of the impurity. The equality $\Xi(\theta_*) = 0$ defines the critical U_c above which the lowest energy solution is magnetic, shown in the top

panel of Fig. C.1. For instance, when $\Gamma/W = 0.04$ we find $U_c \simeq 4.44\,\Gamma$, as shown in the lower panel of Fig. C.1 where we plot $\chi_{\rm imp}$ versus U/Γ. Thus, in the Kondo regime $U/\Gamma \gg 1$ the lowest energy solution is magnetic, which is evidently unphysical.

C.5 Expectation values for the mean-field slave-spin at equilibrium

In the following we summarize some useful result for the slave-spin mean-field approach to the SIAM at equilibrium presented in Section 6.4. In particular, given the effective resonant level model in Eq. (6.43), we derive the analytic expressions for the hybridization (6.45) and the average occupation (6.46).

Before going to the evaluation of the average values we recall the expression of the f_σ fermion Green's function that, in terms of the complex frequency z, reads:

$$G_{f\sigma}(z) = \frac{1}{z + \lambda_\sigma/2 - \Sigma_{f\sigma}(z)}, \tag{C.37}$$

where $\lambda_\downarrow = 0$, while $\lambda_\uparrow$ is given in Eq. (6.44), and

$$\Sigma_{f\sigma}(z) = \sin^2\theta \int \frac{d\epsilon}{\pi} \frac{\Gamma(\epsilon)}{z - \epsilon}. \tag{C.38}$$

(a) *Expectation value of the hybridization;*

$$\begin{aligned} \langle \Psi_* | T | \Psi_* \rangle &= \tfrac{1}{\sqrt{V}} \textstyle\sum_{\mathbf{k}} \sum_\sigma V_k \left(\langle \Psi_* | f_\sigma^\dagger \psi_{\mathbf{k}\sigma} | \Psi_* \rangle + \text{c.c.} \right) \\ &= \tfrac{1}{\sqrt{V}} \textstyle\sum_{\mathbf{k}} \sum_\sigma V_k \left(G_{\mathbf{k}f\sigma}(0^-) + G_{f\mathbf{k}\sigma}(0^-) \right) \end{aligned}$$

where $G_{\mathbf{k}f\sigma}(0^-)$ is the mixed Green's function that, in terms of Matsubara frequencies, reads:

$$G_{\mathbf{k}f\sigma}(i\omega) = \sin\theta \frac{V_{\mathbf{k}}}{i\omega - \epsilon_{\mathbf{k}}} G_{f\sigma}(i\omega),$$

where $G_{f\sigma}(i\omega)$ is given in Eq. (C.37). By straightforward calculations we obtain:

$$\langle \Psi_* | T | \Psi_* \rangle = \frac{2T}{\sin\theta} \sum_{i\omega} \sum_\sigma \Sigma_{f\sigma}(i\omega) G_{f\sigma}(i\omega),$$

which can be equivalently computed on the real axis as:

$$\langle \Psi_* | T | \Psi_* \rangle = \sum_\sigma \int d\omega \left(\omega + \frac{\lambda_\sigma}{2} \right) f(\omega) A_{f\sigma}(\omega) / \sin\theta.$$

(b) *Expectation value of the occupation;*

$$\langle \Psi_* | n_\sigma | \Psi_* \rangle = G_{f\sigma}(0^-) = T \sum_{i\omega} G_{f\sigma}(i\omega) e^{i\omega 0^+}.$$

By deforming the integration contour the previous sum can be computed as an integral along the brunch cut of the integrand:

$$\langle \Psi_* | n_\sigma | \Psi_* \rangle = \int d\omega f(\omega) A_{f\sigma}(\omega).$$

C.6 Details on the mean-field slave-spin applied as impurity solver for DMFT

Once fixed the bath $\Gamma_\sigma(\omega)$, and given the slave-spin configuration $\langle \boldsymbol{\tau}_\sigma \rangle$ the mean-field loop displayed in Fig. 6.7 requires the evaluation of the fermionic average values $\langle T_{1\sigma} \rangle_*$ and $\langle J_{2\sigma} \rangle_*$. In terms of Green's function of the f_σ pseudofermions the latter quantities are:

$$\langle T_{1\sigma} \rangle_* = \frac{2\langle \tau^x_\sigma \rangle}{\pi} \int dx \int dy A_{f\sigma}(x) \Gamma_{11\sigma}(y) \frac{f(x) - f(y)}{x - y},$$

and

$$\langle J_{2\sigma} \rangle_* = \frac{2\langle \tau^y_\sigma \rangle}{\pi} \int dx \int dy\, A_{f\sigma}(x) \Gamma_{22\sigma}(y) \frac{f(x) - f(y)}{x - y},$$

where $\Gamma_{11\sigma}(\omega)$ and $\Gamma_{22\sigma}(\omega)$ are defined in Eq. (6.71), $A_{f\sigma}(\omega)$ is the f_σ pseudofermion spectral function (6.75). The knowledge of $\langle T_{1\sigma} \rangle_*$ and $\langle J_{2\sigma} \rangle_*$ allows us to obtain the new ground state of the spin Hamiltonian (6.74). This procedure is iterated up to the mean-field consistency.

From definitions in Eqs. (6.71) and (6.72) we obtain:

$$\Delta_{11\sigma}(-z) = -\Delta_{11\sigma}(z), \quad \Delta_{22\sigma}(-z) = -\Delta_{22\sigma}(z)$$

and

$$\Delta_{12\sigma}(-z) = \Delta_{12\sigma}(z), \quad \Delta_{21\sigma}(-z) = \Delta_{21\sigma}(z).$$

Previous Eqs. imply:

$$G_{f\sigma}(-z) = -G_{f\sigma}(z),$$

i.e. the f_σ pseudofermion spectral function is symmetric under $\omega \to -\omega$, $A_{f\sigma}(\omega) = A_{f\sigma}(-\omega)$. Finally, we notice that the physical fermion spectral function in Eq. (6.78) is normalized to 1:

$$\int dx A_{d\sigma}(x) = 2\langle \tau^-_\sigma \rangle_\chi \langle \tau^+_\sigma \rangle_\chi - \frac{1}{\pi} \int dx\, \mathrm{Im}\boldsymbol{\Pi}^R_{-+,\sigma}(x) \coth \frac{\beta x}{2} = \langle \{\tau^-_\sigma, \tau^+_\sigma\} \rangle_1 = 1.$$

D

Keldysh Greens' function technique

In this Appendix we briefly review the key concepts of the Keldysh formalism. This method is the fundamental tool used in Chapters 7 and 8. In the following we focus on the fermionic case, for more detailed discussions we refer to the books [12, 138, 229] and to the review articles [21, 137, 230, 263].

D.1 Closed time contour

Quantum averages on interacting many-body systems require the knowledge of the interacting eigenstates, which in many cases is a very hard task. To avoid this issue, the construction of equilibrium many-body theories involve the adiabatic switching on of the interaction at a distant past, say $t = -\infty$, and off at a distant future $t = +\infty$. The crucial assumption is that the non-interacting state at $t = +\infty$, $|+\infty\rangle_0$, differs from the initial state $|-\infty\rangle_0$ by a trivial phase factor:

$$ {}_0\langle -\infty || +\infty\rangle_0 = e^{iL}. $$

Clearly, this assumption does not work in the nonequilibrium case, where the interaction may lead to a final configuration completely different from the initial one. For this class of problems one must use the Keldysh strategy, which consists in evolving the system first in the forward direction in time and then to trace back its evolution backwards. Therefore, time-dependent average are computed respect the initial state and no assumption on the final configuration is made. Following this recipe one ends up, with the need to construct a theory with the time evolution along the two-branch contour, C, depicted on Fig. D.1. In this way the absence of

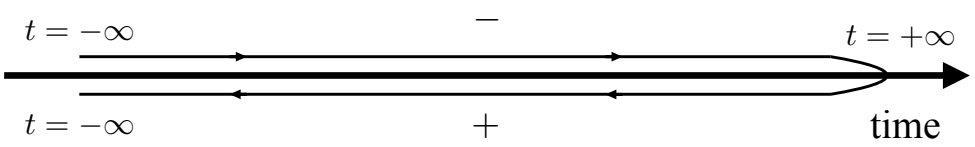

Figure D.1: C is the path along the real axis that goes from $t = -\infty$ to $+\infty$ and then back to the initial time $-\infty$. Times belonging to the upper branch are assigned the sign "-", while the ones in the lower branch are denoted by the sign "+".

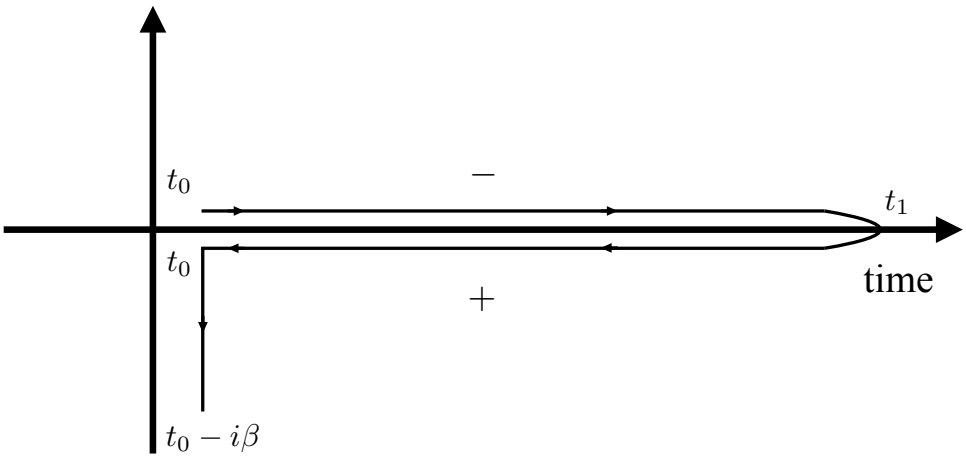

Figure D.2: The Keldysh contour C, ranging from time t_0 to a maximum time t_1, back to time 0, and finally to $-i\beta$ on the imaginary-time branch. The latter segment has been introduced to deal with an interacting initial state.

information about the final state at $t = +\infty$ is bypassed. The price to pay is that there are actually several Green's functions to calculate. In the following we present the different Green's function components defined on the Keldysh contour in Fig. D.1.

We define the time-ordering of two fermion operators in the Keldysh contour as:

$$T_C\left[\psi_\alpha(t)\,\psi^\dagger_\beta(t')\right] = \theta(t,t')\psi(t)\,\psi^\dagger(t') - \theta(t',t)\psi^\dagger(t')\,\psi(t)$$

where $\theta(t,t')$ is different from zero if t is later than t'

$$\theta(t,t') = \begin{cases} 1 & \text{if } t > t', \\ 0 & \text{otherwise.} \end{cases}.$$

We notice that times " + " are always later than " − " ones. Therefore, on the Keldysh contour the single-particle Green's function acquires the 2×2 matrix structure:

$$\hat{G}^{ab}_{\alpha\beta}(t,t') = -i\left\langle T_C\left(\psi_\alpha(t_a)\,\psi^\dagger_\beta(t'_b)\right)\right\rangle,$$

where $a, b = \pm$. In particular we have:

$$\begin{aligned} G^{--}_{\alpha\beta}(t,t') &= -i\left\langle T_t\left(\psi_\alpha(t)\,\psi^\dagger_\beta(t')\right)\right\rangle, \\ G^{-+}_{\alpha\beta}(t,t') &= i\left\langle \psi^\dagger_\beta(t')\,\psi_\alpha(t)\right\rangle, \\ G^{+-}_{\alpha\beta}(t,t') &= -i\left\langle \psi_\alpha(t)\,\psi^\dagger_\beta(t')\right\rangle, \\ G^{++}_{\alpha\beta}(t,t') &= -i\left\langle \overline{T}_t\left(\psi_\alpha(t)\,\psi^\dagger_\beta(t')\right)\right\rangle, \end{aligned} \tag{D.1}$$

where T_t is the ordinary time-ordering:

$$T_t\left[\psi_\alpha(t)\,\psi^\dagger_\beta(t')\right] = \theta(t-t')\psi(t)\,\psi^\dagger(t') - \theta(t'-t)\psi^\dagger(t')\,\psi(t),$$

while $\overline{T}_t$ is the anti-time-ordering:

$$\overline{T}_t\left[\psi_\alpha(t)\,\psi^\dagger_\beta(t')\right] = \theta(t'-t)\psi(t)\,\psi^\dagger(t') - \theta(t-t')\,\psi^\dagger(t')\psi(t).$$

In Eq. (D.1) the average $\langle \cdots \rangle$ is performed respect the state where the system is prepared at the initial time t_0.

We observe that the Keldysh formalism can be generalized to the case of the transient evolution from an initial state at t_0 described by H. In the case of a initial correlated state the statistical average:

$$\langle \cdots \rangle = \mathrm{Tr}\left(e^{-\beta H} \cdots\right)/Z,$$

can be performed by the time propagation along the in imaginary time axis:

$$e^{-\beta H} = exp\left[-i\int_0^{-i\beta} d\tau H\right].$$

Therefore, the Keldysh contour becomes the one depicted in Fig. D.2, where the additional branch parallel to the imaginary axis takes care of the average respect the initial correlated state. This introduces additional Green's function components, for more details we refer to [20, 268]. We conclude by observing that the problems considered in this work are characterized by a non-interacting initial Hamiltonian. Thus, the thermal average $\langle \cdots \rangle$ can be performed exactly and the additional branch parallel to the imaginary axis is not necessary.

D.2 Basic results

From the definition in Eq. (D.1) follows

$$G^{--} + G^{++} = G^{-+} + G^{+-}, \tag{D.2}$$

where we drop fermionic quantum numbers and time variables. From now on we shall adopt the notation:

$$G^{-+} \equiv G^{<}, \quad G^{+-} \equiv G^{>},$$

for the lesser and greater components. We define the retarded and advanced Green's function:

$$\begin{aligned} G^R_{\alpha\beta}(t,t') &= -i\theta(t-t')\left\langle\left\{\psi_\alpha(t), \psi^\dagger_\beta(t')\right\}\right\rangle, \\ G^A_{\alpha\beta}(t,t') &= i\theta(t'-t)\left\langle\left\{\psi_\alpha(t), \psi^\dagger_\beta(t')\right\}\right\rangle, \end{aligned} \tag{D.3}$$

where $\{A, B\}$=A B+B A. It follows that

$$\begin{aligned} G^R &= G^{>} - G^{++}, \\ G^A &= G^{--} - G^{>}, \\ G^R + G^A &= G^{--} - G^{++}. \end{aligned} \tag{D.4}$$

As a result of Eq. D.2 there are only 3 independent Green's functions. It is convenient to express the 2×2 matrix in terms of the independent Green's functions components only:

$$\hat{G} = \begin{pmatrix} G^{--} & G^{<} \\ G^{>} & G^{++} \end{pmatrix} \rightarrow \hat{U} \cdot \hat{G} \cdot \hat{V} = \begin{pmatrix} G^R & G^{<} \\ 0 & G^A \end{pmatrix} \tag{D.5}$$

where:

$$\hat{U} = \sigma^z + \sigma^-, \quad \hat{V} = \mathbf{1} - \sigma^-$$

and $2\sigma^- = \sigma^x - i\sigma^y$. Correspondingly, the self-energy term transforms as:

$$\hat{\Sigma} = \begin{pmatrix} \Sigma^{--} & \Sigma^{<} \\ \Sigma^{>} & \Sigma^{++} \end{pmatrix} \rightarrow \hat{V}^{-1} \cdot \hat{\Sigma} \cdot \hat{U}^{-1} = \begin{pmatrix} \Sigma^R & \Sigma^{<} \\ 0 & \Sigma^A \end{pmatrix}. \tag{D.6}$$

We know that the T_C ordered Green's function on the Keldysh contour satisfies the same perturbation rules valid at equilibrium, see [21, 137] for more details. Therefore, the strategy to perform calculations is to first derive the Dyson's Eq. for the T_C Green's function, perform the change of basis (D.5) and (D.6), then take the particular component G^R, G^A or $G^<$. For instance, the Dyson's Eq. for the T_C component takes the general form

$$\hat{G} = \hat{G}_0 + \hat{G}_0 \circ \hat{\Sigma} \circ \hat{G},$$

the product $\circ$ is defined as

$$\hat{A} \circ \hat{B} \equiv \int dt_1 \, \hat{A}(t, t_1) \cdot \hat{B}(t_1, t'), \tag{D.7}$$

where $\hat{A}$ and $\hat{B}$ are 2×2 matrices in the Keldysh space. Following the steps introduced before we can easily obtain:

$$G^{R/A} = G_0^{R/A} + G_0^{R/A} \bullet \Sigma^{R/A} \bullet G^{R/A},$$

and

$$G^< = G_0^< + G_0^< \bullet \Sigma^A \bullet G^A + G_0^R \bullet \Sigma^< \bullet G^A + G_0^R \bullet \Sigma^R \bullet G^<,$$

where $\bullet$ represents the convolution between two scalar functions:

$$A \bullet B \equiv \int dt_1 \, A(t, t_1) B(t_1, t'). \tag{D.8}$$

D.3 The steady-state regime

In this section we derive analytic expressions for the average values of the hybridization (7.24) and the current (7.36). Morover, we compute the Keldysh's components of the f_σ and ϕ_α fermion Green's function within the Hartree-Fock approximation.

f_σ pseudofermion Green's function; The unperturbed retarded and advanced Green's functions of the contacts are

$$G_{11\sigma}^{R/A}(\epsilon, k) = G_{22\sigma}^{R/A}(\epsilon, k) = \frac{1}{\epsilon - \epsilon_k \pm i0^+},$$
$$G_{12\sigma}^{R/A}(\epsilon, k) = G_{21\sigma}^{R/A}(\epsilon, k) = 0,$$

and

$$G_{11\sigma}^<(\epsilon, k) = G_{22\sigma}^<(\epsilon, k) = 2i\pi\delta(\epsilon - \epsilon_k)\frac{f_L(\epsilon) + f_R(\epsilon)}{2},$$
$$G_{12\sigma}^<(\epsilon, k) = G_{21\sigma}^<(\epsilon, k) = 2i\pi\delta(\epsilon - \epsilon_k)\frac{f_L(\epsilon) - f_R(\epsilon)}{2},$$

where we have already performed the rotation in Eq. (7.10). The Dyson's equation for the f_σ pseudofermion Green's function on the Keldysh's contour is:

$$\hat{G}_{f\sigma} = \hat{G}_{f\sigma}^0 + \hat{G}_{f\sigma}^0 \circ \hat{\Sigma}_f \circ \hat{G}_{f\sigma} \tag{D.9}$$

where $\hat{G}_{f\sigma}$ is the dressed Green's function, $\hat{G}_{f\sigma}^0$ the unperturbed one and we have used the notation in Eq. (D.7). In the stationary regime the time translational invariance is restored, thus, by taking the Fourier transform of Eq. (D.9) we obtain:

$$G_{f\sigma}^{R/A}(\epsilon) = \frac{1}{\epsilon + \lambda_\sigma/2 - \Sigma_{f\sigma}^{R/A}(\epsilon)} \tag{D.10}$$

and

$$G^{<}_{f\sigma}(\epsilon) = G^{A}_{f\sigma}(\epsilon)\,\Sigma^{<}_{f\sigma}(\epsilon)\,G^{R}_{f\sigma}(\epsilon). \tag{D.11}$$

Within mean-field approximation the self-energy $\Sigma_{f\sigma}$ reads:

$$\Sigma^{R/A}_{f\sigma}(\epsilon) = \frac{2}{V}\langle\sigma^x\rangle^2_{st}\sum_{\mathbf{k}}|V_{\mathbf{k}}|^2\,G^{R/A}_{11\sigma}(\epsilon,\mathbf{k}) = 2\langle\sigma^x\rangle^2_{st}\int\frac{d\omega}{\pi}\frac{\Gamma(\omega)}{\epsilon-\omega\pm i0^+}$$

and

$$\Sigma^{<}_{f\sigma}(\epsilon) = \frac{2}{V}\langle\sigma^x\rangle^2_{st}\sum_{\mathbf{k}}|V_{\mathbf{k}}|^2\,G^{<}_{11\sigma}(\epsilon,\mathbf{k}) = 4i\,\langle\sigma^x\rangle^2_{st}\,\Gamma(\epsilon)\,f_{\rm neq}(\epsilon). \tag{D.12}$$

Expectation values; The average occupation on the quantum dot (7.25) follows from Eqs. (D.11) and (D.12). The average value of the hybridization (7.24) involves the lesser component of the mixed Green's function:

$$G^{<}_{1\mathbf{k}f\sigma} = \sqrt{\frac{2}{V}}V_{\mathbf{k}}\langle\sigma^x\rangle_{st}\left[\hat{G}_{11\mathbf{k}\sigma}\circ\hat{G}_{f\sigma}\right]^{<}. \tag{D.13}$$

Thus,

$$\langle H_{T,C}\rangle_{st} = \frac{2}{\langle\sigma^x\rangle_{st}}\sum_{\sigma}\int\frac{d\epsilon}{2\pi}\mathrm{Im}\left[\hat{\Sigma}_{f\sigma}(\epsilon)\circ\hat{G}_{f\sigma}(\epsilon)\right]^{<}. \tag{D.14}$$

By using Eqs. (D.10), (D.11) and D.12 we readily obtain Eq. (7.27) reported in the main text. Finally, we briefly derive the expression for the low-energy contribution to the current Eq. (7.36). In this case the mixed Green's function involved is $G^{<}_{2\mathbf{k}f\sigma}(t,t) = i\langle f^{\dagger}_{\sigma}(t)c_{2\mathbf{k}\sigma}(t)\rangle_{st}$ and its Dyson's equation reads:

$$G^{<}_{2\mathbf{k}f\sigma}(\epsilon) = \sqrt{\frac{2}{V}}V_k\langle\sigma^x\rangle_{st}G^{<}_{21\mathbf{k}\sigma}(\epsilon)G^{A}_{f\sigma}(\epsilon).$$

The average value of the current is:

$$\left\langle I^f_Q\right\rangle_{st} = \sum_{\sigma}\int\frac{d\epsilon}{2\pi}\mathrm{Re}\left[\Sigma^{<}_{21\sigma}(\epsilon)G^{A}_{f\sigma}(\epsilon)\right], \tag{D.15}$$

where

$$\Sigma^{<}_{21\sigma}(\epsilon) = \langle\sigma^x\rangle^2_{st}\frac{2}{V}\sum_{\mathbf{k}}|V_{\mathbf{k}}|^2\,G^{<}_{21\mathbf{k}\sigma}(\epsilon) = 2i\langle\sigma^x\rangle^2_{st}\Gamma(\epsilon)\left(f_L(\epsilon)-f_R(\epsilon)\right).$$

In the wide-band limit Eq. (D.15) gives Eq. (7.36).

ϕ_α fermion Green's function; The Dyson's equation for the ϕ_α fermion reads:

$$\hat{G}_{\phi} = \hat{G}^0_{\phi} + \hat{G}^0_{\phi}\circ\hat{\Sigma}_{\phi}\circ\hat{G}_{\phi}, \tag{D.16}$$

where the Hartee-Fock self-energy, depicted in Fig. 6.4 **d)** is:

$$\hat{\Sigma}_{\phi} = \sigma^x\langle T\rangle_{st}.$$

In Eq. (D.16) we are using the same notation introduced in Eq. (D.7), where the hat refers to the matrix structure (D.5). By performing straightforward calculations we obtain:

$$G^{R(A)}_{\phi}(\epsilon) = \sum_{\mu}\sigma^{\mu}G^{R(A)}_{\phi\mu}(\epsilon),$$

where $\mu = 0$ denotes the identity and $\mu = 1, 2, 3$ the remaining Pauli matrices, while $G^{R(A)}_{\phi 2}(\epsilon) = 0$ and

$$G^{R(A)}_{\phi 0}(\epsilon) = \frac{1}{2}\left(\frac{1}{\epsilon + \omega_0/2 \pm i0^+} + \frac{1}{\epsilon - \omega_0/2 \pm i0^+}\right),$$
$$G^{R(A)}_{\phi 1}(\epsilon) = \frac{\sin\theta}{2}\left(\frac{1}{\epsilon + \omega_0/2 \pm i0^+} - \frac{1}{\epsilon - \omega_0/2 \pm i0^+}\right),$$
$$G^{R(A)}_{\phi 3}(\epsilon) = \frac{\cos\theta}{2}\left(\frac{1}{\epsilon + \omega_0/2 \pm i0^+} - \frac{1}{\epsilon - \omega_0/2 \pm i0^+}\right),$$

with $\omega_0 = U/2\cos\theta$ and θ solution of the self-consistent Eq.. Finally, we report the lesser component:

$$G^<_\phi(\epsilon) = \sum_\mu \sigma^\mu G^<_{\phi\mu}(\epsilon),$$

where $G^<_{\phi 2}(\epsilon) = 0$ and

$$G^<_{\phi 0}(\epsilon) = i\pi f(\epsilon)\left[\delta(\epsilon + \omega_0/2) + \delta(\epsilon - \omega_0/2)\right],$$
$$G^<_{\phi 1}(\epsilon) = i\pi f(\epsilon)\sin\theta\left[\delta(\epsilon + \omega_0/2) - \delta(\epsilon - \omega_0/2)\right],$$
$$G^<_{\phi 3}(\epsilon) = i\pi f(\epsilon)\cos\theta\left[\delta(\epsilon + \omega_0/2) - \delta(\epsilon - \omega_0/2)\right].$$

RPA corrections to the spin correlation function; Consistently with the mean-field decoupling in Eq. 7.20 the Dyson's equation for the $\sigma^x - \sigma^x$ correlation function reads:

$$\hat{\mathbf{\Pi}}_{xx} = \hat{\Pi}_{xx} + \hat{\Pi}_{xx} \circ \hat{\Sigma}_{xx} \circ \hat{\mathbf{\Pi}}_{xx},$$

where we adopt the notation introduced in Eq. (D.7). At RPA level the bosonic self-energy reads:

$$\hat{\Sigma}_{xx} = \hat{\chi}_{TT}, \tag{D.17}$$

with:

$$\chi_{TT}(t, t') = -i\langle T_C(\delta H_{T,C}(t)\delta H_{T,C}(t'))\rangle$$

where $\delta H_{T,C} = H_{T,C} - \langle H_{T,C}\rangle_{st}$, and $H_{T,C}$ is the tunnel-coupling with the metallic leads, Eq. (7.3).

D.4 Gradient expansion for a slowly varying perturbation

By assuming a slowly varying electrochemical potential (7.41), it is possible to perform a controlled expansion in the temporal variation of the external perturbation, i.e. gradient expansion. To this aim we define the Wigner transform of the f_σ pseudofermion Green's function:

$$G^{R(A)}_{f\sigma}(t, \epsilon) = \int d\tau e^{i\epsilon\tau} G^{R(A)}_{f\sigma}\left(t + \frac{\tau}{2}, t - \frac{\tau}{2}\right),$$

which satisfies the Dyson's equation:

$$\left(\epsilon - \Sigma^{R(A)}_{f\sigma}(t, \epsilon)\right) \star G^{R(A)}_{f\sigma}(t, \epsilon) = 1$$

where $\star$ denotes the Moyal product introduced in the main text. The solution of the Dyson's equation up to first-order is:

$$G^{R(A)}_{f\sigma}(t, \epsilon) = \frac{1}{\epsilon - \Sigma^{R(A)}_{f\sigma}(t, \epsilon)}$$

where in the WBL the time-dependent self-energy is $\Sigma^{R(A)}_{f\sigma}(t,\epsilon) = \mp 2i\Gamma_0\langle\sigma^x(t)\rangle^2$. The lesser self-energy is given by:

$$\begin{aligned}\Sigma^{<}_{f\sigma}(t,\epsilon) &= 2i\Gamma_0\langle\sigma^x(t)\rangle^2 - \frac{2\Gamma_0}{\pi}\int d\tau \frac{e^{i\epsilon\tau}}{\tau}\cos\gamma(t,\tau)\left\langle\sigma^x\left(t+\frac{\tau}{2}\right)\right\rangle\left\langle\sigma^x\left(t-\frac{\tau}{2}\right)\right\rangle \\ &\simeq 4\Gamma_0 i\langle\sigma^x(t)\rangle^2 f_{neq}(t,\epsilon),\end{aligned} \tag{D.18}$$

where $\gamma(t,\tau) = \int_{t-\tau/2}^{t+\tau/2}\phi_L(x)dx$ and the nonequilibrium distribution reads

$$f_{neq}(t,\epsilon) = \frac{1}{2} + \frac{i}{2\pi}\int d\tau \frac{e^{i\epsilon\tau}}{\tau}\cos\gamma(t,\tau).$$

In the last passage of Eq. (D.18), we assume that the dependence of $\langle\sigma^x(t)\rangle$ on the relative time τ is negligible. In the following, we report the zeroth and first-order contributions to the gradient expansion of $\langle H_{T,C}(t)\rangle$.

Zeroth order; The zeroth order contribution, first term in Eq. (7.45), reads:

$$\langle H_{T,C}(t)\rangle^{(0)} = \frac{4}{\langle\sigma^x(t)\rangle}\int d\epsilon A_f(t,\epsilon)\epsilon f_{\rm neq}(t,\epsilon),$$

where the f_σ pseudofermion time-dependent spectral function is

$$A_f(t,\epsilon) = \frac{1}{\pi}\frac{\Gamma_*(t)}{\epsilon^2+\Gamma_*(t)^2},$$

with $\Gamma_*(t) = 2\Gamma\langle\sigma^x(t)\rangle^2$.

First order; The first order correction reads:

$$\langle H_{T,C}(t)\rangle^{(1)} = \frac{1}{\pi\langle\sigma^x(t)\rangle}{\rm Im}\int d\epsilon\left[i\left(\partial_\epsilon\Sigma^{<}_f(t,\epsilon)\,\partial_t\Sigma^{A}_f(t,\epsilon) + \partial_t\Sigma^{<}_f(t,\epsilon)\right)G^A_f(t,\epsilon)^2\right].$$

After straightforward calculations we obtain

$$\begin{aligned}\langle H_{T,C}(t)\rangle^{(1)} = -\frac{2\Gamma_*(t)}{\pi\langle\sigma^x(t)\rangle}\int d\epsilon\Big[&{\rm Im}\left[G^A_f(t,\epsilon)^2\right]\partial_t f_{\rm neq}(t,\epsilon) + 2\frac{\partial_t\langle\sigma^x(t)\rangle}{\langle\sigma^x(t)\rangle}\Big(f_{\rm neq}(t,\epsilon){\rm Im}\left[G^A_f(t,\epsilon)^2\right] \\ &+ \partial_\epsilon f_{\rm neq}(t,\epsilon)\Gamma_*(t){\rm Re}\left[G^A_f(t,\epsilon)^2\right]\Big)\Big].\end{aligned}$$

Since $\partial_t\langle\sigma^x(t)\rangle = U\langle\sigma^y(t)\rangle/2$ the latter contribution modifies the Heisenberg equation (7.42) by introducing a finite relaxation in the evolution of the $\langle\sigma^y(t)\rangle$ component.

E

Calculations of the current and shot-noise in the Majorana-Anderson model

In this Appendix we illustrate some details about the calculations carried out in Chapter 8. To start with, We present the Keldysh-Nambu formalism in Section E.1. In Section E.2 we present the surface Green's functions, characterizing the semi-infinite metallic and superconductive chains. Then, in Section (E.3), we briefly compute the impurity's transfer matrix, that is the basic building brick to study transport across the metallic contacts in Fig. 8.2. We perform the calculation of the charge current (8.11) and the shot noise (8.17) in Sections E.4 and E.5, respectively.

E.1 The Keldysh-Nambu formalism

We briefly present the Nambu-Keldysh formalism used to study transport properties of the junction in Fig. 8.2. Within the Nambu formalism we define the Keldysh Green's functions of a fermionic operator ψ_α as:

$$\hat{G}_{\alpha\beta}(t_s, t'_{s'}) = -i\left\langle T_C \begin{pmatrix} \psi_\alpha(t_s)\psi^\dagger_\beta(t'_{s'}) & \psi_\alpha(t_s)\psi_\beta(t'_{s'}) \\ \psi^\dagger_\alpha(t_s)\psi^\dagger_\beta(t'_{s'}) & \psi^\dagger_\alpha(t_s)\psi_\beta(t'_{s'}) \end{pmatrix} \right\rangle, \tag{E.1}$$

where T_C is the contour ordering and $s, s' = \pm, -$ and $+$ are the forward and backward branches of the Keldysh contour, respectively (see Fig. D.2). Therefore, the Green's function (E.1) is a 4×4 matrix in the Nambu-Keldysh space. We stress that the basics results of the Keldysh's formalism, presented in Section D.2, are still valid.

E.2 Boundary Green's functions

The boundary Green's function, used in this Section, was originally introduced in Ref. [275], and implemented for a semi-infinite Kitaev chain in Refs. [108, 133, 258, 292]. In the following we present the results without reporting detailed calculation that can be found in the articles cited before.

Metallic leads. In the 2×2 Nambu space the R and A Green's functions of the metallic leads, evaluated on the boundary site 1, are given by:

$$\hat{\bar{G}}(z)_{11\alpha\alpha} = \frac{z}{2t^2}\left(1 - \sqrt{1 - \left(\frac{2t}{z}\right)^2}\right)\mathbf{1}, \tag{E.2}$$

where R and A are obtained by $z \to \omega \pm i0^+$. The greater and lesser components are

$$\begin{aligned}
\hat{\bar{G}}^{<}_{11\alpha\alpha}(\omega) &= 2i\pi\bar{\rho}(\omega)\begin{pmatrix} f(\omega-\mu_\alpha) & 0 \\ 0 & f(\omega+\mu_\alpha) \end{pmatrix}, \\
\hat{\bar{G}}^{>}_{11\alpha\alpha}(\omega) &= -2i\pi\bar{\rho}(\omega)\begin{pmatrix} 1-f(\omega-\mu_\alpha) & 0 \\ 0 & 1-f(\omega+\mu_\alpha) \end{pmatrix},
\end{aligned} \tag{E.3}$$

with

$$\bar{\rho}(\omega) = \theta(2t - |\omega|)\frac{\sqrt{4t^2-\omega^2}}{2\pi t^2}. \tag{E.4}$$

Kitaev chain. For what concern the Kitaev chain the R and A Green's function components on the boundary site, name site 1, are obtained by:

$$\hat{\bar{G}}^{R/A}_{11} = \hat{G}^{R/A}_{11} - \hat{G}^{R/A}_{10} \bullet \left(\hat{G}^{R/A}_{00}\right)^{-1} \bullet \hat{G}^{R/A}_{01}. \tag{E.5}$$

The Green's function entering in Eq. (E.5) are:

$$\hat{G}_{xx}(z) = \omega\sigma^0\mathcal{F}_{-1}(z) + (2t\mathcal{F}_0(z) - \mu\mathcal{F}_{-1}(z))\,\sigma^z,$$

and

$$\hat{G}_{x+1x}(z) = \sum_\mu \sigma^\mu G_{\mu x+1x}(z), \quad \hat{G}_{xx+1}(z) = \sum_\mu \sigma^\mu G_{\mu xx+1}(z),$$

where

$$\begin{aligned}
G_{0x+1x}(z) &= G_{0xx+1}(z) = -z\mathcal{F}_0(z), \\
G_{2x+1x}(z) &= -G_{2xx+1}(z) = 2i\Delta\left(\frac{1}{4t^2-4\Delta^2} - \mathcal{F}_1(z) + \mathcal{F}_{-1}(z)\right), \\
G_{3x+1x}(z) &= G_{3xx+1}(z) = 2t\left(\frac{1}{4t^2-4\Delta^2} - \mathcal{F}_1(z)\right) + \mu\mathcal{F}_0(z).
\end{aligned}$$

In the previous expression we have introduced the quantity:

$$\mathcal{F}_m(z) = \frac{1}{4(t^2-\Delta^2)}\frac{1}{Q_+(z)-Q_-(z)}\sum_{s=\pm1}\frac{sQ_s^m(z)}{\sqrt{1-1/Q_s^2(z)}},$$

and

$$Q_\pm(\omega) = \frac{1}{2(\Delta^2-t^2)}\left[-t\mu \pm \sqrt{\Delta^2\mu^2 - (\Delta^2-t^2)(z^2-4\Delta^2)}\right].$$

E.3 Impurity transfer matrix

By performing perturbation theory in the tunnel-coupling (8.9) and (8.10) between the leads and the impurity we obtain the following Dyson's equation

$$\hat{\mathbf{G}}_{\eta_\uparrow} = \hat{G}_{\eta_\uparrow} + \hat{G}_{\eta_\uparrow} \circ \hat{\Sigma}_{\eta_\uparrow} \circ \hat{\mathbf{G}}_{\eta_\uparrow}, \tag{E.6}$$

where the impurity electrons self-energy

$$\hat{\Sigma}_{\eta_\uparrow} = \sum_{\alpha=L,R} \hat{V}_c^\alpha \cdot \hat{\bar{G}}_{11\alpha\alpha} \cdot \left(\hat{V}_c^\alpha\right)^\dagger + \hat{V} \cdot \hat{\bar{G}}_{11} \cdot \hat{V}^\dagger, \tag{E.7}$$

with $\hat{\bar{G}}_{11\alpha\alpha}$ boundary Green's function of the metallic lead α and $\hat{\bar{G}}_{11}$ boundary Green's function of the superconductive chain. We report the results in Section E.2. After straightforward calculations we find that:

$$\hat{G}_{1a\eta_\uparrow} = \hat{\bar{G}}_{11aa} \bullet \hat{V}_a^\dagger \cdot \hat{\mathbf{G}}_{\eta_\uparrow}, \quad \hat{G}_{\eta_\uparrow 1\alpha} = \hat{\mathbf{G}}_{\eta_\uparrow} \cdot \hat{V}_a \bullet \hat{\bar{G}}_{11aa}. \tag{E.8}$$

where a refers to one of the three leads connected to the impurity. Finally, the hybridization with the dot induces a direct coupling between different leads:

$$\hat{\bar{\mathbf{G}}}_{11ab} = \delta_{ab}\hat{\bar{G}}_{11aa} + \hat{\bar{G}}_{11aa} \bullet \hat{\mathbf{T}}^{ab}_{\eta_\uparrow} \bullet \hat{\bar{G}}_{11bb} \tag{E.9}$$

where the indices a, b refer to the metallic leads as well as the Kitaev chain and we have introduced the transfer matrix:

$$\hat{\mathbf{T}}^{ab}_{\eta_\uparrow} = \hat{V}_a^\dagger \cdot \hat{\mathbf{G}}_{\eta_\uparrow} \cdot \hat{V}_b. \tag{E.10}$$

In particular transport across the metallic contacts involves $\hat{\mathbf{T}}^{\alpha\beta}_{\eta_\uparrow}$ with $\alpha, \beta = L, R$. From now on we consider symmetric metallic leads, i.e. $\hat{V}_c^L = \hat{V}_c^R = \hat{V}_c$, such that $\hat{\mathbf{T}}^{\alpha\beta}_{\eta_\uparrow} = \hat{\mathbf{T}}_{\eta_\uparrow}$ does not depend on α and β.

E.4 The charge-current

The average value of the current for the lead $\alpha = L, R$ reads:

$$\langle J_\alpha \rangle = \frac{\mathrm{Tr}\left[\sigma^z \cdot \hat{G}^<_{1\alpha\eta_\uparrow}(t,t) \cdot \hat{V}_c\right] - \mathrm{Tr}\left[\sigma^z \cdot \hat{V}_c^\dagger \cdot \hat{G}^<_{\eta_\uparrow 1\alpha}(t,t)\right]}{2}.$$

Therefore, the charge current, $J_Q = (J_L - J_R)/2$, across the junction is

$$\begin{aligned}\langle J_Q \rangle = &\sum_{\alpha=L,R} \mathrm{sign}(\alpha) \int \frac{d\omega}{2\pi} \frac{\mathrm{Tr}\left[\sigma^z \cdot \hat{\bar{G}}^R_{11\alpha\alpha}(\omega) \cdot \hat{\mathbf{T}}^<_{\eta_\uparrow}(\omega)\right] - \mathrm{Tr}\left[\sigma^z \cdot \hat{\mathbf{T}}^<_{\eta_\uparrow}(\omega) \cdot \hat{\bar{G}}^A_{11\alpha\alpha}(\omega)\right]}{4} \\ + &\sum_{\alpha=L,R} \mathrm{sign}(\alpha) \int \frac{d\omega}{2\pi} \frac{\mathrm{Tr}\left[\sigma^z \cdot \hat{\bar{G}}^<_{11\alpha\alpha}(\omega) \cdot \hat{\mathbf{T}}^A_{\eta_\uparrow}(\omega)\right] - \mathrm{Tr}\left[\sigma^z \cdot \hat{\mathbf{T}}^R_{\eta_\uparrow}(\omega) \cdot \hat{\bar{G}}^<_{11\alpha\alpha}(\omega)\right]}{4},\end{aligned} \tag{E.11}$$

where $\mathrm{sign}(L) = +1$ and $\mathrm{sign}(R) = -1$. We notice that L and R leads are characterized by the same hybridization matrix $\hat{V}_c$ as well as the same spectral properties. Therefore, the first contribution to the current in Eq. (E.11) vanishes and:

$$\langle J_Q \rangle = \int \frac{d\omega}{8\pi} \mathrm{Tr}\left[\sigma^z \cdot \left(\hat{\bar{G}}^<_{11LL}(\omega) - \hat{\bar{G}}^<_{11RR}(\omega)\right) \cdot \hat{T}^A(\omega) - \sigma^z \cdot \hat{T}^R(\omega) \cdot \left(\hat{\bar{G}}^<_{11LL}(\omega) - \hat{\bar{G}}^<_{11RR}(\omega)\right)\right], \tag{E.12}$$

where

$$\hat{\bar{G}}^<_{11LL}(\omega) - \hat{\bar{G}}^<_{11RR}(\omega) = 2\pi i \bar{\rho}(\omega) \left(f_L(\omega) - f_R(\omega)\right) \sigma^z,$$

and $\overline{\rho}(\omega)$ is the boundary spectral function of the metallic leads. By rescaling for $-2\pi e^2/h$ we obtain

$$\langle J_Q \rangle = \frac{\pi e^2}{h} \int d\epsilon \overline{\rho}(\epsilon) \left(f_L(\epsilon) - f_R(\epsilon)\right) \mathrm{Im}\mathrm{Tr}\left(\hat{\mathbf{T}}^A_{\eta\uparrow}(\epsilon)\right). \tag{E.13}$$

Moreover, we notice that

$$\hat{\mathbf{T}}^A(\epsilon) = \hat{V}_c^\dagger \cdot \hat{\mathbf{G}}^A_{\eta\uparrow}(\epsilon) \cdot \hat{V}_c, \tag{E.14}$$

and

$$\left[\hat{\mathbf{G}}^A_{\eta\uparrow}(\epsilon)\right]^{-1} = \epsilon \mathbf{1} + \frac{U}{2}\sigma^z - \sum_{\alpha=L,R} \hat{V}_c \cdot \hat{\overline{G}}^A_{11\alpha\alpha}(\omega) \cdot \hat{V}_c^\dagger - \hat{V} \cdot \hat{\overline{G}}^A_{11}(\omega) \cdot \hat{V}^\dagger, \tag{E.15}$$

with $\hat{\overline{G}}^A_{11\alpha\alpha}(\omega)$ boundary Green's function of the metallic contacts (E.2) and $\hat{\overline{G}}^A_{11}(\omega)$ of the Kitaev chain Eqs. (E.5). The value of the current is obtained by averaging Eq. (E.13) over the spin $\downarrow$.

E.5 The shot-noise

The correlation function between currents J_α and J_β reads:

$$S_{\alpha\beta}(t,t') = \langle T_C \left(\delta J_\alpha(t) \delta J_\beta(t')\right)\rangle$$

where T_C is the time-ordering operator on the Keldysh contour, $\delta J_\alpha = J_\alpha - \langle J_\alpha \rangle$. The shot noise, defined in (8.12), contains the $\Omega = 0$ limit of the Fourier transform of the current-current correlation function:

$$\begin{aligned}\langle\{\delta J_\alpha(t), \delta J_\beta(t')\}\rangle &= \langle T_C \left(\delta J_\alpha(t_-)\delta J_\beta(t'_+)\right)\rangle + \langle T_C \left(\delta J_\alpha(t_+)\delta J_\beta(t'_-)\right)\rangle \\ &= S^<_{\alpha\beta}(t,t') + S^>_{\alpha\beta}(t,t').\end{aligned}$$

In the steady-state regime we have:

$$\mathcal{P}_{\alpha\beta} = \lim_{\Omega\to 0} \int dt e^{-i\Omega(t-t')} \frac{\langle\{\delta J_\alpha(t), \delta J_\beta(t')\}\rangle}{2} = \frac{S^<_{\alpha\beta}(\Omega=0) + S^>_{\alpha\beta}(\Omega=0)}{2},$$

where

$$\begin{aligned}S^<_{\alpha\beta}(\Omega=0) = \int \frac{d\omega}{4\pi} \Big[&\mathrm{Tr}\left(\sigma^z \cdot \hat{\mathbf{T}}^<_{\eta\uparrow}(\omega) \cdot \sigma^z \cdot \hat{\overline{\mathbf{G}}}^>_{11\beta\alpha}(\omega)\right) + \mathrm{Tr}\left(\sigma^z \cdot \hat{\overline{\mathbf{G}}}^<_{11\alpha\beta}(\omega) \cdot \sigma^z \cdot \hat{\mathbf{T}}^>_{\eta\uparrow}(\omega)\right) \\ &- \mathrm{Tr}\left(\sigma^z \cdot \hat{V}_c^\dagger \cdot \hat{G}^<_{\eta 1\beta}(\omega) \cdot \sigma^z \cdot \hat{V}_c^\dagger \cdot \hat{G}^>_{\eta 1\alpha}(\omega)\right) - \mathrm{Tr}\left(\sigma^z \cdot \hat{G}^<_{1\alpha\eta}(\omega) \cdot \hat{V}_c \cdot \sigma^z \cdot \hat{G}^>_{1\beta\eta}(\omega) \cdot \hat{V}_c\right)\Big],\end{aligned} \tag{E.16}$$

and

$$\begin{aligned}S^>_{\alpha\beta}(\Omega=0) = \int \frac{d\omega}{4\pi} \Big[&\mathrm{Tr}\left(\sigma^z \cdot \hat{\mathbf{T}}^>_{\eta\uparrow}(\omega) \cdot \sigma^z \cdot \hat{\overline{\mathbf{G}}}^<_{11\beta\alpha}(\omega)\right) + \mathrm{Tr}\left(\sigma^z \cdot \hat{\overline{\mathbf{G}}}^>_{11\alpha\beta}(\omega) \cdot \sigma^z \cdot \hat{\mathbf{T}}^<_{\eta\uparrow}(\omega)\right) \\ &- \mathrm{Tr}\left(\sigma^z \cdot \hat{V}_c^\dagger \cdot \hat{G}^>_{\eta 1\beta}(\omega) \cdot \sigma^z \cdot \hat{V}_c^\dagger \cdot \hat{G}^<_{\eta 1\alpha}(\omega)\right) - \mathrm{Tr}\left(\sigma^z \cdot \hat{G}^>_{1\alpha\eta}(\omega) \cdot \hat{V}_c \cdot \sigma^z \cdot \hat{G}^<_{1\beta\eta}(\omega) \cdot \hat{V}_c\right)\Big].\end{aligned} \tag{E.17}$$

We notice that

$$S^>_{\alpha\beta}(0) = S^<_{\beta\alpha}(0) \implies \mathcal{P}_{LR} = \mathcal{P}_{RL}, \tag{E.18}$$

and

$$S_Q(\Omega=0) = \frac{\mathcal{P}_{LL} + \mathcal{P}_{RR} - 2\mathcal{P}_{LR}}{4}. \tag{E.19}$$

By using Eqs. (E.15), (E.8) and (E.9) we obtain:

$$\begin{aligned} S_Q = \frac{1}{16\pi}\int d\omega \Big[& \mathrm{Tr}\left(\sigma^z\cdot\hat{\mathbf{T}}^{<}_{\eta_\uparrow}(\omega)\cdot\sigma^z\cdot\left(\hat{\bar{G}}^{>}_{11LL}(\omega)+\hat{\bar{G}}^{>}_{11RR}(\omega)\right)\right) \\ & + \mathrm{Tr}\left(\sigma^z\cdot\hat{\mathbf{T}}^{>}_{\eta_\uparrow}(\omega)\cdot\sigma^z\cdot\left(\hat{\bar{G}}^{<}_{11LL}(\omega)+\hat{\bar{G}}^{<}_{11RR}(\omega)\right)\right) \\ & + \mathrm{Tr}\left(\sigma^z\cdot\hat{\mathbf{T}}^{R}_{\eta_\uparrow}(\omega)\cdot\left(\hat{\bar{G}}^{<}_{11LL}(\omega)-\hat{\bar{G}}^{<}_{11RR}(\omega)\right)\cdot\sigma^z\cdot\hat{\mathbf{T}}^{R}_{\eta_\uparrow}(\omega)\cdot\left(\hat{\bar{G}}^{>}_{11RR}(\omega)-\hat{\bar{G}}^{>}_{11LL}(\omega)\right)\right) \\ & + \mathrm{Tr}\left(\sigma^z\cdot\hat{\mathbf{T}}^{A}_{\eta_\uparrow}(\omega)\cdot\left(\hat{\bar{G}}^{<}_{11LL}(\omega)-\hat{\bar{G}}^{<}_{11RR}(\omega)\right)\cdot\sigma^z\cdot\hat{\mathbf{T}}^{A}_{\eta_\uparrow}(\omega)\cdot\left(\hat{\bar{G}}^{>}_{11RR}(\omega)-\hat{\bar{G}}^{>}_{11LL}(\omega)\right)\right)\Big]. \end{aligned} \tag{E.20}$$

From Eqs. (E.2) and (E.3) we have

$$\begin{aligned} \hat{\bar{G}}^{<}_{11LL}(\omega)-\hat{\bar{G}}^{<}_{11RR}(\omega) &= 2i\pi\bar{\rho}(\omega)(f_L(\omega)-f_R(\omega))\sigma^z, \\ \hat{\bar{G}}^{>}_{11RR}(\omega)-\hat{\bar{G}}^{>}_{11LL}(\omega) &= -2i\pi\bar{\rho}(\omega)(f_L(\omega)-f_R(\omega))\sigma^z, \\ \hat{\bar{G}}^{<}_{11LL}(\omega)+\hat{\bar{G}}^{<}_{11RR}(\omega) &= 2i\pi\bar{\rho}(\omega)(f_L(\omega)+f_R(\omega))\sigma^0, \\ \hat{\bar{G}}^{>}_{11LL}(\omega)+\hat{\bar{G}}^{>}_{11RR}(\omega) &= -2i\pi\bar{\rho}(\omega)(2-f_L(\omega)-f_R(\omega))\sigma^0. \end{aligned} \tag{E.21}$$

Finally, the expression of the white-noise component of I_Q fluctuations reads:

$$\begin{aligned} S_Q = \pi\int d\omega\bar{\rho}^2(\omega)\Big[& \frac{2-f_L(\omega)-f_R(\omega)}{2}\,\frac{f_L(\omega)+f_R(\omega)}{2}\,\mathrm{Tr}\left(\hat{\mathbf{T}}^{R}_{\eta_\uparrow}(\omega)\cdot\hat{\mathbf{T}}^{A}_{\eta_\uparrow}(\omega)+\hat{\mathbf{T}}^{A}_{\eta_\uparrow}(\omega)\cdot\hat{\mathbf{T}}^{R}_{\eta_\uparrow}(\omega)\right) \\ & + \frac{f_L(\omega)-f_R(\omega)}{2}\,\frac{f_L(\omega)-f_R(\omega)}{2}\,\mathrm{Tr}\left(\hat{\mathbf{T}}^{R}_{\eta_\uparrow}(\omega)\cdot\hat{\mathbf{T}}^{R}_{\eta_\uparrow}(\omega)+\hat{\mathbf{T}}^{A}_{\eta_\uparrow}(\omega)\cdot\hat{\mathbf{T}}^{A}_{\eta_\uparrow}(\omega)\right)\Big]. \end{aligned} \tag{E.22}$$

Since we are interested in quantum-fluctuations we take the zero-temperature limit:

$$\frac{2-f_L(\omega)-f_R(\omega)}{2}\,\frac{f_L(\omega)+f_R(\omega)}{2} = \frac{f_L(\omega)-f_R(\omega)}{2}\,\frac{f_L(\omega)-f_R(\omega)}{2} = \frac{f_L(\omega)-f_R(\omega)}{4},$$

we have

$$S_Q = \frac{2\pi e^3}{h}\frac{\pi}{4}\int_{-\phi/2}^{\phi/2} d\omega\bar{\rho}^2(\omega)\mathrm{Tr}\Big[\left(\hat{\mathbf{T}}^{R}_{\eta_\uparrow}(\omega)+\hat{\mathbf{T}}^{A}_{\eta_\uparrow}(\omega)\right)\cdot\left(\hat{\mathbf{T}}^{R}_{\eta_\uparrow}(\omega)+\hat{\mathbf{T}}^{A}_{\eta_\uparrow}(\omega)\right)\Big], \tag{E.23}$$

where $2\pi e^3/h$ is the rescaling factor, $\bar{\rho}(\omega)$ is the boundary DOS of the metallic chain (E.4). The shot noise is obtained by averaging over the spin $\downarrow$.

E.6 Scattering matrix approach

The Hamiltonian (8.8) can be exactly solved looking for the solutions of the secular equation:

$$[\Gamma_{E,\delta}, H] = E\Gamma_{E,\delta}.$$

Through the ansatz

$$\Gamma_{E,\delta} = \sum_{j=1}^{\ell}\sum_{\alpha=L,R}\left(u_{\alpha;j}c_{\alpha j}+v_{\alpha;j}c^{\dagger}_{\alpha j}\right)+\left(u_d d_\uparrow+v_d d^{\dagger}_\uparrow\right)+\phi\,\gamma_1,$$

the Bogoliubov-de Gennes (BdG) equations take the form

$$\begin{aligned} -t_\alpha\left(u_{\alpha;j-1}+u_{\alpha;j+1}\right)-\mu_\alpha u_{\alpha;j} &= E u_{\alpha;j} \\ t_\alpha\left(v_{\alpha;j-1}+v_{\alpha;j+1}\right)+\mu_\alpha v_{\alpha;j} &= E v_{\alpha;j} \end{aligned} \tag{E.24}$$

within the bulk of the metallic leads, that is for $j > 1$. At the boundary BdG equations are

$$\begin{aligned} -t_\alpha u_{\alpha;2}-\mu_\alpha u_{\alpha;1}-V_\alpha u_d &= E u_{\alpha;1} \\ t_\alpha v_{\alpha;2}+\mu_\alpha v_{\alpha;1}+V_\alpha v_d &= E v_{\alpha;1} \end{aligned} \tag{E.25}$$

for the endpoints of the leads,

$$\begin{aligned} -V_L u_{L;1}-V_R u_{R;1}-2iV\phi+qU u_d &= E u_d \\ V_L v_{L;1}+V_R v_{R;1}-2iV\phi-qU v_d &= E v_d \end{aligned} \tag{E.26}$$

for the dot, and

$$iV v_d + iV u_d = E \tag{E.27}$$

for the two Majorana fermions. The solutions of the BdG equation inside the bulk take the form

$$\begin{pmatrix} u_{\alpha;j} \\ v_{\alpha;j} \end{pmatrix} = \begin{pmatrix} u_\alpha \\ v_\alpha \end{pmatrix} e^{ik_\alpha j} \tag{E.28}$$

that inserted into Eq. (E.24) gives the secular equation

$$\begin{pmatrix} E+2t\cos(k_\alpha)+\mu_\alpha & 0 \\ 0 & E-2t\cos(k_\alpha)-\mu_\alpha \end{pmatrix}\begin{pmatrix} u_\alpha \\ v_\alpha \end{pmatrix} = \begin{pmatrix} 0 \\ 0 \end{pmatrix}, \tag{E.29}$$

and the dispersion relation

$$E^2-(2t\cos(k_\alpha)+\mu_\alpha)^2 = 0. \tag{E.30}$$

The latter equation admits four kind of waves (incoming particle in-p, outgoing particle out-p, incoming hole in-h, outgoing hole out-h), such that the most general eigenfunction with energy E is given by

$$\begin{pmatrix} u_{\alpha;j} \\ v_{\alpha;j} \end{pmatrix} = A^\alpha_{p-in}\begin{pmatrix} 1 \\ 0 \end{pmatrix} e^{-ik_{p;\alpha}j} + A^\alpha_{p-out}\begin{pmatrix} 1 \\ 0 \end{pmatrix} e^{ik_{p;\alpha}j} + A^\alpha_{h-in}\begin{pmatrix} 0 \\ 1 \end{pmatrix} e^{ik_{h;\alpha}j} + A^\alpha_{h-out}\begin{pmatrix} 0 \\ 1 \end{pmatrix} e^{-ik_{h;\alpha}j} \tag{E.31}$$

with

$$\cos k_{p;\alpha} = -\frac{E+\mu_\alpha}{2t}, \quad \cos k_{h;\alpha} = \frac{E-\mu_\alpha}{2t}. \tag{E.32}$$

The actual energy eigenstates are determined imposing the boundary BdG equation. Scattering through the quantum dot junction is fully encoded in the single-particle scattering matrix, S, that relates the outgoing waves, $\bar{A}_{out} = \left(A^1_{p-out}, A^2_{p-out}, A^1_{h-out}, A^2_{h-out},\right)^t$, to the incoming waves, $\bar{A}_{in} = \left(A^1_{p-in}, A^2_{p-in}, A^1_{h-in}, A^2_{h-in},\right)^t$. Combining Eq. (E.27) and Eq. (E.26) together we can write

$$\begin{pmatrix} u_d \\ v_d \end{pmatrix} = \begin{pmatrix} Q_+ & Q_0 \\ Q_0 & Q_- \end{pmatrix}\begin{pmatrix} -V_L u_{L;1}-V_R u_{R;1} \\ V_L v_{L;1}+V_R v_{R;1} \end{pmatrix} \tag{E.33}$$

with

$$\begin{aligned} Q_{\pm} &= \frac{E\left(E^2 \pm EqU - 2V^2\right)}{E^4 - E^2q^2U^2 - 4E^2V^2}, \\ Q_0 &= \frac{E\left(2V^2\right)}{E^4 - E^2q^2U^2 - 4E^2V^2}. \end{aligned} \tag{E.34}$$

Inserting Eq. (E.33) into Eq. (E.25), we finally arrive to

$$\left(\hat{M}\hat{\Phi}_1 + \hat{t}\hat{\Phi}_2\right)\bar{A}_{out} + \left(\hat{M}\hat{\Phi}_1^{\dagger} + \hat{t}\hat{\Phi}_2^{\dagger}\right)\bar{A}_{in} = 0, \tag{E.35}$$

where we have defined

$$\hat{M} = E\mathbb{I} + \sigma_z \otimes \begin{pmatrix} \mu_1 & 0 \\ 0 & \mu_2 \end{pmatrix} + \begin{pmatrix} -Q_+ & Q_0 \\ Q_0 & -Q_- \end{pmatrix} \otimes \begin{pmatrix} V_L^2 & V_L V_R \\ V_L V_R & V_R^2 \end{pmatrix}, \tag{E.36}$$

and

$$\hat{t} = \sigma_z \otimes \begin{pmatrix} t_1 & 0 \\ 0 & t_2 \end{pmatrix}, \tag{E.37}$$

and

$$\hat{\Phi}_j = \begin{pmatrix} e^{ik_{p;\alpha}j} & 0 & 0 & 0 \\ 0 & e^{-ik_{p;\alpha}j} & 0 & 0 \\ 0 & 0 & e^{-ik_{h;\alpha}j} & 0 \\ 0 & 0 & 0 & e^{ik_{h;\alpha}j} \end{pmatrix}. \tag{E.38}$$

We have then

$$\begin{aligned} \bar{A}_{out} &= \left[\left(\hat{M}\hat{\Phi}_1 + \hat{t}\hat{\Phi}_2\right)^{-1}\left(\hat{M}\hat{\Phi}_1^{\dagger} + \hat{t}\hat{\Phi}_2^{\dagger}\right)\right]\bar{A}_{in} \\ &= \hat{S}\left(E\right)\bar{A}_{in}. \end{aligned} \tag{E.39}$$

The scattering matrix is an unitary matrix that encodes all the possible single-particle processes at the junction with E the energy of the incoming particle/hole from the leads. Consistently with the notation above, we have

$$\hat{S}\left(E\right) = \begin{pmatrix} r_{1,1}^{p,p} & t_{1,2}^{p,p} & a_{1,1}^{p,h} & c_{1,2}^{p,h} \\ t_{2,1}^{p,p} & r_{2,2}^{p,p} & c_{2,1}^{p,h} & a_{2,2}^{p,h} \\ a_{1,1}^{h,p} & c_{1,2}^{h,p} & r_{1,1}^{h,h} & t_{1,2}^{h,h} \\ c_{2,1}^{h,p} & a_{2,2}^{h,p} & t_{2,1}^{h,h} & r_{2,2}^{h,h} \end{pmatrix}, \tag{E.40}$$

where $r_{\alpha,\alpha}^{\mu,\mu}\left(E\right)$ denotes the reflection amplitude of a particle or of an hole, $t_{\alpha,\bar{\alpha}}^{\mu,\mu}\left(E\right)$ is the trasmission amplitude between the leads, $a_{\alpha,\alpha}^{\mu,\bar{\mu}}\left(E\right)$ corresponds to the Andreev reflection, that is the conversion of a particle (hole) into an hole (particle) within the same lead, finally $c_{\alpha,\bar{\alpha}}^{\mu,\bar{\mu}}\left(E\right)$ is the crossed Andreev reflection amplitude, that is the conversion of a particle (hole) in one lead to an hole (particle) in the other lead. The scattering matrix allows us to introduce the four kind of eigenstates that define the scattering states basis. We have:

(i) incoming particle from left lead (pL)

$$\begin{aligned} \begin{pmatrix} u_{L;j}^{pL} \\ v_{L;j}^{pL} \end{pmatrix} &= A_{pL}\begin{pmatrix} e^{-ik_{p,1}j} + r_{1,1}^{e,e}e^{ik_{p,1}j} \\ a_{1,1}^{h,e}e^{-ik_{h,1}j} \end{pmatrix} \\ \begin{pmatrix} u_{R;j}^{pL} \\ v_{R;j}^{pL} \end{pmatrix} &= A_{pL}\begin{pmatrix} t_{2,1}^{e,e}e^{ik_{p,2}j} \\ c_{2,1}^{h,e}e^{-ik_{h,2}j} \end{pmatrix}; \end{aligned} \tag{E.41}$$

(ii) incoming particle from right lead (pR)

$$\begin{pmatrix} u^{pR}_{L;j} \\ v^{pR}_{L;j} \end{pmatrix} = A_{pR} \begin{pmatrix} t^{e,e}_{1,2} e^{ik_{p,1}j} \\ c^{h,e}_{1,2} e^{-ik_{h,1}j} \end{pmatrix}$$
$$\begin{pmatrix} u^{pR}_{R;j} \\ v^{pR}_{R;j} \end{pmatrix} = A_{pR} \begin{pmatrix} e^{-ik_{p,2}j} + r^{e,e}_{2,2} e^{ik_{p,2}j} \\ a^{h,e}_{2,2} e^{-ik_{h,2}j} \end{pmatrix}; \tag{E.42}$$

(iii) incoming hole from left lead (hL)

$$\begin{pmatrix} u^{hL}_{L;j} \\ v^{hL}_{L;j} \end{pmatrix} = A_{hL} \begin{pmatrix} a^{e,h}_{1,1} e^{ik_{p,1}j} \\ e^{ik_{h,1}j} + r^{h,h}_{1,1} e^{-ik_{h,1}j} \end{pmatrix}$$
$$\begin{pmatrix} u^{pL}_{R;j} \\ v^{pL}_{R;j} \end{pmatrix} = A_{hL} \begin{pmatrix} c^{e,h}_{2,1} e^{ik_{p,2}j} \\ t^{h,h}_{2,1} e^{-ik_{h,2}j} \end{pmatrix}; \tag{E.43}$$

(iv) incoming hole from right lead (hR)

$$\begin{pmatrix} u^{hR}_{L;j} \\ v^{pR}_{L;j} \end{pmatrix} = A_{hR} \begin{pmatrix} c^{e,h}_{1,2} e^{ik_{p,1}j} \\ t^{h,h}_{1,2} e^{-ik_{h,1}j} \end{pmatrix}$$
$$\begin{pmatrix} u^{hR}_{R;j} \\ v^{pR}_{R;j} \end{pmatrix} = A_{hR} \begin{pmatrix} a^{e,h}_{2,2} e^{ik_{p,2}j} \\ e^{ik_{h,2}j} + r^{h,h}_{2,2} e^{-ik_{h,2}j} \end{pmatrix}; \tag{E.44}$$

with A_δ appropriate normalization constants. In the following, to simplify the notation, we will assume particle-hole symmetry, $S^{\mu,\lambda}_{\alpha,\beta}(E) = \left[S^{\lambda,\mu}_{\alpha,\beta}(-E)\right]^*$, and assume the junction to be symmetric respect the lead exchange, $S^{\mu,\lambda}_{\alpha,\beta}(E) = S^{\mu,\lambda}_{\beta,\alpha}(E)$. Because of these symmetries, we have only four relevant scattering coefficients, $\left|S_{i,j}\right|^2$, that fully describe the physics at the junction. We refer to them as $R(E)$, normal reflection, $T(E)$, normal transmission, $A(E)$, Andreev reflection and $C(E)$, crossed Andreev reflection. It is important to highlight that the normal transmission and the Andreev reflection are the only processes that creates an imbalance in the relative number of particles within the two metallic contacts. Whereas Andreev reflection and crossed Andreev reflection do not preserve the total number of particle in the metallic lead subsystem, as shown in Eq. (E.45)

$$\begin{aligned} R &\rightarrow \frac{\left(\dot{N}_L - \dot{N}_R\right)}{2} = 0; \quad \frac{\left(\dot{N}_L + \dot{N}_R\right)}{2} = 0; \\ T &\rightarrow \frac{\left(\dot{N}_L - \dot{N}_R\right)}{2} = 1; \quad \frac{\left(\dot{N}_L + \dot{N}_R\right)}{2} = 0; \\ A &\rightarrow \frac{\left(\dot{N}_L - \dot{N}_R\right)}{2} = 1; \quad \frac{\left(\dot{N}_L + \dot{N}_R\right)}{2} = -1; \\ C &\rightarrow \frac{\left(\dot{N}_L - \dot{N}_R\right)}{2} = 0; \quad \frac{\left(\dot{N}_L + \dot{N}_R\right)}{2} = -1. \end{aligned} \tag{E.45}$$

The coefficients are shown in Fig. 8.3 of Section 8.3.

In the absence of Majorana fermions and for $U = 0$, the junction is trasparent, in the zero energy limit, due the resonance with the zero energy quantum dot states. However, for any finite U, the resonance is suppressed by the interaction that removes low energy states in the quantum dot. On the other hand, in the presence of a MZM we observe a zero bias trasmission and Andreev peaks that persist even for large values of U. Finally, in the presence of two

Majorana, no zero energy state survives due to the hybridization between the Kitaev chains and the quantum dot. The robust topological peak in the scattering matrix coefficients is then expected to be an interesting signature of the presence of a MZM. In the following we will relate these features to physically measurable quantities like the current and the shot noise.

To spell out the relation between the scattering matrix amplitudes and the current, it us useful to express the fermionic creation and annihilation operators in real space as a function of the system eigenvectors

$$\begin{aligned} c_{\alpha j} &= \sum_{E>0}\sum_{\delta}\left(\left[u^{\delta,E}_{\alpha;j}\right]^{*}\Gamma_{\delta,E}+\left[v^{\delta,E}_{\alpha;j}\right]\Gamma^{\dagger}_{\delta,E}\right) \\ c^{\dagger}_{\alpha j} &= \sum_{E>0}\sum_{\delta}\left(\left[u^{\delta,E}_{\alpha;j}\right]\Gamma^{\dagger}_{\delta,E}+\left[v^{\delta,E}_{\alpha;j}\right]^{*}\Gamma_{\delta,E}\right), \end{aligned} \tag{E.46}$$

with δ running over the four scattering states. The eigenvectors satisfy the fermionic algebra

$$\left\{\Gamma_{\delta,E},\Gamma^{\dagger}_{\delta',E'}\right\}=\delta_{\delta,\delta'}\delta_{E,E'} \tag{E.47}$$

all other anticommutator vanish.

The Landauer-Buttiker approach, that consist in shooting particles and holes agains the junction from thermal reservoirs at fixed temperature and voltage biased chemical potentials, allows us to express the transport properties of the systems in terms of the voltage bias into the leads and the scattering matrix amplitudes. By using the expressions (8.11) for the current and the definition of the shot noise (8.12) we obtain results in agreement with those obtained with the Keldysh Green's function approach

References

[1] A. A. Abrikosov. Electron scattering on magnetic impurities in metals and anomalous resistivity effects. *Physics Physique Fizika*, 2:5–20, Sep 1965. doi: 10.1103/PhysicsPhysiqueFizika.2.5. URL https://link.aps.org/doi/10.1103/PhysicsPhysiqueFizika.2.5.

[2] A. A. Abrikosov, I. Dzyaloshinskii, L. P. Gorkov, and R. A. Silverman. *Methods of quantum field theory in statistical physics*. Dover, New York, NY, 1975. URL https://cds.cern.ch/record/107441.

[3] I. Affleck and D. Giuliano. Topological superconductor–luttinger liquid junctions. *Journal of Statistical Mechanics: Theory and Experiment*, 2013(06):P06011, jun 2013. doi: 10.1088/1742-5468/2013/06/p06011. URL https://doi.org/10.1088%2F1742-5468%2F2013%2F06%2Fp06011.

[4] I. Affleck and D. Giuliano. Screening clouds and majorana fermions. *Journal of Statistical Physics*, 157(4):666–691, Dec 2014. ISSN 1572-9613. doi: 10.1007/s10955-014-1056-1. URL https://doi.org/10.1007/s10955-014-1056-1.

[5] I. Affleck and A. W. W. Ludwig. Exact critical theory of the two-impurity kondo model. *Phys. Rev. Lett.*, 68:1046–1049, Feb 1992. doi: 10.1103/PhysRevLett.68.1046. URL https://link.aps.org/doi/10.1103/PhysRevLett.68.1046.

[6] I. Affleck, A. Rahmani, and D. Pikulin. Majorana-hubbard model on the square lattice. *Phys. Rev. B*, 96:125121, Sep 2017. doi: 10.1103/PhysRevB.96.125121. URL https://link.aps.org/doi/10.1103/PhysRevB.96.125121.

[7] R. Aguado and D. C. Langreth. Out-of-equilibrium kondo effect in double quantum dots. *Phys. Rev. Lett.*, 85:1946–1949, Aug 2000. doi: 10.1103/PhysRevLett.85.1946. URL https://link.aps.org/doi/10.1103/PhysRevLett.85.1946.

[8] V. Alba and P. Calabrese. Entanglement and thermodynamics after a quantum quench in integrable systems. *Proceedings of the National Academy of Sciences*, 114(30):7947–7951, 2017. ISSN 0027-8424. doi: 10.1073/pnas.1703516114. URL https://www.pnas.org/content/114/30/7947.

[9] S. M. Albrecht, A. P. Higginbotham, M. Madsen, F. Kuemmeth, T. S. Jespersen, J. Nygård, P. Krogstrup, and C. M. Marcus. Exponential protection of zero modes in majorana islands. *Nature*, 531:206 EP –, 03 2016. URL https://doi.org/10.1038/nature17162.

[10] J. Alicea. New directions in the pursuit of majorana fermions in solid state systems. *Reports on Progress in Physics*, 75(7):076501, jun 2012. doi: 10.1088/0034-4885/75/7/076501. URL https://doi.org/10.1088%2F0034-4885%2F75%2F7%2F076501.

[11] J. Alicea, Y. Oreg, G. Refael, F. von Oppen, and M. P. A. Fisher. Non-abelian statistics and topological quantum information processing in 1d wire networks. *Nature Physics*, 7:412 EP –, Feb 2011. URL https://doi.org/10.1038/nphys1915. Article.

[12] A. Altland and B. D. Simons. *Condensed Matter Field Theory*. Cambridge University Press, 2 edition, 2010. doi: 10.1017/CBO9780511789984.

[13] A. Amo, M. D. Martín, L. Viña, A. I. Toropov, and K. S. Zhuravlev. Photoluminescence dynamics in gaas along an optically induced mott transition. *Journal of Applied Physics*, 101(8): 081717, 2007. doi: 10.1063/1.2722786. URL https://doi.org/10.1063/1.2722786.

[14] F. B. Anders. Steady-state currents through nanodevices: A scattering-states numerical renormalization-group approach to open quantum systems. *Phys. Rev. Lett.*, 101:066804, Aug 2008. doi: 10.1103/PhysRevLett.101.066804. URL https://link.aps.org/doi/10.1103/PhysRevLett.101.066804.

[15] F. B. Anders and A. Schiller. Real-time dynamics in quantum-impurity systems: A time-dependent numerical renormalization-group approach. *Phys. Rev. Lett.*, 95:196801, 2005. doi: 10.1103/PhysRevLett.95.196801. URL http://link.aps.org/abstract/PRL/v95/e196801.

[16] F. B. Anders and A. Schiller. Spin precession and real-time dynamics in the Kondo model:time-dependent numerical renormalization-group study. *Phys. Rev. B*, 74(24):245113, Dec 2006. doi: 10.1103/PhysRevB.74.245113.

[17] P. W. Anderson. Localized magnetic states in metals. *Phys. Rev.*, 124:41–53, Oct 1961. doi: 10.1103/PhysRev.124.41. URL https://link.aps.org/doi/10.1103/PhysRev.124.41.

[18] P. W. Anderson. A poor man's derivation of scaling laws for the kondo problem. *Journal of Physics C: Solid State Physics*, 3(12):2436–2441, dec 1970. doi: 10.1088/0022-3719/3/12/008. URL https://doi.org/10.1088%2F0022-3719%2F3%2F12%2F008.

[19] P. W. Anderson. Experimental constraints on the theory of high-tc superconductivity. *Science*, 256(5063):1526–1531, 1992. ISSN 0036-8075. doi: 10.1126/science.256.5063.1526. URL https://science.sciencemag.org/content/256/5063/1526.

[20] H. Aoki, N. Tsuji, M. Eckstein, M. Kollar, T. Oka, and P. Werner. Nonequilibrium dynamical mean-field theory and its applications. *Rev. Mod. Phys.*, 86:779–837, Jun 2014. doi: 10.1103/RevModPhys.86.779. URL https://link.aps.org/doi/10.1103/RevModPhys.86.779.

[21] P. I. Arseev. On the nonequilibrium diagram technique: derivation, some features and applications. *Phys. Usp.*, 58(12):1159–1205, 2015. doi: 10.3367/UFNe.0185.201512b.1271. URL https://ufn.ru/en/articles/2015/12/b/.

[22] Y. Ashida, T. Shi, M. C. Bañuls, J. I. Cirac, and E. Demler. Solving quantum impurity problems in and out of equilibrium with the variational approach. *Phys. Rev. Lett.*, 121: 026805, Jul 2018. doi: 10.1103/PhysRevLett.121.026805. URL https://link.aps.org/doi/10.1103/PhysRevLett.121.026805.

[23] R. C. Ashoori. Electrons in artificial atoms. *Nature*, 379:413, 1996. doi: 10.1038/379413a0. URL https://doi.org/10.1038/379413a0.

[24] D. Baeriswyl, C. Gros, and T. M. Rice. Landau parameters of almost-localized fermi liquids. *Phys. Rev. B*, 35:8391–8395, Jun 1987. doi: 10.1103/PhysRevB.35.8391. URL https://link.aps.org/doi/10.1103/PhysRevB.35.8391.

[25] S. Barnes. New method for the anderson model. *Journal of Physics F: Metal Physics*, 6(7): 1375–1383, 1976. ISSN 0305-4608. doi: 10.1088/0305-4608/6/7/018.

[26] P. P. Baruselli and M. Fabrizio. Sub-ohmic two-level system representation of the kondo effect. *Phys. Rev. B*, 85:073106, Feb 2012. doi: 10.1103/PhysRevB.85.073106. URL http://link.aps.org/doi/10.1103/PhysRevB.85.073106.

[27] G. Baskaran, Z. Zou, and P. Anderson. The resonating valence bond state and high-tc superconductivity — a mean field theory. *Solid State Communications*, 63(11):973 – 976, 1987. ISSN 0038-1098. doi: https://doi.org/10.1016/0038-1098(87)90642-9. URL http://www.sciencedirect.com/science/article/pii/0038109887906429.

[28] D. N. Basov, R. D. Averitt, and D. Hsieh. Towards properties on demand in quantum materials. *Nature Materials*, 16:1077 EP –, 10 2017. URL https://doi.org/10.1038/nmat5017.

[29] A. W. Bataller, R. A. Younts, A. Rustagi, Y. Yu, H. Ardekani, A. Kemper, L. Cao, and K. Gundogdu. Dense electron–hole plasma formation and ultralong charge lifetime in monolayer mos2 via material tuning. *Nano Letters*, 19(2):1104–1111, 2019. doi: 10.1021/acs.nanolett.8b04408. URL https://doi.org/10.1021/acs.nanolett.8b04408.

[30] J. Bauer and A. C. Hewson. Field-dependent quasiparticles in the infinite-dimensional hubbard model. *Phys. Rev. B*, 76:035118, Jul 2007. doi: 10.1103/PhysRevB.76.035118. URL https://link.aps.org/doi/10.1103/PhysRevB.76.035118.

[31] B. Béri and N. R. Cooper. Topological kondo effect with majorana fermions. *Phys. Rev. Lett.*, 109:156803, Oct 2012. doi: 10.1103/PhysRevLett.109.156803. URL https://link.aps.org/doi/10.1103/PhysRevLett.109.156803.

[32] B. Béri and N. R. Cooper. Topological kondo effect with majorana fermions. *Phys. Rev. Lett.*, 109:156803, Oct 2012. doi: 10.1103/PhysRevLett.109.156803. URL https://link.aps.org/doi/10.1103/PhysRevLett.109.156803.

[33] N. E. Bickers. Review of techniques in the large-n expansion for dilute magnetic alloys. *Rev. Mod. Phys.*, 59:845–939, Oct 1987. doi: 10.1103/RevModPhys.59.845. URL https://link.aps.org/doi/10.1103/RevModPhys.59.845.

[34] Y. Blanter and M. Büttiker. Shot noise in mesoscopic conductors. *Physics Reports*, 336(1):1 – 166, 2000. ISSN 0370-1573. doi: https://doi.org/10.1016/S0370-1573(99)00123-4. URL http://www.sciencedirect.com/science/article/pii/S0370157399001234.

[35] P. Bogacki and L. Shampine. An efficient runge-kutta (4,5) pair. *Computers & Mathematics with Applications*, 32(6):15 – 28, 1996. ISSN 0898-1221. doi: https://doi.org/10.1016/0898-1221(96)00141-1. URL http://www.sciencedirect.com/science/article/pii/0898122196001411.

[36] C. J. Bolech and N. Shah. Consistent bosonization-debosonization. ii. the two-lead kondo problem and the fate of its nonequilibrium toulouse point. *Phys. Rev. B*, 93:085441, Feb

2016. doi: 10.1103/PhysRevB.93.085441. URL https://link.aps.org/doi/10.1103/PhysRevB.93.085441.

[37] E. Boulat, H. Saleur, and P. Schmitteckert. Twofold advance in the theoretical understanding of far-from-equilibrium properties of interacting nanostructures. *Phys. Rev. Lett.*, 101 (14):140601, Sep 2008. doi: 10.1103/PhysRevLett.101.140601.

[38] W. F. Brinkman and T. M. Rice. Application of gutzwiller's variational method to the metal-insulator transition. *Phys. Rev. B*, 2:4302–4304, Nov 1970. doi: 10.1103/PhysRevB.2.4302. URL https://link.aps.org/doi/10.1103/PhysRevB.2.4302.

[39] W. F. Brinkman and T. M. Rice. Electron-hole liquids in semiconductors. *Phys. Rev. B*, 7:1508–1523, Feb 1973. doi: 10.1103/PhysRevB.7.1508. URL https://link.aps.org/doi/10.1103/PhysRevB.7.1508.

[40] M. Bugajski, W. Kuszko, and K. Regiåski. Diamagnetic shift of exciton energy levels in gaas-$Ga_{1-x}Al_xAs$ quantum wells. *Solid State Communications*, 60(8):669 – 673, 1986. ISSN 0038-1098. doi: https://doi.org/10.1016/0038-1098(86)90265-6. URL http://www.sciencedirect.com/science/article/pii/0038109886902656.

[41] R. Bulla. Zero temperature metal-insulator transition in the infinite-dimensional hubbard model. *Phys. Rev. Lett.*, 83:136–139, Jul 1999. doi: 10.1103/PhysRevLett.83.136. URL https://link.aps.org/doi/10.1103/PhysRevLett.83.136.

[42] J. Bünemann, F. Gebhard, and R. Thul. Landau-gutzwiller quasiparticles. *Phys. Rev. B*, 67:075103, Feb 2003. doi: 10.1103/PhysRevB.67.075103. URL https://link.aps.org/doi/10.1103/PhysRevB.67.075103.

[43] M. Buzzi, M. Först, R. Mankowsky, and A. Cavalleri. Probing dynamics in quantum materials with femtosecond x-rays. *Nature Reviews Materials*, 3(9):299–311, 2018. doi: 10.1038/s41578-018-0024-9. URL https://doi.org/10.1038/s41578-018-0024-9.

[44] M. Caffarel and W. Krauth. Exact diagonalization approach to correlated fermions in infinite dimensions: Mott transition and superconductivity. *Phys. Rev. Lett.*, 72:1545–1548, Mar 1994. doi: 10.1103/PhysRevLett.72.1545. URL https://link.aps.org/doi/10.1103/PhysRevLett.72.1545.

[45] P. Calabrese and J. Cardy. Time dependence of correlation functions following a quantum quench. *Phys. Rev. Lett.*, 96:136801, Apr 2006. doi: 10.1103/PhysRevLett.96.136801. URL https://link.aps.org/doi/10.1103/PhysRevLett.96.136801.

[46] A. O. Caldeira and A. J. Leggett. Influence of dissipation on quantum tunneling in macroscopic systems. *Phys. Rev. Lett.*, 46:211–214, Jan 1981. doi: 10.1103/PhysRevLett.46.211. URL https://link.aps.org/doi/10.1103/PhysRevLett.46.211.

[47] M. Capello, F. Becca, M. Fabrizio, S. Sorella, and E. Tosatti. Variational description of mott insulators. *Phys. Rev. Lett.*, 94:026406, Jan 2005. doi: 10.1103/PhysRevLett.94.026406. URL https://link.aps.org/doi/10.1103/PhysRevLett.94.026406.

[48] M. Capone, C. Castellani, and M. Grilli. First-order pairing transition and single-particle spectral function in the attractive hubbard model. *Phys. Rev. Lett.*, 88:126403, Mar 2002. doi: 10.1103/PhysRevLett.88.126403. URL https://link.aps.org/doi/10.1103/

PhysRevLett.88.126403. actually study the attractive case at fixed density, which, as mentioned in the text, is equivalent to the repulsive one at fixed magnetisation.

[49] M. Capone, L. de' Medici, and A. Georges. Solving the dynamical mean-field theory at very low temperatures using the lanczos exact diagonalization. *Phys. Rev. B*, 76:245116, Dec 2007. doi: 10.1103/PhysRevB.76.245116. URL https://link.aps.org/doi/10.1103/PhysRevB.76.245116.

[50] G. Carleo and M. Troyer. Solving the quantum many-body problem with artificial neural networks. *Science*, 355(6325):602–606, 2017. ISSN 0036-8075. doi: 10.1126/science.aag2302. URL http://science.sciencemag.org/content/355/6325/602.

[51] A. Cavalleri. Photo-induced superconductivity. *Contemporary Physics*, 59(1):31–46, 2018. doi: 10.1080/00107514.2017.1406623. URL https://doi.org/10.1080/00107514.2017.1406623.

[52] Z. Chen, X. Li, and T. K. Ng. Exactly solvable bcs-hubbard model in arbitrary dimensions. *Phys. Rev. Lett.*, 120:046401, Jan 2018. doi: 10.1103/PhysRevLett.120.046401. URL https://link.aps.org/doi/10.1103/PhysRevLett.120.046401.

[53] M. Cheng, M. Becker, B. Bauer, and R. M. Lutchyn. Interplay between kondo and majorana interactions in quantum dots. *Phys. Rev. X*, 4:031051, Sep 2014. doi: 10.1103/PhysRevX.4.031051. URL https://link.aps.org/doi/10.1103/PhysRevX.4.031051.

[54] A. Chernikov, C. Ruppert, H. M. Hill, A. F. Rigosi, and T. F. Heinz. Population inversion and giant bandgap renormalization in atomically thin ws2 layers. *Nature Photonics*, 9:466 EP –, 2015. URL http://dx.doi.org/10.1038/nphoton.2015.104.

[55] D. Chevallier, P. Szumniak, S. Hoffman, D. Loss, and J. Klinovaja. Topological phase detection in rashba nanowires with a quantum dot. *Phys. Rev. B*, 97:045404, Jan 2018. doi: 10.1103/PhysRevB.97.045404. URL https://link.aps.org/doi/10.1103/PhysRevB.97.045404.

[56] S. B. Chung, X.-L. Qi, J. Maciejko, and S.-C. Zhang. Conductance and noise signatures of majorana backscattering. *Phys. Rev. B*, 83:100512, Mar 2011. doi: 10.1103/PhysRevB.83.100512. URL https://link.aps.org/doi/10.1103/PhysRevB.83.100512.

[57] R. Citro and F. Romeo. Non-equilibrium slave bosons approach to quantum pumping in interacting quantum dots. *Journal of Physics: Conference Series*, 696(1):012014, 2016. URL http://stacks.iop.org/1742-6596/696/i=1/a=012014.

[58] P. Coleman. New approach to the mixed-valence problem. *Phys. Rev. B*, 29:3035–3044, Mar 1984. doi: 10.1103/PhysRevB.29.3035. URL https://link.aps.org/doi/10.1103/PhysRevB.29.3035.

[59] D. L. Cox and A. Zawadowski. Exotic kondo effects in metals: Magnetic ions in a crystalline electric field and tunnelling centres. *Advances in Physics*, 47(5):599–942, 1998. doi: 10.1080/000187398243500. URL https://doi.org/10.1080/000187398243500.

[60] S. M. Cronenwett, T. H. Oosterkamp, and L. P. Kouwenhoven. A Tunable Kondo Effect in Quantum Dots. *Science*, 281(5376):540–544, 1998. doi: 10.1126/science.281.5376.540. URL http://www.sciencemag.org/cgi/content/abstract/281/5376/540.

[61] P. D. Cunningham, A. T. Hanbicki, K. M. McCreary, and B. T. Jonker. Photoinduced bandgap renormalization and exciton binding energy reduction in ws2. *ACS Nano*, 11(12): 12601–12608, 2017. doi: 10.1021/acsnano.7b06885. URL https://doi.org/10.1021/acsnano.7b06885. PMID: 29227085.

[62] A. Das, Y. Ronen, Y. Most, Y. Oreg, M. Heiblum, and H. Shtrikman. Zero-bias peaks and splitting in an al–inas nanowire topological superconductor as a signature of majorana fermions. *Nature Physics*, 8:887 EP –, 11 2012. URL https://doi.org/10.1038/nphys2479.

[63] J. H. de Boer and E. J. W. Verwey. Semi-conductors with partially and with completely filled3d-lattice bands. *Proceedings of the Physical Society*, 49(4S):59–71, aug 1937. doi: 10.1088/0959-5309/49/4s/307. URL https://doi.org/10.1088%2F0959-5309%2F49%2F4s%2F307.

[64] R. de Picciotto, M. Reznikov, M. Heiblum, V. Umansky, G. Bunin, and D. Mahalu. Direct observation of a fractional charge. *Nature*, 389(6647):162–164, 1997. doi: 10.1038/38241. URL https://doi.org/10.1038/38241.

[65] L. déMedici, A. Georges, and S. Biermann. Orbital-selective mott transition in multiband systems: Slave-spin representation and dynamical mean-field theory. *Phys. Rev. B*, 72: 205124, Nov 2005. doi: 10.1103/PhysRevB.72.205124. URL https://link.aps.org/doi/10.1103/PhysRevB.72.205124.

[66] M. T. Deng, S. Vaitiekenas, E. B. Hansen, J. Danon, M. Leijnse, K. Flensberg, J. Nygård, P. Krogstrup, and C. M. Marcus. Majorana bound state in a coupled quantum-dot hybrid-nanowire system. *Science*, 354(6319):1557–1562, 2016. ISSN 0036-8075. doi: 10.1126/science.aaf3961. URL https://science.sciencemag.org/content/354/6319/1557.

[67] F. A. Dessotti, L. S. Ricco, Y. Marques, L. H. Guessi, M. Yoshida, M. S. Figueira, M. de Souza, P. Sodano, and A. C. Seridonio. Unveiling majorana quasiparticles by a quantum phase transition: Proposal of a current switch. *Phys. Rev. B*, 94:125426, Sep 2016. doi: 10.1103/PhysRevB.94.125426. URL https://link.aps.org/doi/10.1103/PhysRevB.94.125426.

[68] P. Devillard, D. Chevallier, and M. Albert. Fingerprints of majorana fermions in current-correlation measurements from a superconducting tunnel microscope. *Phys. Rev. B*, 96: 115413, Sep 2017. doi: 10.1103/PhysRevB.96.115413. URL https://link.aps.org/doi/10.1103/PhysRevB.96.115413.

[69] B. Dong and X. L. Lei. Kondo-type transport through a quantum dot under magnetic fields. *Phys. Rev. B*, 63:235306, May 2001. doi: 10.1103/PhysRevB.63.235306. URL https://link.aps.org/doi/10.1103/PhysRevB.63.235306.

[70] I. K. Drozdov, A. Alexandradinata, S. Jeon, S. Nadj-Perge, H. Ji, R. J. Cava, B. Andrei Bernevig, and A. Yazdani. One-dimensional topological edge states of bismuth bilayers. *Nature Physics*, 10:664 EP –, 08 2014. URL https://doi.org/10.1038/nphys3048.

[71] X. Duan, C. Wang, A. Pan, R. Yu, and X. Duan. Two-dimensional transition metal dichalcogenides as atomically thin semiconductors: opportunities and challenges. *Chem. Soc. Rev.*, 44:8859–8876, 2015. doi: 10.1039/C5CS00507H. URL http://dx.doi.org/10.1039/C5CS00507H.

[72] M. Eckstein, M. Kollar, and P. Werner. Thermalization after an interaction quench in the hubbard model. *Phys. Rev. Lett.*, 103:056403, Jul 2009. doi: 10.1103/PhysRevLett.103.056403. URL https://link.aps.org/doi/10.1103/PhysRevLett.103.056403.

[73] M. Eckstein, M. Kollar, and P. Werner. Interaction quench in the hubbard model: Relaxation of the spectral function and the optical conductivity. *Phys. Rev. B*, 81:115131, Mar 2010. doi: 10.1103/PhysRevB.81.115131. URL https://link.aps.org/doi/10.1103/PhysRevB.81.115131.

[74] J. Eisert, M. Friesdorf, and C. Gogolin. Quantum many-body systems out of equilibrium. *Nature Physics*, 11:124 EP –, 02 2015. URL https://doi.org/10.1038/nphys3215.

[75] V. J. Emery and S. Kivelson. Mapping of the two-channel kondo problem to a resonant-level model. *Phys. Rev. B*, 46:10812–10817, Nov 1992. doi: 10.1103/PhysRevB.46.10812. URL https://link.aps.org/doi/10.1103/PhysRevB.46.10812.

[76] E. Eriksson, C. Mora, A. Zazunov, and R. Egger. Non-fermi-liquid manifold in a majorana device. *Phys. Rev. Lett.*, 113:076404, Aug 2014. doi: 10.1103/PhysRevLett.113.076404. URL https://link.aps.org/doi/10.1103/PhysRevLett.113.076404.

[77] E. Eriksson, A. Nava, C. Mora, and R. Egger. Tunneling spectroscopy of majorana-kondo devices. *Phys. Rev. B*, 90:245417, Dec 2014. doi: 10.1103/PhysRevB.90.245417. URL https://link.aps.org/doi/10.1103/PhysRevB.90.245417.

[78] F. H. L. Essler, H. Frahm, F. Göhmann, A. Klümper, and V. E. Korepin. *The One-Dimensional Hubbard Model*. Cambridge University Press, 2005. doi: 10.1017/CBO9780511534843.

[79] J. C. Estrada Saldaña, R. Žitko, J. P. Cleuziou, E. J. H. Lee, V. Zannier, D. Ercolani, L. Sorba, R. Aguado, and S. De Franceschi. Charge localization and reentrant superconductivity in a quasi-ballistic inas nanowire coupled to superconductors. *Science Advances*, 5(7), 2019. doi: 10.1126/sciadv.aav1235. URL https://advances.sciencemag.org/content/5/7/eaav1235.

[80] M. Fabrizio. Gutzwiller description of non-magnetic mott insulators: Dimer lattice model. *Phys. Rev. B*, 76:165110, Oct 2007. doi: 10.1103/PhysRevB.76.165110. URL https://link.aps.org/doi/10.1103/PhysRevB.76.165110.

[81] M. Fabrizio. The out-of-equilibrium time-dependent gutzwiller approximation. In V. Zlatic and A. Hewson, editors, *New Materials for Thermoelectric Applications: Theory and Experiment*, NATO Science for Peace and Security Series B: Physics and Biophysics, pages 247–273. Springer Netherlands, 2013. ISBN 978-94-007-4983-2. doi: 10.1007/978-94-007-4984-9_16. URL http://dx.doi.org/10.1007/978-94-007-4984-9_16.

[82] M. Fabrizio. Quantum fluctuations beyond the gutzwiller approximation. *Phys. Rev. B*, 95:075156, Feb 2017. doi: 10.1103/PhysRevB.95.075156. URL https://link.aps.org/doi/10.1103/PhysRevB.95.075156.

[83] M. Fabrizio, A. Gogolin, and A. Nersesyan. Critical properties of the double-frequency sine-gordon model with applications. *Nuclear Physics B*, 580(3):647 – 687, 2000. ISSN 0550-3213. doi: https://doi.org/10.1016/S0550-3213(00)00247-9. URL http://www.sciencedirect.com/science/article/pii/S0550321300002479.

[84] L. M. Falicov and J. C. Kimball. Simple model for semiconductor-metal transitions: Smb_6 and transition-metal oxides. *Phys. Rev. Lett.*, 22:997–999, May 1969. doi: 10.1103/PhysRevLett.22.997. URL https://link.aps.org/doi/10.1103/PhysRevLett.22.997.

[85] L. Fidkowski, J. Alicea, N. H. Lindner, R. M. Lutchyn, and M. P. A. Fisher. Universal transport signatures of majorana fermions in superconductor-luttinger liquid junctions. *Phys. Rev. B*, 85:245121, Jun 2012. doi: 10.1103/PhysRevB.85.245121. URL https://link.aps.org/doi/10.1103/PhysRevB.85.245121.

[86] M. Filippone, K. Le Hur, and C. Mora. Giant charge relaxation resistance in the anderson model. *Phys. Rev. Lett.*, 107:176601, Oct 2011. doi: 10.1103/PhysRevLett.107.176601. URL https://link.aps.org/doi/10.1103/PhysRevLett.107.176601.

[87] S. Florens and A. Georges. Slave-rotor mean-field theories of strongly correlated systems and the mott transition in finite dimensions. *Phys. Rev. B*, 70:035114, Jul 2004. doi: 10.1103/PhysRevB.70.035114. URL https://link.aps.org/doi/10.1103/PhysRevB.70.035114.

[88] P. Fritsch and S. Kehrein. Nonequilibrium Kondo model with voltage bias in a magnetic field. *Phys. Rev. B*, 81(3):035113, Jan 2010. doi: 10.1103/PhysRevB.81.035113.

[89] L. Fritz and M. Vojta. Phase transitions in the pseudogap anderson and kondo models: Critical dimensions, renormalization group, and local-moment criticality. *Phys. Rev. B*, 70:214427, Dec 2004. doi: 10.1103/PhysRevB.70.214427. URL https://link.aps.org/doi/10.1103/PhysRevB.70.214427.

[90] L. Fu and C. L. Kane. Superconducting proximity effect and majorana fermions at the surface of a topological insulator. *Phys. Rev. Lett.*, 100:096407, Mar 2008. doi: 10.1103/PhysRevLett.100.096407. URL https://link.aps.org/doi/10.1103/PhysRevLett.100.096407.

[91] M. R. Galpin, A. K. Mitchell, J. Temaismithi, D. E. Logan, B. Béri, and N. R. Cooper. Conductance fingerprint of majorana fermions in the topological kondo effect. *Phys. Rev. B*, 89:045143, Jan 2014. doi: 10.1103/PhysRevB.89.045143. URL https://link.aps.org/doi/10.1103/PhysRevB.89.045143.

[92] F. Gebhard. Equivalence of variational and slave-boson mean-field treatments of the periodic anderson model. *Phys. Rev. B*, 44:992–1003, Jul 1991. doi: 10.1103/PhysRevB.44.992. URL https://link.aps.org/doi/10.1103/PhysRevB.44.992.

[93] F. Gebhard and D. Vollhardt. Correlation functions for interacting fermions in the gutzwiller ansatz. *Phys. Rev. B*, 38:6911–6927, Oct 1988. doi: 10.1103/PhysRevB.38.6911. URL https://link.aps.org/doi/10.1103/PhysRevB.38.6911.

[94] A. Georges and G. Kotliar. Hubbard model in infinite dimensions. *Phys. Rev. B*, 45:6479–6483, Mar 1992. doi: 10.1103/PhysRevB.45.6479. URL https://link.aps.org/doi/10.1103/PhysRevB.45.6479.

[95] A. Georges, G. Kotliar, W. Krauth, and M. J. Rozenberg. Dynamical mean-field theory of strongly correlated fermion systems and the limit of infinite dimensions. *Rev. Mod. Phys.*, 68:13–125, Jan 1996. doi: 10.1103/RevModPhys.68.13. URL https://link.aps.org/doi/10.1103/RevModPhys.68.13.

[96] C. Giannetti, M. Capone, D. Fausti, M. Fabrizio, F. Parmigiani, and D. Mihailovic. Ultrafast optical spectroscopy of strongly correlated materials and high-temperature superconductors: a non-equilibrium approach. *Advances in Physics*, 65(2):58–238, 2016. doi: 10.1080/00018732.2016.1194044. URL https://doi.org/10.1080/00018732.2016.1194044.

[97] D. Giuliano and I. Affleck. Real fermion modes, impurity entropy, and nontrivial fixed points in the phase diagram of junctions of interacting quantum wires and topological superconductors. *Nuclear Physics B*, 944:114645, 2019. ISSN 0550-3213. doi: https://doi.org/10.1016/j.nuclphysb.2019.114645. URL http://www.sciencedirect.com/science/article/pii/S0550321319301312.

[98] D. Giuliano, S. Paganelli, and L. Lepori. Current transport properties and phase diagram of a kitaev chain with long-range pairing. *Phys. Rev. B*, 97:155113, Apr 2018. doi: 10.1103/PhysRevB.97.155113. URL https://link.aps.org/doi/10.1103/PhysRevB.97.155113.

[99] L. I. Glazman and M. E. Raikh. Resonant Kondo transparency of a barrier with quasilocal impurity states. *JETP Lett.*, 47:452, 1988.

[100] A. O. Gogolin and A. Komnik. Full counting statistics for the kondo dot in the unitary limit. *Phys. Rev. Lett.*, 97:016602, Jul 2006. doi: 10.1103/PhysRevLett.97.016602. URL https://link.aps.org/doi/10.1103/PhysRevLett.97.016602.

[101] D. Goldhaber-Gordon, J. Göres, M. A. Kastner, H. Shtrikman, D. Mahalu, and U. Meirav. From the Kondo Regime to the Mixed-Valence Regime in a Single-Electron Transistor. *Phys. Rev. Lett.*, 81:5225, 1998. doi: 10.1103/PhysRevLett.81.5225.

[102] C. Gonzalez-Buxton and K. Ingersent. Renormalization-group study of anderson and kondo impurities in gapless fermi systems. *Phys. Rev. B*, 57:14254–14293, Jun 1998. doi: 10.1103/PhysRevB.57.14254. URL https://link.aps.org/doi/10.1103/PhysRevB.57.14254.

[103] G. Górski, J. Barański, I. Weymann, and T. Domański. Interplay between correlations and majorana mode in proximitized quantum dot. *Scientific Reports*, 8(1):15717, 2018. doi: 10.1038/s41598-018-33529-1. URL https://doi.org/10.1038/s41598-018-33529-1.

[104] P. Grivickas, V. Grivickas, and J. Linnros. Excitonic absorption above the mott transition in si. *Phys. Rev. Lett.*, 91:246401, Dec 2003. doi: 10.1103/PhysRevLett.91.246401. URL https://link.aps.org/doi/10.1103/PhysRevLett.91.246401.

[105] D. Guerci. Transport through a magnetic impurity: A slave-spin approach. *Phys. Rev. B*, 99:195409, May 2019. doi: 10.1103/PhysRevB.99.195409. URL https://link.aps.org/doi/10.1103/PhysRevB.99.195409.

[106] D. Guerci and et al. Time-dependent ghost-gutzwiller wave function: quantum quench dynamics of the hubbard model. Unpublished, 2019.

[107] D. Guerci and M. Fabrizio. Unbinding slave spins in the anderson impurity model. *Phys. Rev. B*, 96:201106, Nov 2017. doi: 10.1103/PhysRevB.96.201106. URL https://link.aps.org/doi/10.1103/PhysRevB.96.201106.

[108] D. Guerci and A. Nava. Probing majorana edge states by measuring transport through an interacting magnetic impurity. arXiv:1907.06444, 2019.

[109] D. Guerci, M. Capone, and M. Fabrizio. Exciton mott transition revisited. *Phys. Rev. Materials*, 3:054605, May 2019. doi: 10.1103/PhysRevMaterials.3.054605. URL https://link.aps.org/doi/10.1103/PhysRevMaterials.3.054605.

[110] Ö. Gül, H. Zhang, J. D. S. Bommer, M. W. A. de Moor, D. Car, S. R. Plissard, E. P. A. M. Bakkers, A. Geresdi, K. Watanabe, T. Taniguchi, and L. P. Kouwenhoven. Ballistic majorana nanowire devices. *Nature Nanotechnology*, 13(3):192–197, 2018. doi: 10.1038/s41565-017-0032-8. URL https://doi.org/10.1038/s41565-017-0032-8.

[111] M. C. Gutzwiller. Effect of correlation on the ferromagnetism of transition metals. *Phys. Rev. Lett.*, 10:159–162, Mar 1963. doi: 10.1103/PhysRevLett.10.159. URL https://link.aps.org/doi/10.1103/PhysRevLett.10.159.

[112] M. C. Gutzwiller. Correlation of electrons in a narrow *s* band. *Phys. Rev.*, 137:A1726–A1735, Mar 1965. doi: 10.1103/PhysRev.137.A1726. URL https://link.aps.org/doi/10.1103/PhysRev.137.A1726.

[113] A. Haim, E. Berg, F. von Oppen, and Y. Oreg. Signatures of majorana zero modes in spin-resolved current correlations. *Phys. Rev. Lett.*, 114:166406, Apr 2015. doi: 10.1103/PhysRevLett.114.166406. URL https://link.aps.org/doi/10.1103/PhysRevLett.114.166406.

[114] H. Haug and A. P. Jauho. *Quantum Kinetics in Transport and Optics of Semiconductors*. Springer, 1996. doi: 10.1007/978-3-540-73564-9.

[115] K. He, N. Kumar, L. Zhao, Z. Wang, K. F. Mak, H. Zhao, and J. Shan. Tightly bound excitons in monolayer wse_2. *Phys. Rev. Lett.*, 113:026803, Jul 2014. doi: 10.1103/PhysRevLett.113.026803. URL https://link.aps.org/doi/10.1103/PhysRevLett.113.026803.

[116] Q. L. He, L. Pan, A. L. Stern, E. C. Burks, X. Che, G. Yin, J. Wang, B. Lian, Q. Zhou, E. S. Choi, K. Murata, X. Kou, Z. Chen, T. Nie, Q. Shao, Y. Fan, S.-C. Zhang, K. Liu, J. Xia, and K. L. Wang. Chiral majorana fermion modes in a quantum anomalous hall insulator–superconductor structure. *Science*, 357(6348):294–299, 2017. ISSN 0036-8075. doi: 10.1126/science.aag2792. URL https://science.sciencemag.org/content/357/6348/294.

[117] A. C. Hewson. *Contents*, pages vii–x. Cambridge Studies in Magnetism. Cambridge University Press, 1993.

[118] B. Horvatić and V. Zlatić. Intermediate valence and kondo features of the anderson model by perturbation theory. *Solid State Communications*, 54(11):957 – 960, 1985. ISSN 0038-1098. doi: https://doi.org/10.1016/0038-1098(85)90163-2. URL http://www.sciencedirect.com/science/article/pii/0038109885901632.

[119] J. Hubbard and B. H. Flowers. Electron correlations in narrow energy bands. *Proceedings of the Royal Society of London. Series A. Mathematical and Physical Sciences*, 276(1365):238–257, 1963. doi: 10.1098/rspa.1963.0204. URL https://royalsocietypublishing.org/doi/abs/10.1098/rspa.1963.0204.

[120] S. D. Huber and A. Rüegg. Dynamically generated double occupancy as a probe of cold atom systems. *Phys. Rev. Lett.*, 102:065301, Feb 2009. doi: 10.1103/PhysRevLett.102.065301. URL https://link.aps.org/doi/10.1103/PhysRevLett.102.065301.

[121] R. Žitko and M. Fabrizio. Z_2 gauge theory description of the mott transition in infinite dimensions. *Phys. Rev. B*, 91:245130, Jun 2015. doi: 10.1103/PhysRevB.91.245130. URL http://link.aps.org/doi/10.1103/PhysRevB.91.245130.

[122] R. Žitko and P. Simon. Quantum impurity coupled to majorana edge fermions. *Phys. Rev. B*, 84:195310, Nov 2011. doi: 10.1103/PhysRevB.84.195310. URL https://link.aps.org/doi/10.1103/PhysRevB.84.195310.

[123] R. Žitko, i. c. v. Osolin, and P. Jeglič. Repulsive versus attractive hubbard model: Transport properties and spin-lattice relaxation rate. *Phys. Rev. B*, 91:155111, Apr 2015. doi: 10.1103/PhysRevB.91.155111. URL https://link.aps.org/doi/10.1103/PhysRevB.91.155111.

[124] Z. Iftikhar, A. Anthore, A. K. Mitchell, F. D. Parmentier, U. Gennser, A. Ouerghi, A. Cavanna, C. Mora, P. Simon, and F. Pierre. Tunable quantum criticality and super-ballistic transport in a "charge" kondo circuit. *Science*, 360(6395):1315–1320, 2018. ISSN 0036-8075. doi: 10.1126/science.aan5592. URL https://science.sciencemag.org/content/360/6395/1315.

[125] L. B. Ioffe and A. I. Larkin. Gapless fermions and gauge fields in dielectrics. *Phys. Rev. B*, 39:8988–8999, May 1989. doi: 10.1103/PhysRevB.39.8988. URL https://link.aps.org/doi/10.1103/PhysRevB.39.8988.

[126] A. Isidori and M. Capone. Rotationally invariant slave bosons for strongly correlated superconductors. *Phys. Rev. B*, 80:115120, Sep 2009. doi: 10.1103/PhysRevB.80.115120. URL https://link.aps.org/doi/10.1103/PhysRevB.80.115120.

[127] D. A. Ivanov. Non-abelian statistics of half-quantum vortices in p-wave superconductors. *Phys. Rev. Lett.*, 86:268–271, Jan 2001. doi: 10.1103/PhysRevLett.86.268. URL https://link.aps.org/doi/10.1103/PhysRevLett.86.268.

[128] B. Jäck, Y. Xie, J. Li, S. Jeon, B. A. Bernevig, and A. Yazdani. Observation of a majorana zero mode in a topologically protected edge channel. *Science*, 364(6447):1255, 06 2019. doi: 10.1126/science.aax1444. URL http://science.sciencemag.org/content/364/6447/1255.abstract.

[129] P. Jacquod and M. Büttiker. Signatures of majorana fermions in hybrid normal-superconducting rings. *Phys. Rev. B*, 88:241409, Dec 2013. doi: 10.1103/PhysRevB.88.241409. URL https://link.aps.org/doi/10.1103/PhysRevB.88.241409.

[130] A.-P. Jauho, N. S. Wingreen, and Y. Meir. Time-dependent transport in interacting and noninteracting resonant-tunneling systems. *Phys. Rev. B*, 50:5528–5544, Aug 1994. doi: 10.1103/PhysRevB.50.5528. URL https://link.aps.org/doi/10.1103/PhysRevB.50.5528.

[131] T. Jiang, R. Chen, X. Zheng, Z. Xu, and Y. Tang. Photo-induced excitonic structure renormalization and broadband absorption in monolayer tungsten disulphide. *Opt. Express*, 26(2):859–869, Jan 2018. doi: 10.1364/OE.26.000859. URL http://www.opticsexpress.org/abstract.cfm?URI=oe-26-2-859.

[132] C. Jin, J. Kim, M. I. B. Utama, E. C. Regan, H. Kleemann, H. Cai, Y. Shen, M. J. Shinner, A. Sengupta, K. Watanabe, T. Taniguchi, S. Tongay, A. Zettl, and F. Wang. Imaging of pure spin-valley diffusion current in ws2-wse2 heterostructures. *Science*, 360(6391): 893–896, 2018. ISSN 0036-8075. doi: 10.1126/science.aao3503. URL https://science.sciencemag.org/content/360/6391/893.

[133] T. Jonckheere, J. Rech, A. Zazunov, R. Egger, and T. Martin. Hanbury brown and twiss noise correlations in a topological superconductor beam splitter. *Phys. Rev. B*, 95:054514, Feb 2017. doi: 10.1103/PhysRevB.95.054514. URL https://link.aps.org/doi/10.1103/PhysRevB.95.054514.

[134] B. A. Jones and C. M. Varma. Study of two magnetic impurities in a fermi gas. *Phys. Rev. Lett.*, 58:843–846, Mar 1987. doi: 10.1103/PhysRevLett.58.843. URL https://link.aps.org/doi/10.1103/PhysRevLett.58.843.

[135] B. A. Jones, C. M. Varma, and J. W. Wilkins. Low-temperature properties of the two-impurity kondo hamiltonian. *Phys. Rev. Lett.*, 61:125–128, Jul 1988. doi: 10.1103/PhysRevLett.61.125. URL https://link.aps.org/doi/10.1103/PhysRevLett.61.125.

[136] R. A. Kaindl, M. A. Carnahan, D. Hägele, R. Lövenich, and D. S. Chemla. Ultrafast terahertz probes of transient conducting and insulating phases in an electron–hole gas. *Nature*, 423: 734 EP –, 06 2003. URL http://dx.doi.org/10.1038/nature01676.

[137] A. Kamenev. Course 3 many-body theory of non-equilibrium systems. In H. Bouchiat, Y. Gefen, S. Guéron, G. Montambaux, and J. Dalibard, editors, *Nanophysics: Coherence and Transport*, volume 81 of *Les Houches*, pages 177 – 246. Elsevier, 2005. doi: https://doi.org/10.1016/S0924-8099(05)80045-9. URL http://www.sciencedirect.com/science/article/pii/S0924809905800459.

[138] A. Kamenev. *Field Theory of Non-Equilibrium Systems*. Cambridge University Press, 2011. doi: 10.1017/CBO9781139003667.

[139] A. Kaminski, Y. V. Nazarov, and L. I. Glazman. Universality of the Kondo effect in a quantum dot out of equilibrium. *Phys. Rev. B*, 62(12):8154–8170, Sep 2000. doi: 10.1103/PhysRevB.62.8154.

[140] J. Kanamori. Electron Correlation and Ferromagnetism of Transition Metals. *Progress of Theoretical Physics*, 30(3):275–289, 09 1963. ISSN 0033-068X. doi: 10.1143/PTP.30.275. URL https://doi.org/10.1143/PTP.30.275.

[141] L. Kappei, J. Szczytko, F. Morier-Genoud, and B. Deveaud. Direct observation of the mott transition in an optically excited semiconductor quantum well. *Phys. Rev. Lett.*, 94:147403, Apr 2005. doi: 10.1103/PhysRevLett.94.147403. URL https://link.aps.org/doi/10.1103/PhysRevLett.94.147403.

[142] D. B. Karki, C. Mora, J. von Delft, and M. N. Kiselev. Two-color fermi-liquid theory for transport through a multilevel kondo impurity. *Phys. Rev. B*, 97:195403, May 2018. doi: 10.1103/PhysRevB.97.195403. URL https://link.aps.org/doi/10.1103/PhysRevB.97.195403.

[143] M. A. Kastner. Artificial atoms. *Physics Today*, 46(1):24–31, 1993. doi: 10.1063/1.881393. URL https://doi.org/10.1063/1.881393.

[144] S. Kehrein. Scaling and decoherence in the nonequilibrium kondo model. *Phys. Rev. Lett.*, 95:056602, Jul 2005. doi: 10.1103/PhysRevLett.95.056602. URL https://link.aps.org/doi/10.1103/PhysRevLett.95.056602.

[145] M. Keller, W. Metzner, and U. Schollwöck. Dynamical mean-field theory for pairing and spin gap in the attractive hubbard model. *Phys. Rev. Lett.*, 86:4612–4615, May 2001. doi: 10.1103/PhysRevLett.86.4612. URL https://link.aps.org/doi/10.1103/PhysRevLett.86.4612.

[146] G. Kiršanskė, P. Tighineanu, R. S. Daveau, J. Miguel-Sánchez, P. Lodahl, and S. Stobbe. Observation of the exciton mott transition in the photoluminescence of coupled quantum wells. *Phys. Rev. B*, 94:155438, Oct 2016. doi: 10.1103/PhysRevB.94.155438. URL https://link.aps.org/doi/10.1103/PhysRevB.94.155438.

[147] M. N. Kiselev and R. Oppermann. Schwinger-keldysh semionic approach for quantum spin systems. *Phys. Rev. Lett.*, 85:5631–5634, Dec 2000. doi: 10.1103/PhysRevLett.85.5631. URL https://link.aps.org/doi/10.1103/PhysRevLett.85.5631.

[148] A. Y. Kitaev. Unpaired Majorana fermions in quantum wires. *Physics-Uspekhi*, 44(10S):131, 2001. ISSN 1063-7869. doi: 10.1070/1063-7869/44/10S/S29. URL http://stacks.iop.org/1063-7869/44/i=10S/a=S29.

[149] Y. Kleeorin and Y. Meir. Quantum phase transition in a realistic double-quantum-dot system. *Scientific Reports*, 8(1):10539, 2018. doi: 10.1038/s41598-018-28822-y. URL https://doi.org/10.1038/s41598-018-28822-y.

[150] T. Kobayashi, S. Tsuruta, S. Sasaki, T. Fujisawa, Y. Tokura, and T. Akazaki. Kondo effect in a semiconductor quantum dot with a spin-accumulated lead. *Phys. Rev. Lett.*, 104:036804, Jan 2010. doi: 10.1103/PhysRevLett.104.036804. URL https://link.aps.org/doi/10.1103/PhysRevLett.104.036804.

[151] C. Kollath, A. M. Läuchli, and E. Altman. Quench dynamics and nonequilibrium phase diagram of the bose-hubbard model. *Phys. Rev. Lett.*, 98:180601, Apr 2007. doi: 10.1103/PhysRevLett.98.180601. URL https://link.aps.org/doi/10.1103/PhysRevLett.98.180601.

[152] Y. Komijani and G. Kotliar. Analytical slave-spin mean-field approach to orbital selective mott insulators. *Phys. Rev. B*, 96:125111, Sep 2017. doi: 10.1103/PhysRevB.96.125111. URL https://link.aps.org/doi/10.1103/PhysRevB.96.125111.

[153] J. Kondo. Resistance Minimum in Dilute Magnetic Alloys. *Progress of Theoretical Physics*, 32(1):37–49, 07 1964. ISSN 0033-068X. doi: 10.1143/PTP.32.37. URL https://doi.org/10.1143/PTP.32.37.

[154] G. Kotliar. Landau theory of the mott transition in the fully frustrated hubbard model in infinite dimensions. *The European Physical Journal B - Condensed Matter and Complex Systems*, 11(1):27–39, 1999. ISSN 1434-6036. doi: 10.1007/s100510050914. URL http://dx.doi.org/10.1007/s100510050914.

[155] G. Kotliar and J. Liu. Superexchange mechanism and d-wave superconductivity. *Phys. Rev. B*, 38:5142–5145, Sep 1988. doi: 10.1103/PhysRevB.38.5142. URL https://link.aps.org/doi/10.1103/PhysRevB.38.5142.

[156] G. Kotliar and A. E. Ruckenstein. New functional integral approach to strongly correlated fermi systems: The gutzwiller approximation as a saddle point. *Phys. Rev. Lett.*, 57:1362–1365, Sep 1986. doi: 10.1103/PhysRevLett.57.1362. URL https://link.aps.org/doi/10.1103/PhysRevLett.57.1362.

[157] H. R. Krishna-murthy, J. W. Wilkins, and K. G. Wilson. Renormalization-group approach to the anderson model of dilute magnetic alloys. i. static properties for the symmetric case. *Phys. Rev. B*, 21:1003–1043, Feb 1980. doi: 10.1103/PhysRevB.21.1003. URL https://link.aps.org/doi/10.1103/PhysRevB.21.1003.

[158] H. R. Krishna-murthy, J. W. Wilkins, and K. G. Wilson. Renormalization-group approach to the anderson model of dilute magnetic alloys. ii. static properties for the asymmetric case. *Phys. Rev. B*, 21:1044–1083, Feb 1980. doi: 10.1103/PhysRevB.21.1044. URL https://link.aps.org/doi/10.1103/PhysRevB.21.1044.

[159] N. Laflorencie. Quantum entanglement in condensed matter systems. *Physics Reports*, 646: 1 – 59, 2016. ISSN 0370-1573. doi: https://doi.org/10.1016/j.physrep.2016.06.008. URL http://www.sciencedirect.com/science/article/pii/S0370157316301582. Quantum entanglement in condensed matter systems.

[160] L. Laloux, A. Georges, and W. Krauth. Effect of a magnetic field on mott-hubbard systems. *Phys. Rev. B*, 50:3092–3102, Aug 1994. doi: 10.1103/PhysRevB.50.3092. URL https://link.aps.org/doi/10.1103/PhysRevB.50.3092.

[161] N. Lanatà and H. U. R. Strand. Time-dependent and steady-state gutzwiller approach for nonequilibrium transport in nanostructures. *Phys. Rev. B*, 86:115310, Sep 2012. doi: 10.1103/PhysRevB.86.115310. URL https://link.aps.org/doi/10.1103/PhysRevB.86.115310.

[162] N. Lanatà, Y. Yao, C.-Z. Wang, K.-M. Ho, and G. Kotliar. Phase diagram and electronic structure of praseodymium and plutonium. *Phys. Rev. X*, 5:011008, Jan 2015. doi: 10.1103/PhysRevX.5.011008. URL https://link.aps.org/doi/10.1103/PhysRevX.5.011008.

[163] N. Lanatà, T.-H. Lee, Y.-X. Yao, and V. Dobrosavljević. Emergent bloch excitations in mott matter. *Phys. Rev. B*, 96:195126, Nov 2017. doi: 10.1103/PhysRevB.96.195126. URL https://link.aps.org/doi/10.1103/PhysRevB.96.195126.

[164] L. Landau and Y. Zeldovich. On the relation between the liquid and the gaseous states of metals. *Acta Phys. Chem. URSS*, 18:194, 1943.

[165] L. D. Landau. The Theory of a Fermi Liquid. *Sov. Phys. JETP*, 3(6):920, 1957. [Zh. Eksp. Teor. Fiz.30,no.6,1058(1956)].

[166] F. Lechermann, A. Georges, G. Kotliar, and O. Parcollet. Rotationally invariant slave-boson formalism and momentum dependence of the quasiparticle weight. *Phys. Rev. B*, 76:155102, Oct 2007. doi: 10.1103/PhysRevB.76.155102. URL https://link.aps.org/doi/10.1103/PhysRevB.76.155102.

[167] M. Lee, J. S. Lim, and R. López. Kondo effect in a quantum dot side-coupled to a topological superconductor. *Phys. Rev. B*, 87:241402, Jun 2013. doi: 10.1103/PhysRevB.87.241402. URL https://link.aps.org/doi/10.1103/PhysRevB.87.241402.

[168] P. A. Lee and N. Nagaosa. Gauge theory of the normal state of high-t_c superconductors. *Phys. Rev. B*, 46:5621–5639, Sep 1992. doi: 10.1103/PhysRevB.46.5621. URL https://link.aps.org/doi/10.1103/PhysRevB.46.5621.

[169] P. A. Lee, N. Nagaosa, and X.-G. Wen. Doping a mott insulator: Physics of high-temperature superconductivity. *Rev. Mod. Phys.*, 78:17–85, Jan 2006. doi: 10.1103/RevModPhys.78.17. URL https://link.aps.org/doi/10.1103/RevModPhys.78.17.

[170] J. Li, S. Jeon, Y. Xie, A. Yazdani, and B. A. Bernevig. Majorana spin in magnetic atomic chain systems. *Phys. Rev. B*, 97:125119, Mar 2018. doi: 10.1103/PhysRevB.97.125119. URL https://link.aps.org/doi/10.1103/PhysRevB.97.125119.

[171] Y. Li, J. Ludwig, T. Low, A. Chernikov, X. Cui, G. Arefe, Y. D. Kim, A. M. van der Zande, A. Rigosi, H. M. Hill, S. H. Kim, J. Hone, Z. Li, D. Smirnov, and T. F. Heinz. Valley splitting and polarization by the zeeman effect in monolayer mose$_2$. *Phys. Rev. Lett.*, 113:266804, Dec 2014. doi: 10.1103/PhysRevLett.113.266804. URL https://link.aps.org/doi/10.1103/PhysRevLett.113.266804.

[172] E. H. Lieb. Two theorems on the hubbard model. *Phys. Rev. Lett.*, 62:1201–1204, Mar 1989. doi: 10.1103/PhysRevLett.62.1201. URL https://link.aps.org/doi/10.1103/PhysRevLett.62.1201.

[173] E. H. Lieb and F. Y. Wu. Absence of mott transition in an exact solution of the short-range, one-band model in one dimension. *Phys. Rev. Lett.*, 20:1445–1448, Jun 1968. doi: 10.1103/PhysRevLett.20.1445. URL https://link.aps.org/doi/10.1103/PhysRevLett.20.1445.

[174] D. E. Liu and H. U. Baranger. Detecting a majorana-fermion zero mode using a quantum dot. *Phys. Rev. B*, 84:201308, Nov 2011. doi: 10.1103/PhysRevB.84.201308. URL https://link.aps.org/doi/10.1103/PhysRevB.84.201308.

[175] R. López, M. Lee, L. m. c. Serra, and J. S. Lim. Thermoelectrical detection of majorana states. *Phys. Rev. B*, 89:205418, May 2014. doi: 10.1103/PhysRevB.89.205418. URL https://link.aps.org/doi/10.1103/PhysRevB.89.205418.

[176] M. F. Ludovico and M. Capone. Enhanced performance of a quantum-dot-based nanomotor due to coulomb interactions. *Phys. Rev. B*, 98:235409, Dec 2018. doi: 10.1103/PhysRevB.98.235409. URL https://link.aps.org/doi/10.1103/PhysRevB.98.235409.

[177] Y. LUH. Bound state in superconductors with paramagnetic impurities. *Acta Physica Sinica*, 21(1):75, 1965. URL http://wulixb.iphy.ac.cn/CN/abstract/article_851.shtml.

[178] R. M. Lutchyn, E. P. A. M. Bakkers, L. P. Kouwenhoven, P. Krogstrup, C. M. Marcus, and Y. Oreg. Majorana zero modes in superconductor–semiconductor heterostructures. *Nature Reviews Materials*, 3(5):52–68, 2018. doi: 10.1038/s41578-018-0003-1. URL https://doi.org/10.1038/s41578-018-0003-1.

[179] G. D. Mahan. Excitons in degenerate semiconductors. *Phys. Rev.*, 153:882–889, Jan 1967. doi: 10.1103/PhysRev.153.882. URL https://link.aps.org/doi/10.1103/PhysRev.153.882.

[180] E. Majorana. Teoria simmetrica dell'elettrone e del positrone. *Il Nuovo Cimento (1924-1942)*, 14(4):171, Sep 2008. ISSN 1827-6121. doi: 10.1007/BF02961314. URL https://doi.org/10.1007/BF02961314.

[181] K. F. Mak, K. He, J. Shan, and T. F. Heinz. Control of valley polarization in monolayer mos2 by optical helicity. *Nature Nanotechnology*, 7:494 EP –, 06 2012. URL https://doi.org/10.1038/nnano.2012.96.

[182] J. Martínez-Blanco, C. Nacci, S. C. Erwin, K. Kanisawa, E. Locane, M. Thomas, F. von Oppen, P. W. Brouwer, and F. Stefan. Gating a single-molecule transistor with individual atoms. *Nature Physics*, 11:640–644, 2015. doi: 10.1038/nphys3385. URL https://doi.org/10.1038/nphys3385.

[183] P. Maślanka. Symmetry breaking in the lattice gauge theory in infinite dimensions. *Acta Phys. Pol.*, B19:269, 1988.

[184] G. Mazza. From sudden quench to adiabatic dynamics in the attractive hubbard model. *Phys. Rev. B*, 96:205110, Nov 2017. doi: 10.1103/PhysRevB.96.205110. URL https://link.aps.org/doi/10.1103/PhysRevB.96.205110.

[185] P. Mehta and N. Andrei. Nonequilibrium transport in quantum impurity models: The bethe ansatz for open systems. *Phys. Rev. Lett.*, 96(21):216802, Jun 2006. doi: 10.1103/PhysRevLett.96.216802.

[186] Y. Meir, N. S. Wingreen, and P. A. Lee. Low-temperature transport through a quantum dot: The anderson model out of equilibrium. *Phys. Rev. Lett.*, 70:2601–2604, Apr 1993. doi: 10.1103/PhysRevLett.70.2601. URL https://link.aps.org/doi/10.1103/PhysRevLett.70.2601.

[187] W. Metzner and D. Vollhardt. Correlated lattice fermions in $d = \infty$ dimensions. *Phys. Rev. Lett.*, 62:324–327, Jan 1989. doi: 10.1103/PhysRevLett.62.324. URL https://link.aps.org/doi/10.1103/PhysRevLett.62.324.

[188] W. Metzner, M. Salmhofer, C. Honerkamp, V. Meden, and K. Schönhammer. Functional renormalization group approach to correlated fermion systems. *Rev. Mod. Phys.*, 84:299–352, Mar 2012. doi: 10.1103/RevModPhys.84.299. URL https://link.aps.org/doi/10.1103/RevModPhys.84.299.

[189] Mihály, L. and Zawadowski, A. Fermi liquid theory of the degenerate anderson model. *J. Physique Lett.*, 39(24):483–486, 1978. doi: 10.1051/jphyslet:019780039024048300. URL https://doi.org/10.1051/jphyslet:019780039024048300.

[190] F. Ming, S. Johnston, D. Mulugeta, T. S. Smith, P. Vilmercati, G. Lee, T. A. Maier, P. C. Snijders, and H. H. Weitering. Realization of a hole-doped mott insulator on a triangular silicon lattice. *Phys. Rev. Lett.*, 119:266802, Dec 2017. doi: 10.1103/PhysRevLett.119.266802. URL https://link.aps.org/doi/10.1103/PhysRevLett.119.266802.

[191] M. Moeckel and S. Kehrein. Interaction quench in the hubbard model. *Phys. Rev. Lett.*, 100:175702, May 2008. doi: 10.1103/PhysRevLett.100.175702. URL https://link.aps.org/doi/10.1103/PhysRevLett.100.175702.

[192] C. Mora. Fermi-liquid theory for SU(n) kondo model. *Phys. Rev. B*, 80:125304, Sep 2009. doi: 10.1103/PhysRevB.80.125304. URL https://link.aps.org/doi/10.1103/PhysRevB.80.125304.

[193] C. Mora, X. Leyronas, and N. Regnault. Current noise through a kondo quantum dot in a SU(n) fermi liquid state. *Phys. Rev. Lett.*, 100:036604, Jan 2008. doi: 10.1103/PhysRevLett.100.036604. URL https://link.aps.org/doi/10.1103/PhysRevLett.100.036604.

[194] C. Mora, C. u. u. u. u. P. m. c. Moca, J. von Delft, and G. Zaránd. Fermi-liquid theory for the single-impurity anderson model. *Phys. Rev. B*, 92:075120, Aug 2015. doi: 10.1103/PhysRevB.92.075120. URL https://link.aps.org/doi/10.1103/PhysRevB.92.075120.

[195] A. Moreo and D. J. Scalapino. Cold attractive spin polarized fermi lattice gases and the doped positive u hubbard model. *Phys. Rev. Lett.*, 98:216402, May 2007. doi: 10.1103/PhysRevLett.98.216402. URL https://link.aps.org/doi/10.1103/PhysRevLett.98.216402.

[196] N. F. Mott. The basis of the electron theory of metals, with special reference to the transition metals. *Proceedings of the Physical Society. Section A*, 62(7):416, 1949. URL http://stacks.iop.org/0370-1298/62/i=7/a=303.

[197] N. F. Mott. The basis of the electron theory of metals, with special reference to the transition metals. *Proceedings of the Physical Society. Section A*, 62(7):416–422, jul 1949. doi: 10.1088/0370-1298/62/7/303. URL https://doi.org/10.1088%2F0370-1298%2F62%2F7%2F303.

[198] N. F. Mott. Metal-insulator transitions. *Contemporary Physics*, 14(5):401–413, 1973. doi: 10.1080/00107517308210764. URL https://doi.org/10.1080/00107517308210764.

[199] V. Mourik, K. Zuo, S. M. Frolov, S. R. Plissard, E. P. A. M. Bakkers, and L. P. Kouwenhoven. Signatures of majorana fermions in hybrid superconductor-semiconductor nanowire devices. *Science*, 336(6084):1003–1007, 2012. ISSN 0036-8075. doi: 10.1126/science.1222360. URL https://science.sciencemag.org/content/336/6084/1003.

[200] T. Mueller and E. Malic. Exciton physics and device application of two-dimensional transition metal dichalcogenide semiconductors. *npj 2D Materials and Applications*, 2(1):29, 2018. doi: 10.1038/s41699-018-0074-2. URL https://doi.org/10.1038/s41699-018-0074-2.

[201] A. Murani, A. Kasumov, S. Sengupta, Y. A. Kasumov, V. T. Volkov, I. I. Khodos, F. Brisset, R. Delagrange, A. Chepelianskii, R. Deblock, H. Bouchiat, and S. Guéron. Ballistic edge states in bismuth nanowires revealed by squid interferometry. *Nature Communications*, 8:15941 EP –, 07 2017. URL https://doi.org/10.1038/ncomms15941.

[202] A. Nava, R. Giuliano, G. Campagnano, and D. Giuliano. Transfer matrix approach to the persistent current in quantum rings: Application to hybrid normal-superconducting rings. *Phys. Rev. B*, 94:205125, Nov 2016. doi: 10.1103/PhysRevB.94.205125. URL https://link.aps.org/doi/10.1103/PhysRevB.94.205125.

[203] A. Nava, R. Giuliano, G. Campagnano, and D. Giuliano. Persistent current and zero-energy majorana modes in a p-wave disordered superconducting ring. *Phys. Rev. B*, 95:155449,

Apr 2017. doi: 10.1103/PhysRevB.95.155449. URL https://link.aps.org/doi/10.1103/PhysRevB.95.155449.

[204] C. Nayak, S. H. Simon, A. Stern, M. Freedman, and S. Das Sarma. Non-abelian anyons and topological quantum computation. *Rev. Mod. Phys.*, 80:1083–1159, Sep 2008. doi: 10.1103/RevModPhys.80.1083. URL https://link.aps.org/doi/10.1103/RevModPhys.80.1083.

[205] Y. V. Nazarov and Y. M. Blanter. *Quantum Transport: Introduction to Nanoscience*. Cambridge University Press, 2009. doi: 10.1017/CBO9780511626906.

[206] D. Newns and N. Read. Mean-field theory of intermediate valence/heavy fermion systems. *Advances in Physics*, 36(6):799–849, 1987. doi: 10.1080/00018738700101082. URL http://dx.doi.org/10.1080/00018738700101082.

[207] T. K. Ng and P. A. Lee. On-site coulomb repulsion and resonant tunneling. *Phys. Rev. Lett.*, 61(15):1768–1771, Oct 1988. doi: 10.1103/PhysRevLett.61.1768.

[208] F. Nichele, A. C. C. Drachmann, A. M. Whiticar, E. C. T. O'Farrell, H. J. Suominen, A. Fornieri, T. Wang, G. C. Gardner, C. Thomas, A. T. Hatke, P. Krogstrup, M. J. Manfra, K. Flensberg, and C. M. Marcus. Scaling of majorana zero-bias conductance peaks. *Phys. Rev. Lett.*, 119:136803, Sep 2017. doi: 10.1103/PhysRevLett.119.136803. URL https://link.aps.org/doi/10.1103/PhysRevLett.119.136803.

[209] J. Nilsson, A. R. Akhmerov, and C. W. J. Beenakker. Splitting of a cooper pair by a pair of majorana bound states. *Phys. Rev. Lett.*, 101:120403, Sep 2008. doi: 10.1103/PhysRevLett.101.120403. URL https://link.aps.org/doi/10.1103/PhysRevLett.101.120403.

[210] P. Nordlander, M. Pustilnik, Y. Meir, N. S. Wingreen, and D. C. Langreth. How long does it take for the kondo effect to develop? *Phys. Rev. Lett.*, 83:808–811, Jul 1999. doi: 10.1103/PhysRevLett.83.808. URL https://link.aps.org/doi/10.1103/PhysRevLett.83.808.

[211] P. Nozières. *Theory of interacting Fermi systems*. Advanced book classics. Addison-Wesley, Reading, MA, 1964. URL https://cds.cern.ch/record/362749.

[212] P. Nozières. A "fermi-liquid" description of the kondo problem at low temperatures. *Journal of Low Temperature Physics*, 17(1):31–42, Oct 1974. ISSN 1573-7357. doi: 10.1007/BF00654541. URL https://doi.org/10.1007/BF00654541.

[213] P. Nozières and S. Schmitt-Rink. Bose condensation in an attractive fermion gas: From weak to strong coupling superconductivity. *Journal of Low Temperature Physics*, 59(3):195–211, May 1985. ISSN 1573-7357. doi: 10.1007/BF00683774. URL http://dx.doi.org/10.1007/BF00683774.

[214] Nozières, P. and Blandin, A. Kondo effect in real metals. *J. Phys. France*, 41(3):193–211, 1980. doi: 10.1051/jphys:01980004103019300. URL https://doi.org/10.1051/jphys:01980004103019300.

[215] E. v. Oelsen, G. Seibold, and J. Bünemann. Time-dependent gutzwiller theory for multiband hubbard models. *Phys. Rev. Lett.*, 107:076402, Aug 2011. doi: 10.1103/PhysRevLett.107.076402. URL http://link.aps.org/doi/10.1103/PhysRevLett.107.076402.

[216] Y. Oreg, G. Refael, and F. von Oppen. Helical liquids and majorana bound states in quantum wires. *Phys. Rev. Lett.*, 105:177002, Oct 2010. doi: 10.1103/PhysRevLett.105.177002. URL https://link.aps.org/doi/10.1103/PhysRevLett.105.177002.

[217] R. Orús. A practical introduction to tensor networks: Matrix product states and projected entangled pair states. *Annals of Physics*, 349:117 – 158, 2014. ISSN 0003-4916. doi: https://doi.org/10.1016/j.aop.2014.06.013. URL http://www.sciencedirect.com/science/article/pii/S0003491614001596.

[218] Y. Pan, J. Yang, S. C. Erwin, K. Kanisawa, and S. Fölsch. Reconfigurable quantum-dot molecules created by atom manipulation. *Phys. Rev. Lett.*, 115:076803, Aug 2015. doi: 10.1103/PhysRevLett.115.076803. URL https://link.aps.org/doi/10.1103/PhysRevLett.115.076803.

[219] S. Park, N. Mutz, T. Schultz, S. Blumstengel, A. Han, A. Aljarb, L.-J. Li, E. J. W. List-Kratochvil, P. Amsalem, and N. Koch. Direct determination of monolayer MoS2 and WSe2 exciton binding energies on insulating and metallic substrates. *2D Materials*, 5(2): 025003, jan 2018. doi: 10.1088/2053-1583/aaa4ca. URL https://doi.org/10.1088%2F2053-1583%2Faaa4ca.

[220] Y. Peng, F. Pientka, Y. Vinkler-Aviv, L. I. Glazman, and F. von Oppen. Robust majorana conductance peaks for a superconducting lead. *Phys. Rev. Lett.*, 115:266804, Dec 2015. doi: 10.1103/PhysRevLett.115.266804. URL https://link.aps.org/doi/10.1103/PhysRevLett.115.266804.

[221] F. Pientka, A. Romito, M. Duckheim, Y. Oreg, and F. von Oppen. Signatures of topological phase transitions in mesoscopic superconducting rings. *New Journal of Physics*, 15(2): 025001, feb 2013. doi: 10.1088/1367-2630/15/2/025001. URL https://doi.org/10.1088%2F1367-2630%2F15%2F2%2F025001.

[222] E. A. A. Pogna, M. Marsili, D. De Fazio, S. Dal Conte, C. Manzoni, D. Sangalli, D. Yoon, A. Lombardo, A. C. Ferrari, A. Marini, G. Cerullo, and D. Prezzi. Photo-induced bandgap renormalization governs the ultrafast response of single-layer mos2. *ACS Nano*, 10(1): 1182–1188, 01 2016. doi: 10.1021/acsnano.5b06488. URL https://doi.org/10.1021/acsnano.5b06488.

[223] A. Polkovnikov, K. Sengupta, A. Silva, and M. Vengalattore. Colloquium: Nonequilibrium dynamics of closed interacting quantum systems. *Rev. Mod. Phys.*, 83:863–883, Aug 2011. doi: 10.1103/RevModPhys.83.863. URL https://link.aps.org/doi/10.1103/RevModPhys.83.863.

[224] V. N. Popov and S. A. Fedotov. The functional-integration method and diagram technique for spin systems. *Sov. Phys. JETP*, 67(3):535, 1988. [Zh. Eksp. Teor. Fiz. 67,no.3,535(1988)].

[225] M. Pustilnik and L. Glazman. Kondo effect in quantum dots. *Journal of Physics: Condensed Matter*, 16(16):R513–R537, apr 2004. doi: 10.1088/0953-8984/16/16/r01. URL https://doi.org/10.1088%2F0953-8984%2F16%2F16%2Fr01.

[226] A. Rahmani, X. Zhu, M. Franz, and I. Affleck. Phase diagram of the interacting majorana chain model. *Phys. Rev. B*, 92:235123, Dec 2015. doi: 10.1103/PhysRevB.92.235123. URL https://link.aps.org/doi/10.1103/PhysRevB.92.235123.

[227] A. Rahmani, X. Zhu, M. Franz, and I. Affleck. Emergent supersymmetry from strongly interacting majorana zero modes. *Phys. Rev. Lett.*, 115:166401, Oct 2015. doi: 10.1103/PhysRevLett.115.166401. URL https://link.aps.org/doi/10.1103/PhysRevLett.115.166401.

[228] R. Raimondi and P. Schwab. Andreev tunneling in strongly interacting quantum dots. *Superlattices and Microstructures*, 25(5):1141 – 1153, 1999. ISSN 0749-6036. doi: https://doi.org/10.1006/spmi.1999.0723. URL http://www.sciencedirect.com/science/article/pii/S0749603699907231.

[229] J. Rammer. *Quantum Field Theory of Non-equilibrium States*. Cambridge University Press, 2007. doi: 10.1017/CBO9780511618956.

[230] J. Rammer and H. Smith. Quantum field-theoretical methods in transport theory of metals. *Rev. Mod. Phys.*, 58:323–359, Apr 1986. doi: 10.1103/RevModPhys.58.323. URL https://link.aps.org/doi/10.1103/RevModPhys.58.323.

[231] M. Rasetti. *The Hubbard Model: Recent Results*. Series on advances in statistical mechanics. World Scientific, 1991. ISBN 9789810206239. URL https://books.google.it/books?id=pIpwtAEACAAJ.

[232] N. Read. Role of infrared divergences in the 1/n expansion of the u=∞ anderson model. *Journal of Physics C: Solid State Physics*, 18(13):2651–2665, may 1985. doi: 10.1088/0022-3719/18/13/012. URL https://doi.org/10.1088%2F0022-3719%2F18%2F13%2F012.

[233] N. Read and D. Green. Paired states of fermions in two dimensions with breaking of parity and time-reversal symmetries and the fractional quantum hall effect. *Phys. Rev. B*, 61:10267–10297, Apr 2000. doi: 10.1103/PhysRevB.61.10267. URL https://link.aps.org/doi/10.1103/PhysRevB.61.10267.

[234] T. Rice. The electron-hole liquid in semiconductors: Theoretical aspects. volume 32 of *Solid State Physics*, pages 1 – 86. Academic Press, 1978. doi: https://doi.org/10.1016/S0081-1947(08)60438-5. URL http://www.sciencedirect.com/science/article/pii/S0081194708604385.

[235] T. M. Rice and K. Ueda. Gutzwiller method for heavy electrons. *Phys. Rev. B*, 34:6420–6427, Nov 1986. doi: 10.1103/PhysRevB.34.6420. URL https://link.aps.org/doi/10.1103/PhysRevB.34.6420.

[236] S. Rommer and S. Östlund. Class of ansatz wave functions for one-dimensional spin systems and their relation to the density matrix renormalization group. *Phys. Rev. B*, 55:2164–2181, Jan 1997. doi: 10.1103/PhysRevB.55.2164. URL https://link.aps.org/doi/10.1103/PhysRevB.55.2164.

[237] A. Rosch, J. Paaske, J. Kroha, and P. Wölfle. Nonequilibrium transport through a Kondo dot in a magnetic field: Perturbation theory and poor man's scaling. *Phys. Rev. Lett.*, 90(7):076804, Feb 2003. doi: 10.1103/PhysRevLett.90.076804.

[238] A. Rosch, D. Rasch, B. Binz, and M. Vojta. Metastable superfluidity of repulsive fermionic atoms in optical lattices. *Phys. Rev. Lett.*, 101:265301, Dec 2008. doi: 10.1103/PhysRevLett.101.265301. URL https://link.aps.org/doi/10.1103/PhysRevLett.101.265301.

[239] G. Rossbach, J. Levrat, G. Jacopin, M. Shahmohammadi, J.-F. Carlin, J.-D. Ganière, R. Butté, B. Deveaud, and N. Grandjean. High-temperature mott transition in wide-band-gap semiconductor quantum wells. *Phys. Rev. B*, 90:201308(R), Nov 2014. doi: 10.1103/PhysRevB.90.201308. URL https://link.aps.org/doi/10.1103/PhysRevB.90.201308.

[240] A. Rüegg, S. D. Huber, and M. Sigrist. z_2-slave-spin theory for strongly correlated fermions. *Phys. Rev. B*, 81:155118, Apr 2010. doi: 10.1103/PhysRevB.81.155118. URL https://link.aps.org/doi/10.1103/PhysRevB.81.155118.

[241] C. Ruppert, A. Chernikov, H. M. Hill, A. F. Rigosi, and T. F. Heinz. The role of electronic and phononic excitation in the optical response of monolayer ws2 after ultrafast excitation. *Nano Letters*, 17(2):644–651, 2017. doi: 10.1021/acs.nanolett.6b03513. URL https://doi.org/10.1021/acs.nanolett.6b03513. PMID: 28059520.

[242] A. Rusinov. Superconductivity near a paramagnetic impurity. *JETP Lett. (USSR) (Engl. Transl.); (United States)*, 9, 1 1969.

[243] M. Sandri and M. Fabrizio. Nonequilibrium dynamics in the antiferromagnetic hubbard model. *Phys. Rev. B*, 88:165113, Oct 2013. doi: 10.1103/PhysRevB.88.165113. URL https://link.aps.org/doi/10.1103/PhysRevB.88.165113.

[244] F. Schindler, Z. Wang, M. G. Vergniory, A. M. Cook, A. Murani, S. Sengupta, A. Y. Kasumov, R. Deblock, S. Jeon, I. Drozdov, H. Bouchiat, S. Guéron, A. Yazdani, B. A. Bernevig, and T. Neupert. Higher-order topology in bismuth. *Nature Physics*, 14(9):918–924, 2018. doi: 10.1038/s41567-018-0224-7. URL https://doi.org/10.1038/s41567-018-0224-7.

[245] M. Schiró. Nonequilibrium dynamics across an impurity quantum critical point due to quantum quenches. *Phys. Rev. B*, 86:161101, Oct 2012. doi: 10.1103/PhysRevB.86.161101. URL https://link.aps.org/doi/10.1103/PhysRevB.86.161101.

[246] M. Schiró and M. Fabrizio. Real-time diagrammatic monte carlo for nonequilibrium quantum transport. *Phys. Rev. B*, 79:153302, Apr 2009. doi: 10.1103/PhysRevB.79.153302. URL https://link.aps.org/doi/10.1103/PhysRevB.79.153302.

[247] M. Schiró and M. Fabrizio. Time-dependent mean field theory for quench dynamics in correlated electron systems. *Phys. Rev. Lett*, 105(7):076401, 2010.

[248] M. Schiró and M. Fabrizio. Quantum quenches in the hubbard model: Time-dependent mean-field theory and the role of quantum fluctuations. *Phys. Rev. B*, 83:165105, Apr 2011. doi: 10.1103/PhysRevB.83.165105.

[249] P. Schmitteckert. Nonequilibrium electron transport using the density matrix renormalization group method. *Phys. Rev. B*, 70:121302, Sep 2004. doi: 10.1103/PhysRevB.70.121302. URL https://link.aps.org/doi/10.1103/PhysRevB.70.121302.

[250] P. Schmitteckert and F. Evers. Charge susceptibility in kondo systems at half filling: Dmrg study. *Annalen der Physik*, 524(3-4):L1–L4, 2012. doi: 10.1002/andp.201100298. URL https://onlinelibrary.wiley.com/doi/abs/10.1002/andp.201100298.

[251] H. Schoeller. A perturbative nonequilibrium renormalization group method for dissipative quantum mechanics. *The European Physical Journal Special Topics*, 168(1):179–266, Feb 2009. ISSN 1951-6401. doi: 10.1140/epjst/e2009-00962-3. URL https://doi.org/10.1140/epjst/e2009-00962-3.

[252] K. Schönhammer. Variational results as saddle-point approximations: The anderson impurity model. *Phys. Rev. B*, 42:2591–2593, Aug 1990. doi: 10.1103/PhysRevB.42.2591. URL https://link.aps.org/doi/10.1103/PhysRevB.42.2591.

[253] G. Seibold and J. Lorenzana. Time-Dependent Gutzwiller Approximation for the Hubbard Model. *Phys. Rev. Lett.*, 86:2605, 2001. doi: 10.1103/PhysRevLett.86.2605.

[254] F. Sekiguchi and R. Shimano. Rate equation analysis of the dynamics of first-order exciton mott transition. *Journal of the Physical Society of Japan*, 86(10):103702, 2017. doi: 10.7566/JPSJ.86.103702. URL https://doi.org/10.7566/JPSJ.86.103702.

[255] F. Sekiguchi, T. Mochizuki, C. Kim, H. Akiyama, L. N. Pfeiffer, K. W. West, and R. Shimano. Anomalous metal phase emergent on the verge of an exciton mott transition. *Phys. Rev. Lett.*, 118:067401, Feb 2017. doi: 10.1103/PhysRevLett.118.067401. URL https://link.aps.org/doi/10.1103/PhysRevLett.118.067401.

[256] E. Sela, Y. Oreg, F. von Oppen, and J. Koch. Fractional shot noise in the kondo regime. *Phys. Rev. Lett.*, 97:086601, Aug 2006. doi: 10.1103/PhysRevLett.97.086601. URL https://link.aps.org/doi/10.1103/PhysRevLett.97.086601.

[257] E. Sela, Y. Oreg, F. von Oppen, and J. Koch. Fractional shot noise in the kondo regime. *Phys. Rev. Lett.*, 97:086601, Aug 2006. doi: 10.1103/PhysRevLett.97.086601. URL https://link.aps.org/doi/10.1103/PhysRevLett.97.086601.

[258] G. Shankar and J. Maciejko. Exactly solvable majorana-anderson impurity models. arXiv:1905.06983, 2019.

[259] H. Shiba. Classical Spins in Superconductors. *Progress of Theoretical Physics*, 40(3):435–451, 09 1968. ISSN 0033-068X. doi: 10.1143/PTP.40.435. URL https://doi.org/10.1143/PTP.40.435.

[260] Y. Shimazaki, M. Yamamoto, I. V. Borzenets, K. Watanabe, T. Taniguchi, and S. Tarucha. Generation and detection of pure valley current by electrically induced berry curvature in bilayer graphene. *Nature Physics*, 11:1032 EP –, 11 2015. URL https://doi.org/10.1038/nphys3551.

[261] R. Shindou, A. Furusaki, and N. Nagaosa. Quantum impurity spin in majorana edge fermions. *Phys. Rev. B*, 82:180505, Nov 2010. doi: 10.1103/PhysRevB.82.180505. URL https://link.aps.org/doi/10.1103/PhysRevB.82.180505.

[262] E. J. Sie, A. Steinhoff, C. Gies, C. H. Lui, Q. Ma, M. Rösner, G. Schönhoff, F. Jahnke, T. O. Wehling, Y.-H. Lee, J. Kong, P. Jarillo-Herrero, and N. Gedik. Observation of exciton redshift–blueshift crossover in monolayer ws2. *Nano Letters*, 17(7):4210–4216, 2017. doi: 10.1021/acs.nanolett.7b01034. URL https://doi.org/10.1021/acs.nanolett.7b01034. PMID: 28621953.

[263] L. M. Sieberer, M. Buchhold, and S. Diehl. Keldysh Field Theory for Driven Open Quantum Systems. *Rept. Prog. Phys.*, 79(9):096001, 2016. doi: 10.1088/0034-4885/79/9/096001.

[264] A. H. Simon, S. J. Kirch, and J. P. Wolfe. Excitonic phase diagram in unstressed ge. *Phys. Rev. B*, 46:10098–10112, Oct 1992. doi: 10.1103/PhysRevB.46.10098. URL https://link.aps.org/doi/10.1103/PhysRevB.46.10098.

[265] L. M. Smith and J. P. Wolfe. Second condensed phase of electron-hole plasma in si. *Phys. Rev. Lett.*, 57:2314–2317, Nov 1986. doi: 10.1103/PhysRevLett.57.2314. URL https://link.aps.org/doi/10.1103/PhysRevLett.57.2314.

[266] L. M. Smith and J. P. Wolfe. Time-resolved study of electron-hole plasmas near the liquid-gas critical point in si: Evidence for a second condensed phase. *Phys. Rev. B*, 51: 7521–7543, Mar 1995. doi: 10.1103/PhysRevB.51.7521. URL https://link.aps.org/doi/10.1103/PhysRevB.51.7521.

[267] F. Stefan, J. Martínez-Blanco, J. Yang, K. Kanisawa, and S. C. Erwin. Quantum dots with single-atom precision. *Nature Nanotechnology*, 9:505–508, 2014. doi: 10.1038/nnano.2014.129. URL https://doi.org/10.1038/nnano.2014.129.

[268] G. Stefanucci and R. van Leeuwen. *Nonequilibrium Many-Body Theory of Quantum Systems: A Modern Introduction*. Cambridge University Press, 2013. doi: 10.1017/CBO9781139023979.

[269] P. Steinleitner, P. Merkl, P. Nagler, J. Mornhinweg, C. Schüller, T. Korn, A. Chernikov, and R. Huber. Direct observation of ultrafast exciton formation in a monolayer of wse2. *Nano Letters*, 17(3):1455–1460, 2017. doi: 10.1021/acs.nanolett.6b04422. URL https://doi.org/10.1021/acs.nanolett.6b04422. PMID: 28182430.

[270] M. Stern, V. Garmider, V. Umansky, and I. Bar-Joseph. Mott transition of excitons in coupled quantum wells. *Phys. Rev. Lett.*, 100:256402, Jun 2008. doi: 10.1103/PhysRevLett.100.256402. URL https://link.aps.org/doi/10.1103/PhysRevLett.100.256402.

[271] T. Suzuki and R. Shimano. Exciton mott transition in si revealed by terahertz spectroscopy. *Phys. Rev. Lett.*, 109:046402, Jul 2012. doi: 10.1103/PhysRevLett.109.046402. URL https://link.aps.org/doi/10.1103/PhysRevLett.109.046402.

[272] C. Tomaras and S. Kehrein. Scaling approach for the time-dependent kondo model. *EPL (Europhysics Letters)*, 93(4):47011, 2011. URL http://stacks.iop.org/0295-5075/93/i=4/a=47011.

[273] A. Tsvelick and P. Wiegmann. Exact results in the theory of magnetic alloys. *Advances in Physics*, 32(4):453–713, 1983. doi: 10.1080/00018738300101581. URL https://doi.org/10.1080/00018738300101581.

[274] M. M. Ugeda, A. J. Bradley, S.-F. Shi, F. H. da Jornada, Y. Zhang, D. Y. Qiu, W. Ruan, S.-K. Mo, Z. Hussain, Z.-X. Shen, F. Wang, S. G. Louie, and M. F. Crommie. Giant bandgap renormalization and excitonic effects in a monolayer transition metal dichalcogenide semiconductor. *Nature Materials*, 13:1091 EP –, 08 2014. URL https://doi.org/10.1038/nmat4061.

[275] A. Umerski. Closed-form solutions to surface green's functions. *Phys. Rev. B*, 55:5266–5275, Feb 1997. doi: 10.1103/PhysRevB.55.5266. URL https://link.aps.org/doi/10.1103/PhysRevB.55.5266.

[276] W. G. van der Wiel, S. D. Franceschi, T. Fujisawa, J. M. Elzerman, S. Tarucha, and L. P. Kouwenhoven. The kondo effect in the unitary limit. *Science*, 289(5487):2105–2108, 2000. ISSN 0036-8075. doi: 10.1126/science.289.5487.2105. URL https://science.sciencemag.org/content/289/5487/2105.

[277] E. Vernek, P. H. Penteado, A. C. Seridonio, and J. C. Egues. Subtle leakage of a majorana mode into a quantum dot. *Phys. Rev. B*, 89:165314, Apr 2014. doi: 10.1103/PhysRevB.89.165314. URL https://link.aps.org/doi/10.1103/PhysRevB.89.165314.

[278] S. Vitiello, K. Runge, and M. H. Kalos. Variational calculations for solid and liquid ^{4}He with a "shadow" wave function. *Phys. Rev. Lett.*, 60:1970–1972, May 1988. doi: 10.1103/PhysRevLett.60.1970. URL https://link.aps.org/doi/10.1103/PhysRevLett.60.1970.

[279] D. Vollhardt. Normal ^{3}He: an almost localized fermi liquid. *Rev. Mod. Phys.*, 56:99–120, Jan 1984. doi: 10.1103/RevModPhys.56.99. URL http://link.aps.org/doi/10.1103/RevModPhys.56.99.

[280] D. Vollhardt, P. Wölfle, and P. W. Anderson. Gutzwiller-hubbard lattice-gas model with variable density: Application to normal liquid ^{3}He. *Phys. Rev. B*, 35:6703–6715, May 1987. doi: 10.1103/PhysRevB.35.6703. URL https://link.aps.org/doi/10.1103/PhysRevB.35.6703.

[281] G. Wang, A. Chernikov, M. M. Glazov, T. F. Heinz, X. Marie, T. Amand, and B. Urbaszek. Colloquium: Excitons in atomically thin transition metal dichalcogenides. *Rev. Mod. Phys.*, 90:021001, Apr 2018. doi: 10.1103/RevModPhys.90.021001. URL https://link.aps.org/doi/10.1103/RevModPhys.90.021001.

[282] G. Wang, A. Chernikov, M. M. Glazov, T. F. Heinz, X. Marie, T. Amand, and B. Urbaszek. Colloquium: Excitons in atomically thin transition metal dichalcogenides. *Rev. Mod. Phys.*, 90:021001, Apr 2018. doi: 10.1103/RevModPhys.90.021001. URL https://link.aps.org/doi/10.1103/RevModPhys.90.021001.

[283] Q. H. Wang, K. Kalantar-Zadeh, A. Kis, J. N. Coleman, and M. S. Strano. Electronics and optoelectronics of two-dimensional transition metal dichalcogenides. *Nature Nanotechnology*, 7:699 EP –, 11 2012. URL https://doi.org/10.1038/nnano.2012.193.

[284] P. Werner, T. Oka, and A. J. Millis. Diagrammatic monte carlo simulation of nonequilibrium systems. *Phys. Rev. B*, 79:035320, 2009. doi: 10.1103/PhysRevB.79.035320.

[285] I. Weymann and K. P. Wójcik. Transport properties of a hybrid majorana wire-quantum dot system with ferromagnetic contacts. *Phys. Rev. B*, 95:155427, Apr 2017. doi: 10.1103/PhysRevB.95.155427. URL https://link.aps.org/doi/10.1103/PhysRevB.95.155427.

[286] S. R. White and A. E. Feiguin. Real-time evolution using the density matrix renormalization group. *Phys. Rev. Lett.*, 93:076401, Aug 2004. doi: 10.1103/PhysRevLett.93.076401. URL https://link.aps.org/doi/10.1103/PhysRevLett.93.076401.

[287] K. G. Wilson. The renormalization group: Critical phenomena and the kondo problem. *Rev. Mod. Phys.*, 47:773–840, Oct 1975. doi: 10.1103/RevModPhys.47.773. URL https://link.aps.org/doi/10.1103/RevModPhys.47.773.

[288] D. Withoff and E. Fradkin. Phase transitions in gapless fermi systems with magnetic impurities. *Phys. Rev. Lett.*, 64:1835–1838, Apr 1990. doi: 10.1103/PhysRevLett.64.1835. URL https://link.aps.org/doi/10.1103/PhysRevLett.64.1835.

[289] J. Xiao, M. Zhao, Y. Wang, and X. Zhang. Excitons in atomically thin 2d semiconductors and their applications. *Nanophotonics*, 6:1309–1328, 2016. URL https://doi.org/10.1515/nanoph-2016-0160.

[290] L. Yuan, T. Wang, T. Zhu, M. Zhou, and L. Huang. Exciton dynamics, transport, and annihilation in atomically thin two-dimensional semiconductors. *The Journal of Physical Chemistry Letters*, 8(14):3371–3379, 07 2017. doi: 10.1021/acs.jpclett.7b00885. URL https://doi.org/10.1021/acs.jpclett.7b00885.

[291] R. Žitko. Open source numerical renormalization group code. http://nrgljubljana.ijs.si/.

[292] A. Zazunov, R. Egger, and A. Levy Yeyati. Low-energy theory of transport in majorana wire junctions. *Phys. Rev. B*, 94:014502, Jul 2016. doi: 10.1103/PhysRevB.94.014502. URL https://link.aps.org/doi/10.1103/PhysRevB.94.014502.

[293] H. Zhang, C.-X. Liu, S. Gazibegovic, D. Xu, J. A. Logan, G. Wang, N. van Loo, J. D. S. Bommer, M. W. A. de Moor, D. Car, R. L. M. Op het Veld, P. J. van Veldhoven, S. Koelling, M. A. Verheijen, M. Pendharkar, D. J. Pennachio, B. Shojaei, J. S. Lee, C. J. Palmstrøm, E. P. A. M. Bakkers, S. D. Sarma, and L. P. Kouwenhoven. Quantized majorana conductance. *Nature*, 556:74 EP –, 03 2018. URL https://doi.org/10.1038/nature26142.

[294] W. Zhu, D. N. Sheng, and J.-X. Zhu. Magnetic field dependent dynamics and field-driven metal-to-insulator transition of the half-filled hubbard model: A dmft+dmrg study. *Phys. Rev. B*, 96:085118, Aug 2017. doi: 10.1103/PhysRevB.96.085118. URL https://link.aps.org/doi/10.1103/PhysRevB.96.085118.